

21<sup>st</sup>

ABAF

BRNO 2020

Advanced Batteries, Accumulators  
and Fuel Cells

INTERNATIONAL CONFERENCE

September 6<sup>th</sup> - September 9<sup>th</sup> 2020

**Organised by:**

**Department of Electrical and Electronic Technology,**  
Faculty of Electrical Engineering and Communication,  
Brno University of Technology

**Organizing committee:**

Marie Sedlářiková  
Tomáš Kazda

co-sponsored by



**Honourary Scientific Committee:**

- Petr Vanýsek, *Northern Illinois University, DeKalb, Illinois, USA*
- Arnaldo Visintin, *INIFTA, La Plata, Argentina*
- Günter Fafílek, *TU Wien, Vienna, Austria*
- Elena Shembel, *USCTU, Dnipro, Ukraine*
- Vito Di Noto, *University of Padova, Padova, Italy*
- Alexei Kornyshev, *Imperial College, London, UK*
- Boris Markovsky, *Bar-Ilan University, Tel Aviv, Israel*
- Philipp Adelhelm, *Friedrich Schiller University, Jena, Germany*
- Laurence Hardwick, *University of Liverpool, Liverpool, UK*
- Renata Oriňáková, *UPJŠ, Košice, Slovakia*
- Grzegorz Lota, *Poznan University of Technology, Poznan, Poland*
- Mariusz Walkowiak, *Institute of Non-Ferrous Metals, Poznan, Poland*

**Organisation Committee:**

- Marie Sedlaříková, *FEEC BUT, Brno, Czech Republic*
- Tomáš Kazda, *FEEC BUT, Brno, Czech Republic*
- František Klein, *Brno, Czech Republic*
- Vítězslav Novák, *FEEC BUT, Brno, Czech Republic*
- Miroslav Zatloukal, *FEEC BUT, Brno, Czech Republic*
- Jiří Libich, *FEEC BUT, Brno, Czech Republic*
- Josef Máca, *FEEC BUT, Brno, Czech Republic*
- Tomáš Binar, *FEEC BUT, Brno, Czech Republic*
- Jiří Švarc, *University of Defence, Brno, Czech Republic*

**Program Committee:**

- Marie Sedlaříková, *FEEC BUT, Brno, Czech Republic*
- Mariusz Walkowiak, *Institute of Non-Ferrous Metals, Poznan, Poland*
- Arnaldo Visintin, *INIFTA, La Plata, Argentina*
- Petr Vanýsek, *Northern Illinois University, DeKalb, Illinois, USA*
- Günter Fafílek, *TU Wien, Vienna, Austria*
- Boris Markovsky, *Bar-Ilan University, Tel Aviv, Israel*
- Alexei Kornyshev, *Imperial College, London, UK*
- Philipp Adelhelm, *Friedrich Schiller University, Jena, Germany*
- Laurence Hardwick, *University of Liverpool, Liverpool, UK*
- Josef Máca, *FEEC BUT, Brno, Czech Republic*
- Vítězslav Novák, *FEEC BUT, Brno, Czech Republic*
- Petr Bača, *FEEC BUT, Brno, Czech Republic*
- Tomáš Kazda, *FEEC BUT, Brno, Czech Republic*
- Helena Polsterová, *FEEC BUT, Brno, Czech Republic*
- Miroslav Zatloukal, *FEEC BUT, Brno, Czech Republic*
- Kristýna Jandová, *FEEC BUT, Brno, Czech Republic*
- Andrea Fedorková-Straková, *UPJŠ, Košice, Slovakia*
- Jiří Libich, *FEEC BUT, Brno, Czech Republic*
- Tomáš Binar, *FEEC BUT, Brno, Czech Republic*
- Jiří Švarc, *University of Defence, Brno, Czech Republic*

Main sponsor:



**CEZ GROUP**

Other sponsors:



co-sponsored by



We would like to express our thanks to the Brno University of Technology, Faculty of Electrical Engineering and Communication for support and help with organising 21<sup>st</sup> ABAF conference.



## Contents

### Lithium Batteries and Related Systems

*Xiaoxue Lu, Ningxin Zhang, Marcus Jahn, Wilhelm Pfleging, Hans J. Seifert*

**A Facile Surface Modification through SiO<sub>2</sub> Coating for Improving the Electrochemical Performance of Ni-rich Cathode Material** .....9

*A. R. Kathribail, J. Kahr, A. Rezqita, M. Jahn, M. Berecibar, J. Van Mierlo, A. Hubin*

**Polymerisation of Furfuryl Alcohol as Carbon Coating Method for LiNi<sub>0.6</sub>Mn<sub>0.2</sub>Co<sub>0.2</sub>O<sub>2</sub> Cathode Materials for High-Performance Lithium-ion Battery Applications**.....10

*L. Kavan*

**Interface Engineering in Energy Conversion and Storage: Case Studies of Titania** .....11

*T. Syrový, T. Kazda, L. Kubáč, L. Syrová*

**Printed electrode layers for Li-ion batteries** .....13

*K. Froehlich, W. Pessenhofer, H. Besser, W. Pfleging, M. Jahn*

**Strategies enhancing the electrochemical performance of NMC811 high energy electrodes for xEV applications**.....16

*B. Eschelmüller, K. Fröhlich, M. Jahn*

**Quantification of critical process parameters of Li-ion pouch cell production** .....18

*Y. Zhang, A. Zülke, M.P. Mercer, D. Csala, H. E. Hoster*

**Lithium-Ion Batteries: from Atomic Scale Processes to Data-driven Diagnostics** .....19

*M. A. Kamenskii, A. I. Vypritskaya, S. N. Eliseeva and V. V. Kondratiev*

**Electrochemical Performance of Co<sub>3</sub>O<sub>4</sub> Anode Material with Conductive Binder** .....22

*E. Shembel, V. Kyrychenko, I. Maksyuta, V. Redko, N. Zaderey*

**Melanin as Semiconductor with Polymer Structure is Effective Modifier for Electrodes of High Energy Li - Ion Batteries**

**Influence structure and nature of melanin on efficiency of cathode based on LiMn<sub>2</sub>O<sub>4</sub>** .....25

*E. Shembel, O. Chervakov, A. Markevych, O. Kolomoiets, I. Maksyuta V. Redko, Y. Polishchuk, N. Zaderey, V. Pysny, N. Koltsov*

**Solid Polymer Electrolytes and Modified Electrodes are Basis for New Generation of High-Energy Lithium Batteries**

**Safety, Wide Operating Temperature, High Energy, and Low Price**.....29

*D. Kunicky, L. Chladil*

**Comparison of High-Voltage Cathode Materials for Lithium-ion Batteries** .....30

*J. Maca, J. Libich, T. Kazda and K. Jasso*

**Flame retardant influence on Negative Electrode for Lithium ion accumulators**.....33

*S. S. Madani*

**A Review of Mechanical Stress on Lithium-ion cells** .....35

|   |           |
|---|-----------|
| <i>S. S. Madani</i><br><b>Characterization of Lithium-Ion Battery Cells .....</b>   | <b>38</b> |
| <i>S. S. Madani, E. Schaltz and S. K. Kær</i><br><b>Study of the Effect of External Compressive Loads on the Performance of a Lithium-ion Cell .....</b>  | <b>41</b> |
| <i>A.V. Potapenko, Y.A. Kravets, S. A. Kirillov</i><br><b>Enhancing electrochemical properties of LiMn<sub>2</sub>O<sub>4</sub>/LiNi<sub>0.5</sub>Mn<sub>1.5</sub>O<sub>4</sub> core/shell composites .....</b>                               | <b>46</b> |
| <i>R.D. Apostolova, E.M. Shembel</i><br><b>Electrolytically synthesized K,Na,V-oxide compounds for Li-batteries .....</b>   | <b>49</b> |
| <i>Amrit Kumar Thakur</i><br><b>A State of Art Critical Review on Advancement in Mxenes for Lithium and Sodium Ion Batteries in the view of Atomic Layer Spacing .....</b>  | <b>52</b> |
| <i>I. Veselkova, M. Sedlarikova</i><br><b>Electrochemical characterization of gel polymer electrolyte used in lithium-ion batteries .....</b>   | <b>53</b> |
| <br><b>Supercapacitors</b>  |           |
| <i>R. Holze</i><br><b>Active masses for supercapacitor electrodes based on copolymers and composites of redox-active comonomers and intrinsically conducting polymers .....</b>   | <b>56</b> |
| <i>Le Quoc Bao, Haojie Fei, Constantin Bubulinca, Fahanwi Asabuwa Ngwabeboh, Natalia E. Kazantseva, Petr Saha</i><br><b>Reduced Graphene Oxide Compositated with amorphous Ni-MOF and PANI applied as electrodes for Supercapacitor .....</b> | <b>60</b> |
| <br><b>Fuel Cells</b>   |           |
| <i>M. Mika, D. I. Oren and J. Michal</i><br><b>New Hybrid Phospho-Siloxane Membranes for H<sub>2</sub>/O<sub>2</sub> Fuel Cells .....</b>   | <b>61</b> |
| <i>I. A. Rusetskyi, L. L. Kovalenko, I. A. Slobodyanyuk, M. O. Danilov, S. S. Fomanyuk, V. O. Smilyk, A. G. Belous, G.Ya. Kolbasov</i><br><b>Photoelectrochemical Systems for Hydrogen Evolution Using Ion-Conducting Membranes .....</b>     | <b>66</b> |
| <br><b>Aqueous Batteries</b>  |           |
| <i>P. Mazúr, D. Muller, J. Kvičala, J. Vrána, Z. Burešová, M. Klikar, F. Bureš</i><br><b>Quinone and viologen derivatives for aqueous redox flow battery electrolytes .....</b>   | <b>69</b> |
| <i>J. Mrlík, P. Mazúr, J. Pociďič, J. Vrána, J. Dundálek, J. Charvát, J. Kosek</i><br><b>Deactivation of negative felt electrode of vanadium redox flow battery: Double half-cell set-up experiments .....</b>                                | <b>70</b> |

|   |     |
|---|-----|
| <i>A. Bulat, E. Shembel, Y. Polishchuk, B. Blyuss, V. Redko, N. Zaderey</i><br><b>Synergistic Effect of Nanotechnology and Optimized Industrial Manufacturing Process for Lead Electrodes Enhances the Performance of Lead-Acid Batteries</b> ..... | 71  |
| <i>P. Krivik, S. Vaculik, P. Bača, J. Kazelle</i><br><b>Influence of temperature on impedance changes of lead-acid battery cell</b> .....   | 75  |
| <i>O. I. Bilan and R. K. Nafeev</i><br><b>The Technological Aspects of Iron Electrode Material</b> .....  | 79  |
| <i>L. Chladil, J. Smejkal and T. Bannert</i><br><b>Effect of Surfactants to Decomposition of Supersaturated Zinc Electrolytes in Ni-Zn Battery</b> .....  | 82  |
| <b>New Systems of Batteries</b>   |     |
| <i>T. Kazda, M. Kekelák, P. Čudek</i><br><b>Influence of the water-soluble binders to the properties of Li-S batteries</b> .....  | 85  |
| <i>J. Amici, D. Versaci, C. Torchio, A. Marchisio, R. Colombo, F. Bella, C. Francia and S. Bodoardo</i><br><b>Solid Composite Polymer Electrolytes for High Energy Density and Safe Lithium Metal Cells</b> .....                                   | 87  |
| <i>M. Zúkalová</i><br><b>Novel inorganic host materials for Li-S batteries</b> .....  | 88  |
| <i>A. Straková Fedorková, D. Capková, T. Kazda, K. Gavalierová, M. Sedlaříková, P. Gómez-Romero, E. Shembel</i><br><b>Development of New Cathodes for Stable and Safer Lithium-Sulphur Batteries – results of NATO SPS research project</b> .....   | 90  |
| <i>O. Čech, O. Klvač, T. Kazda, P. Čudek</i><br><b>Inverse Vulcanization of Sulfur – Amorphous Electroactive Polymer for Li-S Batteries</b> .....   | 92  |
| <i>D. Capková, T. Kazda and A. Straková Fedorková</i><br><b>Alternative Binder for Lithium-Sulfur Batteries</b> .....   | 95  |
| <i>O. Čech, P. Benešová, P. Čudek, T. Kazda</i><br><b>Anatase as Anode for Sodium-Ion Cells</b> .....   | 98  |
| <i>K. Jaššo, P. Čudek, T. Kazda</i><br><b>Xanthan gum as the Binder for the Lithium-Sulfur Batteries</b> .....  | 101 |
| <i>N. I. Globa, V. A. Sirosh, Yu. V. Shmatok, S. A. Kirillov</i><br><b>Enhancing of electrochemical characteristics of Li-S system by means of optimization of sulfur electrode and electrolyte composition</b> .....                               | 104 |
| <i>J. Libich, M. Sedlaříková, J. Máca, P. Čudek, Michal Fíbek, A. Chekannikov and G. Fafílek</i><br><b>Intercalation Properties of Expanded Graphite Electrode in Lithium-Ion Battery</b> .....   | 107 |
| <i>Y. Polishchuk, E. Shembel, A. Straková Fedorková</i><br><b>Polymer Structure of Sulfur Ensures Low Self Discharge of Li-S Primary and Secondary Batteries. Synergistic Effect of Sulfur Structure and Design of Sulfur Electrode</b> .....       | 109 |

## Photovoltaics

*P. Maule, J. Vanek and K. Jandova*

**Development of recycling of photovoltaic systems from the point of view of prolonging the total service life of photovoltaic modules and circular energy** .....113

*J. Vanek, M. Svrcek and B. Lima*

**Real-measured properties of photovoltaic modules** .....116

## Corrosion, Applications and Simulations

*P. Šabacká, J. Maxa, P. Vyroubal*

**Temperature profile analysis in supersonic flow in the experimental chamber** .....119

*A. Maxová, J. Maxa, P. Šabacká*

**Temperature running simulations during the pumping of chambers separated by a small aperture** .....123

*V. Horák, B. T. Phan, and L. Do Duc*

**The Thermodynamic Model for Vacuum Technology** .....127

*V. Knap, S. Bęczkowski and D.-I. Stroe*

**Analysis of Battery Performance and Degradation in CubeSat GOMX-3** .....130

*M. Sedlaříková, M. Míka, J. Hrabovský, T. Tkáčová, G. Fafílek and P. Čudek*

**Iron Based Materials for Biodegradable Implants Prepared by Powder Metallurgy** .....131

*M. Sedlaříková, M. Míka, J. Hrabovský, T. Tkáčová, G. Fafílek and P. Čudek*

**Iron-Magnesium Materials for Biodegradable Implants Prepared by Powder Metallurgy** .....135

*V. Redko, V. Khandetsky, E. Shembel, A. Straková Fedorková, T. Pastushkin, P. Novak*

**Innovative Non-Destructive Electromagnetic Testing of Interface Resistance - the Basis of New Technologies for Production Electrodes of High-Energy Batteries** .....139

*R. Cipin, M. Toman, P. Prochazka, I. Pazdera and J. Miklas*

**Approximation of Alkaline Battery Transfer Function Using Neural Network** .....140

*M. O. Danilov, S. S. Fomanyuk, G. I. Dovbeshko, I. A. Rusetskyi, G.Ya. Kolbasov, G. G. Yaremchuk*

**Obtaining Quantum Dots of Graphene from Partially Unzipped Multi-Walled Carbon Nanotubes** .....143

*D. Dobrocky, Z. Pokorný, Z. Joska, Z. Studeny, J. Prochazka, E. Svoboda and P. Dostal*

**Change of Geometric Accuracy of Structural Steels after Carburizing in Gas** .....146

*M. Folprecht, P. Prochazka and D. Cervinka*

**Battery Powered Multipurpose DC-DC Converter** .....147

*Z. Joska, L. Rak, Z. Pokorný, J. Horníček*

**Adhesion of PVD coatings on surface of small arm** .....150

*O. Klvač, O. Čech*

**Ex-situ cell with positioner for XRD measurements in an inert atmosphere** .....151

|   |     |
|---|-----|
| <i>D. Kusmič, O. Čech, L. Klakurková</i><br><b>Corrosion Resistance of Plasma Nitrided Austenitic Stainless Steel AISI 304 (X5CrNi18 10)</b> .....            | 154 |
| <i>M. Mačák, P. Vyroubal</i><br><b>Numerical Model of a Scanning Electrochemical Microscope</b> .....   | 155 |
| <i>M. Mačák, P. Vyroubal</i><br><b>Numerical Model of a Magnetohydrodynamic Pump</b> .....  | 159 |
| <i>S. S. Madani</i><br><b>Thermal management of lithium ion batteries</b> .....   | 162 |
| <i>S. S. Madani</i><br><b>Battery thermal management using air-cooling</b> .....  | 166 |
| <i>J. Prochazka, Z. Pokorny, H. Ch. Nguyen</i><br><b>Possibilities of the Utilization of Nitriding on Case-Hardening Steels</b> .....                         | 168 |
| <i>V. Sítař, L. Raková, T. Hruška, T. Vysloužil</i><br><b>The Usage of the Power Load as a Physical Diagram for Electric Vehicle Charging Modelling</b> ..... | 169 |
| <i>Z. Studeny, Z. Pokorny, D. Dobrocky, Z. Joska and J. Prochazka</i><br><b>Tribological Properties of DLC Coating for Parts of Weapons</b> .....             | 170 |
| <i>M. Toman, R. Cipin and P. Vorel</i><br><b>Thermal Model of Li-ion Battery Pack in PCM Case</b> .....   | 181 |
| <i>R. Tomanek, J. Martis and P. Vorel</i><br><b>Design of Power Coupled Resonant Circuit for Wireless Power Transfer</b> .....                                | 184 |
| <i>J. Martis, P. Vorel, T. Lažek</i><br><b>Compact Battery Power Source for Oscilloscope</b> .....  | 187 |
| <i>P. Vyroubal, T. Kazda, M. Mačák</i><br><b>Simulation of Thermal Runaway Effect in Lithium-Ion Batteries</b> .....  | 190 |
| <i>A. Zsigmond and J. Libich</i><br><b>Testing of a Prototype Device using Electrochemical Impedance Spectroscopy (EIS) Method</b> .....                      | 193 |
| <i>P. Janderka</i><br><b>Pragolab and Bio-Logic SAS: General Company Presentation</b> .....   | 195 |

## A Facile Surface Modification through SiO<sub>2</sub> Coating for Improving the Electrochemical Performance of Ni-rich Cathode Material

Xiaoxue Lu<sup>1,2</sup>, Ningxin Zhang<sup>1</sup>, Marcus Jahn<sup>1</sup>, Wilhelm Pfleging<sup>2</sup>, Hans J. Seifert<sup>2</sup>

<sup>1</sup> Center for Low-Emission Transport, Austrian Institute of Technology GmbH, Giefinggasse 2, 1210 Vienna, Austria;

<sup>2</sup> Institute for Applied Materials - Applied Materials Physics, Karlsruhe Institute of Technology, Hermann-von-Helmholtz-Platz 1, 76344 Eggenstein-Leopoldshafen, Germany

Ni-rich layered cathode materials LiNi<sub>x</sub>Mn<sub>y</sub>Co<sub>z</sub>O<sub>2</sub> (NMC, x+y+z=1) are considered as the most promising cathode materials in Lithium-ion batteries due to their higher discharge capacity and working voltage. However, the application of NMCs is limited by strong capacity decay after long-term cycles mainly caused by surface degradation [1]. As an inexpensive material, SiO<sub>2</sub> can protect the surface from direct physical contact with electrolyte and significantly reduce surface degradation by acting as a HF scavenger [2]. In this research, a homogenous amorphous SiO<sub>2</sub> layer is synthesized facilely via a sol-gel process and applied on commercial NMC622. The physicochemical properties after SiO<sub>2</sub>-coating was analyzed by ICP, XRD, SEM and TEM. Electrochemical tests, i.e. cyclic voltammetry, long-term charge- discharge and rate capability test were carried out to compare the performance of the non-coated and coated NMC622 materials. It is shown that the initial bulk material properties and discharge capacity are not affected by the coating layer. After 700 cycles in the range of 3.0 - 4.3 V with 2C discharge, the cells with coated materials retained 80% of initial capacity, higher than uncoated ones which were 74%. Post-mortem analysis was performed to reveal the stabilizing mechanism of the SiO<sub>2</sub> coated electrodes. It is confirmed that SiO<sub>2</sub> coating is a facile surface protection method to enhance the cyclic stability of Ni-rich NMC materials.

### References

1. H.-H. Ryu, et al., Chem. Mater., 2018, 30, 1155-1163.
2. T. Yim, et al., RSC Adv., 2013, 3, 25657-25661.

## Polymerisation of Furfuryl Alcohol as Carbon Coating Method for LiNi<sub>0.6</sub>Mn<sub>0.2</sub>Co<sub>0.2</sub>O<sub>2</sub> Cathode Materials for High-Performance Lithium-ion Battery Applications

Anish Raj Kathribail<sup>a,b</sup>, Jürgen Kahr<sup>a</sup>, Arlavinda Rezqita<sup>a</sup>, Marcus Jahn<sup>a</sup>, Maitane Berecibar<sup>b</sup>, Joeri Van Mierlo<sup>b</sup>, Annick Hubin<sup>c</sup>

<sup>a</sup> Center for Low-Emission Transport, AIT Austrian Institute of Technology GmbH, Giefinggasse 2, 1210 Vienna, Austria

<sup>b</sup> Department of Electrical Engineering and Energy Technology (ETEC), Vrije Universiteit Brussel, 1050 Brussels, Belgium

<sup>c</sup> Department of Electrochemical and Surface Engineering (SURF), Vrije Universiteit Brussel, 1050 Brussels, Belgium

E-mail: [anish.kathribail@ait.ac.at](mailto:anish.kathribail@ait.ac.at)

The promising cathode material for tomorrow's Li-ion batteries are nickel-rich LiNi<sub>x</sub>Mn<sub>y</sub>Co<sub>z</sub>O<sub>2</sub> (NMC, x+y+z=1) materials. They outperform other contenders for the application of Li-ion batteries due to their high specific energy. However, unwanted side reactions at high potentials (> 4.2 V vs. Li<sup>+</sup>/Li) remain a challenge, leading to structural degradation and hence lower cyclic stability [1]. Surface coating has been proven in several materials fields to solve the problems related to the material degradation caused by side reactions. This study for the first time adopts the approach of polymerising furfuryl alcohol to achieve a homogenous carbon coating, followed by a calcination step to prepare carbon-coated LiNi<sub>0.6</sub>Mn<sub>0.2</sub>Co<sub>0.2</sub>O<sub>2</sub> (NMC622/C) materials since carbon has high conductivity and is stable against the electrolyte. Numerous analytical techniques were performed to characterize the coated materials, i.e. Thermogravimetric Analysis (TGA) to understand the kinetics during carbonization, in-situ High-Temperature X-Ray Diffraction (HT-XRD) to monitor the phase changes, Scanning and Transmission Electron Microscopy (SEM & TEM) were used to observe the morphology of the particle. Fourier-Transform Infrared (FT-IR) spectroscopy was used to observe the presence of polymerisation and the carbon in the sample, CHNS(O) analysis to quantify the amount of carbon in the sample after the heat-treatment step. Furthermore, detailed electrochemical analysis such as cyclic voltammetry, charge-discharge and rate capability tests were carried out to investigate the impact of the carbon coating on the electrochemical performance and structure stability of the material. The results from the XRD show no phase change in the sample after the calcination, SEM and TEM shows the homogenous coating of the carbon on top of the NMC and FT-IR shows the presence of the carbon bonds on the heat-treated samples, TGA results show the decomposition of the polymer approximately 200 °C and formation of carbon. Further, the electrochemical cycling tests show approximately 10 % improvement in the capacity retention of the coated sample when compared to non-coated counterpart.

### References:

- [1] W. Liu, P. Oh, X. Liu, M.J. Lee, W. Cho, S. Chae, Y. Kim, J. Cho, *Angew. Chemie - Int. Ed.* 54 (2015) 4440–4457.
- [2] Z. Chen, Y. Qin, K. Amine, Y.-K. Sun, *J. Mater. Chem.* 20 (2010) 7606–7612.

## Interface Engineering in Energy Conversion and Storage: Case Studies of Titania

Ladislav Kavan

J. Heyrovský Institute of Physical Chemistry, v.v.i., Dolejškova 3, CZ-18223 Prague 8

E-mail: kavan@jh-inst.cas.cz

Titania is a popular n-semiconductor material for energy conversion (dye-sensitized[1,2] or perovskite[3] solar cells) and storage (water splitting[4], or Li-ion batteries[5]). All these applications benefit from the accurate knowledge of electronic structure near the conduction band minimum (CBM), which is described by the Fermi level position, flatband potential, work function and electron affinity. Despite its key significance, this subject is far from being understood, and literature is congested by vaguely defined data and conflicting reports. One of the reasons is that the interfacial effects are often ignored. An example is the CBM position in TiO<sub>2</sub> anatase or rutile: Photoelectron spectroscopy (UPS, XPS) and most theoretical simulations (assuming inherently vacuum environment) support the CBM of anatase being lower (by ca. 0.2 eV) than that of rutile (type II staggered alignment) but electrochemical impedance studies in aqueous electrolyte solution show just the opposite (type IV aligned configuration). Theoretical simulations of the TiO<sub>2</sub>/water interface show that the type IV alignment is ultimately possible in liquid environment[6]. This would put the theoretical simulations and aqueous electrochemistry into qualitative concord, even though the used interface models were quite simple: one or two monolayers of water, molecularly adsorbed or dissociated, which is far from reality in electrochemical experiments. However, modelling a system with high ionic strength, long-range electrostatic interactions and electrochemical double-layer still remains a challenge[6]. The absolute positions of CBM and Fermi levels in TiO<sub>2</sub> are unknown, and there is hardly any ‘universal’ value for the given material. Hence, discrete numbers, which frequently appear in literature dealing with water splitting, solar cells and Li-batteries must be taken with care. Recently, we have carried out a comparative study of several well-defined single-crystal materials (anatase, rutile brookite) in various orientations and environments (vacuum, air, water vapor, aqueous- and non-aqueous electrolyte solutions using the standard techniques, i.e. photoelectron spectroscopy, near-ambient photoelectron spectroscopy, Kelvin probe and electrochemistry). Such a multimethod approach is less frequently encountered in the literature, but it allows exploring the intuitively expected fact that even the used experimental technique (differing e.g. by its surface-sensitivity) can influence the found results to a remarkable extent.

### Acknowledgement

This work was supported and by the Czech National Science Foundation (contract No. 18-08959S).

### References

1. L. Kavan, Electrochemistry and Dye-sensitized Solar Cells, *Curr. Opinion Electrochem*, 2 (2017) 88-96.
2. L. Kavan, Z. Vlckova-Zivcova, M. Zlamalova, S.M. Zakeeruddin, M. Grätzel, Electron-Selective Layers for Dye-Sensitized Solar Cells Based on TiO<sub>2</sub> and SnO<sub>2</sub>, *J. Phys. Chem. C*, 124 (2020) 6512-6521.
3. L. Kavan, Electrochemistry and Perovskite Photovoltaics, *Curr. Opinion Electrochem*, 11 (2018) 122-129.
4. R. Nebel, K.M. Macounova, H. Tarabkova, L. Kavan, P. Krtil, Selectivity of Photoelectrochemical Water Splitting on TiO<sub>2</sub> Anatase Single Crystals, *J. Phys. Chem. C*, 123 (2019) 10857-10867.
5. L. Kavan, Lithium Insertion into TiO<sub>2</sub> (Anatase): Electrochemistry, Raman Spectroscopy, and Isotope Labeling, *J. Solid State Electrochem*, 18 (2014) 2297-2306.
6. R. Rousseau, V.-A. Glezakou, A. Selloni, Theoretical insights into the surface physics and chemistry of redox-active oxides, *Nature Reviews Materials*, 5 (2020) 460-475.

## Printed electrode layers for Li-ion batteries

T. Syrový<sup>a</sup>, T. Kazda<sup>b</sup>, L. Kubáč<sup>c</sup>, L. Syrová<sup>a</sup>

<sup>a</sup> Department of Graphic Arts and Photophysics, University of Pardubice, 533 53 Pardubice, Czech Republic

<sup>b</sup> Department of Electrical and Electronic Technology, Brno University of Technology, 616 00 Brno, Czech Republic

<sup>c</sup> Centre for Organic Chemistry s.r.o., 53354 Rybitví, Czech Republic

Presented study is focused on development of printed electrode layers for Li-ion batteries made by printing technologies. For fabrication of electrodes were used various printing technologies as a screen/stencil printing and micro-dispensing technique, which enabled to print electrode layers with various thickness and specific geometry of electrodes too. By printing were prepared electrode layers based on NMC electrode material for high energy density batteries. For printing of electrode layers was developed printing ink formulations with high content of electrode materials, which was generally in range of 85-95 % in dry electrode layer. By printing was fabricated NMC electrode layers with areal capacity up to 6.6 mAh/cm<sup>2</sup> with gravimetric energy density 566 Wh/kg and specific capacity 149.6 mAh/g at 0.1 C.

### Introduction

In recent years, the main energy storage sources for many stationary and mobile applications are based on lithium ions based batteries. Although the production of given battery technology is stable and provides good characteristics, there are still higher and higher requirements to increasing volumetric and gravimetric energy density. These parameters are limited by value of the cathode's specific capacity or energy density, especially at high current load, what is crucial for mobile applications. The specific capacity of inorganic material based cathodes varies depending on the type of material between 140 - 250 mA.h/g.

In actual applications the most used cathode material is based on NMC [1]. Because development for given family of electrode materials is in progress some stoichiometric modifications especially NMC622 (LiNi<sub>0.6</sub>Mn<sub>0.2</sub>Co<sub>0.2</sub>O<sub>2</sub>) and NMC811 (LiNi<sub>0.8</sub>Mn<sub>0.1</sub>Co<sub>0.1</sub>O<sub>2</sub>) are more often used too. Tuned stoichiometry and crystalline structure enabled a capacity approaching 220 mAh/g at 3.6 V vs. Li/Li<sup>+</sup>, ie at a slightly lower voltage than the LCO [2-3]. The more advanced type of so-called Li-rich NMC, can achieve a capacity exceeding 300 mAh/g due to their structure and Li-ion inserting capabilities [4], which enable to realize a high nickel content NMC based accumulators with voltage up to 4.5 V. In the case of even more advanced cathode materials of the 3b generation such as Li-rich NMC or LiNi<sub>0.5</sub>Mn<sub>1.5</sub>O<sub>4</sub> is the operating voltage at the level of 5 V vs. Li/Li<sup>+</sup> is achieved with specific capacity up to 140 mAh/g [5-6]. Such a high operating voltage is generally problem for currently used electrolytes, because at a given potential they often decompose and thus a rapid decrease in battery life.

From these perspectives the route to achieve higher values of gravimetric energy density, is over new type of materials with high specific capacity and/or to develop of new type of electrolytes

which are electrochemically stable at potentials around 5 V. The next approach how to increase energy density of whole battery is reducing of portion of metallic collector by increasing of areal specific capacity of electrodes. Because it is connected with significant increasing of electrode thickness, such type of thick electrode layers generally more are suitable for stationary application, where low current loads are required.

## Experimental

The ink formulation for printing was based on solvent borne system, where the PVDF was used as a binder and NMP as a solvent. The NMC (Gelon) was used as received. The ratio of NMC to PVDF varied in ink formulation from 8:1 up to 22:1. The solid content of electrode materials in slurry was in range to 25 to 35 % wt. The solid content of electrode materials in dry layer varied from 85 up to 95 % wt. The various carbon based conductive materials was used.

The electrode layers were printed by stencil/screen printing at Al foil, where thickness of wet layers was approximately 100, 175 or 475  $\mu\text{m}$ . The printed layers were dried at 105  $^{\circ}\text{C}$  for 1h. Dry layers were cut off to circle electrode with diameter 16 mm, then was calendared by the pressure of 100  $\text{kg}\cdot\text{cm}^{-2}$ . Prepared electrodes were transferred to Jacomex glovebox with Ar atmosphere. The half cells were assembled with Li chips in coin cell CR2025. As a electrolyte 1 M  $\text{LiPF}_6$  in EC:DMC:EMC in ratio 1:1:1 was used (Central Glass Czech s.r.o.). The assembled cells were characterized at galvanostatic cycling at current load from 0.1 to 5C. For selected cells CV and EIS analysis were performed.

## Results

The NMC based electrode layers with 9.2, 22.5 and 44.3  $\text{mg}/\text{cm}^2$  of active material were printed. The initial columbic efficiency in first cycle at 0.1 C was 80.0, 83.2 and 83.1 %. The maximal columbic efficiency was 99.9, 99.7 and 96.6 %. The maximal specific capacities at 0.1 C in first cycles were 150.5, 150.1 and 149.6  $\text{mAh}/\text{g}$ . The maximal gravimetric energy density was 575, 572 and 564  $\text{Wh}/\text{kg}$ . The thicker layer were more affected by lithium dendrite shortcuts, which for selected cells make fails in cycling.

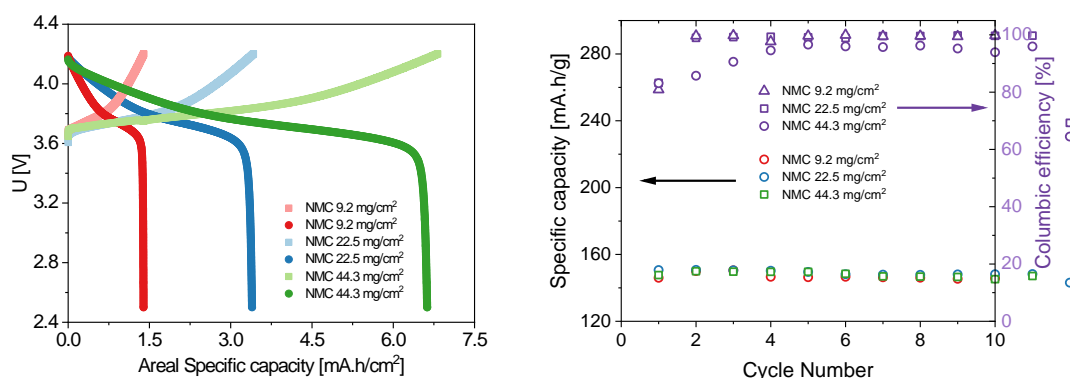


**Figure 1.** (A) Charging/discharging curves at cycling rate 0.1C for  $\text{LiPF}_6$  electrolyte for electrodes based on NMC with various amount of electrode materials per area (B) Galvanostatic cycling at rate 0.1 for carbonates-based type Li electrolytes for electrodes based on NMC with various amount of electrode materials per area.

## Conclusion

By printing technique was prepared set of cathode electrode layers based on NMC electrode material. It was printed various thickness of electrode layer where the maximal amount of electrode material was 44.3 mg/cm<sup>2</sup>. Even for such high loading, the high specific capacity was achieved – 149.6 mAh/g at current load 0.1C. The maximal columbic efficiency for given electrode was 96.6 % which indicate quite big loss in charging/discharging process. The thinner layers with areal capacity 1.4 mAh/cm<sup>2</sup> and 3.4 mAh/cm<sup>2</sup> exhibit more efficient cycling behavior and were less prone to shortcuts caused by lithium dendrite growth.

## Acknowledgments

The work was supported from European Regional development Fund-Project "Organic redox couple based batteries for energetics of traditional and renewable resources (ORGBAT)" No.CZ.02.1.01/0.0/0.0/16\_025/0007445 and by BUT specific research programme (project No. FEKT-S-20-6206).

## References

1. PISTOIA, G. *Lithium-ion batteries: advances and applications*. First edition. Oxford: Newnes (2013)
2. STEEN, M., N. LEBEDEVA, F. DI PERSIO a L. BOON-BRETT. Publications Office of the European Union, 2017.
3. NOH, Hyung-Joo, Sungjune YOUN, Chong Seung YOON a Yang-Kook SUN. *Journal of Power Sources*. 2013, **233**(7)
4. YAN, Jianhua, Xingbo LIU a Bingyun LI. *RSC Adv* 2014, **4**(108)
5. ZHAO, Jianqing, Xiaoxiao KUAI, Xinyu DONG, Haibo WANG, Wei ZHAO, Lijun GAO, Ying WANG a Ruiming HUANG. *Journal of Alloys and Compounds*. 2018, **732**(1), 385-395.
6. KAZDA, T., J. VONDRÁK, V. Di NOTO, M. SEDLAŘÍKOVÁ, P ČUDEK, L. OMELKA, L. ŠAFARÍKOVÁ a V. KAŠPÁREK. *Journal of Solid State Electrochemistry*. 2015, **19**(6), 1579-1590

## Strategies enhancing the electrochemical performance of NMC811 high energy electrodes for xEV applications

K. Froehlich<sup>a</sup>, W. Pessenhofer<sup>b</sup>, H. Besser<sup>c,d</sup>, W. Pfleging<sup>c,d</sup>, M. Jahn<sup>a</sup>

<sup>a</sup>Electric Drive Technologies, AIT Austrian Institute of Technology GmbH, Vienna, Austria

<sup>b</sup>New coatings, Miba eMobility GmbH, Vorchdorf, Austria

<sup>c</sup>Institute for Applied Materials (IAM-AWP), Karlsruhe Institute of Technology, P.O. Box 3640, 76021, Karlsruhe, Germany

<sup>d</sup>Karlsruhe Nano Micro Facility (KNMF), H.-von-Helmholtz-Pl. 1, 76344, Egg.-Leopoldshafen, Germany

Layered oxide cathodes are among the most promising candidates meeting future requirements for Li-ion batteries for application in electric drives. Lithium nickel manganese cobalt oxides, NMC, as one of the most common representatives, is therefore under constant investigations, whereas most of the recent studies focus on low Co [1] and Ni-rich NMCs such as NMC622 or further NMC811. Besides cost reduction, these compounds promise higher cut-off voltages and increased energy densities.

Unfortunately, in NMC cathodes the reactivity increases directly proportional to the Ni content, leading to structural changes and further reduced cyclability and thermal stability [2],[3]. With high Ni content, the stability decreases drastically, even leading to difficulties and significant capacity decay when being stored under ambient conditions [4],[5]. To stabilize the nickel-rich NMC cathodes, different approaches such as doping [6], coating [7], gradient particles [8],[9], and adoption of the electrochemical system such as electrolyte additives [10] are currently under investigation.

Another drawback of NMCs is that they suffer from low high rate compatibility and corresponding low capacity retention at higher charging/discharging rates. This effect is even more pronounced for thick high energy electrodes. Increasing the high current cyclability is currently studied via more sophisticated electrode designs such as 3D electrode design via incorporation of carbon nanotubes [11] or laser structuring [12].

Two strategies for the improvement of NMC811 are presented:

- 1) Increasing the stability via particle coating using different coatings and methods (namely physical vapor deposition and atomic layer deposition) and
- 2) Ultrafast laser ablation for improved Li<sup>+</sup>-diffusion kinetics, and reduced overpotentials at elevated C-rates.

Improved NMC811 electrodes with enhanced cycling stability and transport kinetics will be presented and compared to untreated NMC811. The optimization strategies lead to high energy NMC811 based Li-ion batteries with reasonable specific capacities and rate capability for next generation xEV applications

## Acknowledgments

This work was financially supported by the Austrian Federal Ministry for Transport, Innovation and Technology (bmvit).

## References

1. C. of the European Parliament, Tackling the Challenges in commodity markets on raw materials, “Tackling the Challenges in commodity markets on raw materials.” 2011.
2. S. M. Bak et al., “Structural changes and thermal stability of charged  $\text{LiNi}_x\text{Mn}_y\text{Co}_z\text{O}_2$  cathode materials studied by combined in situ time-resolved XRD and mass spectroscopy,” *ACS Appl. Mater. Interfaces*, 2014, doi: 10.1021/am506712c.
3. R. Jung, M. Metzger, F. Maglia, C. Stinner, and H. A. Gasteiger, “Oxygen Release and Its Effect on the Cycling Stability of  $\text{LiNi}_x\text{Mn}_y\text{Co}_z\text{O}_2$  (NMC) Cathode Materials for Li-Ion Batteries,” *J. Electrochem. Soc.*, vol. 164, no. 7, pp. A1361–A1377, 2017, doi: 10.1149/2.0021707jes.
4. X. Han et al., “A review on the key issues of the lithium ion battery degradation among the whole life cycle,” *eTransportation*, vol. 1, p. 100005, 2019, doi: 10.1016/j.etrans.2019.100005.
5. R. Jung et al., “Effect of Ambient Storage on the Degradation of Ni-Rich Positive Electrode Materials (NMC811) for Li-Ion Batteries,” *J. Electrochem. Soc.*, vol. 165, no. 2, pp. A132–A141, 2018, doi: 10.1149/2.0401802jes.
6. F. Xin et al., “Li–Nb–O Coating/Substitution Enhances the Electrochemical Performance of the  $\text{LiNi}_{0.8}\text{Mn}_{0.1}\text{Co}_{0.1}\text{O}_2$  (NMC 811) Cathode,” *ACS Appl. Mater. Interfaces*, vol. 11, no. 38, pp. 34889–34894, Sep. 2019, doi: 10.1021/acsami.9b09696.
7. X. Cheng, J. Zheng, J. Lu, Y. Li, P. Yan, and Y. Zhang, “Realizing superior cycling stability of Ni-Rich layered cathode by combination of grain boundary engineering and surface coating,” *Nano Energy*, vol. 62, no. May, pp. 30–37, 2019, doi: 10.1016/j.nanoen.2019.05.021.
8. S. Maeng, Y. Chung, S. Min, and Y. Shin, “Enhanced mechanical strength and electrochemical performance of core–shell structured high–nickel cathode material,” *J. Power Sources*, vol. 448, no. October 2019, p. 227395, 2020, doi: 10.1016/j.jpowsour.2019.227395.
9. N. Zhang et al., “Cobalt-Free Nickel-Rich Positive Electrode Materials with a Core–Shell Structure,” *Chem. Mater.*, vol. 31, no. 24, pp. 10150–10160, Dec. 2019, doi: 10.1021/acs.chemmater.9b03515.
10. T. Li, X.-Z. Yuan, L. Zhang, D. Song, K. Shi, and C. Bock, *Degradation Mechanisms and Mitigation Strategies of Nickel-Rich NMC-Based Lithium-Ion Batteries*, vol. 3, no. 1. Springer Singapore, 2019.
11. A. Shah et al., “A Layered Carbon Nanotube Architecture for High Power Lithium Ion Batteries,” *J. Electrochem. Soc.*, vol. 161, no. 6, pp. A989–A995, 2014, doi: 10.1149/2.052406jes.
12. W. Pflöging, “A review of laser electrode processing for development and manufacturing of lithium-ion batteries,” *Nanophotonics*, vol. 7, no. 3, 2018.

## Quantification of critical process parameters of Li-ion pouch cell production

Bernd Eschelmüller<sup>a,b</sup>, Katja Fröhlich<sup>a</sup>, Marcus Jahn<sup>a</sup>

<sup>a</sup>Electric Drive Technologies, AIT Austrian Institute of Technology GmbH, Vienna,

<sup>b</sup>Department Technik, Green Mobility, FH Campus Wien, Vienna

Knowledge about critical process parameters in battery cell production could be used to reduce costs of future production plants and to increase production yield, lifetime and safety of energy storage systems.

This work deals with the impact of assembly errors and production imperfections and provides information about critical process parameters during the assembly of Li-ion pouch cells. Their influence on the electrochemical performance and the sensitivity to certain process parameters during manufacturing are evaluated under realistic conditions. We place special focus on single process steps such as cutting electrodes, stacking, electrolyte filling, formation and degassing, which are investigated and evaluated.

Therefore, a statistical screening design is carried out to get a general information regarding the impact of defined process failures on performance characteristics.

After evaluation of the given data, requirements for the assembly process for Li-ion pouch cells are derived and will be presented in this talk.

## Lithium-Ion Batteries: from Atomic Scale Processes to Data-driven Diagnostics

Y. Zhang, A. Zülke, M.P. Mercer, D. Csala, H. E. Hoster

<sup>a</sup> Energy Lancaster, Lancaster University, Lancaster LA1 4YB, UK;  
ALISTORE European Research Institute, CNRS FR 3104, 80039, Amiens, France

<sup>b</sup> The Faraday Institution, Didcot OX11 0RA, UK

Non-destructive methods of analyzing state-of-health of Lithium-Ion Batteries rely on externally measurable quantities such as voltage, current, and temperature. Such data are interpreted “classically” via models and parameter fitting on the one hand, and also in a purely “data-driven” approach on the other.

Here, we will demonstrate how those two approaches can work together, and we will give some examples of how certain “features” that feed into data-driven methods do actually relate to atomic-scale processes such as phase-transitions. Observable voltage profiles split into anode- and cathode-related features. Those features shift with respect to each other as the cell degrades. It is important to understand to which extend those features are path dependent in terms of their shapes and position, which we will briefly illustrate at the example of graphite electrodes.

**Data-driven approaches** of capturing and predicting battery degradation are a quickly growing field of research [1-3]. This is not only, but also driven by the fact that experimental studies with Lithium-Ion Batteries (LIBs) are inherently slow and thus expensive for industry. At the same time, understanding the performance and degradation of LIBs requires uniting the current scales gap between atomistic, continuum and cell level models.

The **State-of-Health** (SOH) of a Li-ion cell at a specific point in time can be defined as the capacity at that moment divided by the initial capacity of that cell (“Relative Capacity”). Figure 1 illustrates a typical cell degradation study, bundling charge-discharge cycles in batches of 50, interrupted by check-up cycles. In those check-up cycles, a slow charge (over 20 hours) provides good estimates of the remaining relative capacity and also of the type and intensity of internal degradation processes. In real-world operation, State-of-Health estimates rely on less comprehensive data sets. In particular, slow charges from 0-100 % will be scarce, so that estimates of the actual capacity must rely on fewer data points.

**Machine Learning** (ML) tools (here: random-forest regression) can be used to derive SoH estimates based on small sub-sets of full charge curves (Figure 2). Such sub-sets are available in typical battery re-charging scenarios, even if the charging does neither start at 0 % nor go all the way to 100 %. For ML algorithms, the shape of the curve in the evaluated voltage window serves as a “feature” that bears sufficient information to estimate the capacity of the cell even without charging it to the end [1,2].

**Physical interpretation** of voltage profile features and their change over time often involves a step of numerical differentiation, producing Differential Voltage Analysis (DVA) profiles (Figure

3). They can be broken down into anode- and cathode related contributions, which change in amplitude and relative position as a cell degrades.

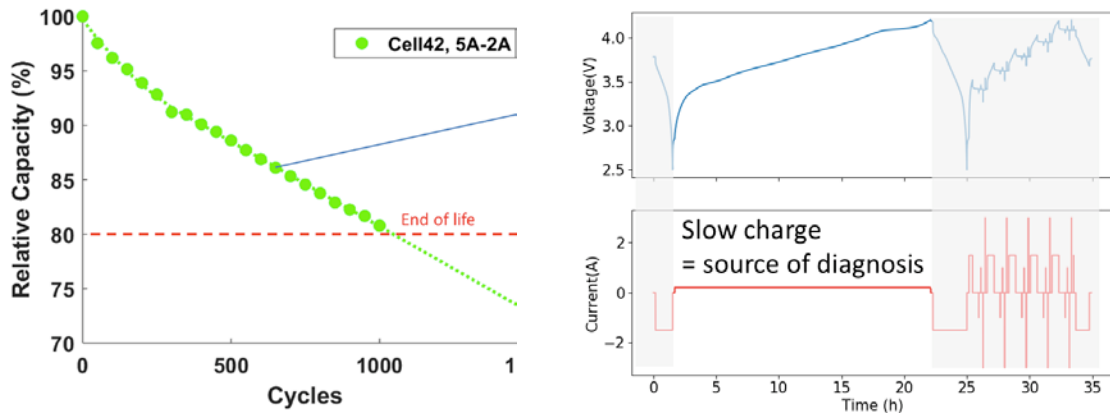


**Figure 1.** Relative capacity as a measure for state-of-health declines over the course of repeated charge/discharge cycles. Slow constant-current charging is a common way to determine the capacity and to extract voltage profiles that contain useful diagnostic information.

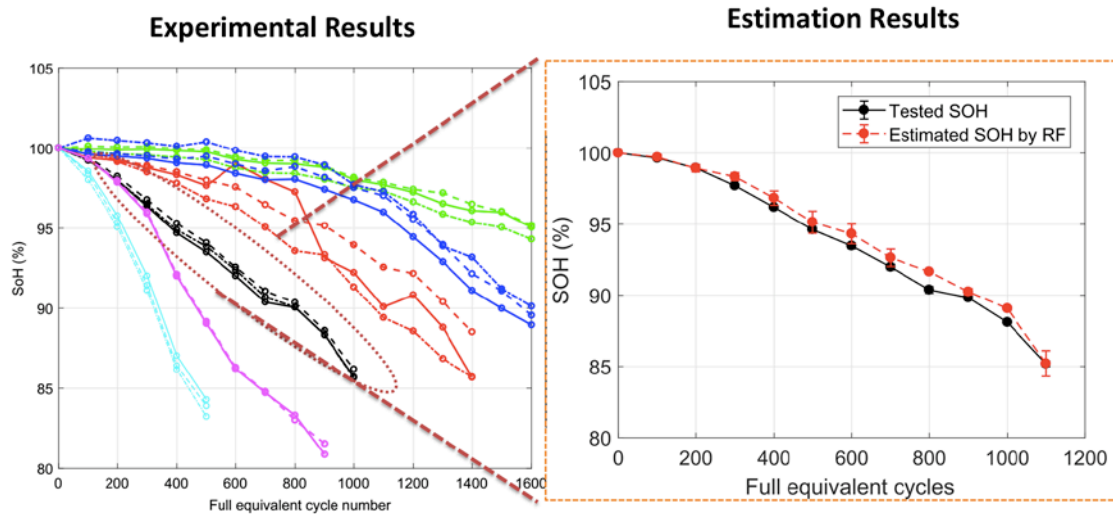
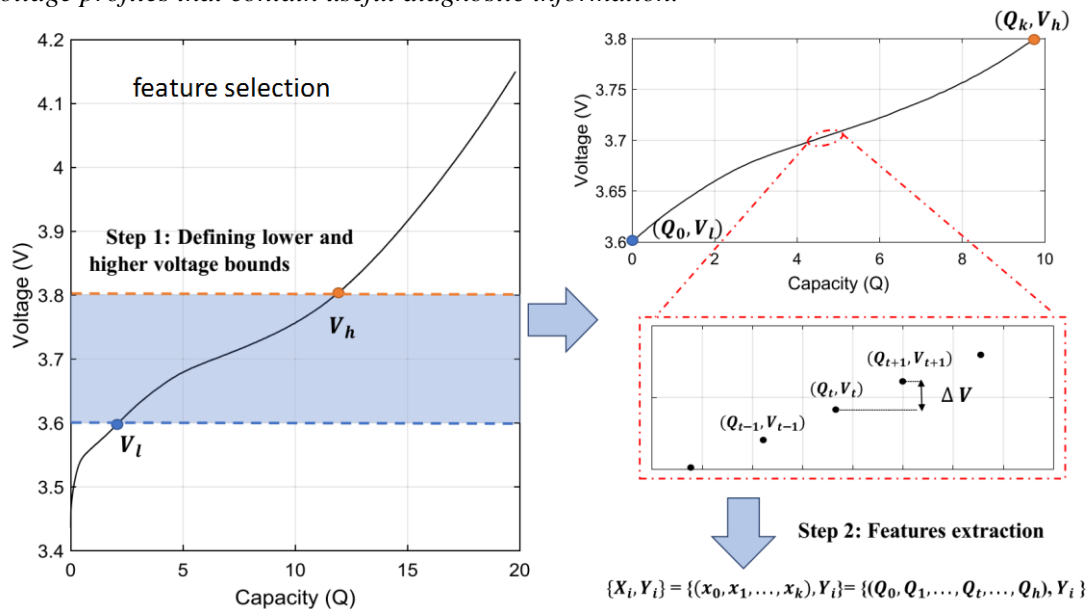


**Figure 2.** Random forest regression approach for state-of-health estimation [1,2].

Those changes provide insights into the underlying degradation mechanisms, which in turn improves forecasts of the longer-term degradation behaviour of a given cell under varying conditions of usage. A comprehensive picture requires the combined application of data-driven and physics-based interpretation of cell degradation and diagnosis data.

**Path- and history dependence** makes interpreting **voltage profiles** less straightforward. At the example of graphite anodes, we will demonstrate that some phase transitions come with a history-dependent behaviour that prevails even at higher temperature [4]. We will highlight the experimental evidence of that behaviour and provide some ab-initio-based insights into the underlying entropy- and enthalpy-driven processes.

In summary, data-driven and physics-based cell diagnosis should ideally work hand-in-hand to select the most suitable features for powerful ML algorithms, to avoid artefacts, and to get a deeper understanding of battery degradation processes at the same time.

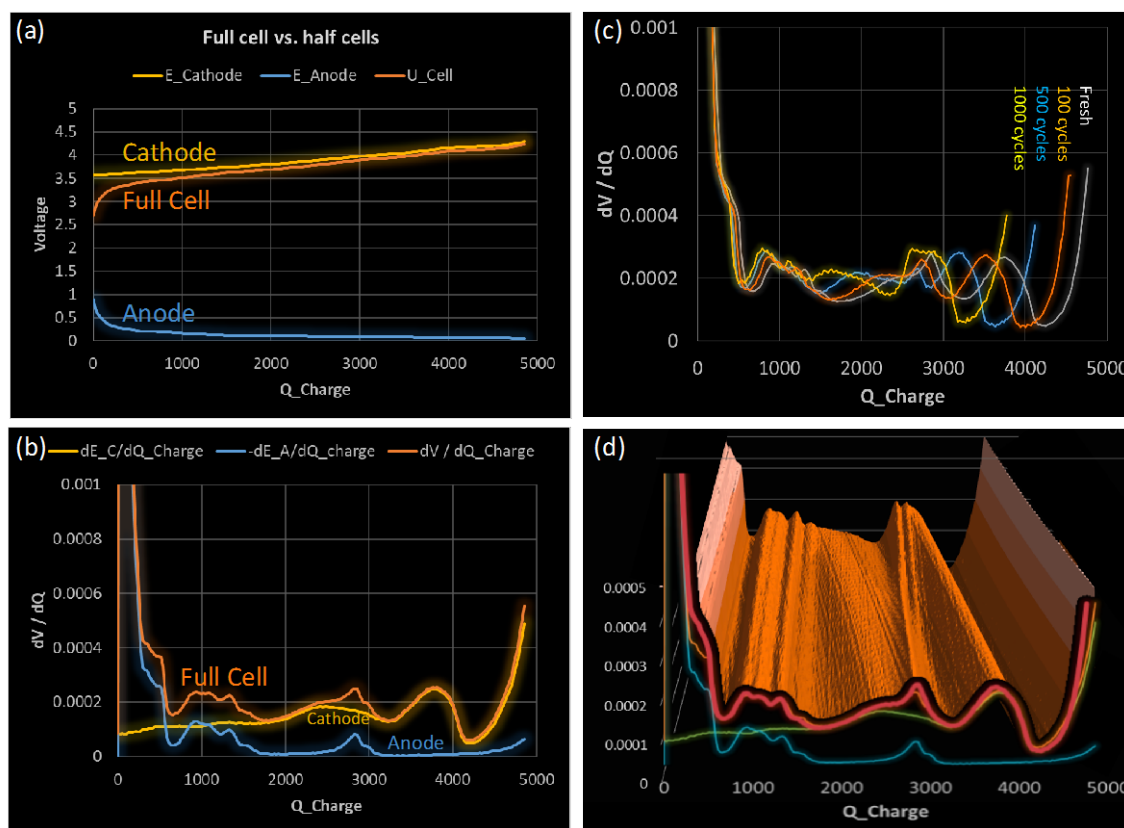


**Figure 3.** (a) voltage profile during slow charging, broken down into anode and cathode contributions; (b)  $dV/dQ$  (Differential Voltage Analysis) of the same profiles; (c) change of the DVA profiles during cycle ageing; (d) 3D visualisation of the DVA development during ageing.

## References

1. Y. Li et al., Renewable and Sustainable Energy Reviews **113** (2019) 109254.
2. Y. Li et al., Applied Energy **232** (2018) 197.
3. K. A. Severson et al., Nature Energy **4** (2019) 383.
4. M.P. Mercer et al., under review.

## Electrochemical Performance of Co<sub>3</sub>O<sub>4</sub> Anode Material with Conductive Binder

M. A. Kamenskii<sup>a</sup>, A. I. Vypritskaya<sup>a</sup>, S. N. Eliseeva<sup>a</sup> and V. V. Kondratiev<sup>a</sup>

<sup>a</sup> Institute of Chemistry, St Petersburg State University, St Petersburg, 199034, Russia

A water-soluble conductive binder consisting of poly-3,4-ethylenedioxythiophene:polystyrene sulfonate and carboxymethyl cellulose was proposed for conversion Co<sub>3</sub>O<sub>4</sub> anode material. This type of electrode shows ultrahigh specific capacity value and brilliant C-rate capability in comparison with electrode where composition of poly(acrylic acid) and carboxymethyl cellulose was used. It also demonstrates better stability during continuous cycling at 0.2 C. Long-term cycling voltammetry measurements show that using of conducting polymer as binder component lead to superior stability of the Co<sub>3</sub>O<sub>4</sub> electrodes.

### Introduction

Transition metal oxides (such as TiO<sub>2</sub>, SnO<sub>2</sub>, Fe<sub>3</sub>O<sub>4</sub>, Co<sub>3</sub>O<sub>4</sub>) are perspective anode materials for lithium-ion batteries due to their high specific capacity (> 600 mAh·g<sup>-1</sup>) which is much higher than for commercial graphite anode (372 mAh·g<sup>-1</sup>) (1). Among them, Co<sub>3</sub>O<sub>4</sub> has drawn attention owing to its high theoretical capacity (890 mA·h·g<sup>-1</sup>). Nevertheless, practical application of Co<sub>3</sub>O<sub>4</sub> is sophisticated because of its low electronic conductivity (2) and high volume expansion during charge-discharge processes (3) which leads to loss of electronic contact (4) and on account of this fact stability of electrode during charge/discharge process is low.

One of the ways to improve cycle life of Co<sub>3</sub>O<sub>4</sub> electrode and enhance electrochemical properties is application of different types of binder in the composite electrode material. In particular, it was demonstrated that using of water-soluble binder consisting of poly(acrylic acid) (PAA) and carboxymethyl cellulose (CMC) led to superior performance of Co<sub>3</sub>O<sub>4</sub> electrode in comparison with conventional electrode which contains polyvinylidene fluoride as binder (5).

In our previous works combination of conducting polymer poly-3,4-ethylenedioxythiophene:polystyrene sulfonate (PEDOT:PSS) and CMC was used for some intercalation electrode materials (6). Herein we present an application of this binder for Co<sub>3</sub>O<sub>4</sub> anodes.

### Experimental Details

Co<sub>3</sub>O<sub>4</sub> electrodes were prepared by mechanically mixing of electroactive grains with carbon black and binder in the following ratio: 70 wt% of Co<sub>3</sub>O<sub>4</sub>, 20 wt% of carbon and 10 wt% of binder (PAA/CMC and PEDOT:PSS/CMC (1/1 w/w)). The resulting viscous slurry was cast onto a Cu foil (blade gap height for coating – 150 μm, mass loading of Co<sub>3</sub>O<sub>4</sub> ~ 3.0 mg·cm<sup>-2</sup>), dried in a vacuum oven at 50 °C for 12 h. Electrodes were assembled in CR2032 coin cells vs. Li foil. Electrochemical tests were performed by galvanostatic charge/discharge (current range 0.2 – 1 C), cyclic voltammetry (CV) at scan rate 0.1 mV·s<sup>-1</sup> and electrochemical impedance spectroscopy at different potentials.

## Results and Discussion

At first cycle of CV curves of  $\text{Co}_3\text{O}_4$  electrodes strong peaks are observed at  $E = 0.8$  V for both electrodes (dashed lines), corresponding to the reduction of  $\text{Co}_3\text{O}_4$  into metallic Co and formation of amorphous solid-electrolyte interface (SEI) film (7). Further a reversible oxidation ( $E = 2.09$  V) and reduction ( $E = 1.07$  V) process is observed according to the following equation:



Potentials and current densities of peaks at first cycle of CVs  $\text{Co}_3\text{O}_4$  electrodes are close to each other, regardless of the type of binder. The capacity values calculated from CVs data are given in Table I, and all these values at first cycle are higher than  $1000 \text{ mA}\cdot\text{h}\cdot\text{g}^{-1}$ . This ultrahigh capacity has been observed earlier and was explained by several effects: reversible formation of gel-like polymer film on the surface of electrode (pseudo-capacity-type) and ability of nanomaterials to introduce extra  $\text{Li}^+$  ions (8).

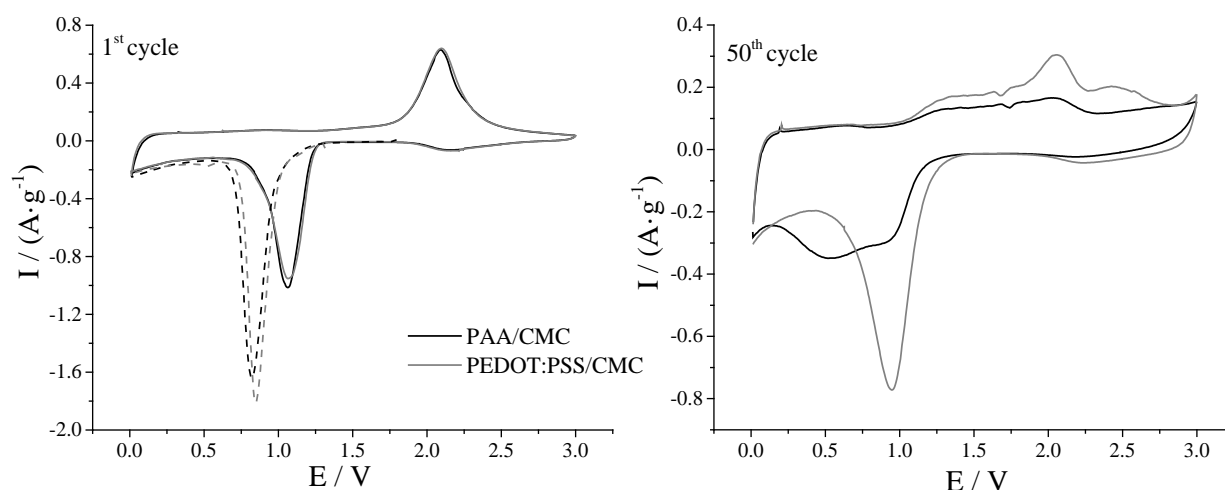


**Figure 1.** Cyclic voltammograms of  $\text{Co}_3\text{O}_4$  electrodes with different binders (PAA/CMC and PEDOT:PSS/CMC) at scan rate  $0.1 \text{ mV}\cdot\text{s}^{-1}$ .

**TABLE I.** Cathodic capacity values of the  $\text{Co}_3\text{O}_4$  electrodes calculated from CVs.

| Cycle | $Q / \text{mAh}\cdot\text{g}^{-1}$ (PAA/CMC) | $Q / \text{mAh}\cdot\text{g}^{-1}$ (PEDOT:PSS/CMC) |
|-------|--|--|
| 1     | 1000   | 1040   |
| 10    | 1080   | 1100   |
| 30    | 1100   | 1200   |
| 50    | 890  | 1200   |

During 50 cycles of CVs the shape of curves is changed. For  $\text{Co}_3\text{O}_4$  electrode with PAA/CMC binder anodic peak currents decrease by a factor of 5, the splitting of cathodic peak into two is observed and it shifted toward more negative potentials (close to 0.46 V).  $\text{Co}_3\text{O}_4$  electrode with conductive binder is more stable, however, a shoulder of anodic peak at  $E = 2.42$  V while the main peak at  $E = 2.09$  V is still remains. Cathodic peak is stable; decrease of current is less than for  $\text{Co}_3\text{O}_4$  electrode with PAA/CMC. Capacity value of electrodes with conductive polymer is stable over 50 cycles, while for another electrode it dropped more significantly ( $1200 \text{ mAh}\cdot\text{g}^{-1}$  and  $890 \text{ mAh}\cdot\text{g}^{-1}$ , respectively).

Galvanostatic charge/discharge measurements showed the similar results: Co<sub>3</sub>O<sub>4</sub> electrode with conductive polymer is more stable in full current range and during continuous cycling at low current density (0.2 C).

### Acknowledgments

This work was supported by Saint Petersburg State University (grant № 26455158). The authors would like to thank the Center for X-ray Diffraction Methods, the Interdisciplinary Center for Nanotechnology and Resource Center of Physical methods of surface investigations of Research park of Saint Petersburg State University.

### References

1. S. Fang, D. Bresser and S. Passerini, *Adv. Energy Mater.*, **10**, 1902485 (2020).
2. J. Zheng and B. Zhang, *Ceram. Int.* **40**, 11377 (2014).
3. Y. Yang, J. Huang, J. Zeng, J. Xiong and J. Zhao, *ACS Appl. Mater. Interfaces*, **9**, 32801 (2017).
4. D. Larcher, G. Sudant, J.-B. Leriche, Y. Chabre and J.-M. Tarascon, *J. Electrochem. Soc.*, **149**, A234 (2002).
5. J. Ming, H. Ming, W.J. Kwak, C. Shin, J. Zheng and Y.K. Sun, *Chem. Commun.*, **50**, 13307 (2014).
6. S.N. Eliseeva, M.A. Kamenskii, E.G. Tolstopjatova and V. V. Kondratiev, *Energies*, **13**, 2163 (2020).
7. H. Wang, Y. Zhu, C. Yuan, Y. Li and Q. Duan, *Appl. Surf. Sci.*, **414**, 398 (2017).
8. S. Wu, T. Xia, J. Wang, F. Lu, C. Xu, X. Zhang, L. Huo and H. Zhao, *Appl. Surf. Sci.*, **406**, 46 (2017).

## Melanin as Semiconductor with Polymer Structure is Effective Modifier for Electrodes of High Energy Li - Ion Batteries

### Influence structure and nature of melanin on efficiency of cathode based on $\text{LiMn}_2\text{O}_4$

Elena Shembel<sup>b,c</sup>, Volodymyr Kyrychenko<sup>a</sup>, Irina Maksyuta<sup>c</sup>, Vlad Redko<sup>b</sup>, Nellya Zaderey<sup>c</sup>

<sup>a</sup>Sunoil-Agro, Pavlograd, 51400, Ukraine

<sup>b</sup>Enerize Corporation, Coral Springs, FL, 33067, USA

<sup>c</sup>Scientific Research Laboratory of Chemical Power Sources of Ukrainian State University of Chemical Technology, Dnipro, 49005, Ukraine

Melanin is a biological organic polymer and has semiconductor properties. The structure of organic semiconductors, including melanin, determines the mechanism of their conductivity, electrical and catalytic properties. Research into the properties of melanin, which are synthesized on the basis of innovative technologies developed by Sunoil-Agro, confirms the innovating prospects for using melanin. In current presentation using the melanin we investigated and developed the method to modify the cathode materials of Li-ion batteries. Increasing the energy and power characteristics of  $\text{LiMn}_2\text{O}_4$  - based cathodes as a result of their modification with melanin will be presented in our abstract. More detailed information will be presented in the followed presentation during Conference

### Introduction

In order to increase the energy and power of the Li-ion battery, innovative composite cathode materials are developed and used, which have numerous advantages, for example:  $\text{LiNi}_0.5\text{Mn}_{1.5}\text{O}_4$ ;  $\text{LiNi}_x\text{Co}_y\text{Mn}_{1-x-y}\text{O}_2$ . A recent publication [1] present innovating materials for cathodes of Li-ion batteries layered oxide materials, and in particular  $\text{LiNi}_{1-x-y}\text{Co}_x\text{Mn}_y\text{O}$  (NCM) and  $\text{LiNi}_{1-x-y}\text{Co}_x\text{Al}_y\text{O}_2$  (NCA), which are promising for Li-ion batteries with the high energy and high power.

At the same time, modification of cathode materials is also an important factor in improving the performance of Li-ion power sources. In our studies, we proceeded from the fact that the unique properties of melanin can provide an effective modification of the electrode materials of lithium power sources. Melanin is an organic polymer with unique, multifunctional semiconductor properties. It exhibits a switching effect from a weakly conductive to a highly conductive state at relatively low electric fields.

Our presentation is dedicated to the modification by Melanin the cathode materials, which are now widely used in the production of lithium power sources. In the future, the developed modification method using Melanin can be used for new cathode materials. The experience of the authors of this presentation in the field of modification of cathode materials  $\text{LiMn}_2\text{O}_4$  using  $\text{Al}_2\text{O}_3$  is presented in the patent [2].  $\text{LiMn}_2\text{O}_4$  has certain advantages over the widely used cathode materials based on  $\text{LiCoO}_2$  and  $\text{LiFePO}_4$ .  $\text{LiMn}_2\text{O}_4$  is environmentally friendly, has a relatively

high electronic conductivity and provides a high electrode discharge voltage.  $\text{LiCoO}_2$  is environmentally harmful and expensive.  $\text{LiFePO}_4$  has a low conductivity, therefore, a larger amount of highly conductive carbon material must be added to the cathode mass. The discharge voltage of the  $\text{LiFePO}_4$  cathode is relatively low compared to the discharge voltage of Li-ion batteries with cathode based on  $\text{LiMn}_2\text{O}_4$

Below presented results of Melanin's modification of a  $\text{LiMn}_2\text{O}_4$ -based cathode. In the research and development of the modification of electrode materials, we used various types of Melanin, which was synthesized by Sunoil-Agro. The technology for the synthesis of various types of melanin was also developed by Sunoil-Agro. An important factor is that to modify cathode materials various forms of melanin were used, including those that differed in the nature and valence of the cation in the melanin structure.

## Experimental

Electrodes with two types compositions have been fabricated and tested: 1)  $\text{LiMn}_2\text{O}_4$  -64 % wt. Меланин – 16 % wt. Carbon black- 7.5% wt.; Graphite with high conductivity – 7.5 % wt. Fluoroplastic binder F4D-5% wt. and 2)  $\text{LiMn}_2\text{O}_4$  -85% wt., Carbon black- 5% wt.; Graphite with high conductivity - 5% wt. Fluoroplastic binder F4D-5% wt.  $\text{LiMn}_2\text{O}_4$  from company Merck has been used. Conductivity of powders of  $\text{LiMn}_2\text{O}_4$  and Melanin have been tested using innovating non-contact, non-destructive electromagnetic method that developed by company Enerize Corporation [3, 4]. The cells with coin 2325 design have been used for testing. All procedures were carried out in an Ar-filled glove box. The negative electrodes were made of lithium foil. The fiberglass was used as the separator. Electrolyte composition: 1M  $\text{LiClO}_4$ , DMC and EC (1:1). In this abstract results of electrochemical tests, which have been carried out by recording the charge-discharge curves in a galvanostatic mode presented. Cycling has been carried out in the potential range of 3 ÷ 4.3 and at a constant value of the charging current and discharge currents equal to 0.1 C. Impedance spectra were obtained using VoltaLab PGZ 301 analytical radiometer. The frequency range has been from 100 MHz to 100 kHz. Used two types of Melanin. Melanin # 1 contains cations with a +1 valence. Melanin # 2 contains cations with a valence +3. More detailed results will be illustrated during presentation.

## Results

Fig 1 presents the dynamics of changes from the cycle number of the specific discharge capacity of the cathodes, which contains Melanin # 1 (curves 1 and 2); and a cathode that does not contain Melanin (curve 3)

Presented results illustrate that the electrodes, which modified with Melanin, have higher discharge capacity

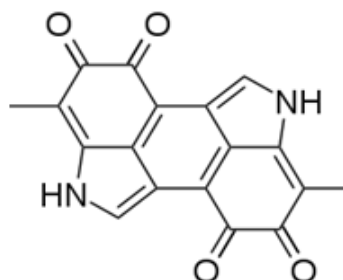
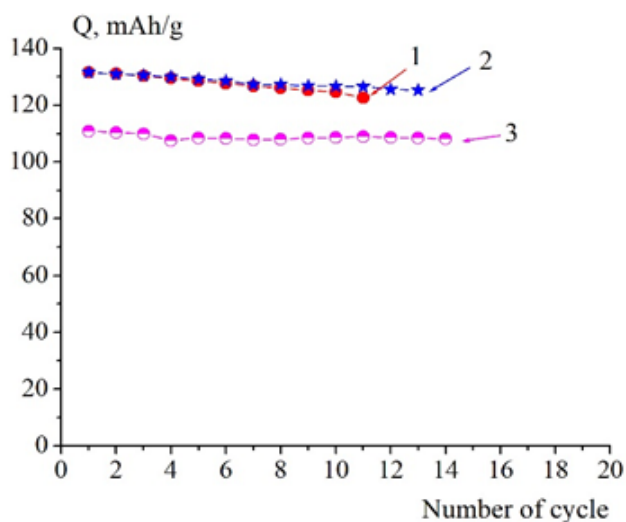


**Figure 1.** Dynamics of changes the discharge capacity of electrodes from cycle number

**Figure 2.** Melanin.  $C_{18}H_{10}N_2O_4$

Curves 1,2: Electrodes based on composite of  $LiMn_2O_4$  and Melanin # 1

Curve 3: Electrode based on  $LiMn_2O_4$  without Melanin

Ha Fig. 3 Discharge - Charging curves of electrodes based on  $LiMn_2O_4$  with Melanin and without Melanin for different cycle numbers are presented.

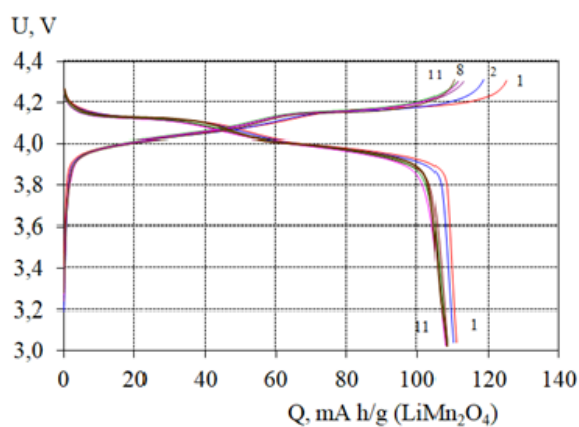
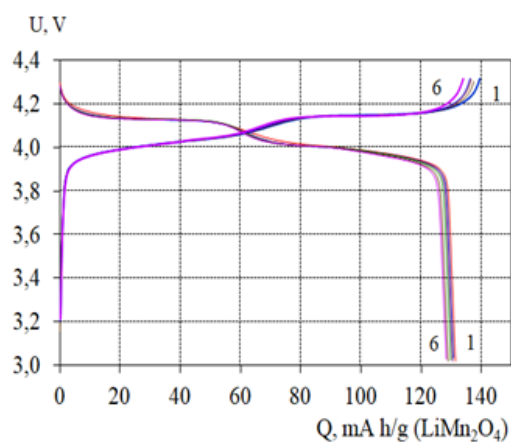


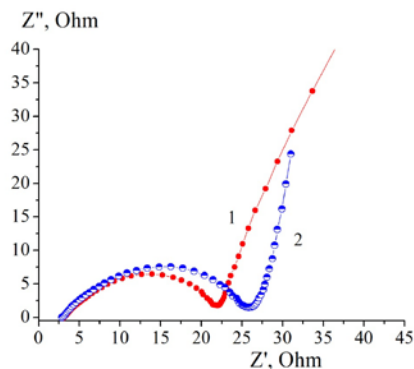
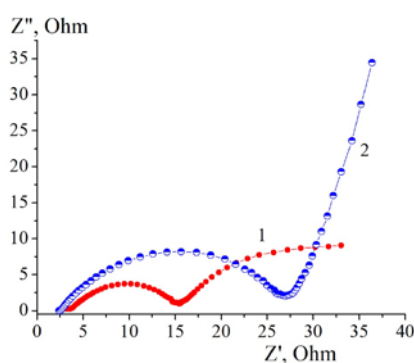
**Figure 3A.**

Discharge - Charging curves of electrodes based on  $LiMn_2O_4$ . The numbers on the curves correspond to the cycle number. On the Fig. 3A results of cycling electrode  $LiMn_2O_4$  that has been modified by Melanin #1 are presented. On the Fig. 3B results of cycling electrodes  $LiMn_2O_4$  without the Melanin are presented.

**Figure 3B.**

These results also illustrate that the electrodes, which modified with Melanin, have higher discharge capacity

Impedance characteristics of  $LiMn_2O_4$  electrodes, which are modified with different types of Melanin are presented in Fig. 4

**Figure 4A.****Figure 4B.**

Comparison of the impedance characteristics of electrodes based on  $\text{LiMn}_2\text{O}_4$  modified by Melanin (curves 1) and electrodes based on  $\text{LiMn}_2\text{O}_4$  that NOT modified by Melanin (curves 2)

On the Fig. 4A curve 1 corresponds to electrode  $\text{LiMn}_2\text{O}_4$  that modified with Melanin # 1

On the Fig. 4B curve 1 corresponds to electrode  $\text{LiMn}_2\text{O}_4$  that modified with Melanin # 2

Increasing discharge capacity of cathodes that modified with Melanin # 1 will result in increasing the energy of Li-ion cells with  $\text{LiMn}_2\text{O}_4$  active cathode material. Decreasing the impedance of cathode that modified with Melanin #1 will result in increasing the power of Li-ion cell with  $\text{LiMn}_2\text{O}_4$  active cathode material.

Developed method and conception for modification electrode material of Li batteries using the Melanin could be successfully used for modification the wide areas of new electrode materials.

The Nature / Structure of Melanin and the Nature / Structure of the electrode material determines the synergistic effect of the influence the modification on increasing the energy and power characteristics of Li-ion batteries electrodes.

## References

1. A. Chakraborty, S. Kunnikuruvaan, S. Kumar, B. Markovsky, D. Aurbach, M. Dixit, and D. T. Major. *Chem. Mater*, **32**, (3), 915–952 (2020)
2. I. M. Maksuta, A. V. Markevych, L. I. Neduzko, N. D. Zaderey, and E. M. Shembel Method producing the modified active cathode material for lithium-ion batteries. Ukrainian Patent application # a 2015 00834
3. V.I. Redko, E.M. Shembel, etc. Method and Apparatus for Measuring Conductivity of Powder Materials Using Eddy Currents. US Patent No. 7,288,941
4. V.I. Redko, E.M. Shembel, etc. Method and Device for Rapid Non-Destructive Quality Control of Powdered Materials. US Patent No. 8,102,181

## **Solid Polymer Electrolytes and Modified Electrodes are Basis for New Generation of High-Energy Lithium Batteries Safety, Wide Operating Temperature, High Energy, and Low Price**

E. Shembel<sup>a,b</sup>, O. Chervakov<sup>a</sup>, A. Markevych<sup>a</sup>, O. Kolomoiets<sup>a</sup>, I. Maksyuta<sup>a</sup>, V. Redko<sup>a,b</sup>, Y. Polishchuk<sup>a</sup>, N. Zaderey<sup>a</sup>, V. Pysny<sup>a</sup>, N. Koltsov<sup>a</sup>

<sup>a</sup>Scientific Research Laboratory of Chemical Power Sources of Ukrainian State University of Chemical Technology, Dnipro, 49005, Ukraine.

<sup>b</sup>Enerize Corporation, Coral Springs, FL, 33067, USA

The presentation and the followed publication of article results of investigation, developing, manufacturing, and test experimental samples of innovating lithium batteries with 1) anode based on Lithium or Lithium alloys (instead of anode that are based on carbon materials); 2) solid polymer electrolytes with performance in temperatures from minus 30°C and up to plus 120°C; and 3) cathode, which is based on modified lithium oxides, will be illustrated. Innovating solid polymer electrolyte is modified using ionic liquids. Cathode has been based on LiMn<sub>2</sub>O<sub>4</sub>, which have been synthesized using Ukrainian manganese ores.

Testing protocols for the developed solid polymer electrolyte in a wide temperature range up to plus 200°C confirm the unique stability of the properties of the ionic liquid-modified electrolyte. Exactly the solid polymer electrolyte, which has been developed, makes it possible to use the Li-based anode. And it was the use of a Lithium anode that provided the high energy of this current source.

For the successful manufacturing of this innovative batteries technologies have also been developed: manufacture of current leads for the cathode and for the anode, ensuring low resistance at the interface of current leads and electrode mass; and ensuring low resistance at the interface of a solid polymer electrolyte with the structure of the anode and cathode.

Results of tests experimental samples of innovating lithium batteries in the mode that includes many number cycles: discharge / charge mode under wide operating range of current and temperature from minus 30°C up to 120°C, confirm unique properties of developed Lithium batteries.

*More detailed information will be presented in the followed version of this abstract*

## Comparison of High-Voltage Cathode Materials for Lithium-ion Batteries

D. Kunicky, L. Chladil

Institute of Electrotechnology, Faculty of Electrical Engineering and Communication, BUT,  
Technicka 10, 616 00 Brno, Czech Republic

The article brings an overview of several material development approaches in the field of high-voltage layered-spinel cathode materials which could be used in HEVs, PHEVs and EVs due to their promising electrochemical properties. The commercially used batteries are not satisfactory in terms of increasing demand for higher capacities, higher voltage and eco-friendly materials. The materials discussed in this paper could be an excellent alternate to them as they do not contain cobalt, has high capacity and are cheaper. There are identified their superior properties throughout the article and at the end is the summary of electrochemical characteristics.

### Introduction

Current research of lithium-ion batteries is focused on developing non-toxic and inexpensive cathode materials that would be better than commercially used LFP and NMC cathodes. LFPs biggest advantage is their cost and safety operation but their low theoretical capacity and low operating voltage suits only very narrow field of use. NMC cathodes are great in term of electrochemical properties but their biggest disadvantage is the cobalt included in the structure. The very promising cathode materials are composites of layered ( $\text{LiMnO}_2$ ) and spinel ( $\text{LiMn}_2\text{O}_4$ ) structures. Maintaining high operational voltage around 4-5 V, thus providing high energy densities, can be used in modern PHEVs, HEVs or EVs. Its three-dimensional structure provides high rate capabilities because of the better lithium ions diffusion.

### Discussion

Layered-spinel cathodes delivers best properties from both layered and spinel phases. First mentioned phase implements the structural integrity and delivers high capacities, meanwhile, the spinel phase improves the diffusion of the lithium ions due to their 3D interstitial space thus improving the electrochemical performance of the cells.

Many researches are focused on layered-spinel cathode materials containing cobalt, but there are also cobalt free composites that are promising alternates in EVs battery packs and decreasing their costs. All mentioned researches are in Table 1 at the end of article.

The composites could be simple and complex. One of the simple ones is the research conducted by Liu [ 1] where was used  $\text{Li}_{1.3}\text{Ni}_{0.25}\text{Mn}_{0.75}\text{O}_{2.4}$  cathode material prepared by co-precipitation method and quenched in liquid nitrogen after heating at 500 °C for 4 h and 850 °C for 12 h. This cooling is important to obtain sub-micron size particles which results in enhanced rate performance and greater discharge capacity. Layered-spinel structure was confirmed by the HRTEM and FFT technology. Discharge capacity retention after 40 cycles at 0.2 C current is 98.2 %. Extending this study by long term cycling stability and elevated temperature measurements could lead to better understand this material and its possibility of usage in commercial applications.

Liu [ 2] doped similar structure  $\text{Li}_{1.1}\text{Ni}_{0.235}\text{Mn}_{0.735}\text{Cr}_{0.03}\text{O}_{2.3}$  with chromium, which is widely used as a dopant [ 3]. Chromium enhances the kinetics of lithium-ion diffusion and charge transfer reaction. Doped material shows better discharge capacity, coulombic efficiency and rate performance and is also structurally stabilized. It has superior discharge capacity rate of 100.1 % after 50 cycles at 0.2 C and good discharge capacity of  $113 \text{ mAh}\cdot\text{g}^{-1}$  under 10 C rate while pristine is only  $93 \text{ mAh}\cdot\text{g}^{-1}$ .

More complex composite is e.g.  $0.2\text{LiNi}_{0.5}\text{Mn}_{1.5}\text{O}_4\cdot 0.8\text{Li}[\text{Li}_{0.2}\text{Ni}_{0.2}\text{Mn}_{0.6}]\text{O}_2$  which was also made by co-precipitation method [ 4]. There were prepared three samples with different sintering temperature of 900 °C, 1000 °C and 1100 °C. Best properties had the first mentioned sample mainly because of the smallest primary particles. Interesting fact is that the specific capacity is lower at the 1<sup>st</sup> cycle than at the 60<sup>th</sup> cycle. This is explained by activating layered structure of  $\text{Li}[\text{Li}_{0.5}\text{Ni}_{0.25}\text{Mn}_{0.75}]\text{O}_2$  with contribution of spinel structure  $\text{LiNi}_{0.5}\text{Mn}_{1.5}\text{O}_4$ . There was a little decrease in discharge capacity after 50 cycles mainly due to the existence of Jahn-Teller distortion. This phenomenon is one of the major problems of cathodes involving manganese.

According to the size of the particles there is study aiming on nanofibers of spinel-layered  $0.5\text{LiMnTiO}_4\cdot 0.5\text{Li}_2\text{Mn}_{0.5}\text{Ti}_{0.5}\text{O}_3$  [ 5]. Electrospinning method was used to synthesize the composite nanofibers with diameter of approximately 80 nm. Material has lower discharge capacity in contrast to the above-mentioned cathodes but has excellent cyclability – the discharge capacity rate is 95.3 % after 100 cycles at 1 C rate. Titanium is in the +4 oxidation state ( $\text{Ti}^{4+}$ ) and is electrochemically inactive.

Very important aspect, which is often omitted, is the elevated temperature performance of batteries. But there are researches that along general measurements includes elevated temperature measurements for instance [ 6] where spinel-layer-layer composite  $0.5\text{Li}[\text{Ni}_{0.5}\text{Mn}_{1.5}]\text{O}_4\cdot 0.5[\text{Li}_2\text{MnO}_3\cdot \text{Li}(\text{Mn}_{0.5}\text{Ni}_{0.5})\text{O}_2]$  was encapsulated by various concentrations of  $\text{ZrO}_2$  (1 %, 3 % and 5 % wt.%). The  $\text{ZrO}_2$  did not influence the structure of the material. Its superior properties under elevated temperatures (55 C) are outstanding, showing good capacity retention of 86 % after 30 cycles at 1 C. During the high temperatures reacts the  $\text{PF}_6$  and produce unwanted reactions with electrolyte and cause irreversible structural changes. Only 1 wt.% can suppress this reaction and preserve electrochemical properties.

**Table 1.** Summary of discussed cathode materials.

| Formula   | Method                     | Electrolyte                        | Discharge capacity ( $\text{mAh}\cdot\text{g}^{-1}$ ) | Volt. [V] | Discharge capacity rate (%)                                | Ref. |
|---|----------------------------|------------------------------------|---|-----------|--|------|
| $\text{Li}_{1.3}\text{Ni}_{0.25}\text{Mn}_{0.75}\text{O}_{2.4}$   | Co-precipitation           | 1M $\text{LiPF}_6$<br>EC-DMC (1:1) | 282.0<br>(0.1 C)                                      | 4.8       | 98.2<br>40 cycles<br>0.2 C                                 | [ 1] |
| $\text{Li}_{1.1}\text{Ni}_{0.235}\text{Mn}_{0.735}\text{Cr}_{0.03}\text{O}_{2.3}$   | Co-precipitation           | 1M $\text{LiPF}_6$<br>EC-DMC (1:1) | 261.9<br>(0.1 C)                                      | 4.8       | 100.1<br>50 cycles<br>0.2 C                                | [ 2] |
| $0.2\text{LiNi}_{0.5}\text{Mn}_{1.5}\text{O}_4\cdot 0.8\text{Li}[\text{Li}_{0.2}\text{Ni}_{0.2}\text{Mn}_{0.6}]\text{O}_2$  | Co-precipitation           | 1M $\text{LiPF}_6$<br>EC-DMC (1:1) | 276.0   | 4.8       | 176 at 1 <sup>st</sup><br>276 at 60 <sup>th</sup><br>0.1 C | [ 4] |
| $\text{Li}_2\text{MnTiO}_{4+z}$   | electrospinning            | 1M $\text{LiPF}_6$<br>EC-DMC (1:1) | 210.0   | 4.8       | 95.3<br>100 cycles<br>at 1 C                               | [ 5] |
| 1 wt.% $\text{ZrO}_2$ doped $0.5\text{Li}[\text{Ni}_{0.5}\text{Mn}_{1.5}]\text{O}_4\cdot 0.5[\text{Li}_2\text{MnO}_3\cdot \text{Li}(\text{Mn}_{0.5}\text{Ni}_{0.5})\text{O}_2]$ | Co-precipitation + Sol-gel | 1M $\text{LiPF}_6$<br>EC-DMC (1:1) | 234.0   | 4.8       | 86 at 55 °C<br>30 cycles<br>1 C                            | [ 6] |

## Conclusions

Among many other systems of lithium-based batteries are manganese-based batteries closest to the commercial market and composites of spinel and layer structures deliver adequate electrochemical properties – high discharge capacity  $> 200 \text{ mAh g}^{-1}$ , high operating voltage  $> 4 \text{ V}$  and good cyclability. It is believed that these materials are promising alternate to current materials used commercially. It is obvious that various doping elements and approaches to the structure of materials in terms of the coexistence of layer and spinel phases have significant influence on specific capacity, stability, rate capability, energy density and operating voltage. There is also a demand to research electrolytes that can would be stable during high operational voltages and high temperatures. More research should be performed in this field with other possible materials to develop cheaper, stable, eco-friendlier and more powerful batteries with higher energies that can replace energy storages based on fossil fuels and non-renewable energy sources.

## Acknowledgement

This work was supported by the specific graduate research of the Brno University of Technology No. FEKT-S-20-6206.

## References

1. Y. Liu, Y. Gao and A. Dou, *Journal of Power Sources*, **vol. 248**, 679-684 (2014).
2. Y. Liu, Z. Zhang, Y. Gao, G. Yang, C. Li, J. Zheng, A. Dou, Q. Wang and M. Su, *Journal of Alloys and Compounds*, **vol. 657**, 37-43 (2016).
3. T. Kazda, O. Cech, J. Vondrak, A. Strakova Fedorkova, A. Visintin, P. Cudek and V. Kasparek, *ECS Transactions*, **vol. 63**, 15-21 (2014).
4. T. Ge, Z. Guo, M. Wu, R. Sun, W. Li and G. Yang, *Journal of Alloys and Compounds*, **vol. 801**, 254-261 (2019).
5. N. Vu, V. Dao, H. Van, L. Huy, N. Quang, H. Huu, S. Choi and W. Im, *Solid State Sciences*, **vol. 103** (2020).
6. G. Lee, I. Choi, M. Oh, S. Park, K. Nahm, V. Aravindan and Y. Lee, *Electrochimica Acta*, **vol. 194**, 454-460 (2016).

## Flame retardant influence on Negative Electrode for Lithium ion accumulators

J. Maca<sup>1,2</sup>, J. Libich<sup>1,2</sup>, T. Kazda<sup>1,2</sup> and K. Jasso<sup>1,2</sup>

<sup>1</sup>Centre for Research and Utilization of Renewable Energy, Technická 10, Brno, 616 00, Czech Republic

<sup>2</sup>Brno University of Technology, Technická 10, Brno, 616 00, Czech Republic

Almost every person is using batteries on daily base. From small appliances to larger power tools to large stores and electric cars. Requirements for lithium ion batteries getting higher every year either from view of capacity, cycle number or high current flow. With higher requirements is also the safety of batteries connected. Lithium ion batteries need to work safely and reliably at higher temperatures and loads. From flame safety view is necessary non-flammability of all battery parts. One of potential risk is organic solvents based electrolyte. This paper focus on influence, of flame retardant additive in electrolyte and it compatibility with the negative electrode in lithium ion battery. Several phosphorous based flame retardants were tested and their influence on capacity of negative electrode was determined.

### Introduction

A sum of experiments was made on carbon negative electrode and standard electrolyte for lithium ion accumulators. As electrolyte a mixture of ethylene carbonate (EC) and dimethyl carbonate (DMC) in weight ratio 1:1 and 1 mol LiPF<sub>6</sub> was used. To the electrolytes was added 5 vol.% of additive in form of flame retardant. Selected flame retardants were chosen by results obtained by previous flashpoint measurements. The galvanostatic cycling was made in 0,2C current. The results of one selected flame retardant are shown in Fig. 1. Shown flame retardant is triethyl phosphate (TEP). The reached capacity was 270 mAh/g and was stable in first ten cycles. Used flame retardant does not decrease dramatically the capacity of the negative electrode and have no influence on the stability of the electrode.

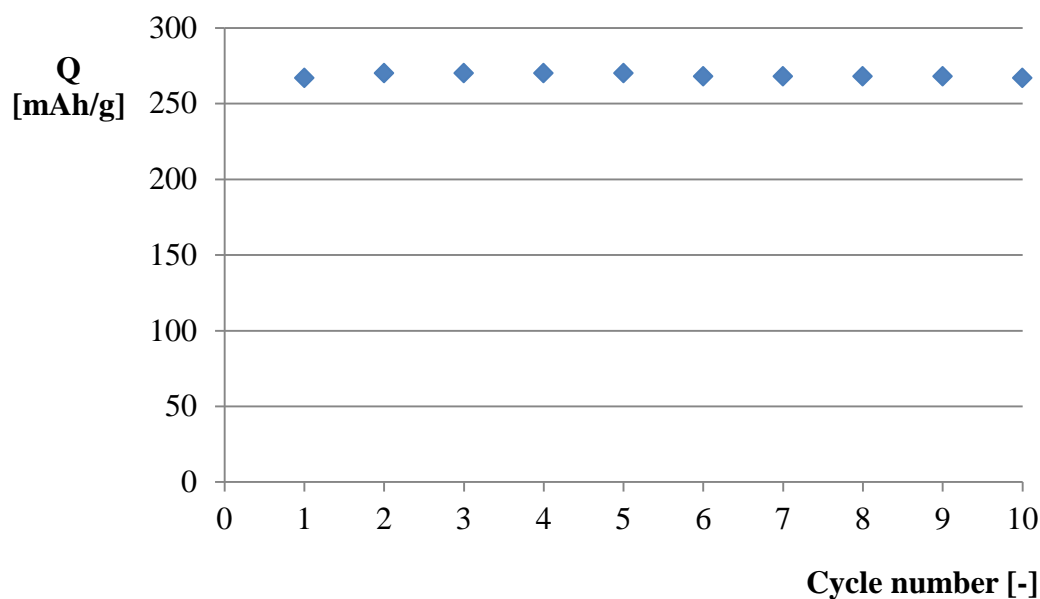


**Figure 1.** Capacity of negative electrode and TEP flame retardant,

### Acknowledgement

Authors gratefully acknowledge the financial support from the Ministry of Education, Youth and Sports of the Czech Republic under project No. LTT19001 and BUT specific research programme (project No. FEKT-S-20-6206)

### References

1. DENG, Kuirong, Qingguang ZENG, Da WANG, et al., 2020. Nonflammable organic electrolytes for high-safety lithium-ion batteries. *Energy Storage Materials*. DOI: 10.1016/j.ensm.2020.07.018. ISSN 24058297.
2. LIU, Binghe, Yikai JIA, Chunhao YUAN, Lubing WANG, Xiang GAO, Sha YIN a Jun XU, 2020. Safety issues and mechanisms of lithium-ion battery cell upon mechanical abusive loading: A review. *Energy Storage Materials*. 24, 85-112
3. WANG, Wei, Can LIAO, Longxiang LIU, et al., 2019. Comparable investigation of trivalent and pentavalent phosphorus based flame retardants on improving the safety and capacity of lithium-ion batteries. *Journal of Power Sources*. 420, 143-151.
4. WANG, Lubing, Sha YIN, Zhexun YU, et al., 2018. *Unlocking the significant role of shell material for lithium-ion battery safety*. 160, 601-610. DOI: 10.1016/j.matdes.2018.10.002. ISSN 02641275.

## A Review of Mechanical Stress on Lithium-ion cells

S. S. Madani

Aalborg University, Department of Energy Technology, Aalborg, DK-9220, Denmark

Email: ssm@et.aau.dk

Shocks and mechanical vibrations are accompany by lithium-ion batteries especially in mobile applications. The mechanical properties and performance of the lithium-ion battery cells in mobile applications especially electric vehicles are affected by the shocks and mechanical vibrations. Notwithstanding, the impacts of vibration on the performance, degradation, cycle life and thermal properties of lithium-ion batteries and components are unknown.

### Introduction

A model was designed which provides to simulate the disorderly vibrations energy accumulation, and gathering the changed electric energy in the battery cell which planned to provide the brightness at the dim time[1].

Cycle life experiments were performed to disclose the impact of dissimilar cut-off voltages and charging current rates on the aging mechanism of batteries[2].

An investigation was accomplished to specify the durability of commercially accessible battery cells and calculates both the mechanical and electrical vibration-induced degradation by calculating variations in battery cell natural frequency, impedance and capacity. In addition, the influence of the in-pack orientation and battery cell state of charge was evaluated [3].

An investigation was demonstrated that presents the impact which the variation in electrical properties of vibration several aged battery cells could have on the control strategy which was used through the battery cell management system of a hybrid electric vehicle[4].

An investigation was accomplished to which found out that both the mechanical properties and electrical performance of the lithium-ion cells were comparatively unchanged when encountered to vibration power which is corresponding to a common vehicle life[5].

The mechanical frequency feedback function was studied as a non-destructive technique to quantify parameters including damping and stiffness of pouch cells and their correspondence with the temperature, state of health and the state of charge of the battery cell[6].

Standard vibration requirements was compared with vibration magnitude in an electric vehicle for lithium-Ion batteries by employing energy spectral density study[7].

An approach was characterized for dynamic optimization and investigation of an electric vehicle suspension system by employing the motor in-wheel technology[8].

A procedure was determined to construct unpredictable energy spectral density profiles which were characteristic of one hundred thousand miles of UK customer electric vehicle application employing vibration dimensions from three electric vehicles, for taking vibration durability assessments of underfloor installed rechargeable power storage systems[9].

The different international regulations and standards for safety analysis of lithium ion batteries in automotive utilizations under different abusive environments was reviewed [10].

Mechanical design and strategic placement methodology of a robust battery pack for electric vehicles applications was reviewed [11].

### Result and discussion

Performance and mechanical properties of lithium-ion batteries could be severely affected by the acceleration inertia, road irregularity and abrupt crash. In recent years, the effect of the mechanical vibration on lithium-ion batteries has attracted more and more consideration from researchers [12-14]. A research was presented to specify the durability of commercially available battery cells and determines both the mechanical and electrical vibration-induced degradation via quantifying alterations in battery cell natural frequency, impedance and capacity. In addition, the influence of the in-pack orientation and cell state of charge was evaluated. The focus of attention of disclosed experimental outcomes was potential for essential mechanical and electrical properties in the battery cell to diverge, attributable to the utilization of vibration energy, which is accomplished with a regular road vehicle life [12-14].

The vibration experiments of lithium-ion battery module, which was employed for electric vehicle, were investigated regarding open circuit voltage [15]. The wettability of the negative and positive plates of the battery cell was altered in the electrolyte during the vibrating process, remaining for a course lengthy enough following vibration, the battery keeps its wettability constant and its discharge capacity was partially regained. The outcomes exhibited that the construction of the lithium-ion battery module stays fixed. In addition, the temperature and voltage stays steady in the vibrating process. After and before the vibration process, no evident variation was seen in the AC internal resistance of the battery module. Conductivity of the active particles of the battery was considerably decreased, resulting in decline in charge capacity and rise in DC internal resistance of battery module [15].

### References

1. Sergey Shevtsov , Shun-Hsyung Chang, Modeling of vibration energy harvesting system with power PZT stack loaded on Li-Ion battery, international journal of hydrogen energy 41(2016)1 2618-12625
2. Yang Gao , Jiuchun Jiang , Caiping Zhang , Weige Zhang , Zeyu Ma, Yan Jiang , Lithium-ion battery aging mechanisms and life model under different charging stresses, Journal of Power Sources 356 (2017) 103-114.
3. James Michael Hooper , James Marco , Gael Henri Chouchelamane and Christopher Lyness, Vibration Durability Testing of Nickel Manganese Cobalt Oxide (NMC) Lithium-Ion 18,650 Battery Cells, Energies 2016, 9, 52; doi:10.3390/en9010052.
4. Thomas Bruen , James Michael Hooper , James Marco , Miguel Gama, and Gael Henri Chouchelamane , Analysis of a Battery Management System (BMS) Control Strategy for Vibration Aged Nickel Manganese Cobalt Oxide (NMC) Lithium-Ion 18650 Battery Cells, Energies 2016, 9, 255; doi:10.3390/en9040255.
5. James Michael Hooper , James Marco, Gael Henri Chouchelamane , Christopher Lyness ,and James Taylor, Vibration Durability Testing of Nickel Cobalt Aluminum Oxide (NCA) Lithium-Ion 18650 Battery Cells, Energies 2016, 9, 281; doi:10.3390/en9040281.

6. Hartmut Popp , Gregor Glanz , Karoline Alten , Irina Gocheva ,Wernfried Berghold ,and Alexander Bergmann , Mechanical Frequency Response Analysis of Lithium-Ion Batteries to Disclose Operational Parameters, *Energies* 2018, 11, 541; doi:10.3390/en11030541.
7. Jenny Frodelius Lang, Gunnar Kjell, Comparing vibration measurements in an electric vehicle with standard vibration requirements for Li-ion batteries using power spectral density analysis, *Int. J. Electric and Hybrid Vehicles*, Vol. 7, No. 3, 2015.
8. Humberto Gonçalves, José Meireles, Jorge Martins, VIBRATION ANALYSIS OF INTEGRATED SYSTEMS TO ELECTRIC VEHICLES, 5th International Operational Modal Analysis Conference.
9. J.M. Hooper, J Marco, Defining a Representative Vibration Durability Test for Electric Vehicle (EV) Rechargeable Energy Storage Systems (RESS), EVS29 Symposium Montréal, Québec, Canada, June 19-22, 2016.
10. V. Ruiz, A. Pfrang, A. Kriston, N. Omar, P. Van den Bossche, L. Boon-Brett, A review of international abuse testing standards and regulations for lithium ion batteries in electric and hybrid electric vehicles, *Renewable and Sustainable Energy Reviews* 81 (2018) 1427–1452.
11. Shashank Arora , Weixiang Shen, Ajay Kapoor, Review of mechanical design and strategic placement technique of a robust battery pack for electric vehicles, *Renewable and Sustainable Energy Reviews* 60(2016)1319–1331.
12. J. Lee, J. Yeo, M. Jang, J. Yoon, and D. M. Kang, “Mechanical durability and electrical durability of an aluminium-laminated lithium-ion polymer battery pack for a hybrid electric vehicle,” vol. 224, pp. 765–773, 2010.
13. J. Michael and J. Marco, “Characterising the in-vehicle vibration inputs to the high voltage battery of an electric vehicle,” vol. 245, pp. 510–519, 2014.
14. J. M. Hooper and J. Marco, “Experimental modal analysis of lithium-ion pouch cells,” vol. 285, pp. 247–259, 2015.
15. H. Wang, Z. Tao, Y. Fu, and W. Li, “Analysis on Vibration of Li-ion Battery Module Used for Electric Vehicle,” no. Icsmse, pp. 3–5, 2016.

## Characterization of Lithium-Ion Battery Cells

S. S. Madani

Aalborg University, Department of Energy Technology, Aalborg, DK-9220, Denmark

Email: ssm@et.aau.dk,

A comprehensive experiential laboratory characterization experiment method was established and exerted to different lithium-ion batteries. Consequently, the batteries' power, open circuit voltage, capacity, capability, internal resistance, and signal AC impedance were determined for different load currents and over an extensive temperature range. According to these performance outcomes, battery models, which were capable of predicting the dynamic behavior of the lithium-ion batteries were improved and experimentally validated under different operating conditions.

### Introduction

Due to their big power and energy densities, lithium-ion batteries are a considerably essential element of electric vehicles. Their application has enhanced noticeably in the last few years [1-7]. One of the important issues of employing lithium ion batteries in electric and hybrid vehicles is appropriate thermal management. Proper thermal management is essential with the intention of controlling degradation at a satisfactory rate. In addition, it is important to decrease the risk of thermal runaway.

It is usually appropriately comprehended that enhancing the working temperature of a lithium ion battery tends to raise the rate of degradation. Notwithstanding, there is insufficient comprehension regarding the advantageous technique in which to thermally control the lithium-ion battery cells in a battery pack. In addition, the influences of temperature gradients among battery cells in a battery pack are not well-understood [8-12].

Thermal management of the lithium-ion battery is a considerably complicated problem. The solution for thermal management will be dissimilar for different pack topologies, battery cells, and different applications.

The investigation, which is represented in this research, demonstrates a considerable scientific advancement and improvement in the comprehension of thermal management in lithium ion battery cells.

Various experimental research has been accomplished on the thermal and electrical performances of lithium-ion batteries. Experimental investigations were restricted to surface temperatures integrated with the thermal or analytical modeling of heat dissipation with the intention of achieving battery temperatures and to determine the battery cell total heat loss.

This section studies the performance behavior of a lithium titanate oxide-based battery at different working conditions. Battery cell performance analysis were put into research appertaining to comprehensive experimental laboratory measurements. Different load profiles were applied to the lithium titanate oxide-based battery. To assess the performance of the lithium titanate oxide-based battery cell, extensive laboratory characterization experiments were accomplished.

Characterization of the battery cell behavior under dissimilar conditions is very important and has different application such as fully parameterization of the performance model of the li ion batteries. Therefore, comprehensive laboratory tests are essential for the investigated lithium titanate oxide-based battery cell.

Consequently, an approach to characterize the battery cell behavior under dissimilar conditions such as load current, temperature and SOC was established and exerted to a lithium titanate oxide-based battery cell.

### Preconditioning test

The initial movement toward the characterization method comprised of a relaxation test and preconditioning test. The main purpose of doing a preconditioning test was to eliminate any potential passivating to which the battery cell was exposed to, among the primary experiments and the manufacturing time. Furthermore, another objective of this experiment was to notice if the battery cell temperature, voltage and capacity are balanced. In addition, it has to be emphasized that the preconditioning experiment was exerted to all the lithium titanate oxide-based battery cells.

### Capacity test

The purpose of conducting a capacity measurement was to specify the dependency of the discharged and charged capacity of the lithium titanate oxide-based battery cell on the load current and temperature. Consequently, the battery capacity was measured at dissimilar temperatures and discharge-charge current rates. The battery cell capacity was measured throughout discharge and charge at the particular current rates and temperature. It can be observed that the capacity of lithium titanate oxide-based battery cell is greatly reliant on the applied current rate and temperature.

### Open-circuit voltage measurements

Consistent with the majority of the lithium titanate oxide-based battery cell parameters, the OCV is greatly depending on the working conditions and it alters with the temperature and the SOC. The goal of fulfilling this experiment was to acquire the relationship among SOC and OCV for discharging and charging states at dissimilar temperatures and for SOCs among 0% and 100%, by taking 5% SOC resolution into consideration.

### Hybrid Pulse Power Characterization Test

The hybrid pulse power characterization test was applied to the lithium titanate oxide-based battery cell at different temperature and current rates. The measurement profile, which was applied to the battery cell, is demonstrated in Figure 3.4. As it can be seen, the current profile consists of successive discharging and charging DC current pulses of dissimilar current rate. The pulse time was appointed to 20 s and the relaxation duration among each two successive pulses was assigned to fifteen min. For a comparison between different conditions and to understand the effect of temperature on the hybrid pulse power characterization experiments, the tests were repeated at different temperature.

### References

1. A. Ritchie, W. Howard, Recent developments and likely advances in lithiumion batteries, *Journal of Power Sources* 162 (2) (2006) 809–812.
2. M. Malik, I. Dincer, M.A. Rosen, Review on use of phase change materials in battery thermal management for electric and hybrid electric vehicles, *International Journal of Energy Research* 40 (8) (2016) 1011–1031.
3. M.A. Hannan, M.M. Hoque, A. Mohamed, and A. Ayob. Review of energy storage systems for electric vehicle applications: Issues and challenges. *Renewable and Sustainable Energy Reviews*, 69:771–789, 2017.
4. S. Chauque, F.Y. Olivia, A. Visintin, D. Barraco, and O.R. Leiva, E.P.M. Camara. Lithium titanate as anode material for lithium ion batteries: Synthesis, posttreatment and its electrochemical response. *Journal of Electroanalytical Chemistry*, 799:142–155, 2017.
5. A. Farmann, W.Waag, and Dirk Uwe Sauer. Application-specific electrical characterization of high power batteries with lithium titanate anodes for electric vehicles. *Energy*, 112:294–306, 2016.
6. D. Andre, M. Meiler, K. Steiner, C. Wimmer, T. Soczka-Guth, and D.U.Sauer. Characterization of high-power lithium-ion batteries by electrochemical impedance spectroscopy. I. Experimental investigation. *Journal of Power Sources*, 196:5334–5341, June 2011.
7. L. Zhang, H. Peng, Z. Ning, Z. Mu, and C. Sun. Comparative Research on RC Equivalent Circuit Models for Lithium-Ion Batteries of Electric Vehicles. *Applied Sciences*, 7:1–16, 2017.
8. Q. Wang, P. Ping, X. Zhao, G. Chu, J. Sun, C. Chen, Thermal runaway caused Fire and explosion of lithium ion battery, *Journal of Power Sources* 208 (2012) 210–224.
9. L. Lu, X. Han, J. Li, J. Hua, M. Ouyang, A review on the key issues for lithium-ion battery management in electric vehicles, *Journal of Power Sources* 226 (2013) 272–288.
10. T.Y. Lu, C.C. Chiang, S.H. Wu, K.C. Chen, S.J. Lin, C.Y. Wen, C.M. Shu, Thermal hazard evaluations of 18650 lithium-ion batteries by an adiabatic calorimeter, *Journal of Thermal Analysis and Calorimetry* 114 (3) (2013) 1083–1088.
11. S. Bhide, T. Shim, Novel Predictive Electric Li-Ion Battery Model Incorporating Thermal and Rate Factor Effects, *IEEE Transactions on Vehicular Technology* 60 (3) (2011) 819–829.
12. X.W. Zhao, G.Y. Zhang, L. Yang, J.X. Qiang, Z.Q. Chen, A new charging mode of batteries with LiFePO<sub>4</sub>/C composites under low temperature, *Journal of Thermal Analysis and Calorimetry* 104 (2) (2011) 561–567.

## Study of the Effect of External Compressive Loads on the Performance of a Lithium-ion Cell

S. S. Madani \*, E. Schaltz and S. K. Kær

Department of Energy Technology, Aalborg University, DK-9220 Aalborg, Denmark;  
esc@et.aau.dk (E.S.); Skk@et.aau.dk (S.K.K.);

\*Correspondence: ssm@et.aau.dk (SSM);

Lithium-ion batteries are being implemented in different large-scale applications including aerospace and electric vehicles. For these utilizations, it is essential to improve battery cells with big cycle life because battery substitute is costly. For their implementation in real applications, lithium-ion battery cells undergo extension during the course of discharging and charging. To avoid disconnection among battery pack ingredients and deformity during cycling, compacting force is exerted to battery packs in electric vehicles. This investigation strives to demonstrate how exterior force affects the performance and behavior of a lithium-ion battery cell corresponding to static exterior force by monitoring the applied pressure at dissimilar state of charge. Electrochemical impedance spectroscopy was used as the main technique for this research. It was concluded that the profiles of the achieved spectrums from the experiments seems completely dissimilar in comparison with the cases without external pressure.

### Introduction

The effect of externally and internally mechanical stresses against the electrochemical performance of lithium-ion batteries was studied. Focused attention was on the dependency of the ion transport inside the separator against the stress condition. It was concluded that utilization of external pressure on the battery cell brings about stresses [1].

The impact of the utilization of pressure throughout the procurement of LiCoO<sub>2</sub> cathodes and compound flaky synthetic graphite anodes on their electrochemical performance in Li intercalation and de-intercalation processes was investigated by employing electrochemical impedance spectroscopy, chronopotentiometry and voltammetry . It was concluded the utilization of pressure throughout the procurement of LiCoO<sub>2</sub> and graphite has opposed impacts on their performance [2].

Stress development in lithium-ion compound electrodes throughout electrochemical cycling and consequential interior pressures on the cell casing was investigated. In addition, a model was introduced to determine the interior pressure that would be produced in a spirally wound battery casing attributable to the electrode stress throughout discharge and charge cycling [3].

The reasons for the abrupt degradation of useable capacity were investigated with the help of supplementary procedures including, post-mortem analyses, computed tomography, and electrochemical studies . The acquired outcomes indicate collectively to inharmonious aging as a main factor for the abrupt degradation of battery cell capacity, which consequently is caused by dissimilarities in regional compression [4].

The thickness variation of a commercial pouch type battery cell was studied at numerous sizes . The shifts of the single separate electrode materials were scrutinized by dilatometry. It was concluded that the cathode cooperates considerably to the thickness variation of the battery and enlarges directly by the delithiated capacity with about two percent [5].

24 big capacity lithium-ion battery cells with great silicon content were cycle under seven dissimilar cycling situations, to investigate the consequence of dissimilar stimulus on the cycle life of Si-anode full battery cells. The impact of different factors was considered such as the discharge current, depth of discharge and ambient temperature. The pressure development was observed through battery lifetime and demonstrates the identical behavior throughout all cycling states. By decreasing the capacity retention, an irreversible pressure growth occurs. An understandable interdependence could be distinguished among pressure behavior and the capacity retention of the Si-alloy cells. This indicates a correspondence among the principal aging mechanism between their irreversible pressure increase and Si-alloy cells [6].

The impacts of exterior compacting on the ageing and performance of single-layer lithium ion pouch cells were researched by using a spring-loaded structure. In addition, a coupling between mechanics and electrochemistry was demonstrated. Four different pressure were applied to the battery to investigate the effect of different pressure from 0.66 to 1.98 MPa on impedance in new battery cells. In addition, the impedance was characterized at different pressure levels. After cycling the new battery cells, the aged cells were investigated for impedance increase and capacity fade. The impact of pressure distribution was simulated. The outcomes demonstrated that the mass transport and kinetic resistance raised with pressure in a new battery cell [7].

To decrease cyclable-lithium loss throughout cycling the most appropriate and beneficial pressure was determined around 1.3 MPa. Ageing pressure influences the charge transfer resistance of the ohmic resistance of the cell and both graphite and NMC electrodes. It was concluded that pressure distribution causes current distribution whereas the increased current throughput at lesser pressures does not speed up its ageing [7].

An experimental setup was designed and constructed to determine electrical performance of NMC based 25Ah lithium-ion battery cells for various applied pressures . The temperature range was considered between 0-45°C. External pressure influences the voltage and capacity of the cell. It was seen that raised pressure increased the cell capacity and voltage during charge and decreased it during discharge . The impedance rises, which was the most considerable parameters demonstrated bulk transport variation for active materials with applied pressure. Power capability and greater capacity of the cells were mainly seen when there is no external pressure condition [8].

An experiment was accomplished to specify the influence of external pressure on different electrical parameters such as galvanostatic electrochemical impedance spectroscopy, capacity variation, voltage, current, for a pouch cell . Outcomes demonstrated that the external static pressure does have not influence on ohmic contribution, nevertheless, it could improve ion diffusion for pressure between 0.125 MPa and 1 MPa . It was observed that lithium ion pouch cell produced dynamic pressure during discharge and charge processes near 50 % state of charge, which agreed with capacity change. In addition, it was seen that the pressure speed was affected by current rate. The dynamic pressure is not influenced by current rate in charged condition. Nevertheless, voltage was influenced among 35%-65% state of charge [9].

The impacts of mechanical stress on commercial lithium-ion battery life were studied by observing the capacity and stack pressure of constrained lithium-ion pouch cells during charging and discharging . It was found that stack stress is a dynamic amount. The stress oscillating with discharge and charge. It was seen that it gradually raised irreversibly during long period of time with charging and discharging . Changes in primary stack pressure was shown as a significant

parameter, which could be controlled by manufacturer. It was observed that by changing the primary stack pressure the cells experience various stress evolution over their lifetime . It was concluded that battery cells, which were manufactured with greater stack pressure demonstrated lower cycle lives [10].

The effect of compressive pressure on battery degradation was investigated. Battery cells were cycled 1200 times under 0, 5 psi and 15 psi compressive pressure loads . It was seen that capacity fade for 0, 5 and 15 psi pressure loads were 11.0%, 8.8% and 8.4%. Correspondent power fade demonstrated an opposite trend compared to the capacity fade . This contradictory behavior was found to be pertaining to the separator creep and wettability rise in the cell after pressure load was applied . The investigation determined the progress of compressive loads over numerous cycles and it was concluded that pressure raises with cycling [11].

The previous studies and achievements, which were discussed are restricted to specific sections of lithium-ion batteries and the connection among force generation and coulombic efficiency and also capacity change throughout charge and discharge under several current is not obviously described.

This investigation suggests a principal method with the intention of determination of the effect of external force on the performance and behavior of a lithium-ion battery cell. Initially, the primary aim is to present the impedance properties variation in external static force condition for the lithium-ion battery cell. The influence of external force on the battery cell performance at dissimilar state of charge is an important aspect, which up to the present time is not completely comprehended. The main idea of this investigation was to present the excellent experimental set up to provide constant pressure on battery cell during cycling, and to investigate the mechanism in battery cell when pressure is applied.

The main purpose of this investigation is accordingly to quantify and determine battery state of charge impacts on lithium ion cell performance owing to cycling under force by using electrochemical impedance spectroscopy. In addition, the impact of external force on capacity decline and impedance change with cycling was studied. The procedures and experimental configuration in this investigation is presented in Part 2. Following introducing the outcomes attributable to applying cycling and force, an explanation of the outcomes was summarized in Part 3. Eventually, the main conclusion was outlined in Part 4.

## Result and discussion

Figure 12 demonstrates the feedback of impedance experiments in the Nyquist plane for the battery cell at different state of charge in the absence of external pressure. Figure 13 demonstrates electrochemical impedance spectroscopy results of Li-ion battery cell under external static force equal to 8 kN. The profile of these spectrums appears different compared to the case without external pressure. The figure could be divided into two sections. In the first section, there is an important value, which is the amount of crossing with the real axis ( $R_1$ ) and it appertains to the aggregate of inner ohmic resistances of the separator, electrolyte, cabling and current collector. The arc might be corresponding to the interface among the active material and electrolyte or to the solid electrolyte interface. In addition, it could be representing the charge transmission mechanism at electrolyte-electrode interface [12,13]. The second section corresponds to the transmission of lithium ion mostly attributable to relocation and diffusion phenomena [12,13]. For better view of the results, zooming of the electrochemical impedance spectroscopy results for both cases are illustrated in Figure 14.

To comprehend stress development plots of the restrained battery cell it is essential to comprehend the fixed thickness character of the solid constraint.

The constraint, which is illustrated in Figure 4, restrains the battery cell to keep a fixed thickness in such a manner which stress and not thickness, is free to expand. Stress evolution consequently is relevant to the cell thickness variations that would happen in the nonattendance of a solid constraint, accompanied by the quantified stress alteration being identical to the exerted stress essential to invert the battery cell thickness alteration. The fixed thickness scheme contributes a well explanation of batteries which are mainly located in solid constraints.

In this investigation two important parameters were employed to study the achieved data form electrochemical impedance spectroscopy measurements. The initial parameter is  $R_1$ , which is the amount on the real axis where the impedance spectrum intersection with the axis. This resistance is commonly named as the ohmic contributions.

The secondary parameter is  $R_2$ , which is the amount of battery impedance on the real axis while negative imaginary section reaches to a local minimum after a local maximum.  $R_2$  is usually refers to the total resistance of the battery cell because it contains electrochemical impedances and ohmic resistance.

Comparison of electrochemical impedance spectroscopy results at different state of charge in the present and absence of external pressure for the battery cell in the Nyquist plane is illustrated in Figure 15. As could be seen from the figures by increasing the external force,  $R_1$  increased with external force at the investigated temperature. Notwithstanding, total resistance  $R_2$  decreases, as external force rises at the investigated temperature. This demonstrates external force alters the bulk transmission characteristics of active materials of the battery cell [14].

Contemplating  $R_1$ , considerable change was seen for  $R_1$ . Accordingly, the external static force appears to have a great influence on the separator, electrolyte, cabling and current collector properties. Consequently, it could be assumed that this amount is influenced by the external pressure.

In Figure 14, demonstrates that the diffusion part moves left when decreasing the state of charge in load condition. This movement appears to begin from the commencement of different sections for dissimilar state of charge. It could be concluded that the external pressure in this experiment could increase the ion diffusion in electrode [15].

## References

1. R. Behrou, K. Maute, and K. Smith, "Numerical Simulation of Pressure Management Strategies for Lithium-ion Pouch Cells," vol. 1, no. June, pp. 1–2, 2014.
2. J. S. Gnanaraj, Y. S. Cohen, M. D. Levi, and D. Aurbach, "The effect of pressure on the electroanalytical response of graphite anodes and LiCoO<sub>2</sub> cathodes for Li-ion batteries," J. Electroanal. Chem., vol. 516, no. 1–2, pp. 89–102, 2001.
3. S. P. V. Nadimpalli, V. A. Sethuraman, D. P. Abraham, A. F. Bower, and P. R. Guduru, "Stress Evolution in Lithium-Ion Composite Electrodes during Electrochemical Cycling and Resulting Internal Pressures on the Cell Casing," J. Electrochem. Soc., vol. 162, no. 14, pp. A2656–A2663, 2015.
4. T. C. Bach et al., "Nonlinear aging of cylindrical lithium-ion cells linked to heterogeneous compression," J. Energy Storage, vol. 5, pp. 212–223, 2016.

5. B. Rieger, S. Schlueter, S. V. Erhard, J. Schmalz, G. Reinhart, and A. Jossen, "Multi-scale investigation of thickness changes in a commercial pouch type lithium-ion battery," *J. Energy Storage*, vol. 6, pp. 213–221, 2016.
6. G. Berckmans et al., "Comprehensive Aging Analysis of Volumetric Constrained Lithium-Ion Pouch Cells with High Concentration Silicon-Alloy Anodes," *Energies*, vol. 11, no. 11, p. 2948, 2018.
7. A. S. Mussa, M. Klett, G. Lindbergh, and R. W. Lindström, "Effects of external pressure on the performance and ageing of single-layer lithium-ion pouch cells," *J. Power Sources*, vol. 385, no. February, pp. 18–26, 2018.
8. A. Barai, Y. Guo, A. McGordon, and P. Jennings, "A study of the effects of external pressure on the electrical performance of a lithium-ion pouch cell," 2013 Int. Conf. Connect. Veh. Expo, ICCVE 2013 - Proc., pp. 295–299, 2013.
9. Y. C. Zhang, O. Briat, J. Y. Deletage, C. Martin, G. Gager, and J. M. Vinassa, "Characterization of external pressure effects on lithium-ion pouch cell," *Proc. IEEE Int. Conf. Ind. Technol.*, vol. 2018–February, pp. 2055–2059, 2018.
10. J. Cannarella and C. B. Arnold, "Stress evolution and capacity fade in constrained lithium-ion pouch cells," *J. Power Sources*, vol. 245, pp. 745–751, 2014.
11. A. McGordon et al., "The effect of external compressive loads on the cycle lifetime of lithium-ion pouch cells," *J. Energy Storage*, vol. 13, pp. 211–219, 2017.
12. J. Vetter, P. Novak, M. R. Wagner, C. Veit, K. C. Moeller, J. O. Besenhard, M. Winter, M. Wohlfahrt-Mehrens, C. Vogler, and A. Hammouche, "Ageing mechanisms in lithium-ion batteries," *Journal of Power Sources*, vol. 147, no. 1–2, pp. 269–281, 2005.
13. D. Andre, M. Meiler, K. Steiner, C. Wimmer, T. Soczka-Guth, and D.U. Sauer, "Characterization of high-power lithium-ion batteries by electrochemical impedance spectroscopy. I. Experimental investigation," *Journal of Power Sources*, vol. 196, no. 12, pp. 5334–5341, 2011.
14. Waag, W., S. Käbitz, and D.U. Sauer, "Experimental investigation of the lithium-ion battery impedance characteristic at various conditions and aging states and its influence on the application". *Applied Energy*, vol. 102(0), pp. 885-897, 2013.
15. R. Fu, M. Xiao, and S. Choe, "Modeling, validation and analysis of mechanical stress generation and dimension changes of a pouch type high power Li-ion battery," *Journal of Power Sources*, vol. 224, pp.211–224, 2013.

## Enhancing electrochemical properties of $\text{LiMn}_2\text{O}_4/\text{LiNi}_{0.5}\text{Mn}_{1.5}\text{O}_4$ core/shell composites

A.V. Potapenko, Y.A. Kravets, S. A. Kirillov

Joint Department of Electrochemical Energy Systems,  
38A Vernadsky Ave., 03680 Kyiv, Ukraine

The electrochemical properties of modified spinel samples at different current densities are presented. The  $\text{LiMn}_2\text{O}_4$  electrode with a maximum percentage of covering (14% of  $\text{LiNi}_{0.5}\text{Mn}_{1.5}\text{O}_4$ ) can endure higher current loads compared with the sample consisting 7% of surface layer. The capacity values for the samples at 45 and 30 C are 21.7 and 30.5  $\text{mAh}\cdot\text{g}^{-1}$ , respectively. Thus, it can be concluded that the proposed method of modification can be an effective tool for obtaining electrode materials for the new generation of LIBs.

### Introduction

Lithium-ion batteries are widely used in portable electronics and electric vehicles and are of increasing popularity for military and aerospace applications. Nevertheless, modern LIBs have several disadvantages from the point of view of safety and reliability, so that numerous attempts are made worldwide for raising the improvements of their components. Among strategies aimed at obtaining safer and more reliable cathode materials, a one suggested by Sun and Amine leans on the application of a thin protective shell onto the surface of a material, which forms a core [1]. Since 2005, this approach attracts much attention of experimentalists and is broadly reviewed, see, e.g., Refs [2,3].

The core-shell strategy can be subdivided into two directions. One of them deals with materials where core and shell are of no structural (and sometimes chemical) relations. Another operates with structurally related (isomorphous) components, which can be adjoined forming a particle with a concentration gradient. There are many examples of gradient materials first dealing with layered cathodes of  $\text{LiMO}_2$  family, where  $\text{M}=\text{Co}$ ,  $\text{Ni}$  and  $\text{Mn}$ ; in addition to Ref. [2] and latest reviews [2, 3] see Ref. [4] where lithium- and nickel-rich oxides are obtained in according with both strategies.

One of materials promising for the core-shell gradient structure formation is lithium-manganese spinel,  $\text{LiMn}_2\text{O}_4$  [5]. It is widely studied, manufactured in great amounts and applied in numerous commercial LIBs, including those for electric vehicles. On the one hand, lithium-manganese spinel is cheap, non-toxic and environmentally friendly, so that can substitute more spread, expensive and toxic  $\text{LiCoO}_2$ . On the other hand, in spite of quite high theoretical capacity ( $Q_{\text{sp.}}=148 \text{ mAh}\cdot\text{g}^{-1}$ ) and wide electrochemical window (3.4-4.5 V vs  $\text{Li}^+|\text{Li}$ ), it endures the capacity fading due to the interaction with an electrolyte generating manganese losses through a decomposition reaction. In this paper, we use a citric acid aided method for obtaining  $\text{LiMn}_2\text{O}_4$  covered with  $\text{LiNi}_{0.5}\text{Mn}_{1.5}\text{O}_4$ .

## Experimental

For obtaining  $\text{LiMn}_2\text{O}_4$ , 1 M solutions of  $\text{Mn}(\text{NO}_3)_2$ ,  $\text{LiNO}_3$  and citric acid (all of analytical grade from Makrochim, Ukraine) are mixed in a stoichiometric ratio of cations and twice excess of the acid. After evaporation at 80 °C to the stage of a glassy residue, the latter is grinded and decomposed at 120 °C, pyrolyzed in air at 400 °C for 1 h and annealed in air at 700 °C for 24 h.

For preparation core/shell composites,  $\text{LiMn}_2\text{O}_4$  is put into a mixture of 1 M solutions of  $\text{Ni}(\text{NO}_3)_2$  (analytical grade, Makrochim, Ukraine),  $\text{Mn}(\text{NO}_3)_2$ ,  $\text{LiNO}_3$  and citric acid with a proper ratio of components and all operations are performed as described above.

## Results and Discussion

XRD patterns of the surface modified materials are given in Fig. 1. As follows from these data, the presence of the modifier is difficult to discern because of the close resemblance of X-ray pictures of both spinels (JCPDS 35-0782 and JCPDS 32-0581, respectively). The fact is that both phases belong to the same space group ( $Fd3m$ ,  $Z=8$ ) and have close unit cell dimensions ( $a=8.248$  and 8.172 Å, respectively). Just a minor shift of reflexes to greater angles may signify the presence of  $\text{LiNi}_{0.5}\text{Mn}_{1.5}\text{O}_4$  in surface modified samples.

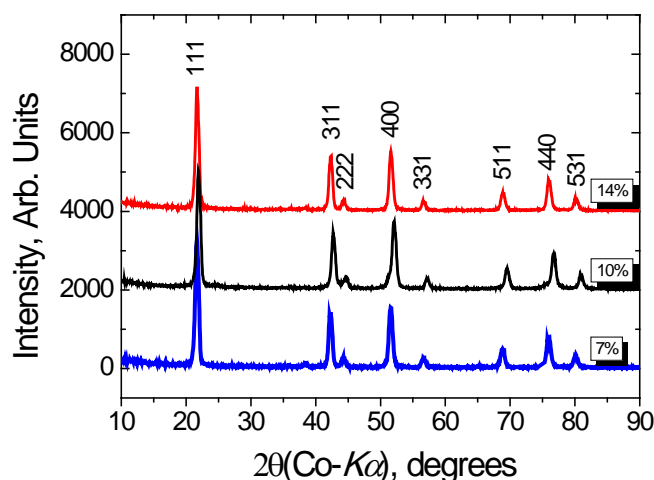


**Figure 1.** XRD patterns for bare  $\text{LiMn}_2\text{O}_4$  and  $\text{LiMn}_2\text{O}_4/\text{LiNi}_{0.5}\text{Mn}_{1.5}\text{O}_4$  surface modified materials with a different percentage of covering.

As follows from TEM micrographs, surface modification does not cause changes in the morphology of the core material,  $\text{LiMn}_2\text{O}_4$  (Fig. 2). For the pristine  $\text{LiMn}_2\text{O}_4$  and the  $\text{LiMn}_2\text{O}_4/\text{LiNi}_{0.5}\text{Mn}_{1.5}\text{O}_4$  composite containing 7 % coverage, the mean particle size is close to 85 nm.

In Fig. 3, the electrochemical properties of modified spinel samples at different current densities are presented. The  $\text{LiMn}_2\text{O}_4$  electrode with a maximum percentage of covering (14% of  $\text{LiNi}_{0.5}\text{Mn}_{1.5}\text{O}_4$ ) can endure higher current loads compared with the sample consisting 7% of surface layer. The specific capacity values for the samples at 45 and 30 C are 22 and 31  $\text{mAh}\cdot\text{g}^{-1}$ , respectively. Thus, it can be concluded that the proposed method of modification can be an effective tool for obtaining electrode materials for the new generation of LIBs.

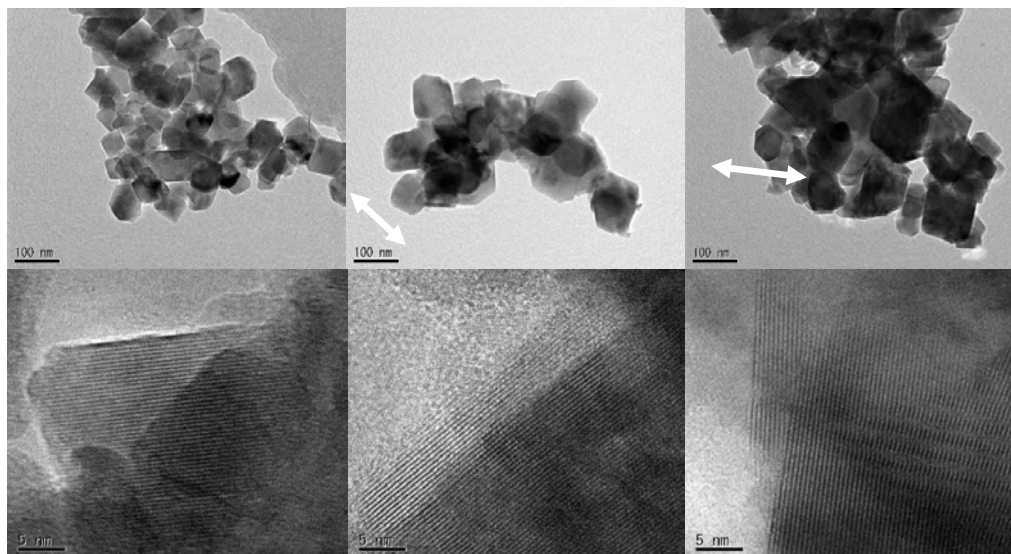


**Figure 2.** TEM images for  $\text{LiMn}_2\text{O}_4/\text{LiNi}_{0.5}\text{Mn}_{1.5}\text{O}_4$  surface modified materials with the different percentage of covering.

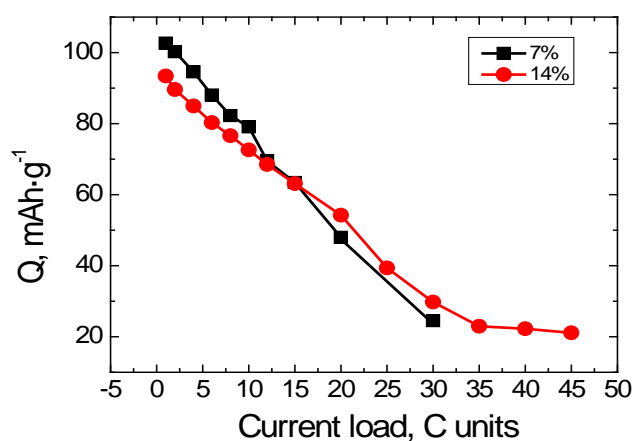


**Figure 3.** High-rate performance of  $\text{LiMn}_2\text{O}_4/\text{LiNi}_{0.5}\text{Mn}_{1.5}\text{O}_4$  surface modified materials at different current loads (1.0C-45.0C).

## References

1. S.-T. Myung, K. Amine, Y.-K. Sun, *Advanced technologies and applications*, ed. by B. Scrosati, K.M. Abraham, W. van Schalkwijk, and J. Hassoun, Wiley, Hoboken, NJ, 2013, p.p. 89-105.
2. D. Zuo, G. Tian, X. Li, D. Chen, K. Shu, *J. Alloys Comp.*, **706**(1), 24 (2017).
3. P. Guan, L. Zhou, Z. Yu, Y. Sun, Y. Liu, F. Wu, Y. Jiang, D. Chu, *J. Energy Chem.*, **43**(1), 220 (2020).
4. E.V. Makhonina, L.S. Maslennikova, V.V. Volkov, A.E. Medvedeva, A.M. Rummyantsev, Yu.M. Koshtyal, M.Yu. Maximov, V.S. Pervov, I.L. Eremenko, *Appl. Surf. Sci.*, **474**(1), 25 (2019).
5. A.V. Potapenko, S.I. Chernukhin, I.V. Romanova, K.Sh. Rabadanov, M.M. Gafurov, S.A. Kirillov, *Electrochim. Acta.*, **134**(1), 442 (2014).

## Electrolytically synthesized K,Na,V-oxide compounds for Li-batteries

R.D. Apostolova, E.M. Shembel

Scientific Research Laboratory of Chemical Power Sources of Ukrainian State University  
of Chemical Technology, Dnipro, 49005, Ukraine

Crystalline  $V_2O_5$  oxide invariably attracts developers of lithium batteries with high specific energy (higher than  $LiCoO_2$ ,  $LiFePO_4$ ) and capacity (higher than  $LiMn_2O_4$ ); low cost and prevalence in nature. The theoretical capacity of  $V_2O_5$  reaches 442 mAh/g. The actual discharge capacity of  $V_2O_5$  decreases due to its structural rearrangement caused by incorporated lithium ions. Various methods of nano- and micro-structuring of  $V_2O_5$  have been proposed, which make it possible to bring the actual discharge capacity closer to the theoretical one. However, the development of the production of  $V_2O_5/Li$ -accumulators is hampered by the complexity of the proposed nanostructuring techniques, additional financial costs, therefore, an acceptable simple and financially low-cost  $V_2O_5$  production technology is required. We have managed to improve the discharge characteristics of thin-layer  $V_2O_5$  oxide by doping it with sodium electrochemically with the formation of monoclinic bronze  $\beta-Na_{0.33}V_2O_5$  [1–3], as well as synthesizing vanadates [4] improved with potassium [5].

Here we present the results of the double effect (K, Na) on the electrochemical conversion of  $V_2O_5$  in a prototype lithium battery. Vanadium oxide compounds were synthesized by a simple electrolysis method, precipitating them onto the anode from solutions of potassium metavanadate in the presence of sodium ions, as well as from solutions of oxovanadium sulfate in the presence of (K, Na) ions.

The composition of the initial metavanadate solutions for synthesis is following:  $K^+$ –0.5 g-ion/l;  $Na^+$  – 0.05 g-ion/l, pH 2.0. The deposits of K,Na,V-oxides were obtained onto a stainless steel anode at  $i_{anode} = 3.5\text{--}4.0$  mA/cm<sup>2</sup>,  $t = 80\text{--}85^\circ$  C, followed by their heat treatment at  $300^\circ$  C for 2.5 h. It was found that the deposits contain sodium vanadates  $Na_5V_{12}O_{32}$  [PCPDF WIN No. 24–1156] and potassium vanadates  $KV_5O_{13}$  [PCPDF WIN No. 40–45]. Table I shows the results obtained with K,Na,V-oxide electrodes, the active mass of which is 30–40 mg/cm<sup>2</sup>, and a lithium counter electrode in the electrolyte 1 mol/l  $LiClO_4$ , propylene carbonate (PC), dimethoxyethane (DME) at a density current  $i_{discharge} = 0.20$  mA/cm<sup>2</sup>,  $i_{charge} = 0.05$  mA/cm<sup>2</sup>. A common characteristic feature of the investigated electrodes is the high open-circuit voltage (OCV > 3.70 V).

Electrodes with an increased mass of the active component show the possibility of conversion with a return of 130 mAh/g (mass 125 mg/cm<sup>2</sup>) and 150 mAh/g (mass 91 mg/cm<sup>2</sup>) when discharged to a voltage of 2.5 V.

**TABLE I.** Results of the study of composite electrodes based on K,Na,V-oxide material, obtained from a solution of potassium metavanadate in the presence of  $Na^+$

| Loading<br>mg/cm <sup>2</sup> | OCV, V    | № cycles | $Q_{disch}$ , mAh/g            |                               |
|-------------------------------|-----------|----------|--------------------------------|-------------------------------|
|                               |           |          | $E_{disch}=3.8\text{--}2.0$ V, | $E_{disch}=3.8\text{--}2.4$ V |
| 31.0–40.0                     | 3.75–3.80 | 1        | 325–280                        | 218–235                       |
|                               |           | 21       |                                |                               |

The deposits were obtained from solutions of oxovanadium sulfate in the presence of (K, Na) ions in the form of a dispersed powder onto an 18N12Kh9T stainless steel anode and in the form of a dense coverage. Deposition conditions: cathodes – titanium alloy VT – 1, anodic current density 15–20 mA/cm<sup>2</sup>,  $t = 80\text{--}85^\circ\text{C}$ . Electrolyte composition: VOSO<sub>4</sub> – 0.20 mol/l, K<sup>+</sup> – 0.50 g-ion/l, Na<sup>+</sup> – 0.05 g-ion/l. The deposits were heated at 300°C for 2.5 h. According to X-ray phase analysis, the deposits contain sodium vanadates Na<sub>10</sub>V<sub>24</sub>O<sub>64</sub> [PCPDF WIN No. 19–1257] and potassium KV<sub>5</sub>O<sub>13</sub> [PCPDF WIN No 40–45]. Traditional composite electrodes based on the synthesized dispersed powder with acetylene black at a discharge of up to 2.6 V provide a capacity of 130–140 mAh/g. When cycling a thin-layer sample that does not contain an electrically conductive additive and a binder, paired with a lithium counter electrode, the discharge capacity are 250–290 mAh/g within a voltage of 3.8–2.0 V in the first cycle and 234 mAh/g in the 21<sup>st</sup> cycle at a current density of 0.05 mA/cm<sup>2</sup> (Figure 1). It can be increased by co-deposition of vanadium oxide with an electrically conductive polymer (such as polypyrrole or polyacetylene).

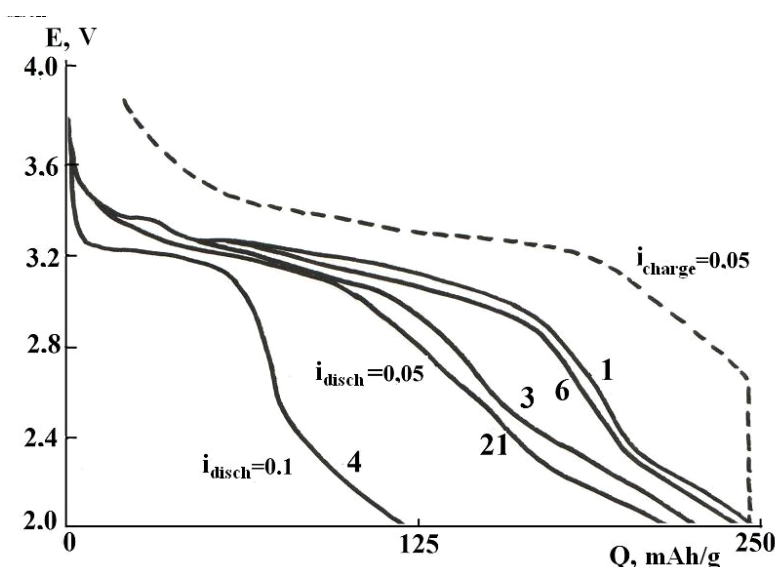


**Figure 1.** Discharge-charge curves of thin-layer ballastless K, Na, V-oxide compounds with a mass of 3 mg/cm<sup>2</sup>, obtained onto the anode from a solution of oxovanadium sulfate in the presence of Na<sup>+</sup> and K<sup>+</sup>.

## Conclusion

Precipitation by electrolysis from metavanadate solutions and solutions of oxovanadium sulfate with the same content of potassium and sodium ions in them leads to a difference in the structure of vanadates. The discharge profile of the synthesized products from a metavanadate solution is characterized by a monotonic decrease in voltage from the OCV passing into an extended horizontal section near 2.60 V. In the high-voltage part of the discharge curves of the synthesized material, obtained from solutions of oxovanadium sulfate, the voltage does not monotonically change from OCV to 2.60 V. There are horizontally inclined voltage sections, which are especially pronounced in thin-layer electrodes (Fig. 1) – near 3.4 V and 3.2 V, as well as near 2.3 V. Such plots are a characteristic feature of the discharge curves of crystalline V<sub>2</sub>O<sub>5</sub> oxide. In these curves of the synthesized material, the length of the sections near 3.4 V and 3.2 V is increased under the influence of K<sup>+</sup>. The horizontal sections near 3.4 and 3.2 V characterize phase transitions in V<sub>2</sub>O<sub>5</sub> oxide ( $\alpha$ - $\epsilon$ ) and ( $\epsilon$ - $\delta$ ), which provide a theoretical capacity for the formation of Li<sub>x</sub>V<sub>2</sub>O<sub>5</sub> ( $x = 1$ ) 147 mAh/g, whereas the actual discharge capacity in micrometer V<sub>2</sub>O<sub>5</sub> is equal 120–110 mAh/g. The synthesized material in these sections reaches the theoretical capacity of

V<sub>2</sub>O<sub>5</sub> oxide or its excess (Figure 1). Along with this, the descending part of the discharge curve of the synthesized material is lengthened under the influence of potassium ions, increasing its discharge capacity. The irreversible capacity of the synthesized material in the 21<sup>st</sup> cycle at a discharge up to 2.0 V does not exceed 10% of the starting capacity, which is much less than in V<sub>2</sub>O<sub>5</sub> oxide.

The double potassium-sodium effect, which promoted the improvement the discharge characteristics of the vanadium-oxide compound obtained from a solutions of Na,K-oxovanadium sulfate, can be useful for the implementation of miniature lithium batteries based on an electrochemically synthesized thin-layer Na,K,V-oxide material.

### References

1. Shembel E., Apostolova R., Markovsky B., Aurbach D. // *Voprosi khimii i khimicheskoy thechnologii* **5**, 203 (2003). (In Russian).
2. Apostolova R., Shembel E., Nagirny V., Aurbach D., Markovsky B., Langzam. Ja. // *Electrochemistry* **37**, 1205 (2000). (In Russian).
3. Markovsky B., Apostolova R., Nagirny V., Aurbach D., Shembel E. // *Voprosi khimii i khimicheskoy thechnologii* **5**, 138 (2003).
4. Apostolova R.D. *Surface Engineering and Applied Electrochemistry* **56**, 216 (2020).
5. Apostolova R.D., Baskevich A.S. *Voprosi khimii i khimicheskoy thechnologii* **5**, 5 (2019). (In Russian).

## **A State of Art Critical Review on Advancement in Mxenes for Lithium and Sodium Ion Batteries in the view of Atomic Layer Spacing**

Amrit Kumar Thakur

Department of Mechanical Engineering, Anna University (CEG Campus), Chennai-600025, India,  
Email: amritt1@gmail.com

### **Abstract**

Recently Mxenes, an emerging family of 2-D metal carbide, nitride and carbo-nitrides have fascinated significant attention in the field of electrochemical energy storage owing to its unique properties such as hydrophilic nature, large surface area to volume ratio and internal surface areas, higher conductivity, larger atomic spacing. MXene can produce remarkably higher volumetric capacitance than the graphene owing of its ultra-high density and pseudo-capacitive charge storage behavior in sulfuric acid and thus, making it most suitable for electrochemical energy storage applications. Even though there have been wide ranging research reported the about MXenes, the most notable characteristics of MXenes are overlooked such as larger and adjustable atomic layer spacing, which makes these novel materials unique from other 2-D materials. By considering the distinguished nature of MXenes, we mainly discuss the role of adjustable interlayer spacing achieved through pillaring technology on performance of anode material for the battery. In addition, future viewpoint and challenges of Mxene composite will be discussed regarding the electrochemical energy storage.

## Electrochemical characterization of gel polymer electrolyte used in lithium-ion batteries

I. Veselkova<sup>a</sup>, M. Sedlaříková<sup>a</sup>

<sup>a</sup> Department of Electrical and Electronic Technology, Brno University of Technology, Technická 10, 616 00 Brno, Czech Republic

The preparation and electrochemical properties of gel polymer electrolytes are briefly reviewed in this paper. Gel polymer electrolytes with LiPF<sub>6</sub> and TEA BF<sub>4</sub> were prepared. Ionic conductivity was calculated from impedance spectroscopy measurement and its dependence on temperature was studied. The electrochemical stability window of the samples was studied by linear sweep voltammetry. The results indicate which gel had higher conductivity and higher electrochemical stability.

### Introduction

Lithium-ion batteries have been paid increasing attention in recent decades due to their high energy density, long cycle lives and high efficiency. Gel polymer electrolytes (GPEs) have been increasingly studied due to several advantages, including no shape restrictions, faster charging and discharging, and higher power density [1], [4].

Gel polymer electrolytes consist of a large quantity of liquid electrolyte and polymer network, which are completely compatible with each other to form a stable gel. Due to the workability of polymers, the gel polymer electrolytes can render the energy storage devices with adjustable shapes and high flexibility, which is promising for burgeoning portable and wearable electronics [4], [5]. Gel polymer electrolytes have become one of the most desirable alternatives among various electrolytes for electrochemical devices, and significant progress has been made in lithium ion batteries and the other kinds of electrochemical energy storage devices. In order to meet the requirements of wearable devices for flexibility and deformability, more special gel polymer electrolytes with tough, stretchable and compressible functionalities have been developed as well [1], [4], [5].

Requirements for gel polymer electrolytes for lithium batteries are high ionic conductivity at ambient and subsurface temperatures, good mechanical strength, significant transference number, thermal and electrochemical stability, and better compatibility with electrodes [6].

### Chemical composition and preparation

Lithium hexafluorophosphate-98% (LiPF<sub>6</sub>), tetraethylammonium tetrafluoroborate-99% (TEA BF<sub>4</sub>), ethylene carbonate (EC), diethyl carbonate (DEC), methyl methacrylate (MMA), ethylene glycol dimethacrylate (EDMA) and benzoin ethyl ether (BEE) were purchased from Sigma Aldrich [2], [3]. Fig. 1 shows chemical formulas of chosen salts.



**Figure 1.** Chemical formulas of chosen salts: (a)  $\text{LiPF}_6$ , (b)  $\text{TEA BF}_4$

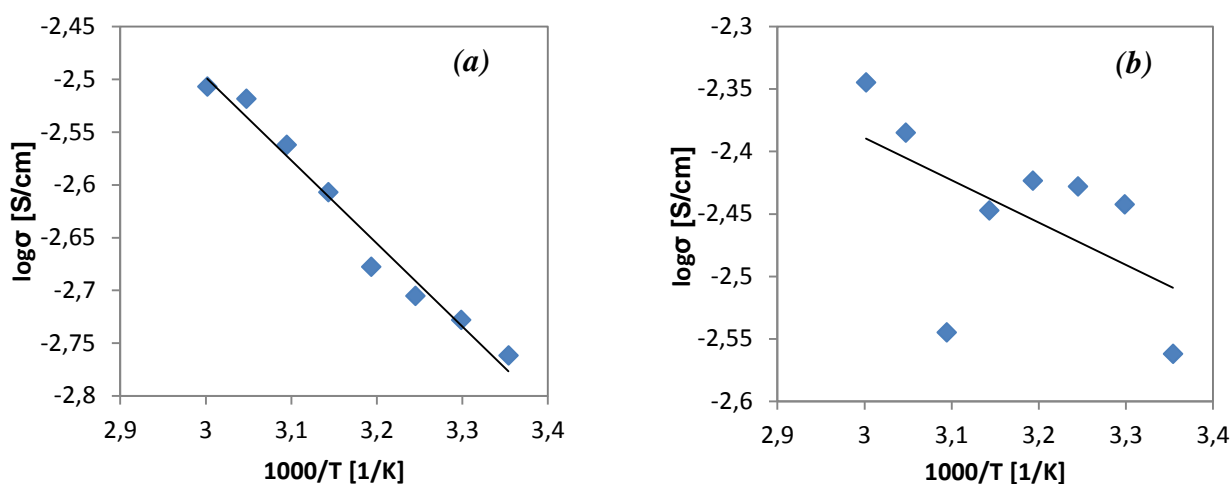
### Preparation of gel polymer electrolyte

Gel precursor solution was prepared by dissolving  $\text{LiPF}_6/\text{TEA BF}_4$  into EC/DEC (in weight 1:1). Monomer MMA, crosslinking agent EDMA and initiator of UV-light polymerization BEE were then added into the solution. Afterward, this solution was stirred 20 min, until all the starting materials had dissolved. Finally, gel electrolyte precursor was exposed to UV irradiation for 60 min to obtain self-standing gel polymer electrolyte [2], [3].

### Experiment

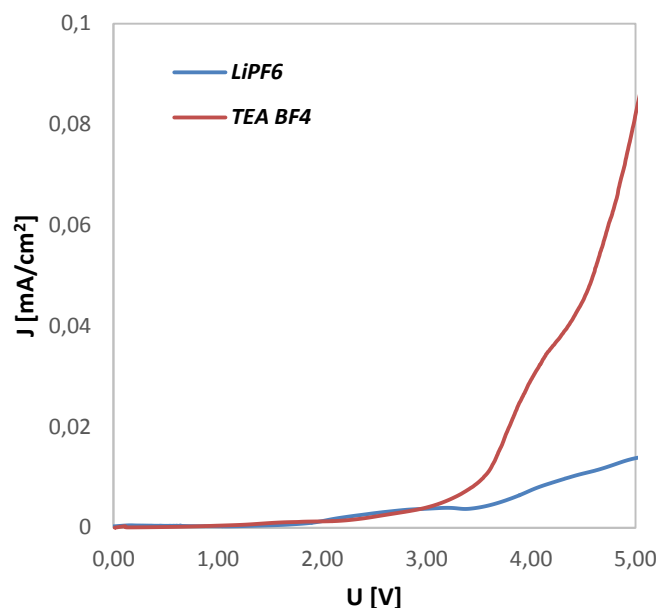
Gel polymer electrolytes with different conductive salts ( $\text{LiPF}_6$ ,  $\text{TEA BF}_4$ ) were prepared during experiment. All manipulation with gel electrolytes was in glove box in argon atmosphere. Electrochemical properties (ionic conductivity, potential window) were measured of prepared gel samples. For measure electrochemical properties gel sample was placed into electrochemical test cell between two steel electrodes.

Figure 2 presents the dependence of ionic conductivity on temperature. The measurements of conductivity were performed from 25°C to 60°C. In this figure we can see that the conductivity of the samples increases with the increase of temperature. The GPE based on  $\text{TEA BF}_4$  had higher conductivity, but conductivity of gel electrolyte with  $\text{LiPF}_6$  increases linearly with increasing temperature.



**Figure 2.** Temperature dependence of ionic conductivity for the gel polymer electrolyte as a function: (a) GPE based on  $\text{LiPF}_6$ , (b) GPE based on  $\text{TEA BF}_4$

Figure 3 illustrates potential windows of prepared gels. The potential window of gel prepared with  $\text{LiPF}_6$  varies from 4.04 V to over then 5.1 V, whereas the potential window of gel electrolyte prepared with  $\text{TEA BF}_4$  varies from 3.42 V to 3.71 V at room temperature (25 °C).



**Figure 3.** Potential windows of prepared gel polymer electrolytes

### Conclusion

Gel polymer electrolytes with the same concentration of conductive salts (such as  $\text{LiPF}_6$  and  $\text{TEA BF}_4$ ) were prepared. The electrochemical properties of these GPEs were measured. The ionic conductivity of these samples increases with increasing temperature and increase have a linear dependence. The gel based on  $\text{TEA BF}_4$  has higher conductivity, but electrochemical stability is low. Conversely, gel based on  $\text{LiPF}_6$  is more stable, but ionic conductivity is low. From the electrochemical analyses, it can be stated that the gel polymer electrolyte system is an effective tool for improving the properties of lithium batteries.

### Acknowledgments

This work was supported by the specific graduate research of the Brno University of Technology No. FEKT-S-20-6206.

### References

1. A. J. Nagajothi, R. Kannan, S. Rajashabala, *Materials Science-Poland*, **36**(2), 2018.
2. I. Veselkova, M. Sedlaříková, G. Fafílek, C. Gierl-Mayer, *ECS Trans.*, (2019).
3. I. Veselkova, S. Peterová, M. Sedlaříková, *ECS Trans.*, (2019).
4. L. Guangchao, L. Zhaohui, Zh. Peng, *Pure Appl. Chem.*, 11 (2008).
5. L. Wangyu, P. Ying, L. Jingyuan, *RSC Advances*, 38 (2017).
6. P. Dvořák, M. Musil, D. Pléha, *Elektrorevue*, **15**, 6 (2013).

## Active masses for supercapacitor electrodes based on copolymers and composites of redox-active comonomers and intrinsically conducting polymers

Rudolf Holze<sup>I,II,III</sup>

<sup>I</sup>Chemnitz University of Technology, Institut für Chemie, AG Elektrochemie, D-09107 Chemnitz, Germany

<sup>II</sup>Saint Petersburg State University, Institute of Chemistry, St. Petersburg, 199034, Russia

<sup>III</sup>State Key Laboratory of Materials-oriented Chemical Engineering, School of Energy Science and Engineering, Nanjing Tech University, Nanjing, 211816, Jiangsu Province, China

Supercapacitors SCs employing charge storage in the electrochemical double layer have established themselves as powerful options to store and release electric energy at high power showing a remarkably high stability (for an introduction see[1-3], for monographs on most relevant aspects see[4-9]). Despite remarkable progress in material and design development the energy density of available devices is considered to be still disappointingly low. In particular for applications where slightly less power at much higher energy storage capability combined with the remarkable stability of SCs is desired approaches to enhanced charge storage in the electrode material finally resulting in higher energy density would be highly welcome.

The utilization of surface-confined redox reactions of metal oxides (later: chalcogenides) has been suggested years ago[10, 11], intrinsically conducting polymers ICPs have been proposed as another option [12]. Redox-active organic materials have been proposed for charge storage, too, driven by environmental and recycling concerns as well as by the limited resources of at least some metals in said chalcogenides (e.g. cobalt). Various conditions should be met by candidate materials:

- Insoluble in the electrolyte solution in order to avoid self-discharge and loss of electrode capacitance
- Fast and reversible electrode reactions to ensure high rate capability of the electrode and high overall energy efficiency
- Cheap and easily available
- Causing no unacceptable environmental concerns

Among candidate materials members of the quinone and the ferrocene families (see Fig. 1) of compounds have attracted particular attention.

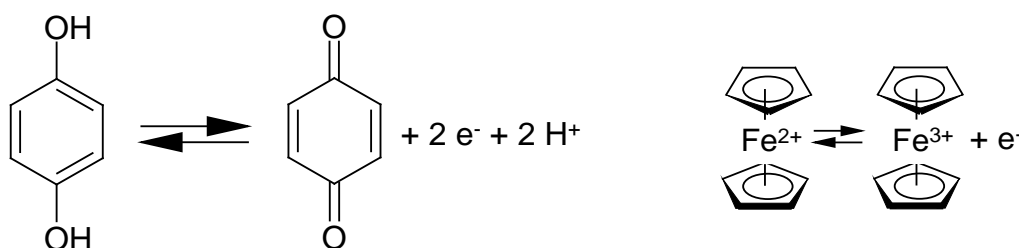


**Figure 1.** Schematic redox reactions of quinone and of ferrocene.

There are various methods of integrating these materials into an actual electrode. The most simple approach would be to deposit the molecules of interest on the carbon material used as the

starting bulk material of the electrode. Given the poor solubility of anthraquinone AQ and aminoanthraquinone AAQ in neutral and acidic aqueous electrolyte solutions soaking the carbon (e.g. powder) in a nonaqueous solution of the AAQ in e.g. acetonitrile appears to be a simple and sufficient option. Depending on the available surface area of the carbon material in a given sample and the amount of dissolved AQ or AAQ the actually introduced amount may be enough to enable a monolayer coverage or more. In any case it remains open whether adsorption (as claimed e.g. in [13]) or simply deposition took place. Determination of adsorption isotherms might help to find out more. Using an ICP instead of the carbon might provide a support which is redox-active for storage itself beyond the double layer storage of carbon materials. This option has apparently not been verified so far, it is part of our ongoing research.

Covalent linking of the molecules to a carbon surface is a further option promising at first glance higher stability against loss of active material into the electrolyte solution and protection against possible failure to exchange electrons with the conducting carbon support. Examples involving chemical synthesis procedures of variable complexity are shown in Fig. 2.

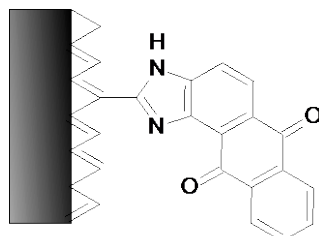


**Figure 2.** Proposed structure of 1,2-diaminoanthraquinone attached to a carbon surface [14].

An option somehow combining aspects of the preceding examples is incorporation of the redox-active material with the ICP to form a copolymer. The molecule may be part of the polymer chain or it might be attached to the chain as a pendant group, examples are shown in Figs. 3 and 4.

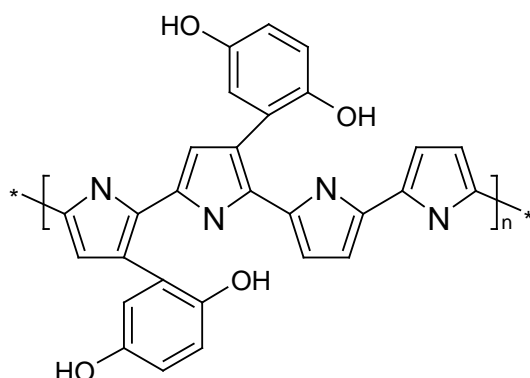


**Figure 3.** ICP chain with pendant quinone redox moieties (simplified scheme).

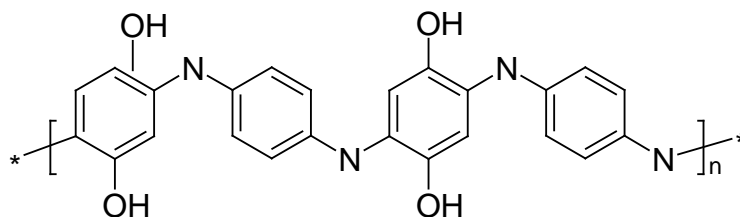


**Figure 4.** ICP with redox moieties incorporated in the molecular chain (simplified scheme).

Both products are true copolymers; on nomenclature and experimental ways for verification see [15]. Although in most concepts the experimental realization will be the crucial test the question

for advantages and disadvantages of both options may be asked. Pendant groups as in Fig. 3 may be preferable because they most likely will interfere less with charge transport along the chain and thus electronic conductance of the ICP. For reported examples no conductance data have been reported, accordingly the question is currently an academic one.

A final possibility somehow resembling the arrangement of Fig. 3 is the use of functionalized redox-active molecules (e.g. anthraquinone-2-sulfonate [16]) as counter-anions for the ICP. Upon oxidation of the ICP the counter-anion moves into the ICP and may participate in charge storage. Upon reduction it will be reduced itself provided the electronic charge transfer proceeds effectively, and the ICP will be reduced itself. Because the counter-anion must be sufficiently soluble in the electrolyte solution self-discharge by movement of this anion between the electrodes is likely. If no suitable means to prevent this movement are installed the positive effect of enhanced charge storage <sup>Chyba! Záložka není definována.</sup> may turn out to be rather limited. Adding a membrane may increase the internal resistance of the cell, but gelling of the electrolyte solution may provide an option waiting for verification.

Examples of all presented options will be shown, results as far as available will help to assess the practical achievements.

### Acknowledgments

Preparation of this report has been supported within a research project grant № 26455158 at St. Petersburg State University.

### References

1. D.P. Dubal, Y. Wu, R. Holze, Supercapacitors as fast storage systems for electric energy, *Bunsen-Magazin* 17 (2015) 216-227.
2. A.K. Shukla, S. Sampath, K. Vijayamohan, Electrochemical supercapacitors: Energy storage beyond batteries, *Curr. Sci.* 79 (2000) 1656-1661.
3. D.P. Dubal, Y. Wu, R. Holze, Supercapacitors: from the Leyden jar to electric busses, *Chemtexts* 2 (2016) 13.
4. B.E. Conway: *Electrochemical Supercapacitors: Scientific Fundamentals and Technological Applications*, Springer, New York 1999.
5. *Electrochemical Supercapacitors for Energy Storage and Delivery - Fundamentals and Applications* (A. Yu, V. Chabot, J. Zhang Ed.) CRC Press, Boca Raton 2013.
6. *Electrochemical Capacitors in: Materials Research Foundations Vol. 26* (Inamuddin, M.F. Ahmer, A.M. Asiri, S. Zaidi Eds.) Materials Research Forum LLC, Millersville 2018.
7. *Supercapacitor Design and Applications* (Z. Stevic Ed.) ExLi4EvA2016 2016.
8. *Supercapacitors* (F. Beguin, E. Frackowiak Eds.) Wiley-VCH, Weinheim 2013.
9. J.M. Miller: *Ultracapacitor Applications*, The Institution of Engineering and Technology, London 2011.
10. B.E. Conway: *Electrochemical Capacitors Vol. Proceedings Volume 95-29* (F.M. Delnick, M. Tomkiewicz Eds.) The Electrochemical Society Inc., Pennington, NJ, USA 1996, p. 15
11. B.E. Conway, V. Birss, J. Wojtowicz, The role and utilization of pseudocapacitance for energy storage by supercapacitors, *J. Power Sources* 66 (1997) 1-14.
12. R. Holze, Y.P. Wu, *Intrinsically Conducting Polymers in Electrochemical Energy Technology: Trends and Progress*, *Electrochim. Acta* 122( 2014) 93-107.

13. A.S. Kumar, P. Swetha, Simple adsorption of anthraquinone on carbon nanotube modified electrode and its efficient electrochemical behaviors, *Colloids Surf., A* 384 (2011) 597-604.
14. R.D.L. Smith, P.G. Pickup, Novel electroactive surface functionality from the coupling of an aryl diamine to carbon black, *Electrochem. Commun.* 2009, 11, 10-13.
15. R. Holze, Copolymers - A refined way to tailor intrinsically conducting polymers, *Electrochim. Acta* 56 (2011) 10479-10492.
16. K. Yamamoto, M. Yamada, T. Nishiumi, Doping reaction of redox-active dopants into polyaniline, *Polym. Adv. Technol.* 11 (2000) 710-715.

## **Reduced Graphene Oxide Composited with amorphous Ni-MOF and PANI applied as electrodes for Supercapacitor**

Le Quoc Bao<sup>a, b</sup>, Haojie Fei<sup>a</sup>, Constantin Bubulinca<sup>a</sup>, Fahanwi Asabuwa Ngwabebhoh<sup>c</sup>,  
Natalia E. Kazantseva<sup>a</sup>, Petr Saha<sup>a</sup>

<sup>a</sup> Sino-EU Joint Laboratory of New Energy Materials and Devices, Centre of Polymer Systems, Tomas Bata University in Zlin, Tř. T. Bati 5678, 76001 Zlin, Czech Republic

<sup>b</sup> Conducting polymers in composites and applications Research Group, Faculty of Applied Sciences, Ton Duc Thang University, Ho Chi Minh City, Vietnam

<sup>c</sup> Biocomposite systems Laboratory, Centre of Polymer Systems, Tomas Bata University in Zlin, Tř. T. Bati 5678, 76001 Zlin, Czech Republic

The different composites made from rGO, Ni-MOF and PANI were synthesized via hydrothermal method and tested as electrodes of the supercapacitors. The structure and morphology of the composites were characterized via SEM, XRD and FTIR. The electrochemical properties of electrode materials were studied using CV, galvanostatic charge/discharge and EIS. The results obtained have shown that the incorporation of rGO, Ni-MOF and PANI into the composites leads to increased specific capacitance. It can be explained by formation of thridimensional porous structure, which enhances the contact between electrolyte ions with the composite electrodes. The specific capacitance of rGO/Ni-MOF/PANI in

1 M H<sub>2</sub>SO<sub>4</sub> is about 200 F/g at 0.2 A/g charge/discharge, and the average capacitance retention remained 80% after 5000 cycles at current density 1 A/g.

## New Hybrid Phospho-Siloxane Membranes for H<sub>2</sub>/O<sub>2</sub> Fuel Cells

M. Mika<sup>a</sup>, D. I. Oren, and J. Michal

<sup>a</sup> Department of Glass and Ceramics, University of Chemistry and Technology, Prague, 16628, Czech Republic

Currently, the low operating temperatures of commercial proton conducting polymer membranes and their humidity requirements for achieving sufficiently high proton conductivity add high complexity to fuel cell systems, which impacts their cost and durability. In our research, we focused on the development of new cost-effective polymer nanocomposite membranes with better medium-temperature performance.

### Introduction

To produce cost-effective medium-temperature fuel cells, it is necessary to develop a new type of membrane able to achieve sufficiently high proton conductivity in a dry atmosphere. To meet these criteria, a high concentration of relatively stable hydroxyl groups is required in the structure of the membrane. When such groups are close to each other, they form diffusion pathways suitable for fast proton migration even in a dry atmosphere above 100 °C. Therefore, we developed a nanocomposite membrane based on a hybrid inorganic-organic polymer with a polydimethylsiloxane backbone containing phosphorous heteroatoms with SiO<sub>2</sub> nanoparticles and micro/nanowires.

### Experimental

Our first-generation hybrid inorganic-organic phosphor-siloxane polymer membranes was based on a polydimethylsiloxane backbone containing phosphorous heteroatoms (1). The desired structure of the membrane was formed by the reaction of dimethyldichlorosilane and tetraethoxysilane in molten orthophosphoric acid (Fig.1). For the improved second-generation of our membranes (Fig.2), the first-generation polymers were filled with spherical SiO<sub>2</sub> nanoparticles (5 to 20 nm, specific surface of 200 m<sup>2</sup>·g<sup>-1</sup>) covered with -OH functional groups (2). Moreover, the structure of the membranes was reinforced with microwires and nanowires based on SiO<sub>2</sub>. The membrane proton conductivity (Figs.3 and 4) was precisely measured using electrochemical impedance spectroscopy in a temperature range of 25—200 °C. The impedance data were recorded with an Autolab PGSTAT30 potentiostat in a frequency range of 10 mHz—1 MHz. The resulting impedance spectra were analyzed in Bode and complex Nyquist plane diagrams (Fig.5) using the equivalent circuit approach.

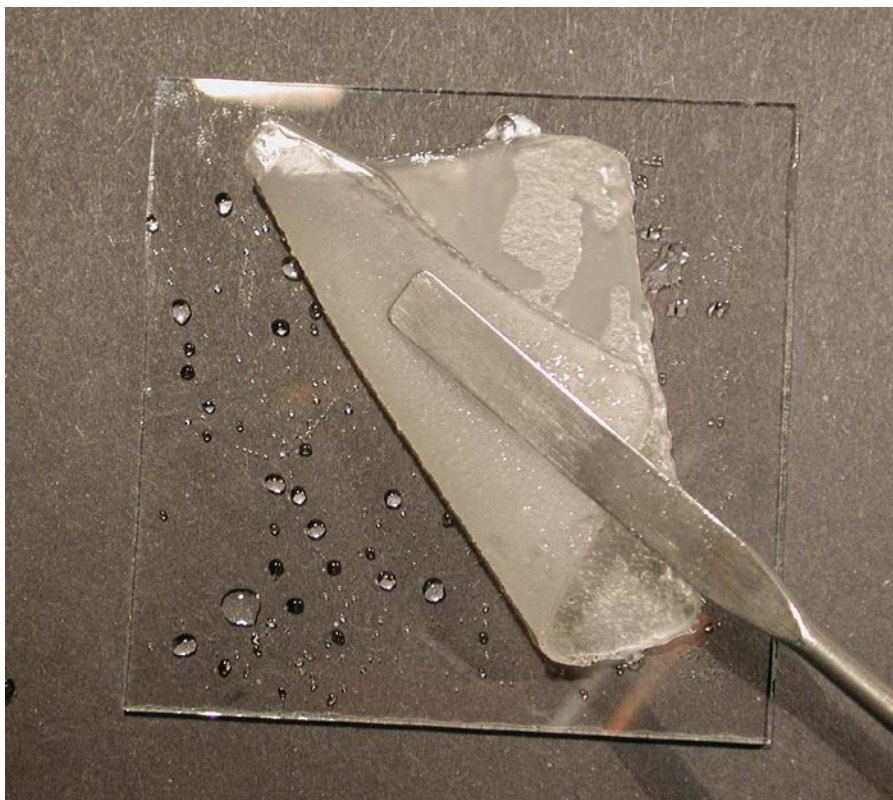


*Figure 1. Flexible membrane 50x50 mm.*

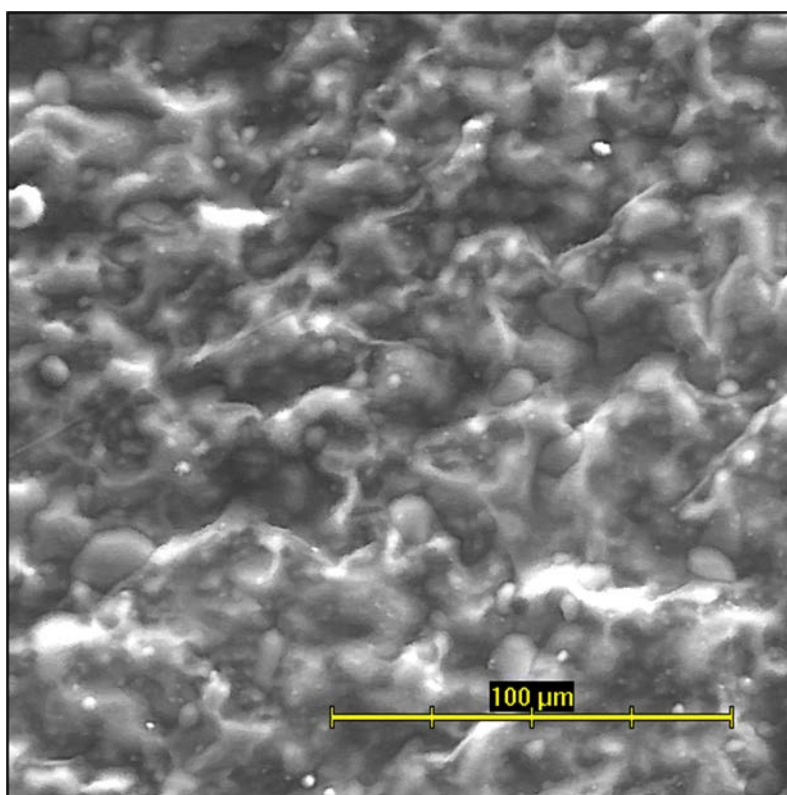


*Figure 2. SEM picture of membrane's surface.*

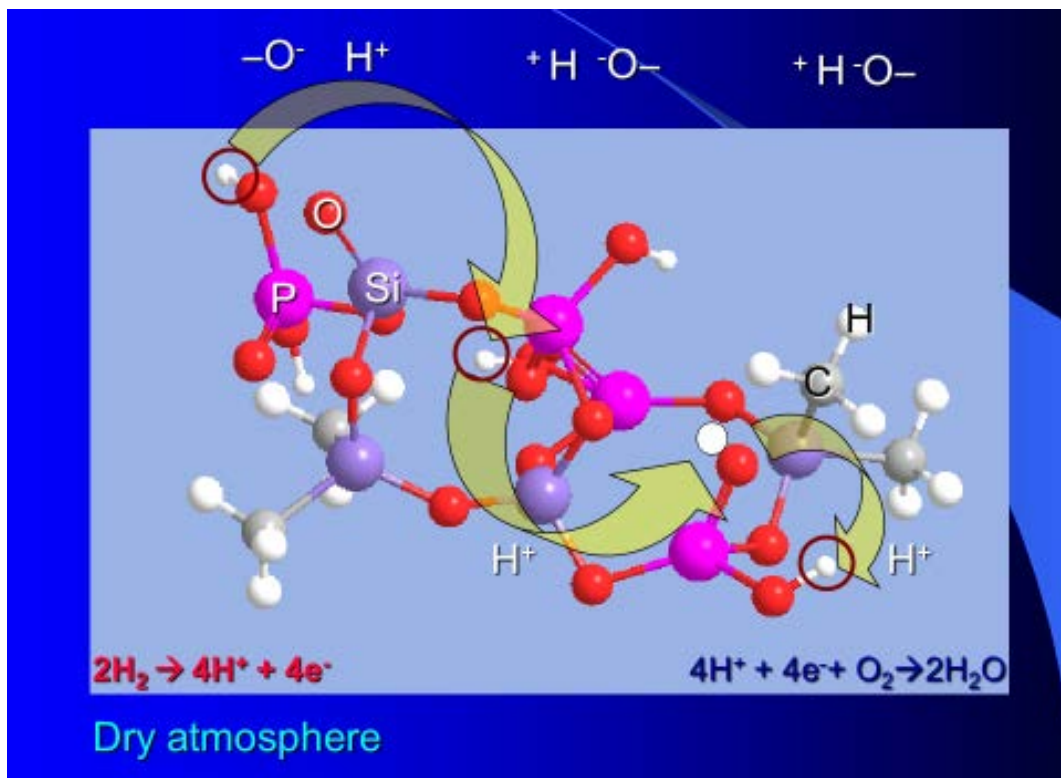


Figure 3. Hopping mechanism of proton conductivity in a membrane.

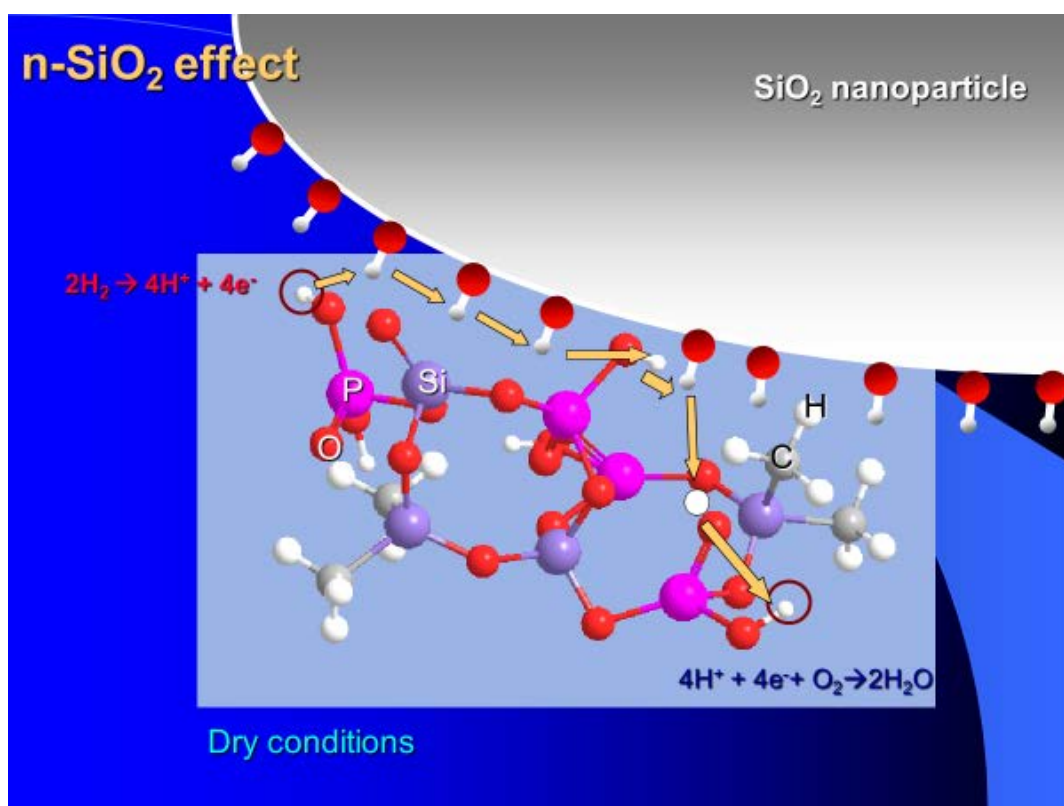


Figure 4. Hopping of protons in the presence of SiO<sub>2</sub> nanoparticles.

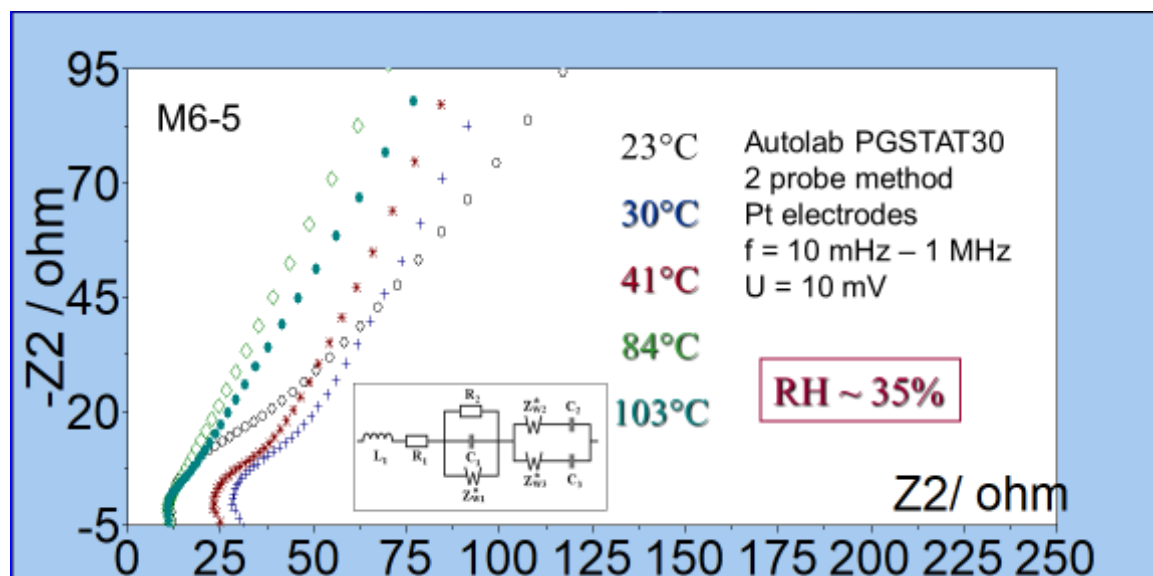


Figure 5. Impedance of a membrane at increased temperature.

## Results and Discussion

The proton conductivity of the first-generation membranes calculated from the circuit parameters was promising. Therefore, using based on them simulations, we optimize the composition and structure of the second-generation membranes. Their proton conductivity was further enhanced when the polymers were filled with spherical  $\text{SiO}_2$  nanoparticles covered with -OH functional groups and their structure was more reinforced by incorporating microwires and nanowires based on  $\text{SiO}_2$ . This resulted in membranes with an improved mechanical strength, elasticity and higher conductivity of about  $9 \text{ S} \cdot \text{m}^{-1}$  at  $150 \text{ }^\circ\text{C}$  in a dry atmosphere. Next, we tested the performance of the membranes in a laboratory  $\text{H}_2/\text{O}_2$  fuel cell in the range from  $20$  to  $180 \text{ }^\circ\text{C}$  using dry  $\text{H}_2$  and  $\text{O}_2$  input gases. The fuel cell was equipped with standard electrodes made of carbon paper with a Pt/C catalyst; the surface area of the electrodes was  $5 \text{ cm}^2$ . The performance of the fuel cell significantly improved as the temperature increased. Power density maxima increased and moved to higher current densities and current/voltage characteristics became less steep. Following these tests, the membranes were characterized using other analytical tools, including optical and electron microscopy, differential thermal analysis, thermal gravimetric analysis, infrared and Raman spectroscopy, and nuclear magnetic resonance. The collected data were used for the simulations to optimize our furthermore advanced phospho-siloxane membranes.

## Conclusion

By introducing the functionalized  $\text{SiO}_2$  nanoparticles and micro/nano wires into the structure of our phospho-siloxane membranes, their proton conductivity, mechanical strength, and electrochemical performance significantly improved. Collectively, our results indicate that the developed hybrid polymer membranes containing nanoparticles, microwires and/or nanowires are promising for the construction of  $\text{H}_2/\text{O}_2$  fuel cells operating at elevated temperatures in a dry atmosphere.

### Acknowledgments

We acknowledge our colleagues M. Paidar, B. Klapste, P. Hron, M. Masinova for their help in the development of our hybrid phospho-siloxane membranes.

### References

1. M. Mika, J. Michal, B. Klapste, P. Hron, *Patent*, **303939** (July 3, 2013).
2. M. Mika, J. Michal, B. Klapste, P. Hron, *Patent*, **304129** (September 25, 2013).

## Photoelectrochemical Systems for Hydrogen Evolution Using Ion-Conducting Membranes

I. A. Rusetskiy, L. L. Kovalenko, I. A. Slobodyanyuk, M. O. Danilov\*,  
S. S. Fomanyuk, V. O. Smilyk, A. G. Belous, G.Ya. Kolbasov

Institute of General and Inorganic Chemistry of the NAS of Ukraine,  
32/34 Academic Palladin Avenue, Kyiv, 03142, Ukraine.

\*Corresponding Author E-mail Address: danilovmickle@rambler.ru

### Introduction

When narrow-gap semiconductors were used in photoelectrochemical cells (PEC), the magnitude of the photo potential is insufficient to decompose water. To solve this problem, you can replace the anodic oxygen evolution reaction with another, for example, by the reaction of oxidation  $xS^{2-} \rightleftharpoons S_x^{2-} + 2(x-1)e^-$  [1, 2]. This process takes place with less overvoltage in the electrochemical system, which allows more efficiently converse a solar energy. In addition, for more efficient production of hydrogen, it is necessary that the cathode chamber is filled with electrolyte with pH = 1 – 2, and the anode chamber with electrolyte with pH = 13 – 14. The high pH difference in the anolyte and catholyte chambers causes the appearance of a chemical potential that promotes the processes of water decomposition in the photoelectrochemical cell. For long-term operation time of such systems, it is necessary to stabilize the electrolyte composition of the anolyte and catholyte chambers (as well as pH), which can be done using a membrane that excludes changes in pH, and the concentrations involved in an electrochemically reactions. We proposed to replace the traditionally used ion-conducting membrane MF4-SK (Nafion type) in such system with a ceramic membrane of the composition  $La_{0.56}Li_{0.33}TiO_3$  ( $LaLiTiO_3$ ) which has high conductivity for lithium ions and additionally introduce into consist of electrolyte lithium compounds. Therefore, the purpose of this work was to determine the fundamental possibility of using a ceramic membrane based on  $LaLiTiO_3$  in a photoelectrochemical cell and to study the characteristics of this system.

### Experimental part

Lanthanum-lithium titanate  $LaLiTiO_3$  was obtained by solid-phase reactions. The initial reagents were:  $La_2O_3$ ,  $Li_2CO_3$ ,  $TiO_2$  rutile. Homogenizing grinding of stoichiometric amounts of the initial reagents, as well as the synthesized mixture, was carried out in a planetary centrifugal mill Retsch PM-100. The fusion of mixture was carried out at a temperature of 1050 °C for 2 hours. The resulting blanks were pressed and sintered in an air atmosphere at a temperature of 1300 °C for 2 hours. From the obtained blanks were cutted discs with thickness 0.7 mm and a 20.5 mm in diameter. This thickness is due to the design of the PEC cell, which allows the membrane to be tightly fixed and prevent mixing of electrolytes. The density of ceramic samples  $LaLiTiO_3$  was measured by pycnometric and geometric methods. The microstructure of the ceramics was examined using a SEM microscope JEOL JSM-6510. To study the conductivity of the  $LaLiTiO_3$  ceramics, contacts were prepared by firing a silver-containing paste. For impedance studies in the 32 MHz – 0.1 Hz range were used impedance analyzer 1260A Impedance / Gain-Phase Analyzer (Solartron Analytical). The electrical equivalent circuit and the values of its components were determined using the ZView computer program. X-ray diffraction (XRD) was performed on a

DRON-4-07 X-ray diffractometer. The current-voltage characteristics were measured in a model of photoelectrochemical cell with two different electrodes with an area of 2 cm<sup>2</sup> (CdSe electrode) and 1 cm<sup>2</sup> (Pt electrode) using a P-8S potentiostat (Elins, Russia). To compare the current-voltage characteristics were used the ceramic membrane from Li<sub>0.56</sub>La<sub>0.33</sub>TiO<sub>3</sub> and MF4-SK membrane (Nafion type) with the same diameter. Electrolytes were: 1M NaOH + 1M Na<sub>2</sub>S + 10% LiOH (anolyte) / 30% H<sub>2</sub>SO<sub>4</sub> + 1M Li<sub>2</sub>SO<sub>4</sub> (catholyte) and 1M NaOH + 1M Na<sub>2</sub>S + 10% LiOH (anolyte) / 30% KOH + 2M LiOH (catholyte). The temperature during measurement was 22 – 24 °C. The photosensitive CdSe semiconductor film was formed by an electrochemical method on substrate from 0.4 mm thick titanium (VT1-0 grade). The substrate was preliminarily degreased in acetone, followed by etching for 1 – 2 min in a mixture of acids: HF - 15 g / l; HNO<sub>3</sub> - 200 g / l. Then, electrochemical treatment was carried out in a solution of 0.7 M H<sub>2</sub>SO<sub>4</sub> (mode: E = 0.2 – 0.65 V; sweep - 10 mV / s; 5 cycles). Electrochemical deposition of a semiconductor CdSe film was carried out at in a potentiostatic mode on a titanium substrate with the potential E = -0.6 V (±0.03 V) relative to a silver-chloride reference electrode. The current density was j = 0.7 – 2 mA / cm<sup>2</sup> and the time was 30 minutes. For electrolysis, a sulfuric acid electrolyte was used with the following components: H<sub>2</sub>SO<sub>4</sub> - 0.7 – 2 mol / l; H<sub>2</sub>SeO<sub>3</sub> - 0.003 – 0.005 mol / l; CdSO<sub>4</sub> - 0.02 – 0.03 mol / l. Annealing of the CdSe electrode was carried out in an air atmosphere at 470 °C for 3 h. Then, the surface was activated in an aqueous solution: HCl - 180 g / l, HNO<sub>3</sub> - 17 g / l for 4 – 5 sec at room temperature. The surface of the CdSe semiconductor film was studied using a SEM electron microscope JSM 6700F.

The results of XRD analysis of the sintered ceramic sample of the LaLiTiO<sub>3</sub> composition show that the main phase is solid solutions with a perovskite structure of the rhombohedral system (space group R $\bar{3}c$ ) with unit cell parameters about a = 5.48 Å and c = 13.42 Å. In addition, the presence of low-intensity peaks of the P4 / mmm tetragonal phase is observed, corresponding to the same chemical composition of LaLiTiO<sub>3</sub> as the rhombohedral phase. It was found from SEM microscopic studies that the grain size of the ceramics were 2 – 10 microns.

XRD analysis of the surface of a CdSe electrode obtained by electrochemical deposition on a titanium substrate and subsequent annealing showed the formation of a hexagonal CdSe phase. It was found from SEM microscopic studies that the particle size of electrochemically deposited CdSe were ≥ 2 μm. In the study of the parameters of the photoelectrochemical cell, it was found that the ion-conducting membranes MF4-SK and the ceramic membranes Li<sub>0.56</sub>La<sub>0.33</sub>TiO<sub>3</sub> effectively operate in the PEC system for the hydrogen evolution. A CdSe photoanode and a Pt cathode were used for measurements. Light power was 10 mW / cm<sup>2</sup>. When the CdSe photoanode was illuminated, the open-circuit voltage ranged from -0.5 V to -1.1 V, depending on the type of used membrane and electrolyte.

In Figure 1 shows the dependences of the photocurrent on time for the PEC cell when the photoanode is illuminated with various electrolytes and membranes. In practical application, in a PEC cell, are realized lower magnitude values of the hydrogen evolution current when using the Li<sub>0.56</sub>La<sub>0.33</sub>TiO<sub>3</sub> membrane (Figure 1 a) due to it higher resistivity in comparison with the MF4-SK membrane (Figure 1 c). Membrane MF4-SK has low polarization losses due to low resistance, but when it is applied, the pH of solutions is equalized during several months (2 ÷ 3 months).

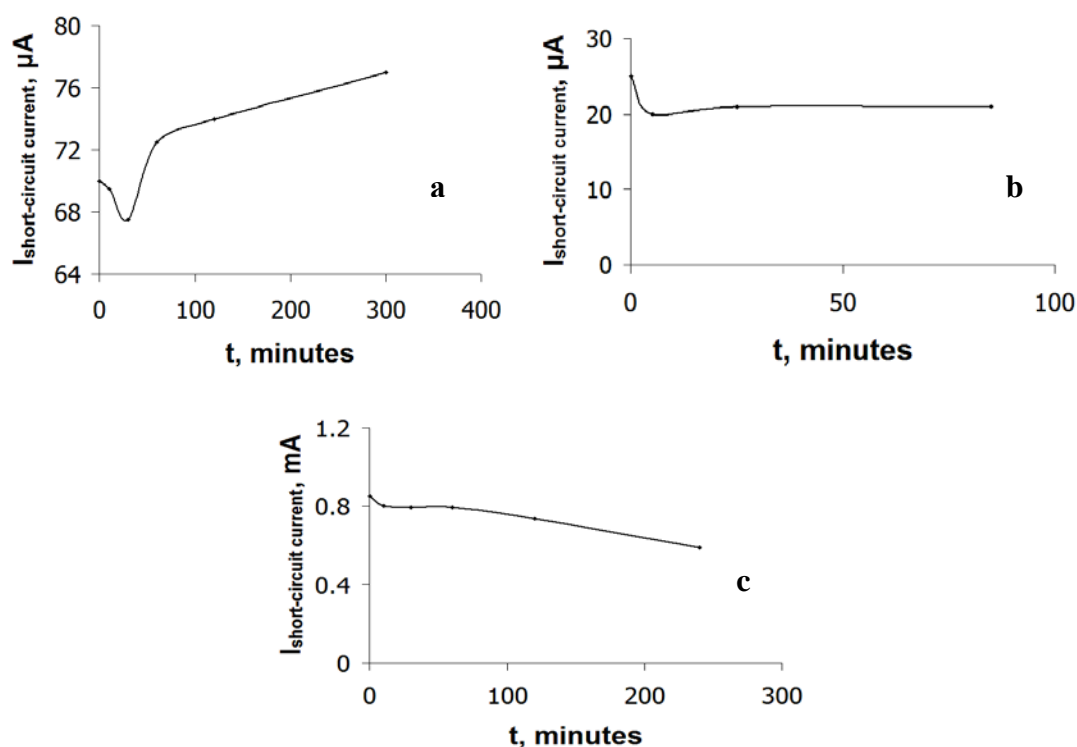


**Figure 1.** Dependence of the photocurrent on time for PFC cell with the membrane:  $\text{Li}_{0.56}\text{La}_{0.33}\text{TiO}_3$  (a, b) and MF4-SK (c) Electrolyte were anolyte / catholyte, respectively:  $1\text{M NaOH} + 1\text{M Na}_2\text{S} + 10\% \text{LiOH} / 30\% \text{H}_2\text{SO}_4 + 1\text{M Li}_2\text{SO}_4$  (a, c);  $1\text{M NaOH} + 1\text{M Na}_2\text{S} + 10\% \text{LiOH} / 30\% \text{KOH} + 2\text{M LiOH}$  (b).

Ceramic membrane  $\text{LaLiTiO}_3$  showed the absolute separation capacity.

## Conclusions

A ceramic membrane for a photoelectrochemical cell was created on the basis of the  $\text{LaLiTiO}_3$  compound. The parameters of a photoelectrochemical cell were investigated using different types of membranes ( $\text{LaLiTiO}_3$  and MF4-SK). It was found that membranes MF4-SK and  $\text{LaLiTiO}_3$  effectively work in the photoelectrochemical systems for hydrogen evolution. In contrast to MF4-SK, the  $\text{LaLiTiO}_3$  ceramic membrane in the electrochemical cell showed an absolute separating ability, but due to its high resistance it has large polarization losses. It is shown the fundamental possibility of creating an electrochemical cell with ceramic membrane based on lanthanum-lithium titanates ( $\text{La,LiTiO}_3$ ). The ceramic membrane has an advantage over MF4-SK at a low current density. For increase the current it's necessary to decrease the resistivity (an increase in its area and a decrease in its thickness).

## References

1. I. A. Rusetskiy, M. O. Danilov, S. S. Fomanyuk, I. A. Slobodyanyuk, V. S. Vorobets, G. Ya. Kolbasov, *Research on Chemical Intermediates*, **45**(8), 4121 (2019).
2. I. A. Rusetskii, L. G. Shcherbakova, M. O. Danilov, I. A. Slobodyanyuk, G. Ya. Kolbasov, S. S. Fomanyuk, Yu. M. Solonin, *ECS Trans.*, **87**(1), 335 (2018).

## Quinone and viologen derivatives for aqueous redox flow battery electrolytes

P. Mazúr<sup>a</sup>, D. Muller<sup>a</sup>, J. Kvíčala<sup>b</sup>, J. Vrána<sup>b</sup>, Z. Burešová<sup>c</sup>, M. Klikar<sup>c</sup>, F. Bureš<sup>c</sup>

<sup>a</sup>University of Chemistry and Technology Prague, Dept. of Chemical Engineering,  
Technická 5, 166 28 Prague, Czech Republic, [mazurp@vscht.cz](mailto:mazurp@vscht.cz);

<sup>b</sup>University of Chemistry and Technology Prague, Dept. of Organic Chemistry,  
Technická 5, 166 28 Prague, Czech Republic

<sup>c</sup>University of Pardubice, Faculty of Chemical technology, Institute of Organic Chemistry and  
Technology, Studentská 573, 532 10 Pardubice

Vanadium redox flow batteries, with several MWh-scale installations worldwide[1], proved to be a safe, reliable and long-lasting energy storage technology. However, high and fluctuating price of vanadium stimulate the seek for alternative active compounds. Organic redox couples are particularly attractive[2, 3] as their relevant properties can be tailored by modification of their chemical structure. Moreover, they can be produced at high volumes and low costs e.g., from oil residues.

In our study a series of organic redox active compounds based on bipyridine or anthraquinone was synthesized and characterized with respect to their application in redox flow battery as active compound of negative electrolyte. General electrochemical characterization was assessed from voltammetric experiments using glassy carbon rotating disc electrode at different pH of electrolyte. Selected molecules were tested in a flow electrolysis cell using carbon felt electrodes to evaluate their electrochemical stability under conditions of application. The change in chemical structure of the redox molecules due to cycling was evaluated by NMR analysis of the electrolytes.

### Acknowledgments

The work was supported from European Regional development Fund-Project "Organic redox couple based batteries for energetics of traditional and renewable resources (ORGBAT)" No.CZ.02.1.01/0.0/0.0/16\_025/0007445.



EVROPSKÁ UNIE  
Evropské strukturální a investiční fondy  
Operační program Výzkum, vývoj a vzdělávání



MINISTERSTVO ŠKOLSTVÍ,  
MLÁDEŽE A TĚLOVÝCHOVY

### References

1. USA, D.o.E.o., [www.energystorageexchange.org/projects](http://www.energystorageexchange.org/projects). 2015, Sandia Corporation.
2. Leung, P., et al., Recent developments in organic redox flow batteries: A critical review. *Journal of Power Sources*, 2017. **360**: p. 243-283.
3. Winsberg, J., et al., Redox-Flow Batteries: From Metals to Organic Redox-Active Materials. *Angewandte Chemie International Edition*, 2017. **56**(3): p. 686-711.

## Deactivation of negative felt electrode of vanadium redox flow battery: Double half-cell set-up experiments

J. Mrlík<sup>a</sup>, P. Mazúr<sup>a</sup>, J. Pociďič, J. Vrána, J. Dundálek<sup>a</sup>, J. Charvát<sup>a</sup>, J. Kosek<sup>a</sup>

<sup>a</sup>University of Chemistry and Technology Prague, Dept. of Chemical Engineering,  
Technická 5, 166 28 Prague, Czech Republic, [mazurp@vscht.cz](mailto:mazurp@vscht.cz);

<sup>b</sup>Pinflow energy storage, s.r.o., Křižovnická 86/6, 110 00 Prague, Czech Republic

The vanadium redox flow battery is one of the most promising technologies for storing of electric energy from renewables. Its advantages are power and capacity independency, high efficiency and outstanding lifetime.

In previous work, we observed energy efficiency decay by 15% during 2000 charge-discharge cycles when using as received carbon felt negative electrode, whereas it decreased only by 1% with thermally treated felt.<sup>1</sup> Nonetheless, even the slow decrease could be a problem on ten years scope.

Thus, here we study influence of operating conditions such as current load (0 and 150 mA cm<sup>-2</sup>), and SoC of negative electrolyte (+25 to +95%) on deactivation rate of as received felt using modified double half-cell setup<sup>2</sup> with single negative electrolyte to evaluate the effect of these well defined conditions for real battery operation and accelerated lifetime testing. Both full-cell and half-cell polarization at 25 mA cm<sup>-2</sup> and electrochemical impedance spectroscopy at OCV were used for deactivation evaluation. Before and after 6-days experiments under given conditions characterization in +50% SoC was performed to compare the performance under identical conditions.

Results showed us that used felt electrodes have significantly different initial performance (charge transfer resistances) and also initial phase of deactivation process is very variable for individual pieces of the same felt material. From these data it seems that current load neither electrolyte SoC does not have huge effect on the deactivation rate. The developed method can be easily adopted for stability evaluation of electrode materials for redox flow batteries of versatile chemistries.

### Acknowledgments

The work was supported from European Regional development Fund-Project "Organic redox couple based batteries for energetics of traditional and renewable resources (ORGBAT)" No.CZ.02.1.01/0.0/0.0/16\_025/0007445 and from the grant of Specific university research – grant A1\_FCHI\_2020\_004.



EVROPSKÁ UNIE  
Evropské strukturální a investiční fondy  
Operační program Výzkum, vývoj a vzdělávání



MINISTERSTVO ŠKOLSTVÍ,  
MLÁDEŽE A TĚLOVÝCHOVY

### References

1. Mazur, P.; Mrlík, J.; Pociďič, J.; Vrána, J.; Dundálek, J.; Kosek, J.; Bystron T., Effect of graphite felt properties on the long-term durability of negative electrode in vanadium redox flow battery. *J. Power Sources* 2019, 414, 354-365.
2. Darling, R.M.; Perry, M.L. Half-Cell Steady-State Flow-Battery Experiments. *ECS Trans.* 2013, 53, 31-38.

## **Synergistic Effect of Nanotechnology and Optimized Industrial Manufacturing Process for Lead Electrodes Enhances the Performance of Lead-Acid Batteries**

A. Bulat<sup>a</sup>, E. Shembel<sup>b,c</sup>, Y. Polishchuk<sup>b</sup>, B. Blyuss<sup>a</sup>,  
V. Redko<sup>c</sup>, N. Zaderey<sup>b</sup>, V. Nefedov<sup>b</sup>, and Y. Pustovalov<sup>c</sup>

<sup>a</sup>M.S. Polyakov Institute of Geotechnical Mechanics under the National Academy of Sciences of Ukraine, Dnipro, 49005, Ukraine

<sup>b</sup>Scientific Research Laboratory of Chemical Power Sources of Ukrainian State University of Chemical Technology, Dnipro, 49005, Ukraine

<sup>c</sup>Enerize Corporation, Coral Springs, FL, 33067, USA

The results of research and development presented in this article confirm the prospects for the use of modifying additives based on Nano dispersed carbon-containing additives in the electrodes of lead-acid batteries. The energy, power, and stability parameters during cycling the electrodes of the lead battery are increased. The developed method is technological, easy to operate, does not require the use of scarce materials and significant production costs for implementation in production. The use of this innovative approach to modifying the technology for manufacturing electrodes of lead-acid batteries solves significant problems that appear for both the positive and negative electrodes

### **Introduction**

To improve the operational characteristics of lead battery, it is necessary to increase the conductivity of the active mass of the electrodes, to reduce the irreversible sulfation of the electrode plates, avoid the destruction the electrode mass of the positive electrode, and etc. Research and development confirm that the solution to these problems can be based on the introduction of nanostructured carbon additives into the electrode mass. Such modifying additives optimize the formation of the skeletal structure of the electrodes of lead-acid batteries and increase the conductivity of the active mass of electrodes.

The presence of nanostructured carbon materials optimizes the porous macrostructure of the electrodes. This contributes to a greater depth of distribution of the electrochemical process in the inner layers of the active mass. And this allows to shorten the period of the mode of formation of electrodes and battery charging. The effect of a nanostructured carbon material depends on its nature, conductivity, specific surface area, particle size, pre-activation, and also on the ratio of the components of the paste. In this work, показан synergistic effect of nanotechnology and optimized industrial manufacturing process for lead electrodes enhances the performance of lead-acid batteries.

## Experimental

The following materials have been investigated and used:

- - Fullerene soot obtained at the M.S. Polyakov Institute of Geotechnical Mechanics under the National Academy of Sciences of Ukraine. Fullerene soot (FS) has been produced by the Huffman-Kretschmer method and consists of approximately 65% C<sub>60</sub> fullerene, 32-33% C<sub>70</sub> fullerene, and 2-3% higher fullerenes;
- Thermo-expanded graphite (TEG), developed and provided by the company Enerize Corporation.
- Natural graphite
- Carbon black
- Electrode paste powders for the positive and negative electrodes of lead-acid batteries.
- Electrode pastes and electrodes have been produced in the course of these studies work.

The determination of the conductivity and density of carbon materials powder and electrode masses based on them have been carried out by innovating an electromagnetic non-destructive contactless method, using a special device. These non-destructive method and device have been developed by the Enerize Corporation (USA) [1, 2].

The complex resistance of the electrodes was determined as a segment on the active resistances axis obtained by extrapolating the impedance spectrum. The frequency range in which the impedance spectra were obtained is 100 kHz - 100 Hz. The amplitude of the voltage is 10 mV. The electrodes were connected according to a 2-electrode scheme: a working electrode based on PbO<sub>2</sub>, a counter electrode based on Pb. An analytical radiometer Voltalab PGZ 301 was used to register the impedance spectra. All measurements were carried out at a temperature of 25 ° C.

## Results

Table 1 shows density and conductivity of power carbon materials. For comparison, the values of conductivity and density of various powders of carbon materials are given, possible candidates for use in lead-acid batteries.

The research results showed that when the fullerene powder is compacted and when the natural graphite powder is compacted with their conductivity does not change. At the same time, compaction of thermally expanded graphite and acetylene black leads to an increase in their conductivity by about an order of magnitude. The conductivity of fullerene soot is 2 times higher than the conductivity of TEG. However, the conductivity of a mixture of dry components of electrode masses with the addition of fullerenes is much lower than the conductivity of dry components of electrode masses with the addition of thermally expanded graphite. Here is a combined effect of two factors: the conductivity and density of powders of carbon materials. TEG graphite is light (0.055 g / cm<sup>3</sup>), while fullerene has a higher density (0.157 g / cm<sup>3</sup>). TEG, due to a larger amount in the same volume, is better distributed in the electrode mass, thereby providing a satisfactory electrical contact between the particles of the mass components. That is, in addition to the conductivity of the carbon material, it is necessary to take into account the macrostructure of the mixture based on it.

**Table I.** Conductivity of various carbon materials powders

| Parameter                       | Not compacted,                  |                      | Compacted,                      |                      |
|---------------------------------|---------------------------------|----------------------|---------------------------------|----------------------|
|                                 | $\rho_3$ ,<br>g/cm <sup>3</sup> | $\sigma$ , S/m       | $\rho_3$ ,<br>g/cm <sup>3</sup> | $\sigma$ , S/m       |
| Fullerene black                 | 0,116                           | $3,32 \cdot 10^{-3}$ | 0,157                           | $3,35 \cdot 10^{-3}$ |
| Graphene                        | 0,099                           | $1,24 \cdot 10^{-3}$ | 0,108                           | $5,15 \cdot 10^{-3}$ |
| Thermo-<br>expanded<br>graphite | 0,042                           | $3,38 \cdot 10^{-4}$ | 0,055                           | $1,27 \cdot 10^{-3}$ |
| Natural graphite                | 0,240                           | $5,63 \cdot 10^{-4}$ | 0,433                           | $6,20 \cdot 10^{-4}$ |
| Carbon black                    | 0,182                           | $6,77 \cdot 10^{-4}$ | 0,223                           | $1,37 \cdot 10^{-3}$ |

. Figure 1 shows the hodographs of the electrodes impedance after the 1st stage of formation.

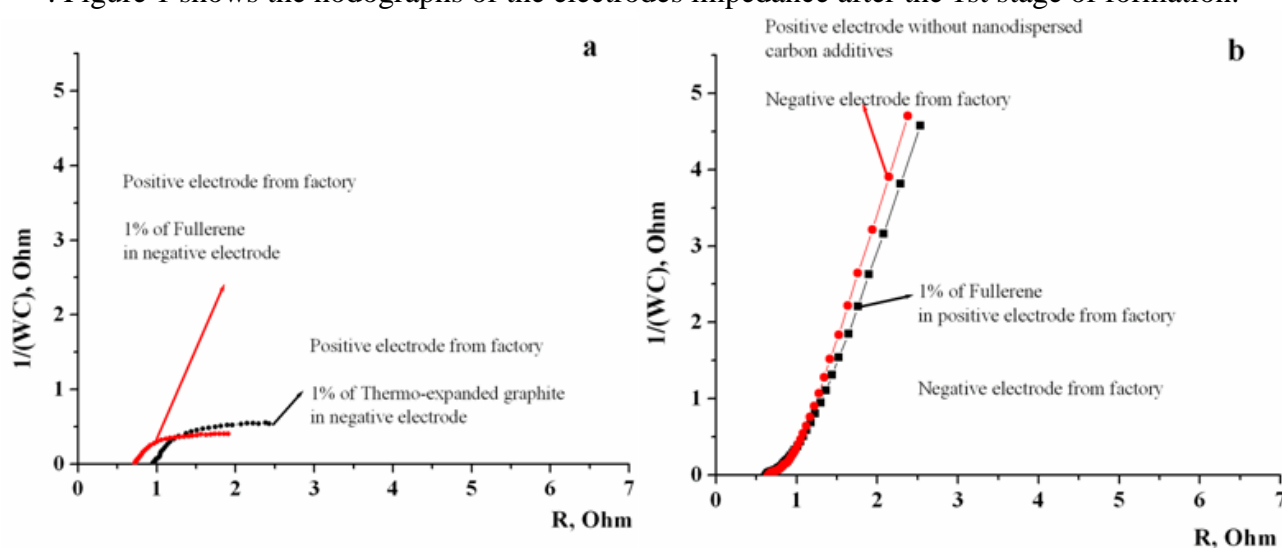


**Figure 1.** Impedance hodographs of electrode for lead-acid cell after 1st step of forming. The electrolyte is sulfuric acid with a density of 1.24 g / cm<sup>3</sup>. Working area of the electrode 15 cm<sup>2</sup>.

**Figure 1a** presents the hodograph impedances of two systems each with two electrodes: 1) positive industrial electrode from the factory and negative electrode that have been modified with Fullerene; and 2) positive industrial electrode from the factory and negative electrode that have been modified with TEG. **Figure 1b** presents the hodograph impedances of two systems each with two electrodes: 1) positive electrode modified with nano dispersed TEG and negative industrial electrode from the factory; and 2) positive electrode modified with Fullerene and negative industrial electrode from the factory;

Presented results illustrate that for positive and negative electrodes, the effect of nanostructured carbon additives is different. The nano dispersed carbon materials– Fullerene and TEG, which could modify the electrodes for lead-acid batteries, dramatically decreased the impedance of negative electrodes. The effect of nano structured carbon additives on the impedance of positive electrodes is much less pronounced.

However if both electrodes in lead-acid batteries – negative and positive –are modified with nanostructured carbon materials, for example, with Fullerene, the impedance parameters of system substantially decreased.(Fig.2).As results the complex resistance of the system decrease and the power of lead-acid battery increase.

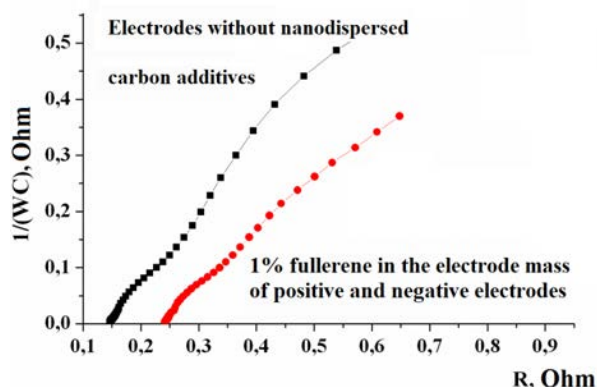


**Figure 2.** Impedance hodographs of two electrodes of lead-acid cell. The electrolyte is sulfuric acid with a density of 1.24 g / cm<sup>3</sup>. Working area of the electrode 15 cm<sup>2</sup>.

Result of investigation shown that the effect of a nanostructured carbon additive on the impedance characteristics of the electrodes of lead-acid batteries depends on the degree of formation of the electrodes

In summary, the complex of research and development illustrates the synergistic effect of the conductivity and macrostructure of a nano dispersed carbon-containing additives, which modify electrodes and dramatic improves the energy and power characteristics of lead-acid batteries.

### References

1. V. Redko, E. Shembel, etc. *US Patent No. 7,288,941* Method and Apparatus for Measuring Conductivity of Powder Materials Using Eddy Currents.
2. V. Redko, E. Shembel, T. Pastushkin, etc. *US Patent No. 8,102,181*. Method and Device for Rapid Non - Destructive Quality Control of Powdered Materials.

## Influence of temperature on impedance changes of lead-acid battery cell

P. Křivík<sup>1</sup>, S. Vaculík<sup>1</sup>, P. Bača<sup>1</sup>, J. Kazelle<sup>1</sup>

<sup>1</sup> Department of Electrotechnology, Faculty of Electrical Engineering and Communication, Brno University of Technology, Technická 10, 616 00 Brno, Czech Republic

The paper deals with the influence of temperature on the cell impedance parameters during discharge and charge of the lead-acid battery cell. Nyquist diagrams for different temperatures were compared.

### Introduction

Use properties of lead-acid batteries are affected by ambient temperature. This can have both positive and negative effects on important cell parameters, such as capacity, power, or cycle life. The operating temperature for lead-acid batteries ranges from 10 to 30 °C (optimally 20 °C ± 5 °C). The manufacturer's specifications are given at 20 °C. Lower temperatures cause an increase in internal resistance and associated drop in capacity. This is due to the slow diffusion processes during discharge and charge of the battery. Higher temperatures cause a decrease in internal resistance and thus an increase in power, but the rate of all parasitic reactions, such as self-discharge, corrosion, and gassing during charging, increases. In open systems, there is increased evaporation of electrolyte and exposure of electrodes. In sealed systems, the oxygen cycle rate increases during charging, causing additional battery heating. This can cause thermal runaway of the battery.

Impedance spectroscopy is suitable method for impedance measurements. Impedance of electrochemical cell is measured in a wide range of frequencies and the results are shown by impedance diagrams. They can be plot either in the Bode diagram (modulus in log scale vs. frequency and phase angle vs. frequency) or in the Nyquist diagram (imaginary part vs. real part). In the Nyquist diagram, electrochemists are used to plot the opposite of the imaginary part on the ordinate axis, so that the capacitive loop appears in the upper quadrant and inductance part in lower quadrant [1 - 8].

In Nyquist diagram of a battery cell is included the ohmic resistance due to the connections, the separator, the resistivity of the electrolyte and the surface coverage of the electrodes by crystallized lead sulphate. This high frequency resistance is in the range of mΩ, which is the real part of the impedance at frequencies higher than 100 Hz. Capacitive loop is determined by the porosity of the electrodes. Frequency range is between 0.1 and 100 Hz. Size of capacitive loop corresponds to charge transfer resistance. Charge-transfer reaction has a speed depending on the temperature, the concentration of the reaction products, and also the potential. For positive electrode in the course of discharge this is the resistance of the electron transfer from crystal to electrolyte and resistance of the charge-transfer of reduction of Pb<sup>4+</sup> to Pb<sup>2+</sup> [9]. Second loop at frequencies lower than 0.1 Hz corresponds to Warburg impedance caused by ionic diffusion in the electrolyte and in the pores of the electrodes and depends on the sulphatation reaction on the electrodes.

All of these resistances are influenced by temperature of the battery. Change of the battery temperature causes change of the shape of the Nyquist diagram and consequently the impedance changes in a wide range of frequencies.

## Experiment

For the experiment exploring changes of impedance in the lead-acid battery cell a sealed lead-acid cell was used, with spiral construction, containing AGM separator with a capacity of 2.5 Ah, with nominal voltage 2V and internal resistance 5 mΩ [10].

The cell was inserted in temperature chamber with constant temperature. In situ measurement comprised discharge with current 0.4 A to end of discharge 1.6 V. After attaining of limiting voltage, charging continued with a charge current 0.4 A with a 2.4 V voltage limitation. In the course of discharge and charge, the potential electrochemical impedance spectroscopy (PEIS) was measured. Amplitude of PEIS was 5 mV, frequency interval was from 6 kHz to 50 mHz, with 6 measured points per decade.

Results of the PEIS measurements are presented in Fig. 1 for discharging of the cell and Fig. 2 for charging. Fig. 1 on the left represents a Nyquist diagram of the cell during discharge (2 % of DoD) for temperatures from -20 to 50.9 °C. It can be seen that as the temperature decreases, both the internal resistance of the cell (intersection of the x-axis) and the charge transfer resistance (loop size) increase.

Fig. 1 in the middle represents a Nyquist diagram of the cell in the course of discharge (40 % of DoD) for temperatures from -20 to 50.9 °C. The internal resistance does not change much for all dependencies. Loops in the low frequency range are more flattened and have a lower radius - the charge transfer resistance decreases.

Fig. 1 on the right represents a Nyquist diagram during discharge of the cell (90 % of DoD) for temperatures from -20 to 50.9 °C. The internal resistance increases at all temperatures. The lowest increase in internal resistance occurs at the lowest temperature. Because of the lowest capacity, so much lead sulfate was not formed at the end of the discharge at the lowest temperature comparing with the higher temperatures. Lead sulphate content has a more influence on the internal resistance increase than the low cell temperature. Loops in the low frequency range are even more flattened and have a larger radius. Thus, at the end of the discharge, there is a small increase in charge transfer resistance compared with state at 40 % of DoD.

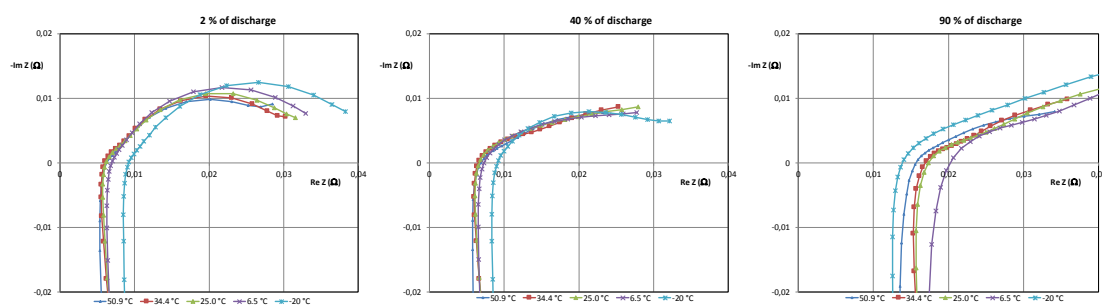


**Figure 1.** Comparison of Nyquist diagrams of the cell during discharge (DoD = 2%, 40% and 90%).

Fig. 2 on the left represents a Nyquist diagram of the cell during charge (10 % of SoC) for temperatures from -20 to 50.9 °C. The internal resistance decreases at all temperatures. The higher internal resistance is at the lowest temperature of -20 °C and, paradoxically, at the highest temperature. The high internal resistance at the highest temperature is probably due to the higher lead sulphate content. The cell at this temperature had the highest capacity and hence the highest lead sulphate content at the end of discharge. The loops in the capacity area are not flattened, their radius increases with decreasing temperature. The highest charge transfer resistance is therefore at the lowest temperature.

Fig. 2 in the middle represents a Nyquist diagram of the cell during charge (40 % of SoC) for temperatures from -20 to 50.9 °C. At all temperatures there is a further decrease in internal resistance. The highest internal resistance is at the lowest temperature of -20 °C. This differs significantly from the internal resistances at other temperatures. The loop radius in the capacity area increases during charging. As the temperature decreases, the loop radius is bigger, so the charge transfer resistance is higher. Thus, the highest charge transfer resistance is at the lowest temperature. The exception is temperature 25 °C, where the loop radius is bigger than at 6.5 °C. The cell at temperature 25 °C and at 40 % of SoC has a lower lead sulphate content than at 6.5 °C and therefore it has a higher charge transfer resistance.

Fig. 2 on the right represents a Nyquist diagram of the cell during charge for temperatures from 6.5 to 50.9 °C for 70 % of SoC (63 % of SoC for 6.5 °C). The dependence at -20 °C could not be measured for this SoC, the cell has already reached a voltage limit of 2.4 V during charging and PEIS measurement failed in this charging mode. At all measured temperatures, the internal resistance further decreases to the lowest value. The highest internal resistance is at the lowest temperature of 6.5 °C. The loop radius in the capacity area reaches the highest values. As the temperature decreases, the loop radius is larger, so the charge transfer resistance is higher.

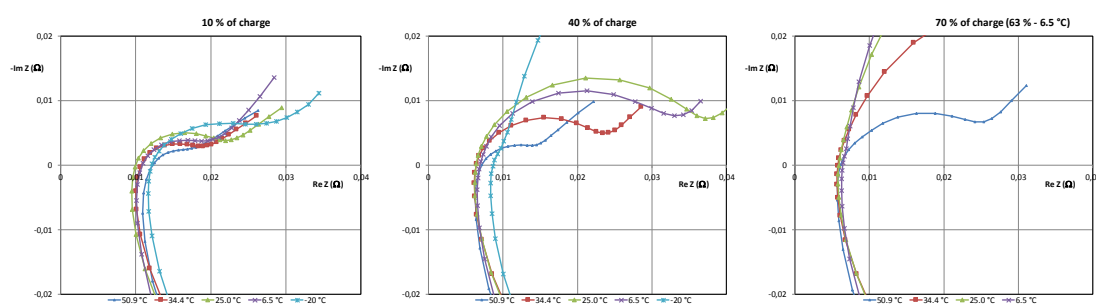


**Figure 2.** Comparison of Nyquist diagrams of the cell during charge (SoC = 10%, 40% and 70%).

## Conclusions

The temperature influences the basic parameters of the lead-acid battery both in current off state and in operation (discharging and charging of the battery). These parameters include capacitance and impedance components - internal resistance and charge transfer resistance. Impedance changes can be detected by the Nyquist diagram. Value of the impedance components is changing with frequency, temperature and state of charge. Both internal resistance and charge transfer resistance increase with decreasing temperature. During discharging and charging, both components of the impedance change their value and this change is influenced by the temperature of the battery. Used frequency during impedance measurements reveals different impedance components of the battery.

## Acknowledgements

This work was supported by specific research of the Brno University of Technology No. FEKT-S-20-6206.

### References

1. C. Gabrielli, Identification of electrochemical processes by frequency response analysis, Solartron, Technical Report No 4183 (1983) 120.
2. N.A. Hampson, S.A.G.R. Karunathilaka, R. Leek, The impedance of electrical storage cells, *J. Appl. Electrochem.* 10 (1980) 3.
3. S. Rodrigues, N. Munichandraiah, A.K. Shukla, A review of state-of-charge indication of batteries by means of ac impedance measurements, *J. Power Sources* 87 (2000) 12.
4. T. Yokoshima et al, Application of electrochemical impedance spectroscopy to ferri/ferrocyanide redox couple and lithium-ion battery systems using a square wave as signal input, *Electrochimica Acta* 180 (2015) 922.
5. F. Huet, A review of impedance measurements for determination of the state-of-charge or state-of-health of secondary batteries, *J. Power Sources* 70 (1998) 59.
6. H. Blanke et al, Impedance measurements on lead-acid batteries for state-of-charge, state-of-health and cranking capability prognosis in electric and hybrid electric vehicles, *J. Power Sources* 144 (2005) 418.
7. P. Křivík, S. Vaculík, Impedance Methods for SoC Determination of Lead-acid Battery Cell, *ECS Transactions* 81 (2017) 151.
8. E. Barsoukov, J. Macdonald, *Impedance Spectroscopy: Theory, Experiment, and Applications*, Wiley (2005).
9. D. Pavlov, G. Petkova, Phenomena That Limit the Capacity of the Positive Lead-acid Battery Plates, *Journal of The Electrochemical Society* 149 (2002) A654.
10. P. Křivík, S. Vaculík, P. Bača, J. Kazelle, Determination of the state of charge of lead-acid battery by EIS, *Journal of Energy Storage* 21 (2019) 581.

## The Technological Aspects of Iron Electrode Material

O. I. Bilan<sup>a</sup> and R. K. Nafeev<sup>b</sup>

<sup>a</sup> Deputy Chief Technologist, LLC “ADS”, Velyki Mosty, Lviv Region 80074, Ukraine

<sup>b</sup> Department of Physics, State University of Telecommunications, Kyiv 03110, Ukraine

Considered main technological aspects of Fe<sub>3</sub>O<sub>4</sub> synthesis and preparing iron electrode from it. Received material has good cycling character, reach 80% current efficiency and 180 Ah/g equivalent discharge capacity.

### Introduction

Iron is one of most common element on the Earth. So using it for large-scale electrical energy storage is promising direction on cost effective and environmental-friendly point of view [1]. For this reason many research attempts dedicated to use this metal in electrochemical systems like nickel – iron, air – iron [1] and even flow [2] batteries.

Solid electrode material has smaller volume and needs less equipment accompaniment, that is why lot of efforts are made for first one. Synthesis of main component of iron electrode determinates it base performance, thus many works were concentrated on it preparing. [1, 3]. In other works were investigated sulfide and bismuth additives [4, 5] to receive maximal activity of iron solid electrode.

Present study considerate the technological aspects of material for iron electrode in alkaline medium.

### Experimental

Fe<sub>3</sub>O<sub>4</sub> were synthesized by two step method [6]. First of all FeSO<sub>4</sub> precipitated with NaOH. Sediment rinsed with distillate water to pH = 7.0 and dried in dilution at 85°C. After that added 2.5% H<sub>2</sub>O, reduction agent (Fe powder for Type I or polyethylene for Type III samples) and annealed at 800°C for 4 hour. Annealed Fe<sub>3</sub>O<sub>4</sub> were cooled in desiccator to room temperature (near 20-25°C). Prepared material (95.85%) mixed with 1% NiSO<sub>4</sub>·7H<sub>2</sub>O dissolved in 3% pure water and added 0.15% sulfur containing agent (pristine sulfur for Type I or equivalent amount FeS for Type II samples). Pressed pellets with mixed material placed in Ni plated steel strep with perforation.

Prepared iron electrode were tested in a three-electrode compartment with pocket type nickel hydroxide counter electrodes and a Zn reference electrode. The electrolyte was prepared from potassium hydroxide (density 1.20 g/ml). Charged 12 hours with current 0.25C (25% of nominal capacity). Discharged with current 0.20C to 0.65V relatively Zn electrode.

### Results

Charge (a) and discharge (b) curves for two Fe<sub>3</sub>O<sub>4</sub> samples synthesized with different reduction agent were mixed with pristine sulfur shown on Fig. 1 (Type I - Fe powder and Type III - polyethylene)

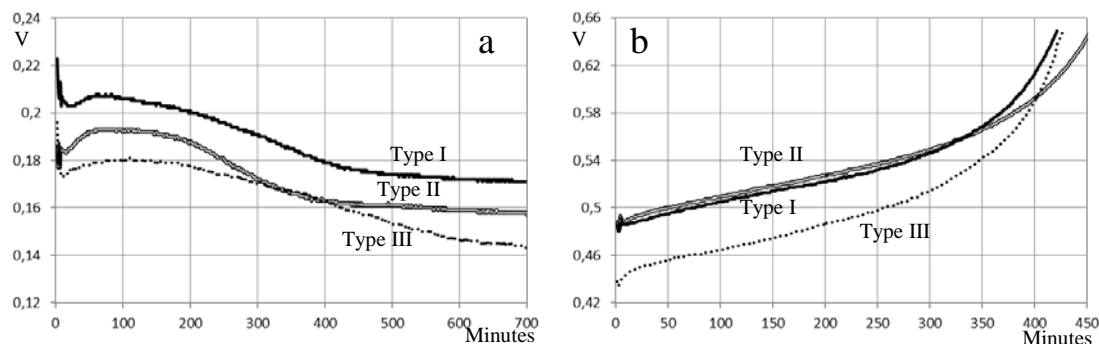


**Figure 1.** Charge and discharge potential depending on time for various Type samples (relatively Zn reference electrode).

Sample Type I potential at constant current charge (Fig. 1, a) is near 30 mV higher, than sample Type III. For nickel – iron battery it implements higher energy efficiency of charge. But at first part of discharge step (Fig. 1, b) sample Type I show lower energy efficiency, because it has near 40 mV higher potential, relatively Type III sample. Considering overall energy efficiency sample Type I is more beneficial owing to more energy uses on charge step (12 hours charge with current 25% of nominal capacity versus 7 hours discharge with current 20% of nominal capacity).

As sulfur containing agent for passivation prohibiting used pristine sulfur for Type I sample or equivalent amount FeS for Type II sample f ( $\text{Fe}_3\text{O}_4$  synthesized with Fe powder reduction agent). At charge step (Fig. 1, a) sample Type II has near 20 mV lower potential than sample Type I. It may be caused low solubility of FeS and accordingly lower activity sulfide-ion. But at discharge (Fig. 1, b) sample Type II has higher equivalent capacity (180 Ah/g) than sample Type I (177 Ah/g).

As described in [1] formation newly-prepared iron electrode repeated from 20 to 50 cycles. In present work stable discharge capacity attained less than 15 cycles (Fig. 2).

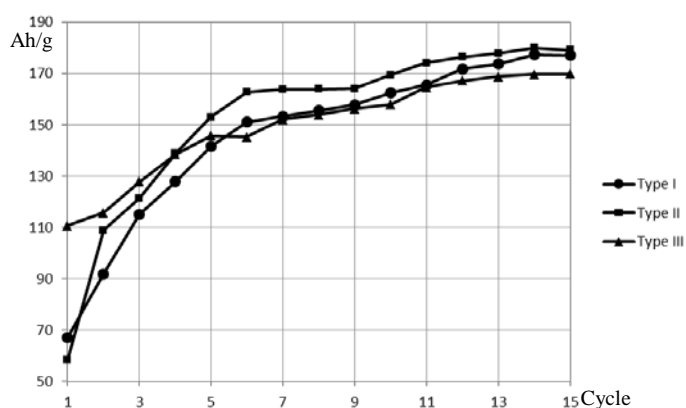


**Figure 2.** Equivalent discharge capacity depending on cycle number.

At the first formation cycle sample Type III has the highest capacity. After full formation process it has the lowest capacity (170 Ah/g). After overall energy efficiency analysis of sample Type I (with highest capacity - 180 Ah/g) had 80% efficiency by current.

## Conclusions

Synthesis Fe<sub>3</sub>O<sub>4</sub> with Fe powder as reduction agent and using FeS as sulfur containing agent allows reach 180 Ah/g equivalent discharge capacity from iron electrode in alkaline medium. Fabricated electrode in real nickel – iron battery shows 80% current efficiency. Considered technology speed up production process because stable discharge capacity attained less then 15 cycles

## References

1. Aswin K. Manohar, Chenguang Yang, Souradip Malkhandi, Bo Yang, G. K. Surya Prakash, and S. R. Narayanan, *J. Electrochem. Soc.*, **159**, A2148-A2155 (2012).
2. Netzahualcoryotl Arroyo-Currars, Justin W. Hall, Jeffrey E. Dick, Richard A. Jones, and Allen J. Bard, *J. Electrochem. Soc.*, **162**, A378-A383 (2015).
3. A. Sundar Rajan, S. Sampath, and A. K. Shukla, *224th ECS Meeting*, **284** (2013).
4. Aswin K. Manohar, Chenguang Yang, and S. R. Narayanan, *J. Electrochem. Soc.*, **162**, A1864-A1872 (2015).
5. Aswin K. Manohar, C. Yang, S. Malkhandi, G. K. Surya Prakash and S. R. Narayanan, *224th ECS Meeting*, **288** (2013).
6. L.A.Abramov, T.D.Moskalenko, R.K.Nafeev, and V.P.Shestov, ISTC “*Problems of accumulation and disposal of dust-containing wastes from industrial enterprises and their solution prospects with regards of the scientific and technical program of the European Union INCO*”, p. 30-31, Kyiv (2010).

## Effect of Surfactants to Decomposition of Supersaturated Zinc Electrolytes in Ni-Zn Battery

L. Chladil<sup>a</sup>, J. Smejkal<sup>a,b</sup> and T. Bannert<sup>a</sup>

<sup>a</sup> Institute of Electrotechnology, Faculty of Electrical Engineering and Communication, BUT, Technická 10, 616 00 Brno, Czech Republic

<sup>b</sup> Central European Institute of Technology, BUT, Technická 10, 616 00 Brno, Czech Republic

This work discussed a process of decomposition of alkaline supersaturated zincate solution (SZS) based on KOH and monitored growth of zinc oxide crystals in broad timescale. Decomposition of SZS is an important process taking place in the entire volume of supersaturated zincate solutions that are the mostly used electrolyte for Ni-Zn or Zinc-Air batteries. SZS is formed primarily at a short distance from the negative electrode during fast discharging of zinc anode or in entire volume of electrolyte in final stage of discharging. A supersaturated 6 mol/l KOH solution was prepared by oversaturation at higher temperature with subsequent cooling. Initial level of supersaturation reached 0,9 mol/l than its balanced concentration in a potassium hydroxide solution.

### Introduction

The one of the most investigation aspects in the field of Ni-Zn alkaline accumulators is the ability of effective suppression of zinc dendrite growth at charging, when the dissolved tetrahedral zinc species are re-deposited from electrolyte onto the surface of negative electrode current collector [1], [2]. Many different approaches to this challenge was investigate and most of them have begun taking the organic cationic, anionic or nonionic surfactants that seems to be effective in dendrite grow inhibition. The presence of these surfactants on the one side can resolve this fractional problem but on the other side also can influence of many other processes which has occurred in the Ni-Zn cells at battery operation. Whereas some of these processes as self-discharging, dendrite inhibition or electrode passivation were studied in details, influence of these additives to decomposition rate of supersaturated zincate solution (SZS) and also to recrystallization were neglected. Decomposition of SZS is important process, which take place in the whole volume of SZS but mainly has occurred in the bulk and at a short distance from the negative electrode, because in this part is the highest degree of supersaturation at discharging. Rate of the decomposition process is influenced by temperature, initial supersaturation concentration of zincate, concentration of hydroxide (pH) and also by presence of specific additives [3]. In relation to the last mentioned, for example the study of  $\text{SiO}_3^{2-}$  additive effect on decomposition kinetics shows that  $\text{SiO}_3^{2-}$  causes complete inhibition of decomposition by its adsorption on the surface of ZnO. At decomposition firstly the formation of nuclei take place and follow these nuclei further grow into the final shape as the supersaturated concentration decrease. In some study it was concluded that specific shape of ZnO crystal strongly influence the cyclability of negative electrodes. Also, many studies were focused to preparing specific shapes ZnO particles by hydrothermal method where the organic additives as CTAB, SDS, Starch etc. were used to determination of appropriate particle shape. It would seem that the presence of dendrite inhibitors that are mostly organic ion-active substances could influence the crystallinity of active materials of negative electrodes and thus

influence also the cyclability or Ni-Zn or Zinc-air batteries. The use of any organic additives should be preceded by a study of how these additives affect the growth of ZnO crystals and how they affect the upcoming recrystallization processes.

### Experimental

For the decomposition, 500 ml of supersaturated zinc solution with potassium hydroxide concentration 6 mol/l and higher zinc oxide concentration than in equilibrated saturated state was prepared. 168,33 g of potassium hydroxide was dissolved in approx. 10 ml of deionized water and then 51,57 g of zinc oxide were gradually dissolved and solution was heated and mixed by magnetic stirrer for 30 minutes. After reaching of fully clear and transparent solution we added the rest of deionized water to obtain 500 ml of supersaturated solution. Solution was dispensed to 100 ml sample containers and these were placed to climatic cell tempered to 30 °C. Then the decomposition process began and the samples of growing crystals were separated after 7 days (168 hours). Separation of ZnO crystals was performed using repeated washing with distilled water and centrifugation until neutral pH of washing solution was reached. Concentration of solute zinc oxide were monitored by chelatometric titration and amount of supersaturated zinc were calculated using equation

$$\frac{V_{std}}{V_{titr}} * C_{chel} * M_{mZnO} = C_{ZnO} \quad (1)$$

Where  $V_{std}$  is amount of titration standard ( $\mu$ l),  $V_{titr}$  is amount of analyzed sample (50  $\mu$ l),  $C_{chel}$  is Chelaton III concentration (0,01 mol/l),  $M_{mZnO}$  is zinc oxide molar mass and  $C_{ZnO}$  corresponds to final concentration of zinc oxide (g/l).

### Results and discussion

Table 1 shows the amount of Chelaton III solution required to reach equivalence point for each measured sample at different decomposition times. Overall amounts of zincate in supersaturated solution is calculated using equation 1. Highlighted cells indicate the times when the crystals were separated from the solutions and subjected to SEM and XRD analysis.

**TABLE 1.** Measured volumes of Chelaton III and calculated values of zincate concentrations

| Time (h)              | 17    | 41    | 66   | 90   | 155  | 167  | 213  | 306  | 404  | 500  | 572  | 665  | 737  |
|-----------------------|-------|-------|------|------|------|------|------|------|------|------|------|------|------|
| Sample 1 ( $\mu$ l)   | 6300  | 6210  | 6120 | 5950 | 5075 | 4648 | 4425 |      |      |      |      |      |      |
| Sample 2 ( $\mu$ l)   | 6185  | 6180  | 6080 | 5930 | 5090 | 4780 | 4425 | 4020 |      |      |      |      |      |
| Sample 3 ( $\mu$ l)   | 6125  | 6175  | 6125 | 5960 | 5010 | 4952 | 4410 | 3990 | 3800 |      |      |      |      |
| Sample 4 ( $\mu$ l)   | 6350  | 6125  | 5980 | 5860 | 5070 | 4851 | 4435 | 3985 | 3850 | 3725 | 3699 |      |      |
| Sample 5 ( $\mu$ l)   | 6275  | 6175  | 6050 | 5990 | 5040 | 4802 | 4430 | 4010 | 3775 | 3672 | 3582 | 3465 | 3420 |
| Avarage ( $\mu$ l)    | 6234  | 6164  | 6059 | 5935 | 5053 | 4848 | 4425 | 4001 | 3808 | 3699 | 3641 | 3465 | 3420 |
| $C_{ZnO}$ (g/l)       | 101,4 | 100,3 | 98,6 | 96,6 | 82,2 | 78,9 | 72,0 | 65,1 | 61,9 | 60,2 | 59,2 | 65,4 | 55,6 |
| $C_{ZnO,SZS}$ (g/l)   | 71,5  | 70,4  | 68,7 | 66,7 | 52,3 | 49,0 | 42,1 | 35,2 | 32,0 | 30,3 | 29,3 | 26,5 | 25,7 |
| $C_{ZnO,SZS}$ (mol/l) | 0,88  | 0,87  | 0,84 | 0,82 | 0,64 | 0,60 | 0,52 | 0,43 | 0,39 | 0,37 | 0,36 | 0,33 | 0,32 |

As can be seen from Tab. 1 and Fig.1, the concentration of ZnO decreases with time. After 737 hours, the concentration of ZnO decreased by almost 50 % but still was 0.3 mol above the equilibrium saturated state. At the beginning part of the experiment, supersaturated concentration seems to be almost stable and only small decrease of zinc concentration is detected. In this part a nuclei of zinc crystal are formed and this consume only small amount of solute zinc. After approx.100 hours, faster decrease in ZnO concentration was detected and this part correspond to significant increase in particle dimension. In Fig. 1 it is possible to observe the time course of

decomposition. The green dots indicate the time when precipitate separated. We performed the first crystal separation after 167 hours and the highest decrease in supersaturated concentration between first two separation indicate significant changes of crystals. Although we would expect a significant increase in particle dimension during this rapid zincate decline, the ESEM images of zinc powder and precise particle analysis revealed that average length of particles stays almost the same in this time. Because of the zincate had to be consumed in some way we assumed, that nucleation and the growth of the new crystals had to still proceed in this stage of decomposition.

In the next three crystal separation - 404 h, 572 h and 737 h we detect important increase of particle dimension from ESEM images. Because of only 0,11 mol/l zincate was consumed we attribute the crystal growth rather to recrystallization processes than to direct growth from SZS decomposition. This is also indicated by the fact that particle distribution profile shows the important increase of the larger  $\mu\text{m}$  sized crystals on the expense of the smaller.

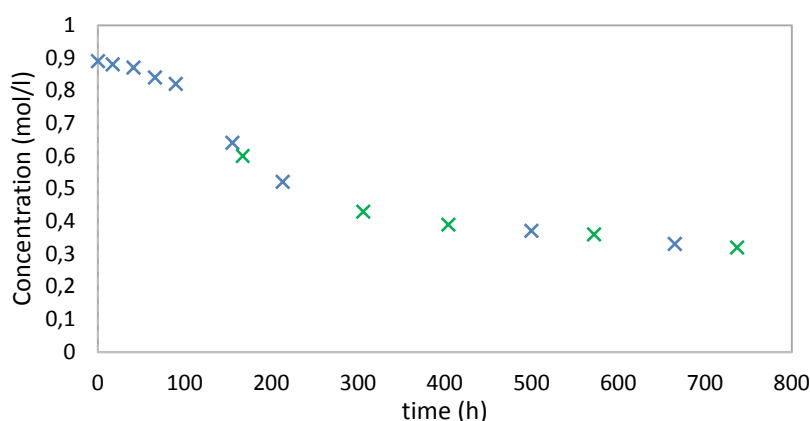


**Figure 1.** Change in zincate concentration in the SZS during its decomposition

## Conclusions

This study brings the initial measurement which aimed to monitoring the zinc oxide crystal growth from supersaturated zincate solution. This study will serve to following comparison with the similar decomposition system affected by different organic additives. Problematics of crystallization and recrystallization of zinc oxide powder play an important role in batteries with zinc anode as are Ni-Zn or Zinc-Air batteries and this study should be helpful in optimization of long-thermal properties of the system when diffusion properties as well as the stable active surface of electrode have to be ensured.

## Acknowledgement

This work was supported by the specific graduate research of the Brno University of Technology No. FEKT-S-20-6206.

## References

1. J. Jindra, *J. Power Sources*, **66**, 15-25 (1997).
2. J. Jindra, *J. Power Sources*, **88**, 202-205 (2000).
3. C. Debiemme-Chouvy and J. Vedel, *J. Electrochem. Soc.*, **138**, 9, 2538-2542 (1991).

## Influence of the water-soluble binders to the properties of Li-S batteries

T. Kazda<sup>a</sup>, M. Kekelák<sup>a</sup>, P. Čudek<sup>a</sup>

<sup>a</sup> Department of Electrical and Electronic Technology, Faculty of Electrical Engineering and Communication, BUT, Technická 10, 616 00 Brno, Czech Republic

Lithium-sulfur batteries are one of the most promising battery systems nowadays. However, this system is devalued with a number of shortcomings. One of the main ones are the volumetric changes during cycling. This deficiency can be compensated by usage of the right binder. This article describes the effect of the water-soluble binders on the stability of the electrode during cycling.

### Introduction

With the pressure to reduce global warming, the importance of renewable power sources is growing. However, renewables are a solution to replace conventional fossil power sources only in combination with energy storage systems. Currently, lithium-ion batteries are the most common type of batteries for stationary energy storage systems. They have several advantages such as high gravimetric energy density, high power density or long cycle life. However, lithium-ion batteries also have their limitations. Intensive research of new battery technologies that would in the future surpass lithium-ion batteries by their parameters is currently underway. One of these technologies are Li-S batteries. The main advantage of Li-S batteries is high theoretical capacity 1672 mAh/g. Which leads in combination with mean value of the discharge plateaus around 2.2 V against lithium to high gravimetric energy density  $\sim 3200$  Wh/kg [1]. Main disadvantage of Li-S batteries is low cycle life which is caused by a process called shuttle effect [2]. During charging and discharging, a whole series of polysulfides are formed, part of these polysulfides are soluble in the electrolyte, which leads to a capacity drop. Dissolved polysulfides are subsequently deposited on the anode surface, thus further decreasing the capacity. Another problem are volumetric changes up to 80% during cycling [3]. These changes can be compensated by a binder with sufficient binding properties and at the same time sufficiently flexibility. In this article, we focus on testing of three kinds of water-soluble binders: Carrageenan, PEO (polyethylenoxid) and CMC (carboxymethyl cellulose). A standard electrode with a PVDF (polyvinylidenfluorid) binder was used for comparison.

### Experimental

The electrode slurry was based on Sulfur as active material consisting of NMP (N-Methyl-2-pyrrolidone) or water (solvent), PVDF or PEO or CMC or Carrageenan (binder) and carbon Super P. The weight ratio of the materials was: active material 60 %, Super P 10 %, PVDF 10 %. The resulting mixture was subsequently deposited by a 200  $\mu\text{m}$  coating bar on an Al foil, dried and pressed. A disk with the diameter of 18 mm was cut out of the coated aluminum foil and inserted into an electrochemical test cell EI-Cell© ECC-STD. The assembly was done in a glove box filled with an argon atmosphere. Metal lithium foil was used as a material for the anode and 0.25 M LiNO<sub>3</sub>+0.7 M LITFSI - DME:DOL 2:1 w/w as the electrolyte. We can see a comparison of capacities during cycling at different C-rate figure 1.

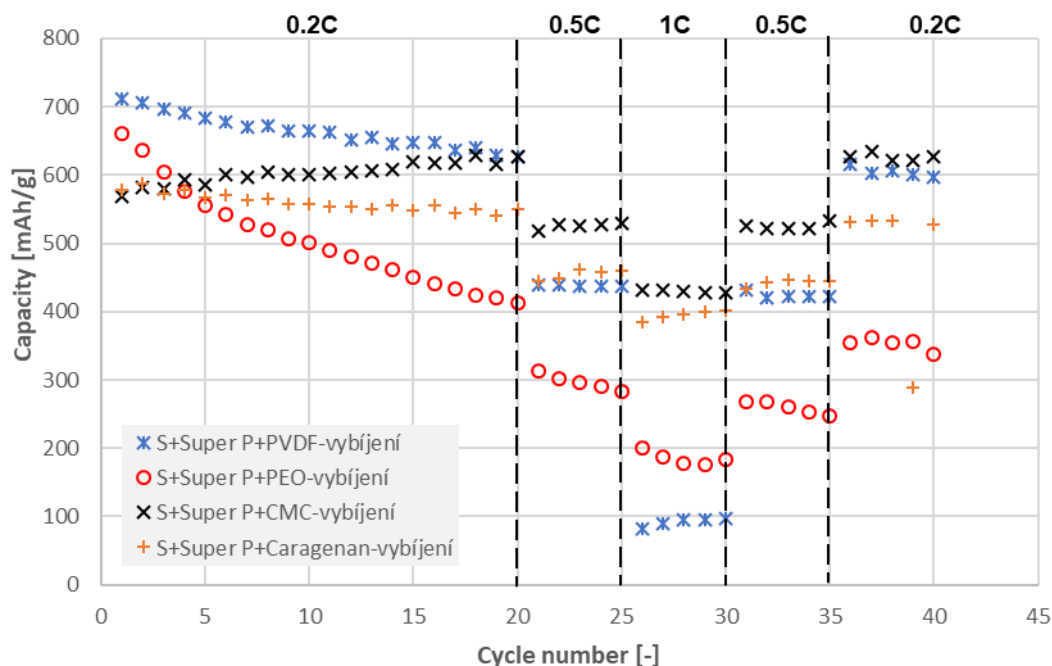


**Figure 1.** Cycling at different C-rate for all tested electrodes with different binders.

### Conclusion

The highest capacity was reached by the cell with the electrode with PVDF binder, however, this capacity at the 0.2 C was not as stable as the capacity of the cell with the CMC or Carrageenan binder. The cell with the Carrageenan binder lost only 8.8 % of its capacity after all cycling. In the case of CMC binder was capacity even higher than before cycling. Cell with PEO electrode was highly unstable. CMC and Carrageenan can be used as a binders for Li-S batteries instead PVDF with lower stability.

### Acknowledgments

This work was supported by the specific graduate research of the Brno University of Technology No. FEKT-S-20-6206.

### References

1. MANTHIRAM, Arumugam, Yongzhu FU, Sheng-Heng CHUNG, Chenxi ZU a Yu-Sheng SU. *Chemical Reviews*. 2014, **114**(23), 11751-11787.
2. PANG, Quan a Linda F. NAZAR. *ACS Nano*. 2016, **10**(4), 4111–4118.
3. YOO, Hyun Deog, Elena MARKEVICH, Gregory SALITRA, Daniel SHARON a Doron AURBACH. *Materials Today*. 2014, **17**(3), 110-121.

## **Solid Composite Polymer Electrolytes for High Energy Density and Safe Lithium Metal Cells**

Julia Amici, Daniele Versaci, Claudia Torchio, Andrea Marchisio, Roberto Colombo, Federico Bella, Carlotta Francia and Silvia Bodoardo

Electrochemistry Group  
Department of Applied Science and Technology (DISAT)  
Politecnico di Torino  
C.so D.ca degli Abruzzi, 24 10128 Torino (TO)  
Julia.amici@polito.it

Nowadays, electrical energy storage is one of the most critical issue to answer global warming by effectively replacing fossil energies by renewable ones. The Li-ion technology, widely studied and available on the market for multiple application is now reaching its limits and does not represent alone a viable option toward energetic transition. Therefore, one option currently under study is the use of metallic lithium as anode both in Li-ion cells and in the so-called “post Li-ion technologies”. In this perspective, lithium metal anode represents the “holy grail” of battery research for its extremely high theoretical specific capacity ( $3860 \text{ mA h g}^{-1}$ ), the lowest redox potential ( $-3.040 \text{ V}$  vs the standard hydrogen electrode) and a low gravimetric density ( $0.534 \text{ g cm}^{-3}$ ).

However, metallic Li also presents many challenges derived primarily from dendrite formation upon cycling causing both safety issues and poor cycling performance. In addition, liquid electrolytes contain combustible organic solvents that can cause leakage and fire risks during overcharge or abused operations, especially in large-scale operation. Therefore, replacement of liquid electrolytes with a solid electrolyte has been recognized as a fundamental approach to effectively address the above problems. Generally, all solid-state electrolytes can be classified into 3 categories: solid polymer electrolytes (SPE), inorganic ceramic electrolytes (ICE) and solid composite electrolytes (SCE). While SPEs suffer from poor ionic conductivity at room temperature and low thermal and electrochemical stability, and ICEs from poor interfacial contact with electrodes, SCEs solve these issues and benefit from their advantages such as good ionic conductivity, good flexibility and intimate contact with the electrodes. For example, the preparation of methacrylate-based polymer matrix, in a solvent free, thermally induced, radical polymerization, allows the addition of a wide range of organic and inorganic additives up to really high ratio. Meanwhile, eventual activation with small amount of liquid electrolyte allowed to obtain SCEs with outstanding room-temperature conductivities for metallic lithium batteries. The simplicity of the formulation and the preparation method open the road to highly versatile electrolytes, adaptable in function of the final application. In particular, the use of inorganic additive permitted to enhance mechanical properties thus avoiding lithium dendrites nucleation and stabilizing Li stripping/plating in Li-ion cells, while addition of dextrin based nanosponges limiting oxygen cross-over phenomenon in Li-O<sub>2</sub> cells allowed to stabilize SEI layer, hence greatly improving cells safety in both cases.

## Novel inorganic host materials for Li-S batteries

M. Zukalová

J. Heyrovský Institute of Physical Chemistry, v.v.i., AS CR, Dolejškova 3, Prague 8, Czech Republic

Lithium–sulfur (Li–S) batteries, being introduced in the early twentieth century, have received a great deal of attention for emerging applications such as electric vehicles, drones, and unmanned aerial vehicles<sup>1</sup>. Based on the electrochemical reaction  $S_8 + 16Li \leftrightarrow 8Li_2S$ , sulfur possesses a theoretical capacity of  $1672 \text{ mAh g}^{-1}$ , almost ten times of that of the current commercial cathode materials for Li-ion batteries such as  $LiCoO_2$ ,  $LiFePO_4$  or  $LiNi_x Co_y Mn_{1-x-y}O_2$  (NMC)<sup>2</sup>. By coupling with a Li metal anode, the theoretical gravimetric energy density and volumetric energy density of Li-S batteries can reach to  $2500 \text{ Wh kg}^{-1}$  and  $2800 \text{ Wh L}^{-1}$ , respectively<sup>2</sup>. Unfortunately, the commercialization of Li-S batteries is hindered by several major challenges. First, both sulfur and lithium (di)sulfide discharge product are electronically and ionically insulating, which leads to low electrochemical utilization and limits the rate capability. High-order lithium polysulfides formed in the initial lithiation of  $S_8$  dissolve into electrolyte, diffuse through the electrolyte and reaches the Li metal anode producing insulating lithium sulfide ( $Li_2S$ ) on the Li metal surface<sup>3</sup>. During the subsequent charge, low-order lithium polysulfides are oxidized to high-order lithium polysulfides and returns to the sulfur cathode by an electric field, constituting the so-called shuttling process. The shuttling process causes self-discharge and impairs cyclability by forming unstable interfaces at both electrodes and losing the active material of the sulfur cathode<sup>1</sup>. Different carbonaceous sulfur additives used to adsorb lithium polysulfides solved this problem to a limited extent only, since purely carbonaceous materials can only partially restrict polysulfide intermediates, and the hydrophilic lithium polysulfide molecules will diffuse out from carbon host over long-term cycling<sup>4</sup>. On the other hand, metal oxides are currently the most promising inorganic compounds to anchor polysulfides in Li-S batteries and attract an attention of many research teams.

In our study, we prepared sulfur composites with transition metal oxides or oxynitrides ( $TiO_2$ ,  $Li_4Ti_5O_{12}$ ,  $TiO_xN_y$ ) with different morphology by synthetic procedure combining melting diffusion, milling and atomic layer deposition (ALD). The prepared samples were characterized by XRD and Raman spectroscopy and their electrochemical performance was evaluated by cyclic voltammetry and galvanostatic chronopotentiometry. Difference in electrochemical performance of evaluated composite materials and strategies of future research will be discussed. A cathode consisting of sulfur- nanofibrous  $TiO_xN_y$  composite exhibited the most stable performance during cycling. On the other hand,  $TiO_2$  layers made by ALD on composite electrode surface have a blocking effect even after thermal post treatment at  $450^\circ\text{C}$ .

### Acknowledgments

This work was supported by the Grant Agency of the Czech Republic (contract No. 20-3564S).

### References

1. Yim, T.; Han, S. H.; Park, N. H.; Park, M.-S.; Lee, J. H.; Shin, J.; Choi, J. W.; Jung, Y.; Jo, Y. N.; Yu, J.-S.; Kim, K. J. Effective Polysulfide Rejection by Dipole-Aligned  $BaTiO_3$  Coated Separator in Lithium-Sulfur Batteries. *Adv Funct Mater* 2016, 26, 7817-7823.

2. Xue, W. J.; Miao, L. X.; Qie, L.; Wang, C.; Li, S.; Wang, J. L.; Li, J. Gravimetric and volumetric energy densities of lithium-sulfur batteries. *Curr. Opin. Electrochem.* 2017, 6, 92-99.
3. Yao, H.; Zheng, G.; Li, W.; McDowell, M. T.; Seh, Z.; Liu, N.; Lu, Z.; Cui, Y. Crab shells as sustainable templates from nature for nanostructured battery electrodes. *Nano Lett* 2013, 13, 3385-90.
4. Dong, C.; Gao, W.; Jin, B.; Jiang, Q. Advances in Cathode Materials for High-Performance Lithium-Sulfur Batteries. *iScience* 2018, 6, 151-198.

## Development of New Cathodes for Stable and Safer Lithium-Sulphur Batteries – results of NATO SPS research project

A. Straková Fedorková<sup>1\*</sup>, D. Capková<sup>1</sup>, T. Kazda<sup>2</sup>, K. Gavalierová<sup>1</sup>, M. Sedlaříková<sup>2</sup>,  
P. Gómez-Romero<sup>3</sup>, E. Shembel<sup>4</sup>

<sup>1</sup>Institute of Chemistry, Faculty of Science, P.J. Šafárik University, Moyzesova 11,  
SK-04154 Košice, Slovak Republic

<sup>2</sup>Department of Electrical and Electronic Technology, Faculty of Electrical Engineering and  
Communication, Brno University of Technology, Technická 10, 616 00 Brno, Czech Republic

<sup>3</sup>Institut Català de Nanociència i Nanotecnologia, ICN2, CIN2 / Consejo Superior  
de Investigaciones Científicas (CSIC), Campus UAB, E-08193 Bellaterra, Barcelona, Spain

<sup>4</sup>Ukrainian State University of Chemical Technology, Dnipro, 49005, Ukraine

### Abstract

NATO SPS project investigates new materials that will enable production of components for Li-ion batteries with significantly improved reliability, including greater stability, power density and efficiency. These materials will address questions concerning safety, environmental compatibility, price and efficiency. The project is focusing on the development of new sulfur-based composite cathode materials suitable for high energy lithium-ion batteries.

The lithium-sulfur battery is a “conversion” type battery, because the electrochemical reactions which take place during charging and discharging of the battery result in new chemical compounds [1,2]. The advantage of lithium-sulfur batteries is primarily their superior storage capacity (energy density - theoretical specific capacity is 1672 mAhg<sup>-1</sup>), but they also excel in economic and environmental terms. Sulfur is a relatively inexpensive and abundant raw material, unlike expensive elements, such as cobalt, which are used in lithium-ion batteries. However, various challenges are connected to the lithium sulfur cell chemistry, which need to be solved within systematic studies and by the development of new material concepts. Targeted problems of our project are divided into three main parts:

- Preparation of different sulfur cathode composites with high specific capacity and improved cyclability
- Improving fire safety of lithium rechargeable batteries
- Electrochemical and structural testing of our active materials and final small Li-S cells

Several samples with different composition were prepared and tested. The electrochemical properties of composites were investigated by cyclic voltammetry (CV), electrochemical impedance spectroscopy (EIS) and galvanostatic charge/discharge measurements. Structural, stability and safety tests were also performed. The best samples were chosen and tested in small laboratory prototypes (Fig. 1). Results obtained from electrochemical characterization of final prototypes showed improved stability, performance and sustained cycle stability and low decay rate after 200 cycles.

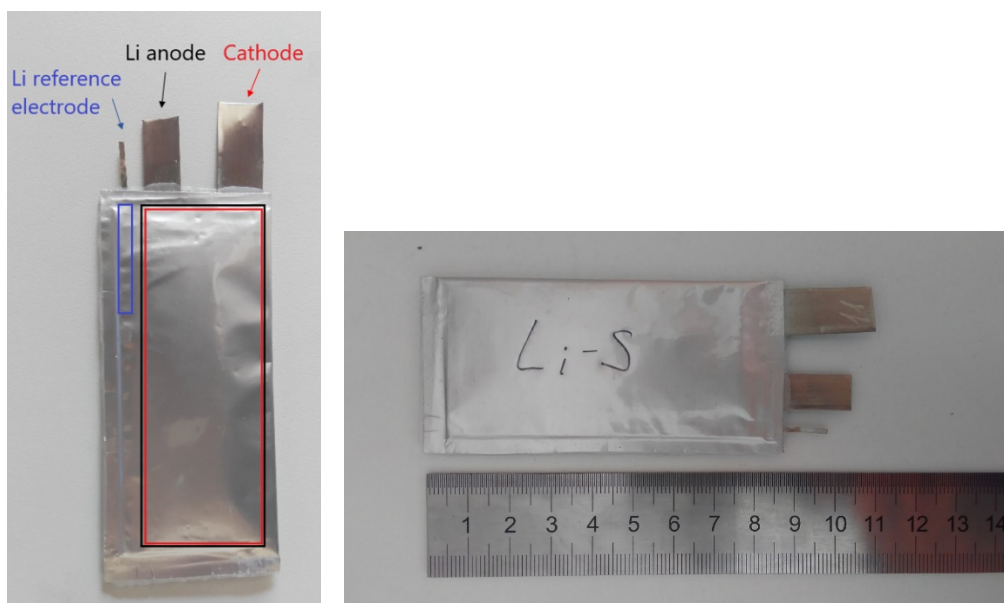


*Figure 1. Li-S laboratory prototypes prepared within NATO SPS research project.*

### Acknowledgement

This research was sponsored by the NATO Science for Peace and Security Programme under grant 985148 and by the project iCoTS ITMS No. 313011V334.

### References

1. X. Ji, L.F. Nazar, *J. Mater. Chem.*, 20 (2010) 9821.
2. D. Capkova et al., *Electrochim. Acta*, 354 (2020) 13664.

## **Inverse Vulcanization of Sulfur – Amorphous Electroactive Polymer for Li-S Batteries**

O. Čech, O. Klvač, T. Kazda, P. Čudek

Department of Electrical and Electronic Technology, Faculty of Electrical Engineering and Communication, BUT, Technická 10, 616 00 Brno, Czech Republic

Lithium-sulfur batteries have the potential to increase battery capacity while maintaining their weight and volume. This is possible due to the high theoretical energy density of sulfur. However, these batteries suffer from several failing, which still hinder practical use. Inverse vulcanization of sulfur seems to be perspective method for the preparation of polymer sulfur, because it prevents its recrystallization and stabilizes amorphous sulfur. The contribution also deals with the estimation of solubility of inversely vulcanized sulfur samples in common process solvents and solvents used in electrolytes.

### **Introduction**

Lithium-ion (Li-Ion) batteries currently dominate energy storage. However, their further development is limited by a theoretical energy density of 400 Wh / kg, which is insufficient to meet the growing demands. A potential solution is to use batteries based on a combination of lithium sulfur (Li-S), which can bring a theoretical energy density of up to 2600 Wh / kg [1]. However, the use of sulfur is problematic due to its low specific electrical conductivity of 10-30 S / cm. During the cycle, polysulfides are also formed, which cause morphological and structural changes, further reducing the effective contact and conductivity of the entire electrode [2]. Higher polysulfides are soluble, migrate through the separator electrolyte, and react irreversibly with the lithium anode. This work is focused on the preparation of materials from inversely vulcanized polymer sulfur (IVS). Current research shows that sulfur in amorphous form achieves higher cyclic stability as well as charge efficiency compared to its crystalline form [2]. The inverse vulcanization method, in which polymer sulfur is crosslinked by reaction with a crosslinking agent such as 1,3-diisopropenylbenzene (DIB), stabilizes the polymer sulfur. This prevents recrystallization, which causes problems in the further use of polymeric sulfur materials.

### **Experimental**

Copolymer material with different ratios of starting materials was prepared by the method of inverse vulcanization (IVS), developed by Griebel, Pyun and colleagues [3]. The temperature of addition of DIB to the sulfur melt proved to be a critical factor in the preparation. If the procedure of the authors of the method was followed, the samples recrystallized sulfur and formed crystalline phases in the sample, which was proved by XRD. Stable results have been achieved by modifying the preparation process, and our preparation method thus produces an amorphous polymeric material which does not recrystallize and precipitate elemental sulfur even after several years.

IVS samples with sulfur, 70, 60, 50 and 40 wt.% Were synthesized. %. In the case of sulfur 70 wt. % was not the resulting solid phase copolymer at room temperature, but was highly viscous. In the case of samples with a sulfur content of 60 wt. % and less the substance was in a glassy state

after cooling and in the long run the substance was stable in its properties. As the ratio of the input substances changed, the color shade of the resulting copolymer changed, see Figure. 1

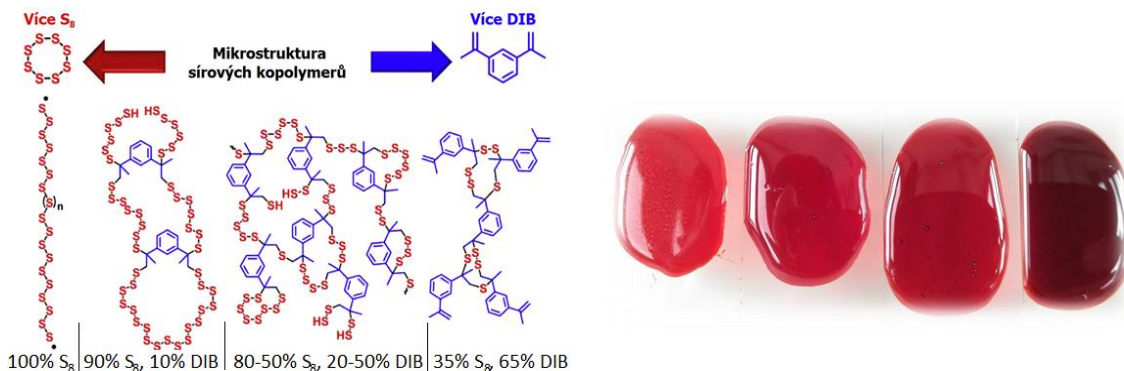


**Figure 1.** Left - IVS structure with different degrees of crosslinking using DIB. Right - IVS cast on glass with sulfur content gradually from the left 70, 60, 50 and 40 wt.

### Electrochemical characterization of electrode material

Based on the recorded results of the previous sections, a material with a ratio of elemental sulfur and DIB input precursors was chosen for the preparation of the electrode paste in the ratio 70:30 wt. %. This material was chosen for characterization because of all the samples it has the lowest solubility in electrolytes due to the lowest DIB content,

this is related to the largest theoretical capacity for the total weight of the electrode of all prepared samples. The conductivity of the selected material is also the highest of all examined, although this difference is not significant. Electrodes whose material was ground by various methods were examined.

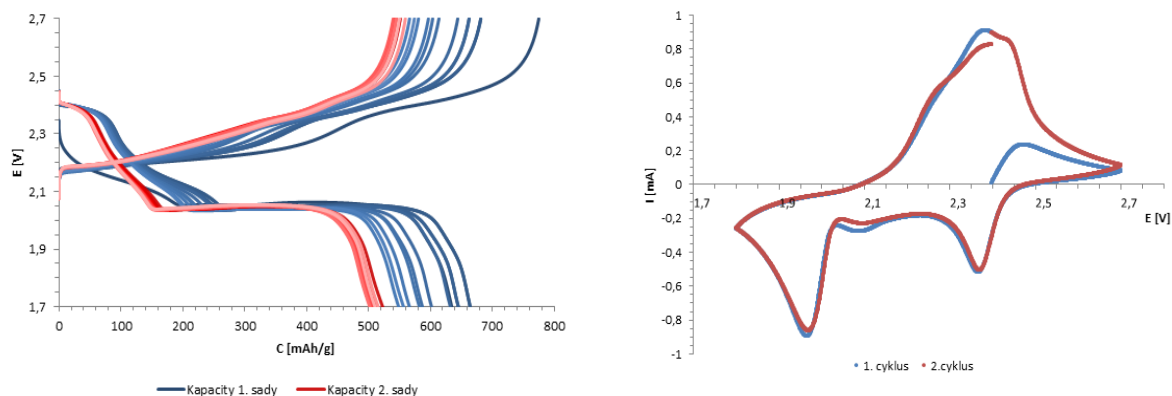


**Figure 2.** IVS charging and discharging characteristics with a sulfur content of 70% at 0.1C (left), cyclic voltammetry (right).

### Conclusion

Based on the study of known methods for the preparation of polymeric sulfur, especially the method of inverse vulcanization of sulfur using 1,3-diisopropenylbenzene, sulfurized polymeric materials with different ratios of input precursors were synthesized. These materials have great potential as electroactive materials for the positive electrodes of lithium-sulfur batteries, but this technology still suffers from a number of unresolved negative aspects, and the study of new high-

sulfur polymeric materials could contribute to their solution. An important factor in the inverse vulcanization of sulfur is the temperature at which the components are mixed, in this case the addition of the crosslinker 1,3-diisopropenylbenzene. The crosslinker must be added when the temperature of the sulfur melt reaches 159 ° C, otherwise there are problems with the miscibility of the two materials.

### Acknowledgments

This work was supported by the project of specific research: Materialy a technologie pro elektrotechniku III, reg. no. FEKT-S-17-4595. CzechNanoLab project LM2018110 funded by MEYS CR is gratefully acknowledged for the financial support of the measurements at CEITEC Nano Research Infrastructure.

### References

1. J. Doe and R. Hill, *J. Electrochem. Soc.*, **152**, H1902 (2005).
2. R. Smith, *Electrochem. Solid-State Lett.*, **10**, A1 (2007).
3. E. Gaura and R. M. Newman, *ECS Trans.*, **4**(1), 3 (2006).
4. D. Warren and J. M. Woodall, in *Semiconductor Cleaning Technology/1989*, J. Ruzyllo and R. E. White, Editors, PV 90-9, p. 371, The Electrochemical Society Proceedings Series, Pennington, NJ (1990).
5. F. P. Fehlner, *Low Temperature Oxidation: The Role of Vitrous Oxides*, p. 23, Wiley Interscience, New York (1986).
6. N. J. DiNardo, in *Metallized Plastics 1*, K. L. Mittal and J. R. Susko, Editors, p. 137, Plenum Press, New York (1989).

## Alternative Binder for Lithium-Sulfur Batteries

D. Capková<sup>a</sup>, T. Kazda<sup>b</sup>, and A. Straková Fedorková<sup>a</sup>

<sup>a</sup> Department of Physical Chemistry, Faculty of Sciences, Pavol Jozef Šafárik University in Košice, Moyzesova 11, 04154, Košice, Slovak Republic

<sup>b</sup> Department of Electrical and Electronic Technology, Faculty of Electrical Engineering and Communication, Brno University of Technology, Technická 10, 616 00, Brno, Czech Republic

Demand for clean and efficient energy storage is constantly growing due to concerns about limited global energy supply, environmental and climate change. Batteries with expected energy density values in the range of several hundred watts per kilogram are currently receiving special attention. One of the most common examples of high-energy batteries are lithium-sulfur batteries and they may replace Li-ion batteries in their applications. Sulfur has the advantages of low price, natural affluence, and compatibility with nature. However, several shortcomings of this technology need to be solved before commercialization. By using a suitable binder in the production of the positive electrodes, some of them could be repressed.

### Introduction

Sulfur as a cathode has been studied since the 1960s, but great advances in the preparation of composites that can be used commercially have been made recently. Chemistry of sulfur is different from typical intercalation materials (e.g.  $\text{LiFePO}_4$ ). Sulfur forms molecular structure consisting of eight atom ring ( $\text{S}_8$ ). The  $\text{S}_8$  ring is opened during discharging, the length of sulfur chain is shortened, and the discharge product is  $\text{Li}_2\text{S}$  (1). Elemental sulfur provides a gravimetric capacity of  $1672 \text{ mAh g}^{-1}$  though the multielectron redox conversion and the theoretical energy density of  $\sim 2600 \text{ Wh kg}^{-1}$  (2). In addition, sulfur is commonly found on the earth's surface, financially unpretentious and environmentally nontoxic (3).

However, lithium-sulfur (Li-S) battery system has some barriers that blocks the successful commercial production. Sulfur as an electrode material must overcome low electricity conductivity at the insulator level and the positive electrode must contain conductive material, which reduces the content of active material. Next drawback is the volumetric expansion during cycling which may negatively affect the electrode structure. The higher order polysulfides are soluble in the organic electrolyte, which results in significant capacity fading. The higher polysulfides diffuses to lithium anode and react with lithium ions, the product of this reaction are lower polysulfides and they irreversibly deposit on the anode surface. The process of polysulfide migration is known as the shuttle effect. The consequence of shuttle effect is loss of active material, low columbic efficiency, or rapid capacity fading (3, 4).

The binder is connecting sulfur, conductive material and current collector. The binder has a significant role on electrochemical and physical properties of the electrode. Polyvinylidene fluoride (PVDF) is the most common used binder in the lithium battery industry. Although, PVDF is soluble only in organic compounds such as N-methyl-2-pyrrolidone (NMP), which is slightly toxic and volatile. Natural binders like carrageenan are made from naturally available organic sources such as

plants. Carrageenan is a bioderived polymer from polysaccharides in seaweed and it is water-soluble binder (5).

### Experimental

The working electrode with carrageenan as a binder was prepared by slurry coating method. The slurry consisting of 60 % sulfur, 23 % Super P, 7 % Ketjen Black and 10 % carrageenan (Sulfate 29.42 %) was mixed on magnetic stirrer for 24 hours. Carrageenan was dissolved in the mixture of water and ethanol in the ratio 2:1. Dried electrodes were pressed using a pressure of 325 kg cm<sup>-2</sup>. The electrolyte in composition of DME (1,2-Dimethoxyethane):DOL (1,3-Dioxolane) 2:1 with 0.7 M LiTFSI (Lithium bis(trifluoromethanesulfonyl)imide) + 0.25 M LiNO<sub>3</sub> (Lithium nitrate) was saturated in glass fiber separator and pure lithium was used as an anode. The electrochemical test cells (El-Cell<sup>®</sup>) were assembled in argon glove box (Jacomex). The sulfur loading of the electrode with Sulfate 29.42 % was ~1.47 mg cm<sup>2</sup>.

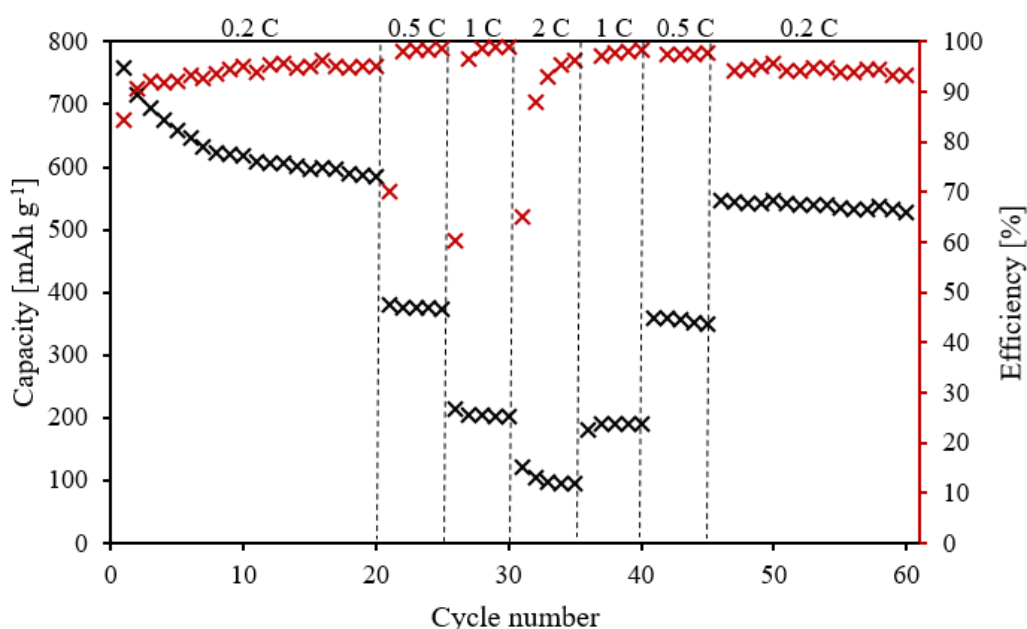


**Figure 1.** The discharge capacities and the efficiency of the electrode with carrageenan as a binder.

Galvanostatic cycling at different currents was performed (Figure 1). The initial discharge capacity of the electrode with carrageenan was 759 mAh g<sup>-1</sup> at 0.2 C. The capacity during cell cycling was decreasing faster through first five cycles, than it was stable around 600 mAh g<sup>-1</sup>. With the increase of discharge current, the electrode shows rate performances at 0.5 C, 1 C and 2 C with specific capacities of 381 mAh g<sup>-1</sup>, 214 mAh g<sup>-1</sup>, and 120 mAh g<sup>-1</sup>. After cycling at 2 C the current returns stepwise back at the same C-rates down to 0.2 C. The discharge capacity at sixtieth cycle correspond to 70 % of the initial discharge capacity. Columbic efficiency was around 96 % during the whole cycling procedure.

## Conclusions

It was demonstrated that carrageenan (Sulfate 29.42 %) can be used as a binder for positive electrodes in Li-S batteries. Carrageenan, the water-soluble binder, is natural polysaccharide that is ecofriendly, low-cost and there is not necessary to use toxic organic solution. In order to be able to use carrageenan as a common binder for Li-S batteries, it is necessary to preform additional measurements and experiments.

## Acknowledgments

This research was sponsored by the Ministry of Education, Youth and Sports of the Slovak Republic under project DSV No. 313011V334 and VEGA No. 1/0745/17. The authors gratefully acknowledge the financial support from BUT specific research program (project No. FEKT-S-20-6206).

## References

1. E. Scott, and L. F. Nazar, *Accounts of chemical research*, 46 (5), 1135-1143 (2013).
2. Z. Yuan, H.J. Peng, T.Z. Hou, J.Q. Huang, C.M. Chen, D.W. Wang, X.B. Cheng, F. Wei, and Q. Zhang, *Nano letters*, 16 (1), 519-527 (2016).
3. G. Ma, Z. Wen, M. Wu, C. Shen, Q. Wang, J. Jin, and X. Wu, *Chemical Communications*, 50 (91), 14209-14212 (2014).
4. D. Gueon, J.T. Hwang, S.B. Yang, E. Cho, K. Sohn, D.K. Yang, and J.H. Moon, *ACS nano*, 12 (1), 226-233 (2018).
5. H. Chen, M. Ling, L. Hencz, H.Y. Ling, G. Li, Z. Lin, G. Liu, and S. Zhang, *Chemical reviews*, 118 (18), 8936-8982 (2018).

## Anatase as Anode for Sodium-Ion Cells

O. Čech<sup>a</sup>, P. Benešová<sup>a</sup>, P. Čudek<sup>a</sup>, T. Kazda<sup>a</sup>

<sup>a</sup> Department of Electrical and Electronic Technology, Faculty of Electrical Engineering and Communication, Brno University of Technology, Technická 10, 616 00, Brno, Czech Republic

In the proposed work, we used conventional TiO<sub>2</sub> anatase powder consisting of submicron particles as anode material for sodium-ion cells. In our experiment, we demonstrate that this material is stable during cycling, reveals strong formation effect and we discuss the electrochemical performance and structural properties.

### Introduction

Sodium, a highly abundant element with almost inexhaustible supplies and much lower cost than lithium, is one of the candidates for use in the areas of electromobility and non-portable power storage for large-scale applications. Although the knowledge gained by studying materials for lithium-ion batteries can be assumed to some extent, there are still a number of obstacles preventing the commercial expansion of sodium-ion technology. A large number of suitable cathode materials are currently being explored, such as layered oxide structures, polyanionic compounds, etc. However, little has been found in anode materials with the desired properties and it is, therefore, necessary to continue their research. Carbon materials, especially hard carbon, and titanium dioxide TiO<sub>2</sub> materials are currently the most promising. Titanium dioxide as the anode material for sodium-ion batteries excels in price, good stability, low volumetric expansion, non-toxicity, and availability. Of the known titanium dioxide polymorphs, anatase, which can theoretically accommodate the highest amount of sodium ions, offers a working potential of 0.8V vs Na<sup>+</sup>/Na, but suffers from low electron and ionic conductivity, which is usually compensated by its nanostructuring, composite preparation or by applying surface layers, eg Al<sub>2</sub>O<sub>3</sub> [1; 2].

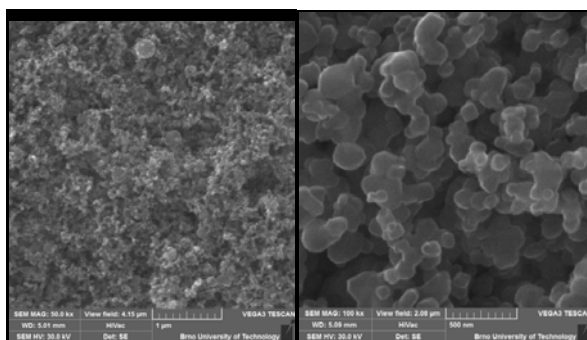
Also, the use of suitable electrolytes, which greatly affect the thickness and stability of the SEI layer, is a widely discussed topic. An article by Xu et al. compares the use of ethers-based solvents (DEGDME, DME) and carbonates (EC / DEC, EC / PC).

### Experimental

The negative electrode of the sodium ion battery was prepared by the conventional method of applying an electrode paste to the copper foil. The electroactive material studied was nanostructured anatase from Sigma-Aldrich. The electrode composite was prepared in a manner common to testing lithium-ion battery electrode materials, where anatase was mixed with Super P carbon black (Timcal) and polyvinylidene fluoride (PVDF) polymer binder, which was dissolved in N-methyl pyrrolidone (NMP). The ratio of dry components in the composite was 80% anatase, 10% Super P and 10% PVDF. The electrode paste was coated with a Spiral Bar Coater (Neurtek) on a copper foil, dried, and 18 mm disks were cut from the electrode and subsequently used in an electrochemical cell. The battery was sealed in El-Cell-Std in a glove box.

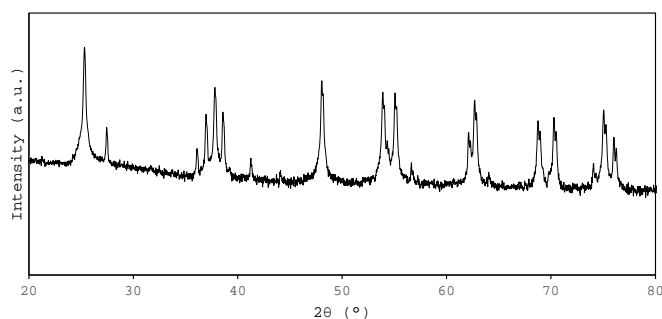
### Structural analysis

Figure 1 shows TiO<sub>2</sub> anatase images from a scanning electron microscope showing that the material consists of submicron spherical particles (dimensions in the range of 200-800 nm), but which are partially sintered and interconnected. During the mixing of the electrode paste, it was evident that the material was well dispersed, but it was unlikely that the mass was completely separated and dispersed at the submicron level.



**Figure 1.** Images of used TiO<sub>2</sub> anatase from electron scanning microscope, view field 4.15 and 2.08 μm

The X-ray diffraction spectroscopy in Figure 2 confirmed that the material obtained is pure anatase. It is a tetragonal lattice where  $a = b = 3.7842 \text{ \AA}$   $c = 9.5146 \text{ \AA}$ .



**Figure 2.** X-ray diffraction spectroscopy of TiO<sub>2</sub> anatase used for the sodium-ion battery anode. The intensity is plotted on a logarithmic scale.

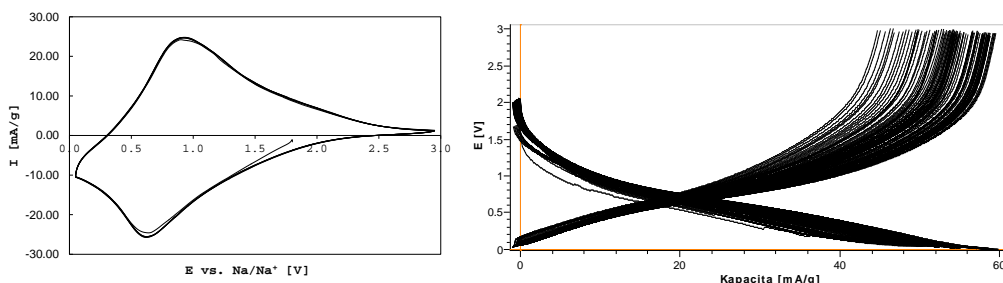


**Figure 3.** Cyclic voltammetry (left) and discharging characteristics (right) of anatase in the sodium-ion cell. Cyclic voltammetry was performed at a sweep rate of  $0.1 \text{ mV} / \text{s}$ , discharge characteristics measured by a specific current of  $0.5C$  ( $80 \text{ \mu A} / \text{cm}^2$ ).

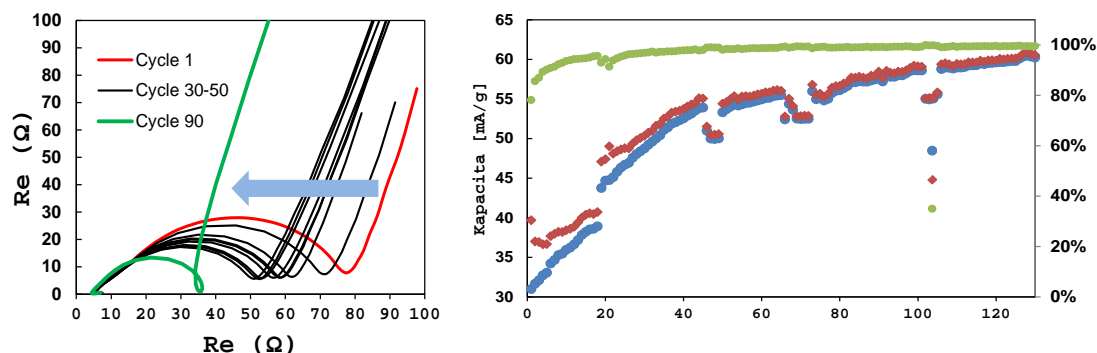


**Figure 4.** Impedance spectra measured during molding cycling (measurement every ten cycles) and the course of forming anode with anatase by galvanostatic cycling with a specific current of 0.5C.

## Results and discussion

From the measured electrochemical characteristics, it can be seen that the mechanism of the reaction of sodium with TiO<sub>2</sub>-anatase is different from the commonly mentioned intercalation in the case of lithium ions. The shape of the cyclic voltammety curve is rather pseudocapacitive in its large area and shape without a sharp transition. The impedance spectroscopy in Figure. 3, which has been inserted after each tenth cycle of galvanostatic cycling, supports the idea of phase-transition forming. The usual tendency is that, based on the formation and eventual growth of the SEI layer, the Rct resistance gradually increases. It can be seen here that with each subsequent cycle it gradually decreases, which would correspond to the fact that a new form of material is preferred for the sodium reaction by cycling. Galvanostatic cycling clearly shows how the gradual formation of a new phase leads to the formation of an electrode. At the beginning of cycling, the efficiency is approx. 80%, but very quickly reaches the threshold of 100%, while capacity grows slowly linearly. It can, therefore, be assumed that at the beginning it is the formation of an SEI layer, which is soon formed and is no longer promoted. The initial anatase specific capacity was 30 mAh / g and doubled in 130 cycles. We attribute local sinks to temperature changes in the measurement room, always a few cycles in succession, which have a lower capacity and do not match the trend.

## Acknowledgments

This work was supported by a specific research grant at BUT (No. FEKT-S-17-4595). Authors gratefully acknowledge the financial support from the Ministry of Education, Youth and Sports of the Czech Republic under project No. LTT19001, BUT specific research programme (project No. FEKT-S-17-4595).

## References

1. J. Doe and R. Hill, *J. Electrochem. Soc.*, **152**, H1902 (2005).
2. R. Smith, *Electrochem. Solid-State Lett.*, **10**, A1 (2007).
3. E. Gaura and R. M. Newman, *ECS Trans.*, **4**(1), 3 (2006).

## Xanthan gum as the Binder for the Lithium-Sulfur Batteries

K. Jaššo<sup>a</sup>, P. Čudek<sup>a</sup>, T. Kazda<sup>a</sup>

<sup>a</sup> Department of Electrical and Electronic Technology, Brno University of Technology, Technická 10, 616 00 Brno, Czech Republic

Lithium-sulfur (Li-S) batteries offer high energy density at a potentially low price and satisfying safety. However, before putting it into real operation, it is necessary to solve several problems, including the so-called shuttle effect. This shuttle effect causes a gradual degradation of capacity and thus affects battery cycle life. One of the Li-S components that can potentially affect its electrochemical properties and help solve certain problems is the binder. In recent years, many different binders have been studied in an effort to improve the electrochemical properties of the resulting Li-S cell. This paper is dedicated to the research of non-toxic water-soluble organic binder - Xanthan gum.

### Introduction

Although, Li-ion battery technology enabled the revolution of portable electronic devices, they cease to suffice with their ever-increasing demands. Ever-increasing energy demand calls for new energy storage capable of meeting the requirements of high energy density and low cost along with long cycling life. Thus, developing advanced energy storage systems is the major technological and scientific challenge of the battery industry and research.

Lithium-sulfur batteries (Li-S) are one of the most promising candidates thanks to their low cost and high theoretical energy density up to 2600 Wh kg<sup>-1</sup> (1). Typical lithium-sulfur cell consists of metallic lithium as negative electrode and elemental sulfur as positive electrode. However, due to low electrical conductivity of sulfur ( $\approx 5 \times 10^{-30}$  S cm<sup>-1</sup>), the negative electrode must be conducted by the addition of a conductive material, most often carbons (2). The volume of active material of the positive electrode is thus reduced by the conductive element and the binder, both of which contribute to the resulting electrochemical properties. According to many research papers, binders besides maintaining the structural integrity and stability of electrode, have a significant effect on the electrochemical performance of batteries (3).

The binder often used in lithium batteries is polyvinylidene fluoride (PVDF). The PVDF binder is in many cases easy to use, compatible with other cell materials and provides good results. However, the traditional PVDF binder interacts with electrode materials via weak Van der Waals forces (4). Thus, PVDF consequently lacks the necessary capabilities required by Li-S batteries, for example, to suppress changes in electrode volume. Many types of research thus focus on functional binders, which are mostly non-toxic, water-soluble, and preferable eco-friendly and low-cost. Such binders include xanthan gum, a common food additive, which is the subject of this research.

## Experimental

Two series of electrodes consisting of 60 wt % sulfur, 30 wt % carbon and 10 wt % binder were prepared. Xanthan gums from CP Kelco under the designations Xantural<sup>®</sup> 75 and Xantural<sup>®</sup> 180 were used as binders. Selected samples were subjected to elemental analysis under SEM and the remaining samples were assembled into an electrochemical measuring cell (E1-cell<sup>®</sup>) and subjected to galvanostatic cycling at various loads (C-rates).

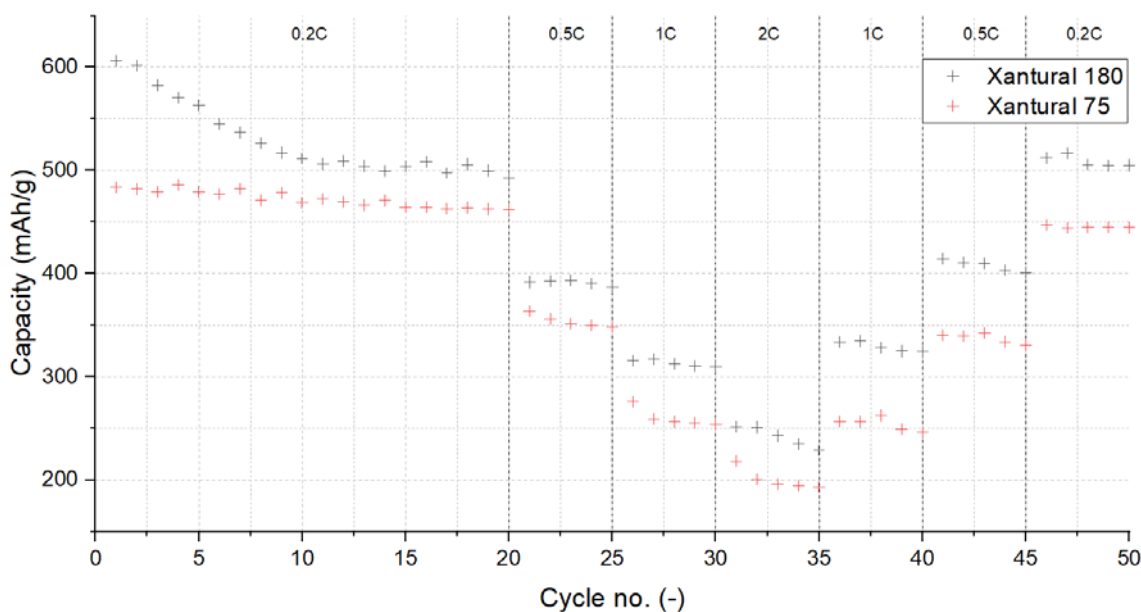


**Figure 1.** Comparison of discharge capacities of electrode samples with different binders at various C-rates.

The Figure 1. shows that the capacity of the Xantural<sup>®</sup> 180 sample in the first cycle of galvanostatic cycling is significantly higher than that of the Xantural<sup>®</sup> 75 binder sample. However, over the next 10 cycles, this capacity decreases sharply and approaches the capacities of the Xantural<sup>®</sup> 75 sample. With increasing load, the capacity of both samples decreases, while the Xantural<sup>®</sup> 180 sample behaves more stably. For a better comparison, the selected values related to the percentage decrease in capacity were plotted in the table.

**TABLE I.** Percentage-related values of the capacity decrease from the Figure 1.

| Cycles                                     | Xantural <sup>®</sup> 75<br>Capacity drop [%] | Xantural <sup>®</sup> 180<br>Capacity drop [%] |
|--|---|--|
| 1 <sup>st</sup> vs 20 <sup>th</sup> cycle  | 4,43  | 18,80  |
| 1 <sup>st</sup> vs 50 <sup>th</sup> cycle  | 8,06  | 16,77  |
| 20 <sup>th</sup> vs 50 <sup>th</sup> cycle | 3,80  | -2,51  |

The Table I. shows that the high capacity in the first cycle of Xantural<sup>®</sup> 180 was reflected in a large percentage decrease in relation to the 20<sup>th</sup> and 50<sup>th</sup> cycle, but when comparing the stable 20<sup>th</sup> cycle and the last cycle of GCPL, a capacity increase of 2.51% can be seen. Furthermore, in the case of Xantural<sup>®</sup> 75 there is a slight steady decrease in capacity below 5% during 0.2C cycling. Both electrodes thus show decent stability during the whole cycling.

## Conclusion

From the values measured so far, it can be stated that the use of Xanthan gum in Li-S batteries is possible, while the binder with the designation Xantural<sup>®</sup> 180 achieves higher capacities.

## Acknowledgments

This research work was supported by the specific graduate research of the Brno University of Technology No. FEKT-S-20-6206.

## References

1. M. Zhao, B. -Q. Li, X. -Q. Zhang, J. -Q. Huang, and Q. Zhang, *ACS Central Science*, **6**, 1095-1104 (2020).
2. T. Li et al., *Adv. Funct. Mater.*, **29** (2019).
3. J. Liu, Q. Zhang, and Y. -K. Sun, *J. Power Sources*, **396**, 19-32 (2018).
4. J. -T. Li et al., *Adv. Energy Mater.*, **7** (2017)

## Enhancing of electrochemical characteristics of Li-S system by means of optimization of sulfur electrode and electrolyte composition

N. I. Globa, V. A. Sirosh, Yu. V. Shmatok, S. A. Kirillov

Joint Department of Electrochemical Energy Systems,

38A Vernadsky Ave., 03680 Kyiv, Ukraine

The paper discusses the effect of the sulfur electrode and TEGDME – LiTFSI salt-solvate electrolyte composition on electrochemical characteristics of Li-S cells at different cycling conditions.

### Introduction

It is known that the main electrochemical processes in lithium-sulfur battery are associated with the formation of polysulfides, whose solubility is determined by the length of polysulfide chain  $\text{Li}_x\text{S}_y$  [1, 2]. Therefore, the electrochemical behavior of sulfur electrode in lithium current sources significantly depends on the electrolyte composition, nature and concentration of carbon conductive additive and electrode manufacturing method. Optimization of the listed parameters brings researchers closer to the realization of high and stable specific capacity during the cycling of the Li-S electrode system in a wide temperature range and allows for reducing the self-discharge level during storage.

The specific capacity of sulfur electrodes during cycling is limited, on the one hand, by a decrease in the sulfur content as a result of the dissolution of polysulfides and, on the other hand, by an increase in the cell resistance as a result of the formation of poorly soluble  $\text{Li}_2\text{S}_2$  and  $\text{Li}_2\text{S}$ . In addition, passing into the electrolyte polysulfides passivate the lithium anode, negatively affecting the overall resistance of the current source. These negative processes can be controlled, in particular, by optimal selection of the electrolyte composition and electrode structure. The composition and nature of carbon additives in turn provide the conductivity of the electrode structure that is extremely necessary in view of the low electrical conductivity of sulfur and contributes to the uniform distribution of polysulfides in the electrode structure.

The paper discusses the results of galvanostatic cycling of sulfur electrode depending on the composition of cathode and TEGDME – LiTFSI salt-solvate electrolytes composition at the room and elevated temperature conditions.

### Experimental

Sulfur electrodes were manufactured from elemental sulfur powder (S) with particle size of  $<150\ \mu\text{m}$ , graphite and carbon black Super P (Timcal, Switzerland) as conducting additives and a polyvinylidene difluoride binder (PVdF, Solef 6020) taken in percentage of 50:17.5:17.5:15 for composition 1 and 70:10:10:10 for composition 2. Slurry was applied to an aluminum foil ( $50\ \mu\text{m}$ ) using a doctor blade. The sulfur mass was  $\sim 2.5\ \text{mg}/\text{cm}^2$  for composition 1 and  $\sim 3\ \text{mg}/\text{cm}^2$  for composition 2. The tests were carried out in 2016 coin cells with a lithium metal counter electrode and a double layer of separators PORP-A (Ufim, Russia) and TF 4030 (Nippon Kodashi, Japan). Salt-solvate electrolytes were prepared using tetraethylene glycol dimethyl ether (TEGDME,

Aldrich, 99%) as a solvent and lithium bis(trifluoromethane)sulfonimide (LiTFSI, Aldrich, 99%) as a salt. The salt concentration was 0.4, 0.33 and 0.25 molar fractions (m. f.). All works were carried out in glove boxes with dry atmosphere. Electrochemical tests were performed on a BTS-3000 multichannel cycling system (Neware, China) in the temperature range of 25÷40 °C.

## Results and Discussion

Salt-solvate electrolytes can be considered as one of the means to optimize the operation of the lithium-sulfur system under cycling conditions. Salt-solvate electrolytes based on TEGDME – LiTFSI solutions have low glass transition temperatures that provide their high electrical conductivity, thermal and electrochemical stability in a wide temperature range. The high solubility of LiTFSI in TEGDME makes it possible to obtain electrolytes with a wide range of salt concentrations (up to 0.5 m. f.) and thus to regulate the dissociation-associative properties in the TEGDME – LiTFSI–Li<sub>x</sub>S<sub>y</sub> systems by changing the Li<sub>x</sub>S<sub>y</sub> solubility.

Figure 1 shows the dependences of specific capacity on cycle number for sulfur electrodes in salt-solvate electrolytes of different composition.

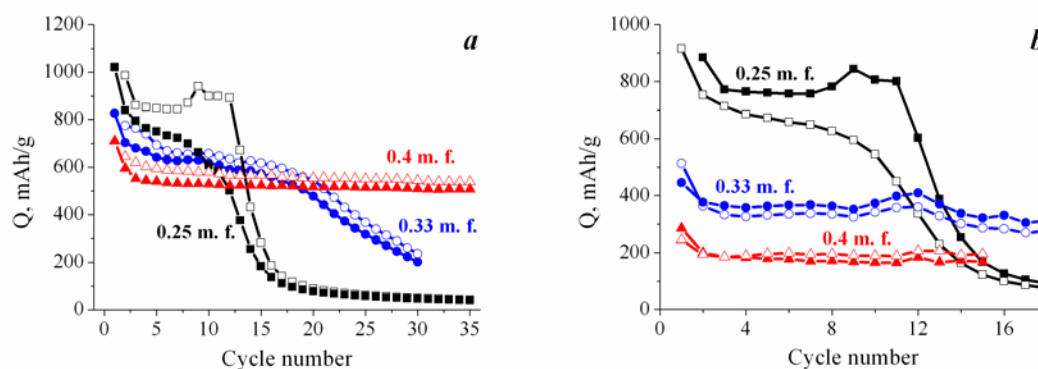


**Figure 1.** Dependences of specific capacity on cycle number for sulfur electrodes of composition 1 (a) and composition 2 (b) in salt-solvate electrolytes TEGDME – LiTFSI.  $I_{ch}=I_{dch}=100 \mu A/cm^2$ .  $U=1.5\div 2.8$  V. Operating temperature – 25°C.

It is important to note the high values of coulombic efficiency of charge-discharge processes obtained in salt-solvate electrolytes. The coulombic efficiency increases with increasing of the salt concentration and reaches its maximum value of ~90% in the case of LiTFSI concentration of 0.4 m. f. The maximum effect of the carbon additive content on specific capacity is manifested in more concentrated salt-solvates. Thus, a decrease in the total content of conductive additives from 35% to 20% leads to a change in the specific capacity from 600 mAh/g to 190 mAh/g at 25°C. The specific capacity of the sulfur electrode becomes less dependent on the cathode composition with an increase in the operation temperature up to 40°C.

It is found that the loss of specific capacity of the cells with TEGDME – 0.4 m. f. LiTFSI electrolyte during the storage at the room temperature conditions for 576 hours is ~38% (for electrode composition 1) and is restored by more than 90% with further cycling. In the case of electrode composition 2, the specific capacity is restored by about 94% after storage for 650 hours.

### References

1. X. Fan, W. Sun, F. Meng, A. Xing and J. Liu, *Green Energy Environ.*, **3**(1), 2 (2018).
2. F. Li, Q. Liu, J. Hu, Y. Feng, P. He and J. Ma, *Nanoscale*, **11**(33), 15418 (2019).

## Intercalation Properties of Expanded Graphite Electrode in Lithium-Ion Battery

J. Libich<sup>a</sup>, M. Sedlaříková<sup>a</sup>, J. Mácá<sup>a</sup>, P. Čudek<sup>a</sup>, M. Fíbek<sup>a</sup>, A. Chekannikov<sup>b</sup> and G. Fafilek<sup>c</sup>

<sup>a</sup>Department of Electrical and Electronic Technology, FEEC, Brno University of Technology, 616 00 Brno, Czech Republic

<sup>b</sup>Moscow Institute of Physics and Technology, 9 Institutskiy per., Dolgoprudny, Moscow, 141701, Russian Federation

<sup>c</sup>Vienna University of Technology, Getreidemarkt 9, 1060 Vienna, Austria

The energy storage become one of most important a strategic area in context of sustainable development of human society. With last two decades, the electrochemical energy storage devices (batteries), got crucial role. The current trend led by electromobility, renewable energy resources set new level of requirements on battery parameters. Since 1991 when the first commercial lithium-ion battery was produced, this battery technology developed to the most advanced battery technology on the market. Lithium-ion batteries found application in wide range of devices from small portable electronic devices, via electric vehicles up to huge stationary energy storage systems. Important parameter of the battery it is the rate capability parameter. The current generation which occurs in the battery during charging-discharging cycle is directly proportional to rate of reactions. And the reaction rate depends on diffusion rate. In this work the diffusion rate expressed by chemical diffusion coefficient is measured and evaluated.

### Introduction

Lithium-ion batteries are the most advanced battery technology of the present time. The lithium-ion batteries possess highest gravimetric and volumetric energy density among all types of batteries. Lithium-ion batteries have a long list of applications, there are not used only for powering small portable electronic device. The range of their application varies from life-saving medical equipments, via electric vehicles, boats, bikes to remote off or on the grid stationary energy storages with capacity in order of MWh. This broad range of applications brings new range of demands like safety, cycle lifespan or peak power. Thanks to continuous research in the field of lithium-ion batteries, the lithium-ion batteries reached significant improvement in many parameters.

One of the most important parameter, especially in power applications such as electric vehicles, is the power density or just peak power crucial parameter. This parameter describes the ability of the battery cell provide current without increasing internal resistance, in different words as much the battery cells acts like ideal current source. An ideal current source produces a known current independent of load.

The lithium-ion battery technology operates in “rocking chair scheme” i.e. lithium ions moving cross the cell via electrolyte from negative electrode to positive electrode and vice versa. Electrode materials in lithium-ion batteries working on insertion or intercalation principle, lithium ions and atoms enter to the bulk of active electrode material. This process is called “solid state

diffusion” and it is the slowest process (thus determining the speed of the reaction) during charging and discharging. This process controls the amount of the current produced by the cell.

In lithium-ion batteries, the negative electrode (anode) is made from graphite, graphite have layer sheet structure as is depicted in Fig. 1. The research of graphite intercalation properties expressed by chemical diffusion coefficient is the main goal of our work [1 – 6].

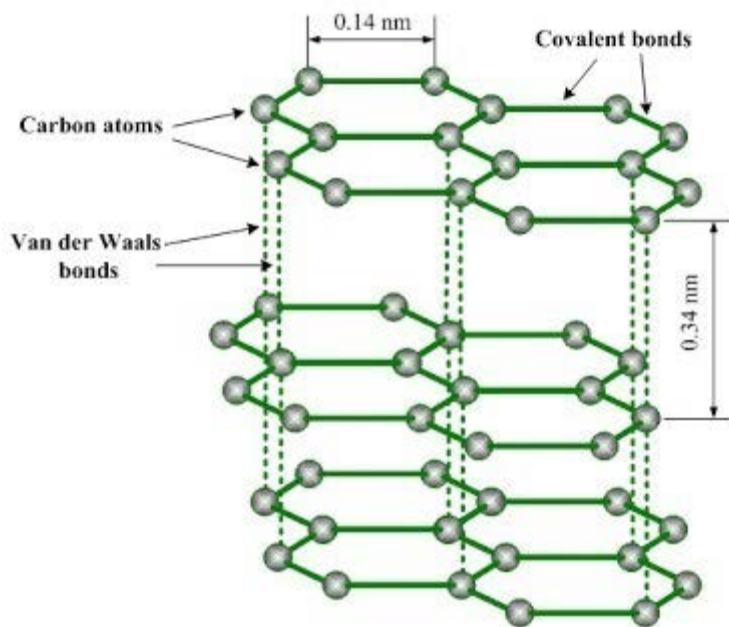


**Figure 1.** Layered structure of the graphite [1].

### Acknowledgments

This work was supported by specific graduate research project of the Brno University of Technology: Materialy a technologie pro elektrotechniku IV., reg. no. FEKT-S-20-6206.

### References

1. N. Kuwata, X. Lu, T. Miyazaki, Y. Iwai, T. Tanabe, and J. Kawamura, *Solid State Ionics*, vol. **294**, pp. 59-66, (2016).
2. N. Kuwata, M. Nakane, T. Miyazaki, K. Mitsuishi, and J. Kawamura, *Solid State Ionics*, vol. **320**, pp. 266-271, (2018).
3. J. T. Sliwinski, N. Kueter, F. Marxer, P. Ulmer, M. Guillong, and O. Bachmann, *Chemical Geology*, vol. **501**, pp. 1-11,(2018).
4. N. Kuganathan, A. Kordatos, M. E. Fitzpatrick, R. V. Vovk, and A. Chroneos, *Solid State Ionics*, vol. **327**, pp. 93-98, (2018).
5. X. Zhou, J. Huang, Z. Pan, and M. Ouyang, *Journal of Power Sources*, vol. **426**, pp. 216-222, (2019).
6. E. Barsoukov, J. H. Kim, C. O. Yoon, and H. Lee, *Journal of Power Sources*, vol. **83**, no. 1-2, pp. 61-70, (1999).

## **Polymer Structure of Sulfur Ensures Low Self Discharge of Li-S Primary and Secondary Batteries. Synergistic Effect of Sulfur Structure and Design of Sulfur Electrode**

Y. Polishchuk<sup>a</sup>, E. Shembel<sup>a,b</sup>, A. Straková Fedorková<sup>c</sup>

<sup>a</sup> Scientific Research Laboratory of Chemical Power Sources of Ukrainian State University of Chemical Technology, Dnipro, 49005, Ukraine

<sup>b</sup> Enerize Corporation, Coral Springs, FL, 33067, USA

<sup>c</sup> Pavol Jozef Safarik University, Košice, SK-04154, Slovak Republic

Dynamics of change in impedance spectra and electrochemical parameters of the Li-S rechargeable batteries with non-aqueous liquid electrolyte 0.7 M LiIm, 0.25 M LiNO<sub>3</sub>, DME: DOL (2:1) during storage after assembly and cycling have been shown. Our investigations confirm that the performance of Li-S batteries is heavily dependent on the electrode technology and design, some constructive materials like current collector.

### **Introduction**

Lithium-sulfur (Li-S) batteries offer a theoretical specific energy of 2500 Wh/kg (or 2800Wh/l) and a specific capacity of 1675Ah/kg of sulfur based on the complete reduction from elemental sulfur to lithium sulfide Li<sub>2</sub>S. The advantage of lithium-sulfur batteries: high capacity and high energy density up to 500 Wh/kg, low price, environmental compatibility. One of the biggest problems of the sulfur cathode is self-discharge due to the formation of polysulfides. This problem can be avoided by different ways: use of electrolyte with composition in which sulfur is insoluble; use of S polymorphs and sulfur-based materials (for example, doped carbon-sulfur composites or conductive organosulfur composites); use of special electrodes design.

In this work, two approaches have been used: insoluble  $\mu$ -S polymorph with a specific polymer structure as active material and special design of positive electrode including porous carbons membrane witch can effectively decrease the resistance of sulfur cathodes. The carbon micropores interlayer with used in this investigations facilitates the absorption of soluble polysulfides shuttling in the electrolyte and makes them available to be reutilized during cycling.

### **Experimental**

The positive electrodes have been fabricated by slurry coating. As the current collector has been used the aluminum foil with modification by fusion of graphite into aluminum [1]. Disk electrodes based on sulfur have the following parameters: d – 1.6 cm, working surface – 2.0 cm<sup>2</sup>. Cathode mass has the following composition: Sulfur - 75% wt.; Carbon black- 10% wt.; Graphite with high conductivity - 10%; PVdF (6020/1001, Solef) - 5% wt. The drying of the cathode was under at 60 °C for 6 h under vacuum and 2 h at 120°C without vacuum.

We used two type of sulfur: polymeric insoluble sulfur Crystex (TM) HD OT 20 “washed” in acetone [2] and natural elemental sulfur.

The cells with coin 2325 design have been used for testing. All procedures were carried out in an Ar-filled glove box. The negative electrodes were made of lithium foil. The microporous polypropylene Celgard@2300 with a thickness of 25 mkm was used as the separator. Electrolyte composition: 0.7M bis(tri fluoromethanesulfone)imide (LiIm), 0.25M LiNO<sub>3</sub>, DME: DOL (2:1).

The following measurements was used: Impedance spectroscopy and galvanostatic cycling Li-S batteries. Impedance spectra were obtained using VoltaLab PGZ 301 analytical radiometer. The frequency range 100 MHz was 100 kHz. Galvanostatic cycling was performed in the range of potentials from 1.8 – to 2.7 B. Charge current were 0.1 mA, discharge current – 0.1-0.3 mA. The measurements have been conducted at the temperature of 25 °C.

## Results

At the first stage of research, a party of Li-S coin cell was produced and some of them were stored for a long time at a temperature of 25±2 °C.

The hodographs of fresh Li batteries with natural S-based electrodes have one semicircle (Fig. 1a). The data for one party of elements have satisfactory reproducibility. The resistance values after a day of storage increase slightly (Fig.1b).

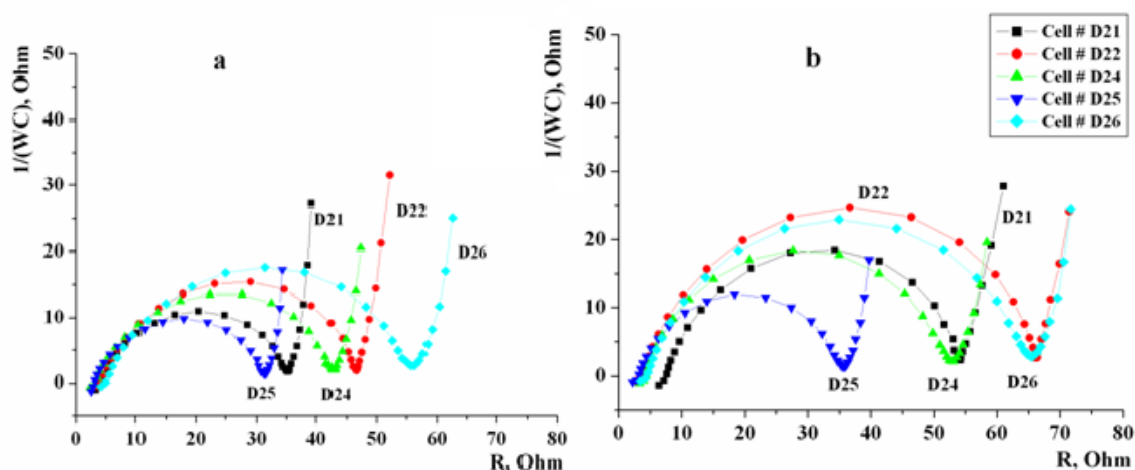


**Figure 1.** Impedance spectra of Li-S cells: a – fresh cell; b – 1 day storage. The cathode contains 75% natural sulfur. Electrode area 2 cm<sup>2</sup>. Electrolyte: 0,7M LiIm, 0,25M LiNO<sub>3</sub>, DME:DOL (2:1). Cell contain of carbon membrane on electrode.

Our results show that a significant OCV change occurs within the first five days of storage. OCV decrease approximately on 0.8-0.9V as compared with the initial value for all cells and after located at a value of 2.4 V up to 80 days.

Fig. 2 shows changes of impedance spectra of D 26 cell during 76 days of storage.

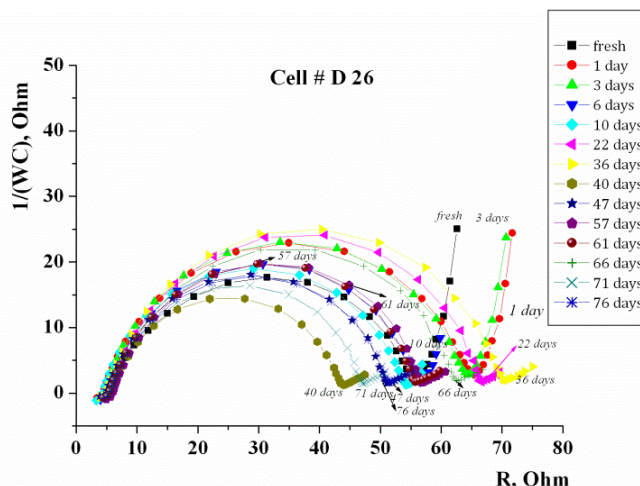


**Figure 2.** Impedance spectra of Li-S cells # D26 during storage. The cathode contains 75% natural sulfur. Electrode area  $2 \text{ cm}^2$ . Electrolyte:  $0,7M \text{ LiIm}$ ,  $0,25M \text{ LiNO}_3$ , DME:DOL (2:1). Cell contain of carbon membrane on electrode.

A slight increase in resistance is observed for forty days, after which the impedance hodograph decreases. This character of changes is observed for all elements. It is known that the properties of films that form both on the cathode and anode change during storage. This is due to the staged mechanism of their formation.

Below the figure 3 shows results of galvanostatic cycling of D 21-D26 elements. The storage time after which the elements were put for testing is indicated in the caption below.

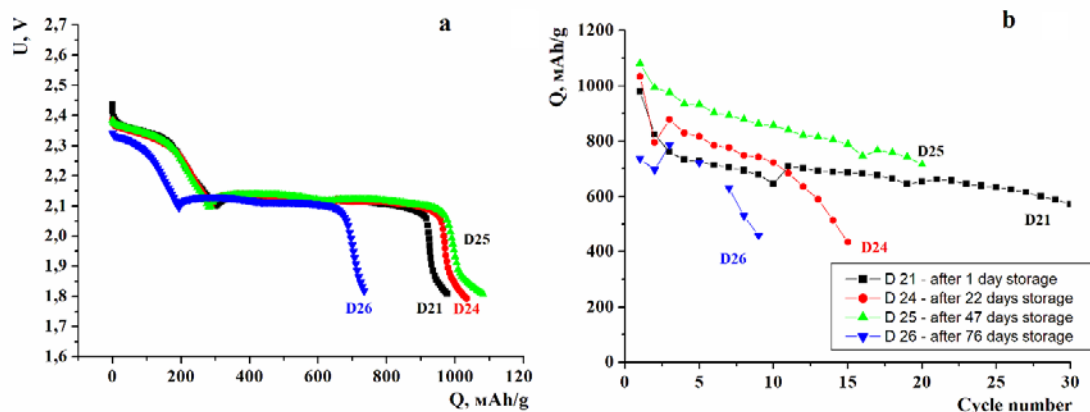


**Figure 3.** Change of 1<sup>st</sup> specific discharge capacity (a) and during cycling (b) for Li-S cell. Electrolyte:  $0,7M \text{ LiIm}$ ,  $0,25M \text{ LiNO}_3$ , DME: DOL (2:1). Natural sulfur content in cathode is 75%. Discharge current –  $0,3 \text{ mA}$ ; charge current –  $0,1 \text{ mA}$ .

Cells with natural sulfur are characterized by low values of the specific capacity. There is no critical drop in capacity in the first cycles, but during cycling it decreases.

Higher and more stable parameters were obtained for batteries with polymer sulfur (Fig. 4a). For the first five cycles, the capacity decreases from 1800 to about 1000 mAh/g and stabilizes at this value.

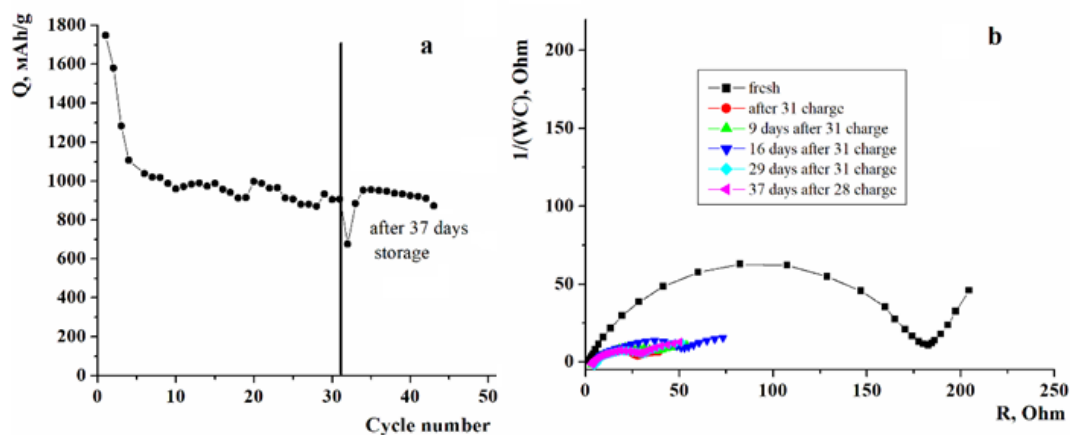


**Figure 4.** Change of specific discharge capacity (a) after 37 days storage and impedance spectra (b) during storage for Li-S cell. Electrolyte: 0.7M LiIm, 0.25M LiNO<sub>3</sub>, DME: DOL (2:1). Polymer sulfur content in cathode is 75%. Discharge current – 0.1 mA; charge current – 0.1 mA.

After 31 charges, the cell was disconnected and stored at  $25 \pm 2$  °C. During storage, the impedance spectra were recorded (Fig. 4b). Even after 37 days of storage in a charged state, the battery has high specific capacity values at the level 900-1000 mAh/g.

The complex of studies allows us to conclude that the structural features and physical parameters of sulfur with a polymer structure and the use of a special electrode design make it possible: – to significantly stabilize the discharge capacity of lithium-sulfur batteries during cycling; – keep a high charge of a battery in a charged state after a long cycling.

### Acknowledgments

This investigations have been carried out in cooperation the Ukrainian State University of Chemical Technology, Scientific Research Laboratory of Chemical Power Sources of and Enerize Corporation, USA. Technologies and materials that are presented in this article are developed also under framework of NATO SPS 985148 project “Development of New Cathodes for Stable and Safer Lithium-Sulfur Batteries”.

### References

1. V. Redko, E. Shembel, T. Pastushkin, A. Markevych, A. Straková Fedorková, O. Girin, O. Kolomoyets and Yu. Polishchuk. *ECS Transactions*, **87** (1), 275 (2018).
2. Yu. Polishchuk, E. Shembel, A. Straková Fedorková, V. Redko, N. Zaderey, T. Vergun and E. Zaginayko, *ECS Transactions*, **95** (1), 27 (2019).

## **Development of recycling of photovoltaic systems from the point of view of prolonging the total service life of photovoltaic modules and circular energy**

P. Maule, J. Vanek and K. Jandova

Faculty of Electrical Engineering and Communication, Brno University of Technology, Technická  
10, 612 00 Brno

The work set itself the task of analyzing and evaluating the extension of the overall service life of photovoltaic systems in relation to the need for quality recycling or the possibility of secondary reuse. Although today all components of photovoltaic systems are not balanced in terms of expected life, the future goal of designers of these systems will be to create a comprehensive long-life system, including hybrid inverters and batteries. Today's measurement results showed that the expected service life of the modules has been extended from the original 20 years to the current 30-35 years. The main increase in time and volume of recycling is postponed at least until the period from 2045 to 2050. This is matched by a number of gradually declining patents and new technologies for the processing of obsolete photovoltaic modules, including newly launched pilot projects focused on recycling.

### **Introduction**

Sales of photovoltaic modules worldwide are constantly growing every year. Defined product lifetimes are moving from the historical 20 years to the 30-year boundaries (McDonald, 2010) according to Figure 1. The actual service life of photovoltaic systems is significantly longer than that of most consumer goods sold, and the utility properties serve many generations. Based on personal evaluation from the data provided on selected German roof installations 20-25 years after the installation date, it was found that at this time photovoltaic modules achieve a decrease in efficiency of about 8%, in accordance with the findings of Hylský, who after 20 years came to a conclusion in the article on the decrease of production (efficiency) by 6-8% (Hylský, 2015) in Fig. 2

At the end of 2019, the total worldwide installed capacity of photovoltaic power plants was 635 GW. The number of countries with more than 1 GW per year increased in 2019 to 18 countries. The use of local battery storage systems on solar farms as well as decentralized photovoltaic power generation systems has increased again due to declining initial costs for electricity storage systems. Therefore, the working lives (Hylský, 2015) will, with a few exceptions (defective production batches, initial and subsequent assembly errors, use of thin glass for mountain areas, etc.), usually reach 40 years or more, it is necessary these days to deal with new pilot projects and experiments in the field of future recycling, as shown in Figure 3.

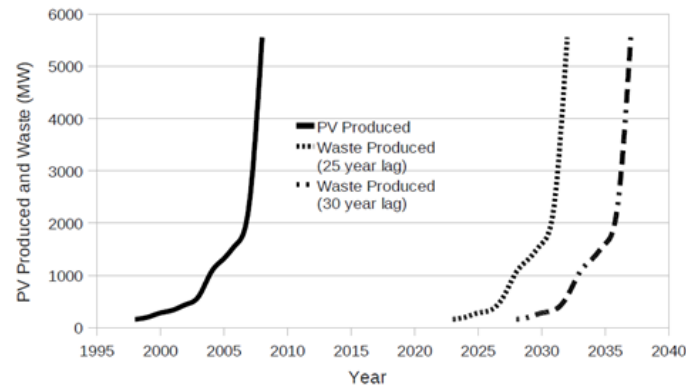


**Figure 1.** Time course of the expected recycling time from the year 2010 [1]

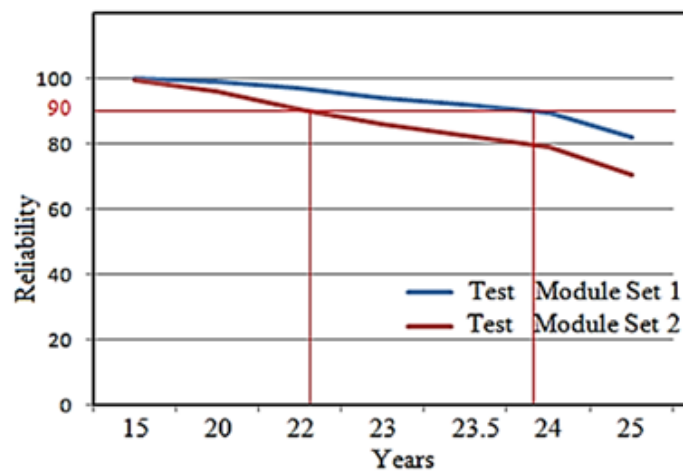


**Figure 2.** Simulation of performance and reliability of tested modules [2]

The topicality of continuation of recycling and secondary use is confirmed by the fact that since the production of the first silicon cells at Bell Labs in 1954, it took almost 58 years for the cumulative installed capacity of photovoltaics to reach 100 GW. It took only five years from 2012 to reach another 100 GW in 2017 and to reach almost 120 GW in 2019 (JÄGER-WALDAU, 2020).

The types of new technologies, their number and places of origin are very well recognizable from the total number of registered and newly patented technological solutions. From the time evolution of the number of newly registered patents for silicon recycling technologies in Figure 3, 2011 was the historic year, which recorded a record of 24 new patents announced by China. The total highest cumulative number of patents was achieved by China with a cumulative value of 48% of the total number. It is followed by Korea with 16% and closely followed by Japan with 15%.

The development of the number of recycling patents today is mostly related to the location of the production of photovoltaic modules, less rarely related to the location of the installed modules, as might be expected. However, this is not a good signal for the recycling economy, as it is the countries with the largest increase in annual installed or cumulative installed capacity that should have many reasons why recycling should take place in their country, with minimal storage, relocation, transport and possible rough, mechanical sorting.

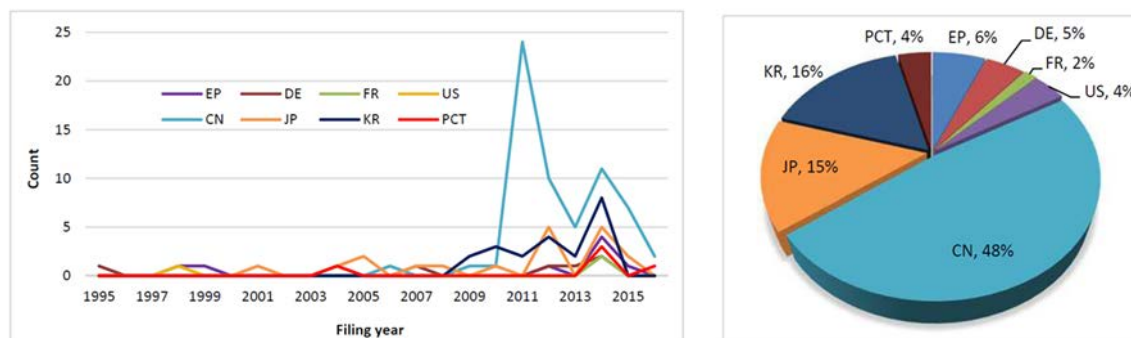


**Figure 3.** Development of the number of patents in years (left) and the cumulative number of patents by country (1995-2016) for silicon modules [4]

We distinguish two basic approaches - destructive and non-destructive. In the case of destructive methods, the recycling object is exposed to temperature, pressure, radiation, gases or liquids, which aim to determine the current state of the semiconductor structure and irreversible damage to the structure occurs. It is therefore always necessary to economically sacrifice a few selected samples to determine the exact state of the modules. In the case of recycling a large number of modules (large-scale recycling), the loss of selected samples is negligible, and therefore it is not suitable for recycling a smaller number of modules. In the case of recycling a small number of modules, non-destructive methods of determining the condition of the structure are usually used.

### Acknowledgments

This work financial support for a specific research project at the Brno University of Technology. FEKT-S-20-6206.

### References

1. MCDONALD, N.C. a J.M. PEARCE, 2010. Producer responsibility and recycling solar photovoltaic modules. *Energy Policy* [online]. 38(11), 7041-7047 [cit. 2020-04-18]. DOI: 10.1016/j.enpol.2010.07.023. ISSN 03014215. Available at: <https://linkinghub.elsevier.com/retrieve/pii/S0301421510005537>
2. HYLISKY, J., D. STRACHALA a J. VAN K, 2015. Analysis of Photovoltaic Modules after 20 Years in Service. *ECS Transactions*. 70(1), 229-237. DOI: 10.1149/07001.0229ecst. ISSN 1938-6737. Also available at: <https://iopscience.iop.org/article/10.1149/07001.0229ecst>
3. JÄGER-WALDAU, Arnulf, 2020. Snapshot of Photovoltaics—February 2020. *Energies*. 13(4). DOI: 10.3390/en13040930. ISSN 1996-1073. Also available at: <https://www.mdpi.com/1996-1073/13/4/930>
4. KOMOTO, Keiichi a Jin-Seok LEE, 2018. End-of-Life Management of Photovoltaic Panels: Trends in PV Module Recycling Technologies [online]. January 2018. IEA PVPS [cit. 2020-05-23]. ISBN 978-3-906042-61-9
5. MIKOŠKA, J., 2020, Pokračovalo odstraňování následků bouřky [online]. July 2020. HZS JmK. <https://www.hzscr.cz/clanek/pokracovalo-odstranovani-nasledku-bourky.aspx>

## Real-measured properties of photovoltaic modules

J. Vanek<sup>a</sup>, M. Svrcek<sup>a</sup>, and B. Lima<sup>b</sup>,

<sup>a</sup> Fakulta elektrotechniky a komunikačních technologií, Vysoké učení technické v Brně, Technická 10, 612 00 Brno

<sup>b</sup> Universidade Federal da Bahia, Brasil

The work deals with the comparison of measured parameters of photovoltaic modules of various current manufacturers with the data given in the catalog sheets. These data are compared with data obtained in the past from a similar measurement with a focus on comparing these data with respect to the continent where these modules were manufactured.

### Introduction

When deciding on the selection of suitable photovoltaic modules for the solar system, the price and then the power that we can get is probably in the first place. At the same time, the quality of the modules, the availability on the market, the chosen material and the related efficiency are looked at, and information about the manufacturer is also in a significant place. As it is known, what guarantee it provides and what is the experience with its modules. For someone, the information about the area of production of photovoltaic modules is also important. Whether they were made in factories in Europe, Asia or America. The myth has long been that modules made in Asia are usually of poor quality and do not have the required parameters. This myth was tried in 2009 to be refuted or confirmed by the German institute TUV Rheinland, which carried out an extensive comparison of modules from Asian and European manufacturers.

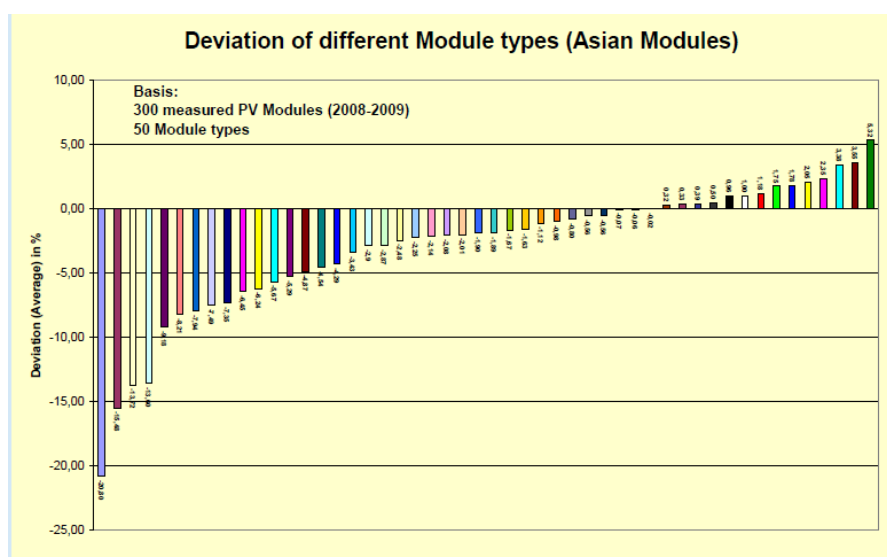


**Figure 1.** Power output measurement of PV modules at TUV Rheinland 2008-2009 - modules manufactured by Asian manufacturers. (1)

As can be seen from Figures 1 and 2, in both areas there are manufacturers who cheat customers and sell modules with worse parameters than stated, but also manufacturers who sell modules with better parameters than indicated in the catalog sheets.

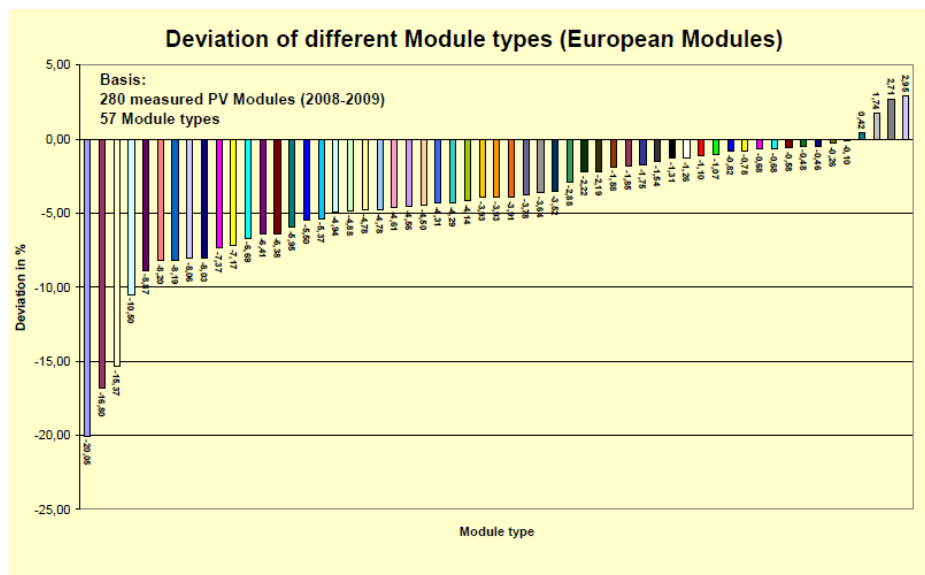


**Figure 2.** Power output measurement of PV modules at TUV Rheinland 2008-2009 - modules manufactured by European manufacturers. (1)

However, from the point of view of statistics, it was more probable that unfortunately in the years 2008-2009 you were cheated by European producers than by Asian ones. Of the European manufacturers of the 57 modules tested, there were only 4 modules with better parameters, while for Asian manufacturers it was 14 of 50. Under a tolerance of 5% lower actual performance than stated, 16 modules were found in Europe and 13 in Asia. 4 modules as 10% and one module worse than 20% was found.

## Experiment

A similar evaluation of the modules, which were delivered to the Czech Republic in the years 2018-2019, this is exactly ten years after the experiment in German institute, took place in the Brno Photovoltaic Laboratory. A total of seventeen modules were obtained from various manufacturers, representing both Asian and European, as well as one whose factories is in Latin America. The PASAN SunSim 3c device with a class A+ solar flash simulator was used for the measurement (The solar simulator has all parameters, which are defined by the standard IEC 60904-9: 2007-10 Ed2.0 "Solar simulator performance requirements", and which sorts the simulators according to their properties into classes A, B and C, twice as good as the definition of class A.), in STC mode with an accredited power tolerance of  $\pm 3.6\%$ . Prior to the measurement itself, an additional calibration of the device was performed to maximally specify the measurement uncertainty. Each module was acclimatized for a long enough time in the laboratory to stabilize at the required temperature and was subsequently measured under STC conditions after insertion into the system (radiation intensity  $1000\text{W} / \text{m}^2$  with vertical impact, panel temperature  $25^\circ\text{C}$ , light spectrum  $\text{AM} = 1,5$ ).

This was followed by an analysis of the results, which focused on comparing the measured values with the values given by the manufacturers in the catalog sheets. To refute or confirm the myth that modules made in Asia are of poor quality and do not have the required properties, information was found on the location of the modules. The obtained results can be seen in Table 1.

**Table 1:** Measured values of tested modules at STC

|                        |          |          |          |          |          |          |          |          |          |
|------------------------|----------|----------|----------|----------|----------|----------|----------|----------|----------|
| PV Module no.          | 1        | 2        | 3        | 4        | 5        | 6        | 7        | 8        | 9        |
| Area of manufacturing  | APAC     | EU       | APAC     | APAC     | APAC     | APAC     | EU       | EU       | APAC     |
| Catalog value [W]      | 280      | 240      | 280      | 325      | 300      | 330      | 290      | 280      | 310      |
| Toleration             | +5/0 [W] | +3/0 [%] | +5/0 [W] |
| Measured value [W]     | 274,569  | 231,796  | 265,804  | 327,287  | 298,869  | 309,769  | 269,197  | 278,083  | 304,630  |
| PV Module no.          | 10       | 11       | 12       | 13       | 14       | 15       | 16       | 17       |          |
| Area of manufacturing  | APAC     | APAC     | APAC     | EU       | LAM      | APAC     | APAC     | APAC     |          |
| Katalogový hodnota [W] | 340      | 320      | 340      | 280      | 400      | 270      | 275      | 310      |          |
| Toleration             | +5/0 [W] | +3/0 [%] | +5/0 [W] |          |
| Measured value [W]     | 329,001  | 314,454  | 337,967  | 269,499  | 358,376  | 270,093  | 274,623  | 302,958  |          |

## Conclusion

Our experiment also confirmed that the best modules come again from Asian manufacturers. We may even find that the modules are better than the manufacturer states. On the other hand, according to the manufacturers' catalog sheets, a positive power tolerance of 0 - 3% or 0 - 5 Wp was guaranteed for at least three-quarters of the modules we measured, which was only confirmed for two modules. Modules from European Union manufacturers came in second, where we have already measured a larger deviation than for modules from Asia. The module made in Latin America ended up in the worst place, with a deviation of over 10% - and it was the most expensive module of all with a current market price of over CZK 12,000. However, compared to measurements ten years ago by the German institute TUV Rheinland, we can state that there were none of the given sample of 17 modules, the performance of which at STC would be different by more than 20%.

## Acknowledgments

This work financial support for a specific research project at the Brno University of Technology. FEKT-S-20-6206

## References

1. R. Haselhuhn: Planning & Instaling Photovoltaic- Systems (3 editions) DGS, 2013, ISBN 978-3-00-9805738-6-3

## Temperature profile analysis in supersonic flow in the experimental chamber

P. Šabacká<sup>a</sup>, J. Maxa<sup>a</sup>, P. Vyroubal<sup>a</sup>,

<sup>a</sup> Department of Electrical and Electronic Technology, Brno University of Technology, Technická 10, 616 00 Brno, Czech Republic

This article deals with the preparation of the experimental chamber on which, among other things, stagnation and static temperature will be measured. The results obtained from the measurements will be compared with the results of mathematical - physics analyzes of the Ansys Fluent system. Analyzes of the expected stagnation temperatures at the tip of the probes were performed with respect to the course of the Mach number from the aperture.

### Introduction

An experimental chamber simulating the state of differential pumping is being in production at the Department of Electrical and Electronic Technology of FEET BUT in Brno, in cooperation with the Institute of Scientific Instruments of The Czech Academy of Sciences (1, 2). This chamber consists of two chambers of different pressures, a specimen chamber with a pressure of 2000 Pa (3, 4), and a differentially pumped chamber with a pressure of 40 Pa, separated by a small aperture with a diameter of 2 mm (5 ,6). These pressure ratios are typical for the Environmental scanning electron microscopy (ESEM) (7, 8) see figure 1.

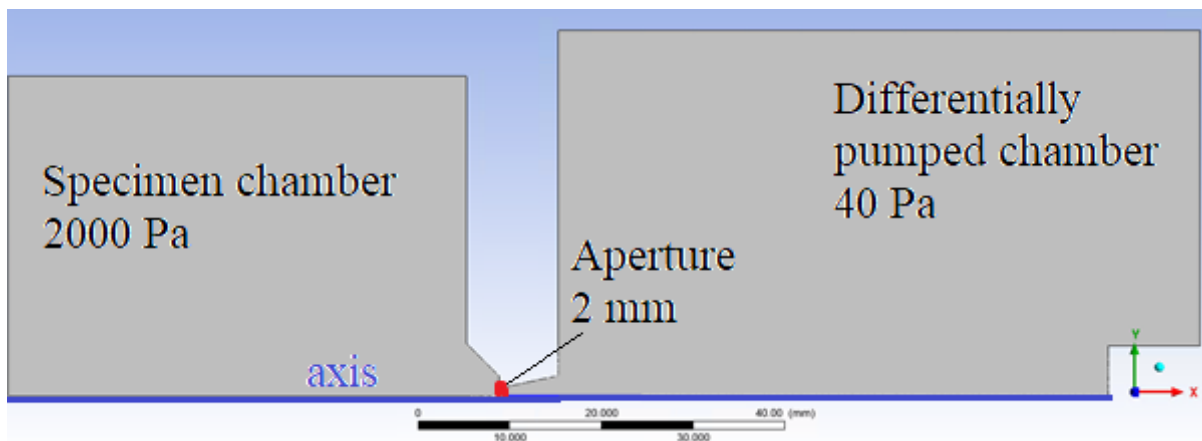


**Figure 1.** 2D axisymmetric profile with boundary condition

In this experimental chamber, several measurements will be made in between them also a static pressure measurement according to the Prandtl theory which says that the static pressure layout is the same in the flow cross-section. Six holes will be spirally placed on the nozzle surface for this purpose, whose perpendicular projection points to these 6 points in the flow axis from which the static pressure and temperature will be captured see figure 2.

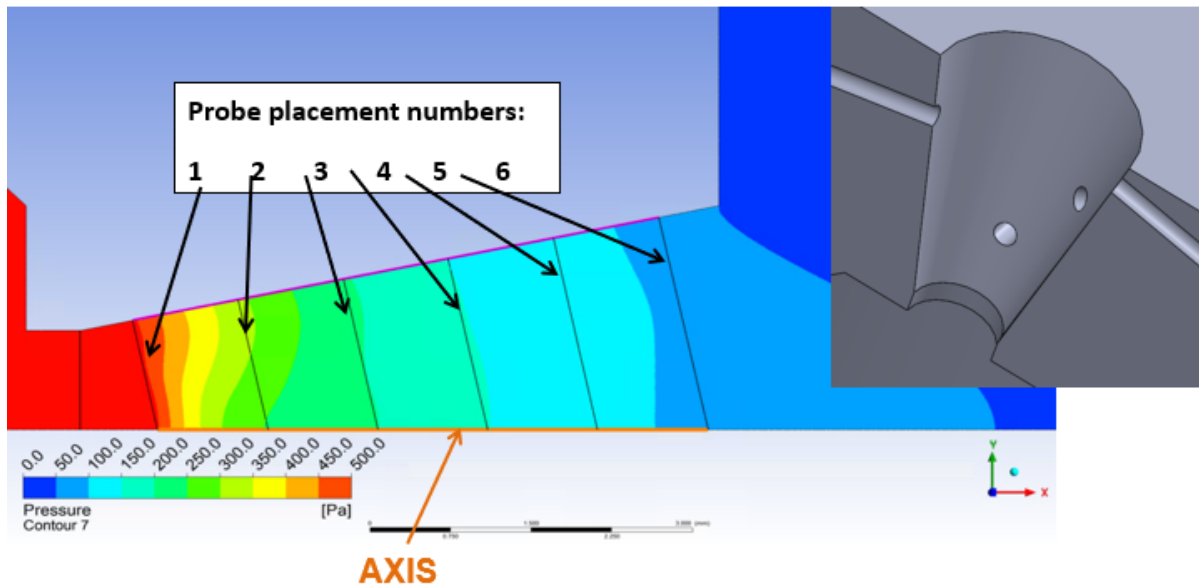


Figure 2. Distribution of measured points based on Prandtl's theory

### Temperature measuring in supersonic flow

As it was mentioned, we will capture the temperature in given six points using thermocouples. Due to the supersonic flow in the experimental chamber, the shock wave is created in front of the probe front behind which flow braking occurs up to stagnation point. On the probe in front of the thermocouple, the stagnation temperature is being captured. But we need a static temperature for our application, so the value of static temperature is necessary to calculate from the relationship 1:

$$\frac{T_s}{T_0} = \left(1 + \frac{\gamma - 1}{2}\right)M^2 \quad [1]$$

where:  $T_s$  – stagnation temperature,  $T_0$  – static temperature,  $\gamma$  – Poisson constant,  $M$  – Mach number.

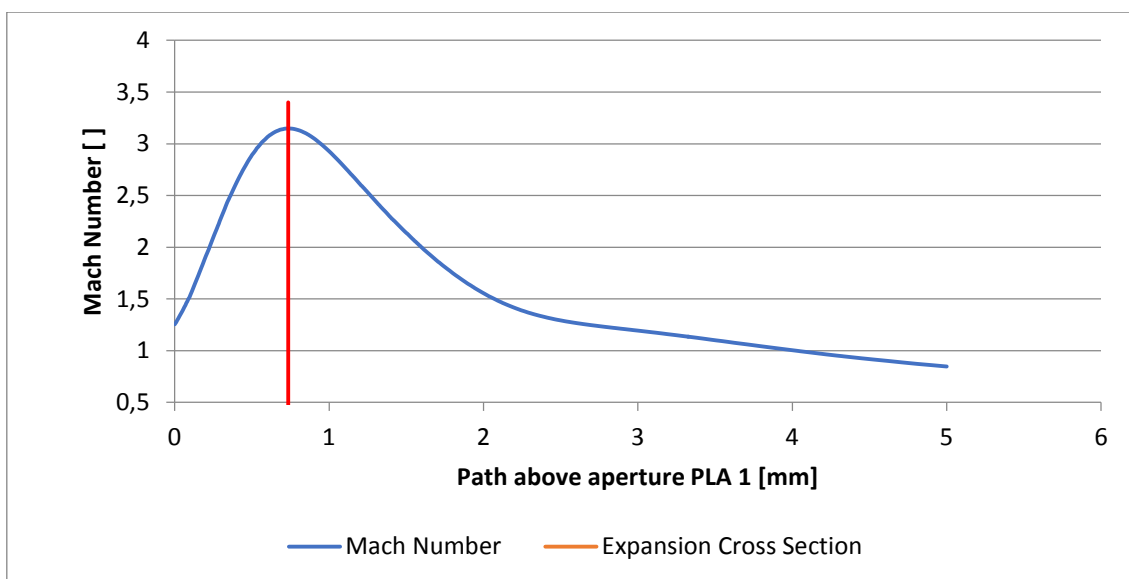


Figure 3. Mach number running on the flow path

There is a Mach number running on the flow axis in figure 3, from which the values in given measured points were taken.

## Results and discussions

Based on mathematical – physics analyzes made in the variant with the free flow ( $T_{free}$ ) also in the variant with the inserted probe ( $T_{stagnation}$ ) we made a comparison of results of the temperature measuring obtained from the theoretical relationship [1] with the results obtained from Ansys Fluent system for all measured spots see figure 4 and table 1. In measured point one, the bigger difference is obvious because of the probe insertion into the aperture mouth, so the result in this point is slightly distorted, but in other points is obvious from the results that the flow does not influence the results.

The results obtained from the experimental measuring will be used for the electron microscopy purpose because the significantly affect the passage of the electron beam through the differentially pumped chamber.

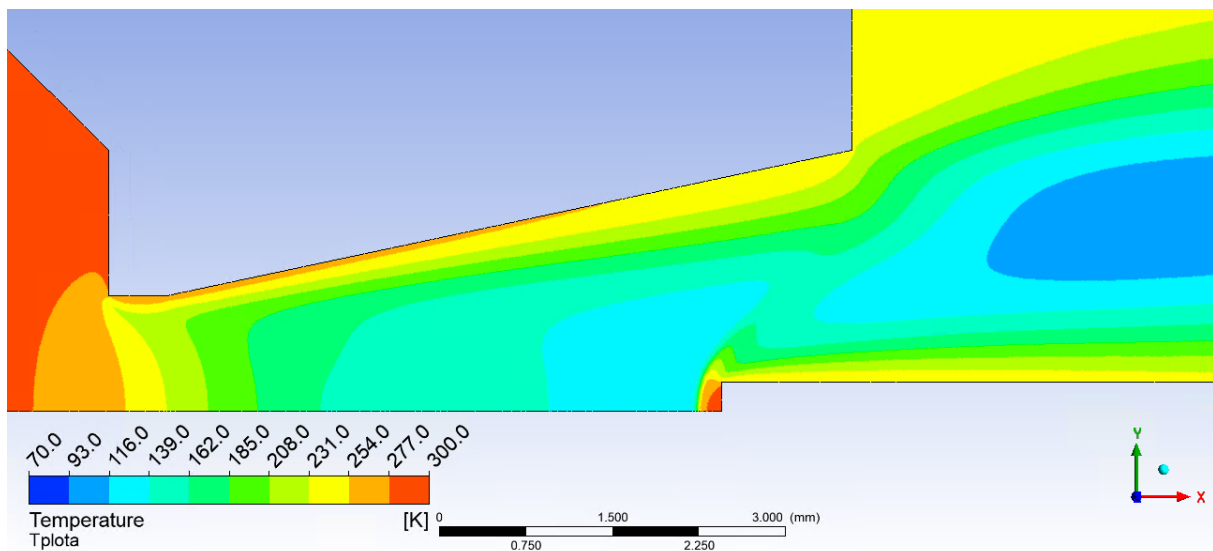


**Figure 4.** Temperature layout from Ansys Fluent system

**Table 1.** Static temperature result comparison obtained from relationship 1 and Ansys Fluent system

|                | Ansys Fluent     |            | Relationship 1 |
|----------------|------------------|------------|----------------|
|                | $T_{stagnation}$ | $T_{free}$ | Calculation    |
| <b>Probe 1</b> | 277              | 200,2      | 186,7          |
| <b>Probe 2</b> | 279,3            | 164        | 160,2          |
| <b>Probe 3</b> | 280,7            | 154,3      | 150,9          |
| <b>Probe 4</b> | 282,6            | 142,1      | 140,3          |
| <b>Probe 5</b> | 283,8            | 131,2      | 128,6          |
| <b>Probe 6</b> | 283,5            | 122,3      | 121,9          |

### Acknowledgments

This work was supported by the specific graduate research of the Brno University of Technology No. FEKT-S-20-6206.

### References

1. V. Neděla; E. Tihlaříková; J. Maxa; K. Imrichová; M. Bučko and P. Gemeiner, Simulation-based optimisation of thermodynamic conditions in the ESEM for dynamical in-situ study of spherical polyelectrolyte complex particles in their native state, *Ultramicroscopy*, (2020).
2. P. Vyroubal; J. Maxa; V. Neděla; J. Jiráček and K. Hladká, Apertures with Laval Nozzle and Circular Orifice in Secondary Electron Detector for Environmental Scanning Electron Microscope, *Advances in Military Technology*, vol. 8, no. 1, p. 59-69, (2013).
3. E. Tihlaříková; V. Neděla and B. Dordevic, In-situ preparation of plant samples in ESEM for energy dispersive x-ray microanalysis and repetitive observation in SEM and ESEM, *Scientific Reports*, vol. 9. ISSN 2045-2322, (2019).
4. J. Maxa and V. Neděla, The Impact of Critical Flow on the Primary Electron Beam Passage through Differentially Pumped Chamber. *Advances in Military Technology*, vol. 6, no. 1, p. 39-46. ISSN 1802-2308, (2011).
5. P. Šabacká; J. Maxa and P. Vyroubal, Correction of the supersonic flow impact on the results of the inserted temperature probe in the differentially pumped chamber, In ABAF 20th issue of ECS Transactions, p. 100-105. ISBN: 978-80-214-5109-4. (2019).
6. A. Maxová; P. Šabacká and J. Maxa, Comparison of the Ansys Fluent system solvers for the possibility of supersonic flow solving at the low pressures. In ABAF 20th issue of ECS Transactions, p. 32-37. ISBN: 978-80-214-5109-4. (2019).
7. J. Maxa; P. Hlavatá and P. Vyroubal, Using the ideal and real gas model for the mathematical - physics analysis of the experimental chamber, In ECS Transactions, p. 377-387. ISBN: 978-80-214-5109-4. ISSN: 1938-5862. (2018).
8. P. Hlavatá; J. Maxa and P. Vyroubal. Analysis of Pitot tube static probe angle in the experimental chamber conditions. In ECS Transactions. ECS Transactions, p. 50-56. ISBN: 978-80-214-5109-4. ISSN: 1938-5862. (2018).

## Temperature running simulations during the pumping of chambers separated by a small aperture.

A. Maxová<sup>a</sup>, J. Maxa<sup>b</sup>, P. Šabacká<sup>b</sup>.

<sup>a</sup> St. Cyril and Methodius Grammar School and Pedagogical Secondary School,  
Lerchova 63, 602 00 Brno, Czech Republic

<sup>b</sup> Department of Electrical and Electronic Technology, Brno University of Technology, Technická  
10, 616 00 Brno, Czech Republic

This article deals with the preparation of the experimental chamber on which, among other things, stagnation and static temperature will be measured. The results obtained from the measurements will be compared with the results of mathematical - physics analyzes of the Ansys Fluent system. Due to the expected temperature drop during pumping, the analyzes of the given pumping process were made for the selection of suitable probes for the cryogenic mode were also performed.

### Introduction

An experimental chamber simulating the state of differential pumping is being in production at the Department of Electrical and Electronic Technology of FECC BUT in Brno, in cooperation with the Institute of Scientific Instruments of The Czech Academy of Sciences (1, 2). This chamber consists of a specimen chamber with a pressure of 2000 Pa and a differentially pumped chamber with a pressure of 40 Pa separated by a small aperture of a diameter of 2mm (3). These pressure ratios are typical for the environmental scanning electron microscope (ESEM) (4) see figure 1. These pressures are achieved by pumping from atmospheric pressure (5).

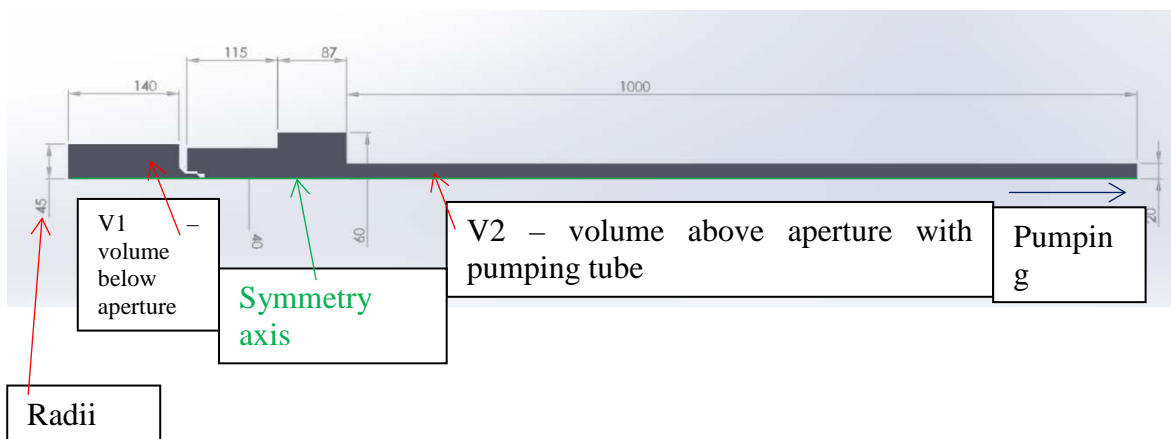


**Figure 1.** 2D axisymmetric profile with boundary condition

Due to a sharp pressure drop during the pumping of the experimental chamber, the sharp temperature drop occurs, so it's necessary to pay attention to proper experimental probes choice.

These probes were chosen based on their differential pressure so their membranes would be able to resist big pressure differences.

We have two types of pumps available, Lavat with the volume flow rate of 25 m<sup>3</sup>h<sup>-1</sup> and Pfeiffer with the volume flow rate 62 m<sup>3</sup>h<sup>-1</sup>.

### Results and discussions

Mathematical-physics analyzes in Ansys Fluent system, where the Pressure Based Solver setting (6) with second-order discretization (7) was used, showed the following pressure and temperature runnings as a function of time. These calculations were performed as 2D axisymmetric time variable calculations (8).

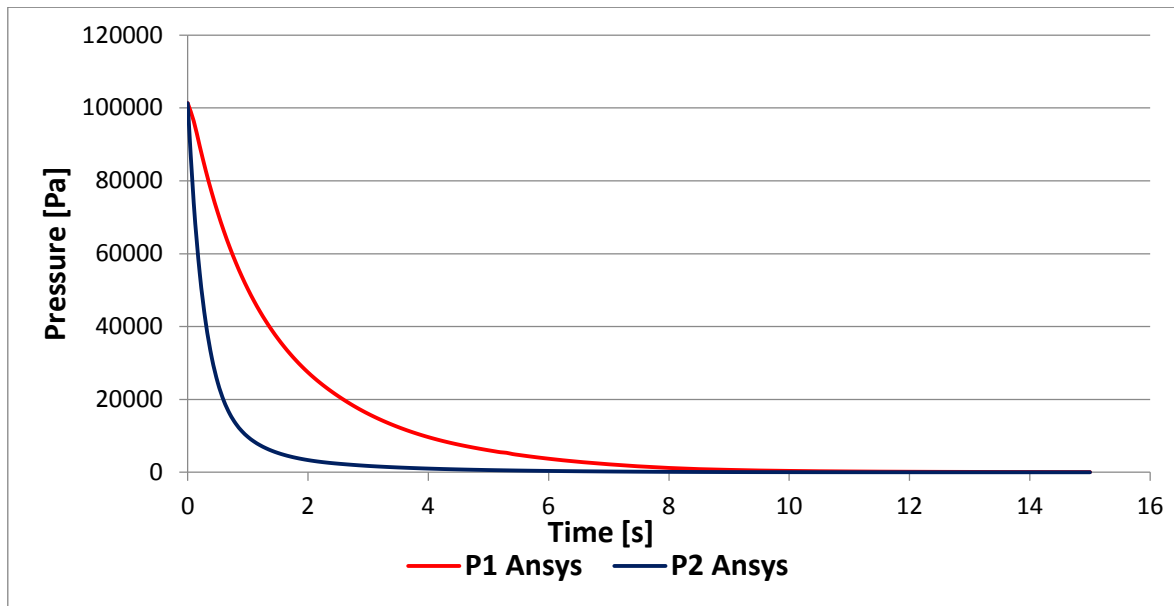


Figure 2. Pressure running depending on time for Lavat pump

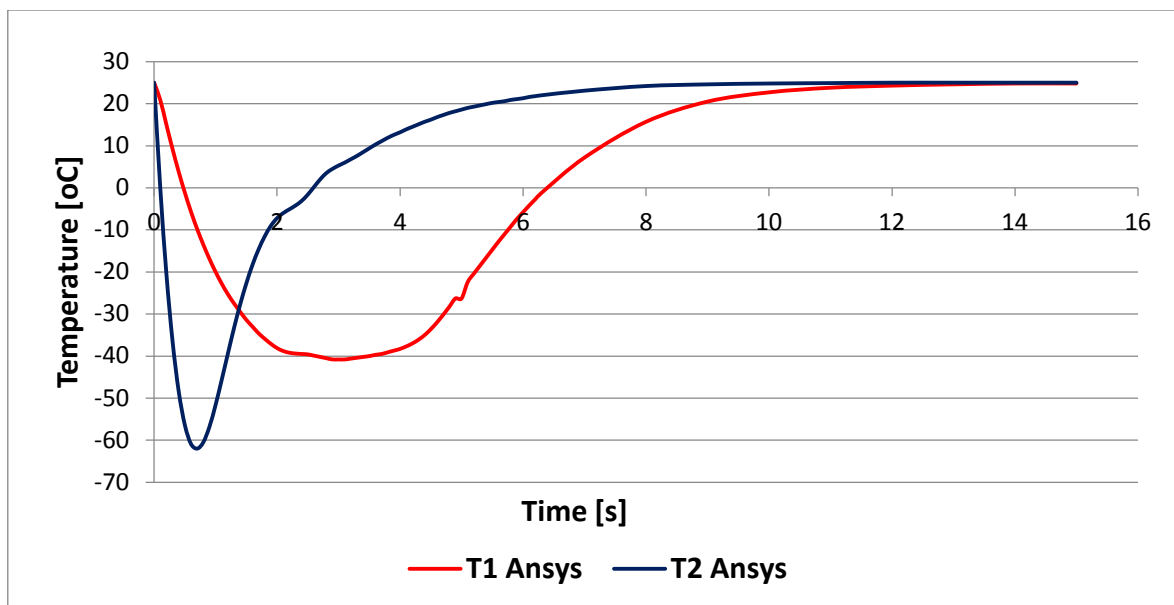
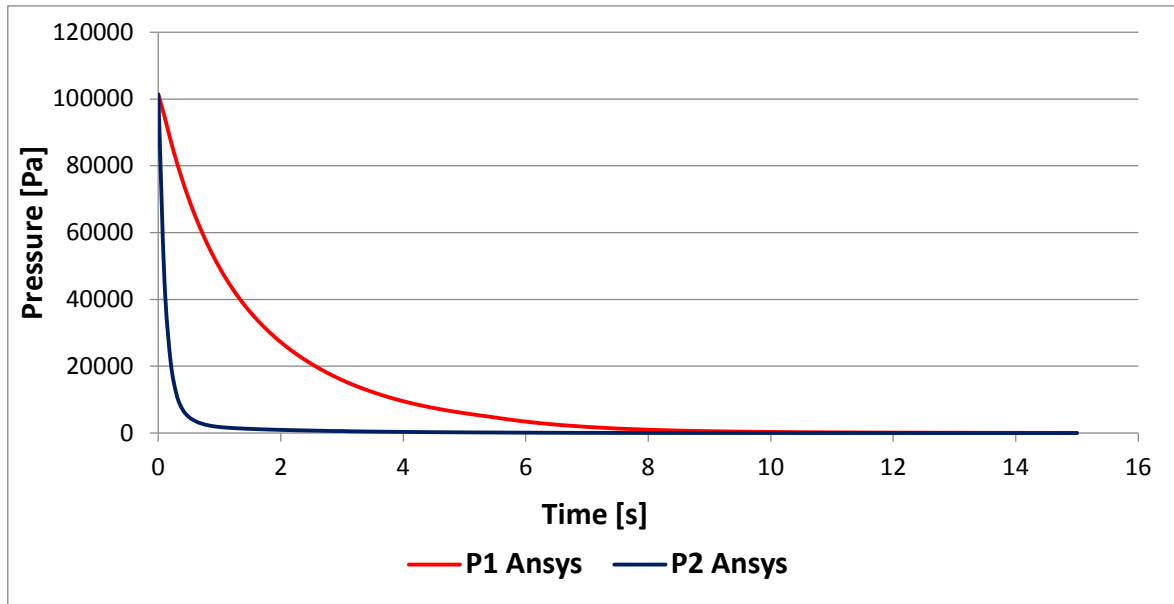
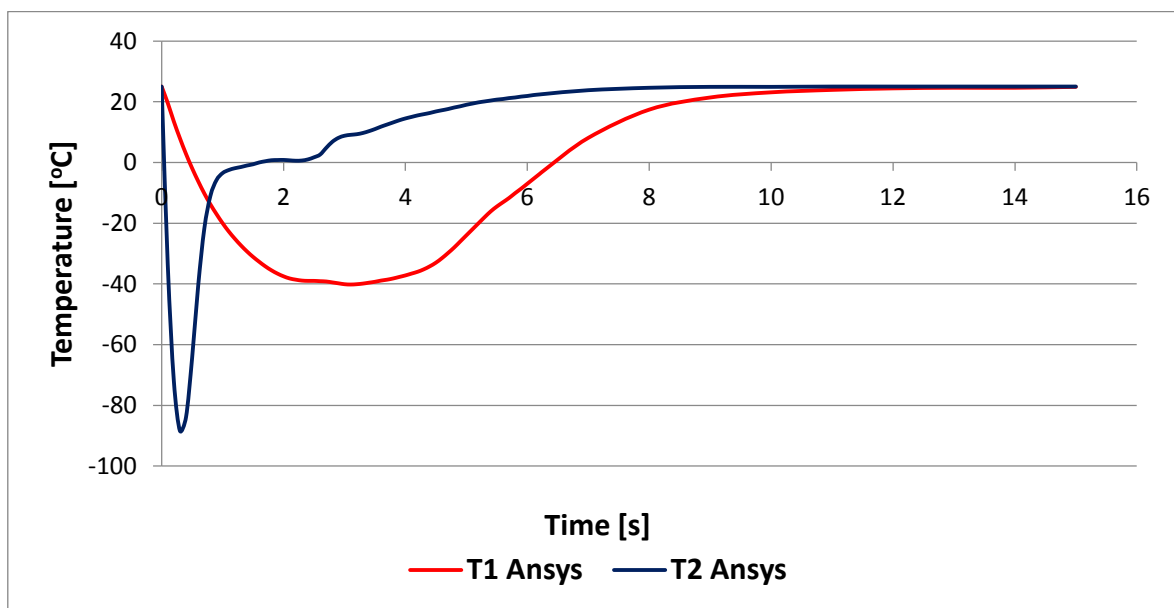


Figure 3. Temperature running depending on time for Lavat pump



**Figure 4.** Pressure running depending on time for Pfeiffer pump



**Figure 5.** Temperature running depending on time for Pfeiffer pump

Mathematical-physical analyzes have shown that the temperature drop during pumping in chamber 1 is  $-40^{\circ}\text{C}$  for both the Lavat pump and the Pfeiffer pump in the range of the second to fourth seconds of pumping, in chamber 2 the temperature drop is  $-60^{\circ}\text{C}$  for the Lavat pump and  $-90^{\circ}\text{C}$  at the Pfeiffer pump. In both cases, this is the first second of pumping. According to the results we have to count on probes for cryogenic mode.

### Acknowledgments

This work was supported by the specific graduate research of the Brno University of Technology No. FEKT-S-20-6206.

### References

1. V. Neděla; E. Tihlaříková; J. Maxa; K. Imrichová; M. Bučko and. P. Gemeiner, Simulation-based optimisation of thermodynamic conditions in the ESEM for dynamical in-situ study of spherical polyelectrolyte complex particles in their native state, *Ultramicroscopy*, (2020).
2. P. Vyroubal; J. Maxa; V. Neděla; J. Jiráček and K. Hladká, Apertures with Laval Nozzle and Circular Orifice in Secondary Electron Detector for Environmental Scanning Electron Microscope, *Advances in Military Technology*, vol. 8, no. 1, p. 59-69, (2013).
3. E. Tihlaříková; V. Neděla and B. Dordevic, In-situ preparation of plant samples in ESEM for energy dispersive x-ray microanalysis and repetitive observation in SEM and ESEM, *Scientific Reports*, vol. 9. ISSN 2045-2322, (2019).
4. J. Maxa and V. Neděla, The Impact of Critical Flow on the Primary Electron Beam Passage through Differentially Pumped Chamber. *Advances in Military Technology*, vol. 6, no. 1, p. 39-46. ISSN 1802-2308, (2011).
5. P. Šabacká; J. Maxa and P. Vyroubal, Correction of the supersonic flow impact on the results of the inserted temperature probe in the differentially pumped chamber, In ABAF 20th issue of ECS Transactions, p. 100-105. ISBN: 978-80-214-5109-4. (2019).
6. A. Maxová; P. Šabacká and J. Maxa, Comparison of the Ansys Fluent system solvers for the possibility of supersonic flow solving at the low pressures. In ABAF 20th issue of ECS Transactions, p. 32-37. ISBN: 978-80-214-5109-4. (2019).
7. J. Maxa; P. Hlavatá and P. Vyroubal, Using the ideal and real gas model for the mathematical - physics analysis of the experimental chamber, In ECS Transactions, p. 377-387. ISBN: 978-80-214-5109-4. ISSN: 1938-5862. (2018).
8. P. Hlavatá; J. Maxa and P. Vyroubal. Analysis of Pitot tube static probe angle in the experimental chamber conditions. In ECS Transactions. ECS Transactions, p. 50-56. ISBN: 978-80-214-5109-4. ISSN: 1938-5862. (2018).

## The Thermodynamic Model for Vacuum Technology

V. Horák<sup>a</sup>, B. T. Phan<sup>a</sup>, and L. Do Duc<sup>b</sup>

<sup>a</sup> Department of Mechanical Engineering, University of Defence in Brno, Czech Republic

<sup>b</sup> Le Quy Don Technical University, Hanoi, Vietnam

The presented paper is focused on the developing a predictive mathematical model for describing unsteady thermodynamic processes connected with the depressurization of vacuum chambers under various conditions. The prediction of time for a system depressurization and the ensuring of the precisely defined vacuum pressure control are important tasks for the design and operation of low-vacuum systems. These specific requirements are especially important for the environmental scanning electron microscopes, where it is possible to observe samples, which contain water in their natural condition. The crucial condition is that the system pressure must not drop below the saturated water vapor pressure. If the vacuum-system pressure drops below the saturated vapor pressure, observed samples will be damaged.

### Discharging Mathematical Model

The exchange of mass and energy between air, chamber and environment takes place in a simple open thermodynamic system, as shown in Fig. 1.

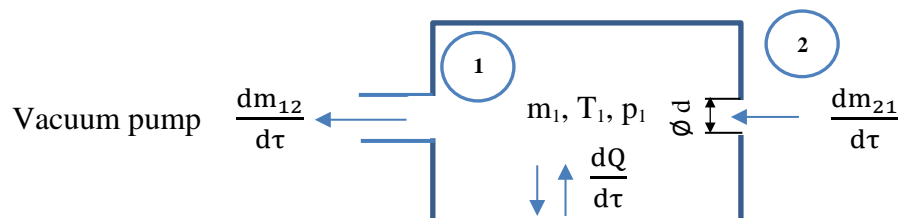


**Figure 1.** Schematic of the vacuum chamber thermodynamic system.

The mass airflows  $dm/d\tau$  leaving and entering across the boundary of the system control volume causes the change in pressure  $p_1$ , temperature  $T_1$  and mass  $m_1$  of air inside the chamber. During the unsteady-state processes of depressurization, the heat transfer  $dQ/d\tau$  process occurs. The system of differential equations has been solved by numerical integration with MATLAB using the explicit fourth-order Runge-Kutta method. The mathematical model requires a set of input parameters and boundary conditions (i.e. the chamber volume, initial temperature, the discharging flow velocity, the heat transfer area of chamber, the convective heat transfer coefficient, the area of the orifice, the flow coefficient and air thermodynamics properties).

Results of the solution are validated by experiment for three cases of the orifice diameters, namely:  $d = 1.044, 1.524$  and  $2.157$  mm. Other input parameters are: the vacuum chamber volume  $V_1 = 0.045$  m<sup>3</sup>, the chamber surface area  $0.7188$  m<sup>2</sup>, the pumping speed  $0.001389$  m<sup>3</sup>s<sup>-1</sup>, the barometric pressure  $98858$  Pa and temperature  $294.5$  K. Results of the solution provide us with the pressure evolution, the temperature, the velocity of airflow in the orifice and the airflow mass rates. These results for the case of the inlet orifice diameter  $d = 1.044$  mm are shown in Fig. 2.

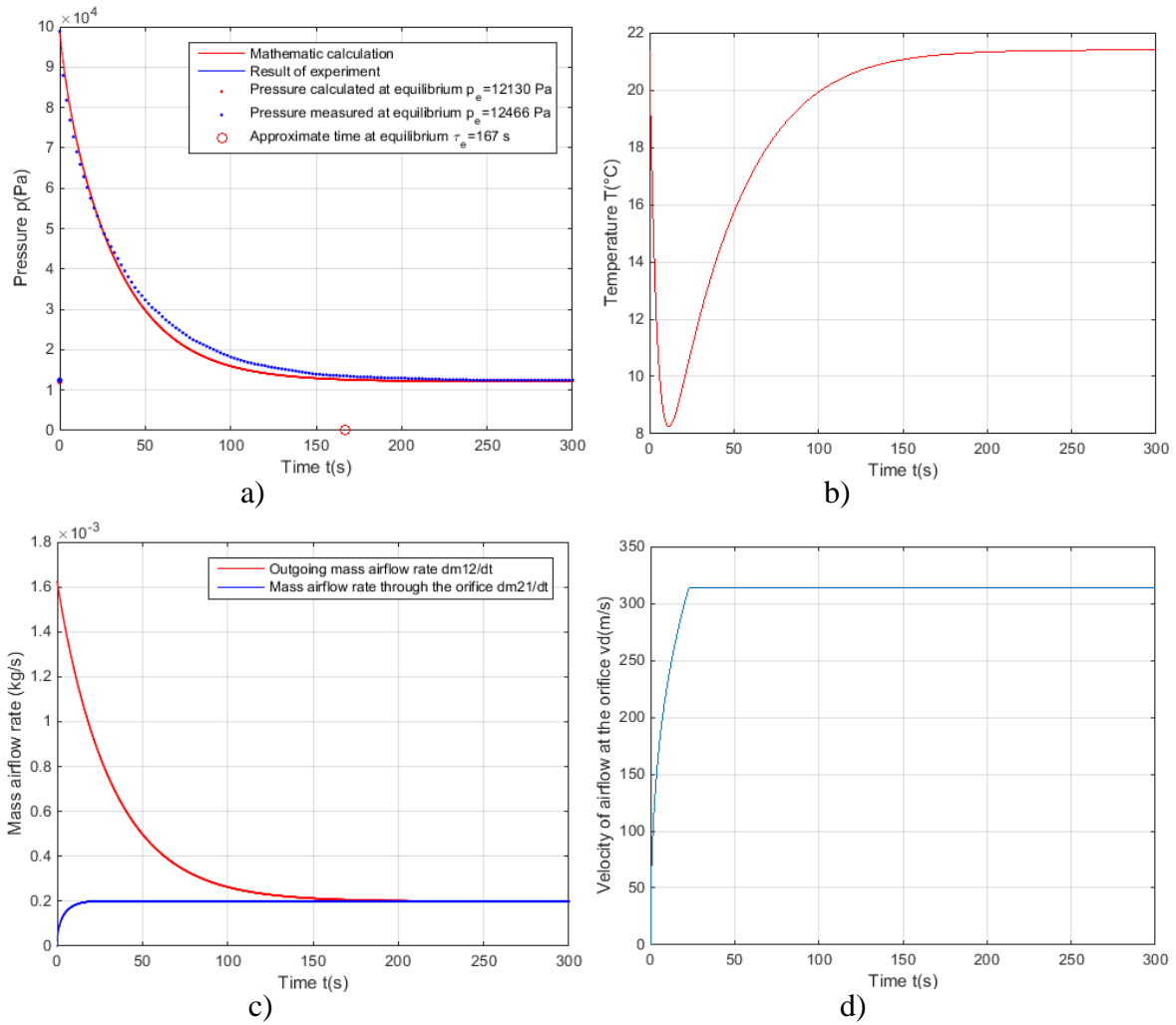


**Figure 2.** Results of depressurization for the case of inlet orifice diameter  $d = 1.044$  mm: a) pressure in the vacuum chamber, b) temperature in the vacuum chamber, c) mass flow rates into and out the vacuum chamber, d) velocity of airflow in the orifice.

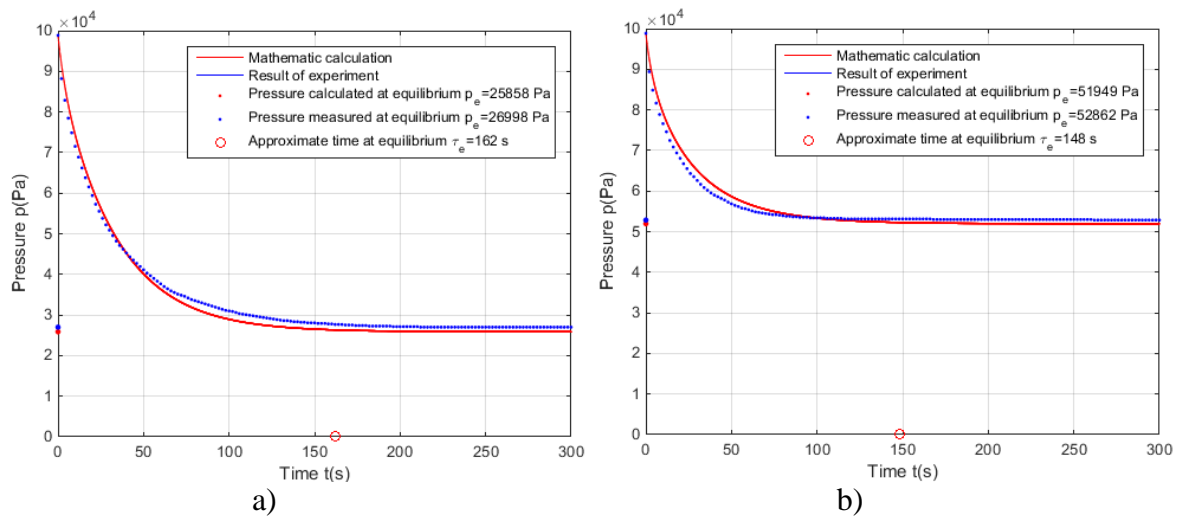


**Figure 3.** Depressurization time history in the vacuum chamber for inlet orifice diameters: a)  $d = 1.524$  mm, b)  $d = 2.157$  mm.

The presented model was validated by the experiment for three cases of airflow to the vacuum chamber through an inlet opening of various diameters. The comparison is shown in Fig. 2 a) and Fig. 3. As can be seen from the figures, the model agrees with the experiment quite well.

### Pressure at Equilibrium and Time to Reach the Pressure Equilibrium

One very useful application is the determination of the relation between the diameter of the inlet opening and the pumping speed of the vacuum pump at the pressure equilibrium. This is the way for ensuring the precisely defined vacuum pressure control as an important task for the design and operation of low-vacuum systems, especially for environmental scanning electron microscopes. The resulting relation between the equilibrium pressure and the opening orifice diameter is shown in Fig. 4. There are also given calculated values of the equilibrium pressure for all the three examined cases of orifice diameters.

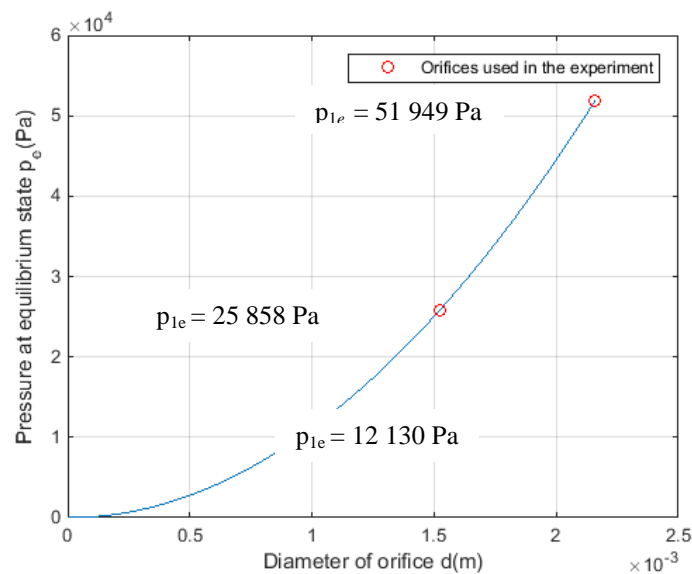


**Figure 4.** Equilibrium pressure versus orifice diameter for barometric temperature 22 °C

The experimental results, shown in Fig. 2 a) and in Fig. 3, provide us with the values of the equilibrium pressure: 12 466 Pa, 26 998 Pa and 52 862 Pa. Here, we can also see a very good agreement between calculated and measured values.

The time  $\tau_e$  required to reach the pressure equilibrium is an important quantity for operation of vacuum systems. After this time the pressure in a pressure chamber remains constant (see Figs. 3a and 4). The prediction of this time is essential to determine the beginning of the normal operation condition of a vacuum system. The corresponding times to reach equilibrium for the observed cases are shown in Fig. 2 a) and Fig. 3.

### Acknowledgment

The work presented in this paper has been supported by the specific research project of the Faculty of Military Technology SV20-216, the University of Defence in Brno.

## Analysis of Battery Performance and Degradation in CubeSat GOMX-3

V. Knap<sup>a,b,c</sup>, S. Bęczkowski<sup>c</sup> and D.-I. Stroe<sup>c</sup>

<sup>a</sup> GomSpace A/S, Aalborg Denmark

<sup>b</sup> Faculty of Electrical Engineering, Czech Technical University in Prague, Czech Republic

<sup>c</sup> Department of Energy Technology, Aalborg University, Aalborg, Denmark

There is an increasing number of small satellites to be launched to space. CubeSat solutions are getting popular due to their increasing capabilities, flexibility, and significantly lower price than ‘classical’ satellites. GOMX-3 was a 3U CubeSat built by GomSpace and launched in collaboration with ESA in order to demonstrate capabilities of nano-satellites in terms of attitude control, RF sensing and high-speed downlink. Its mission lasted for about one year and the satellite was afterwards successfully de-orbited.

Batteries are an essential part of every satellite as their reliable operation is crucial for a success of nearly every mission. Thus, the battery performance and lifetime have to be sufficient, while avoiding unnecessary oversizing of the battery system, which would negatively affect economy and technical design of such spacecrafts. In this case, GOMX-3 is a great opportunity to learn from an actual satellite. Battery telemetry data, such as current, voltage and temperature, was collected during the mission. Their detailed analysis provide insights about the conditions to which the battery was exposed to and how the battery parameters were evolving throughout the time.

In order to support the satellite battery data analysis, ground testing on the same type of the cells were performed. Characterization tests were conducted for various temperature levels to obtain specific battery parameters such as open-circuit voltage and internal resistance, and to form a battery model, which is used to explain the behavior observed from the battery telemetry. Moreover, cycling and calendar degradation tests were conducted to determine the expected degradation of the cells throughout the mission.

The presented work aims to strengthen the practical experience about batteries used in CubeSats and it contributes to the telemetry processing methods. Future work in this area is to develop an advance state-of-charge and state-of-health algorithms, which will provide even deeper insight and it will allow for on-ground or on-board battery performance tracking to enhance the satellite operation.

## Iron Based Materials for Biodegradable Implants Prepared by Powder Metallurgy

M. Sedlaříková<sup>a</sup>, M. Míka<sup>b</sup>, J. Hrabovský<sup>a</sup>, T. Tkáčová<sup>a</sup>, G. Fafílek<sup>c</sup> and P. Čudek<sup>a</sup>

<sup>a</sup> Faculty of Electrical Engineering and Communications, Brno University of Technology, Brno, Czech Republic

<sup>b</sup> Department of Glass and Ceramics, University of Chemistry and Technology, Prague, Czech Republic

<sup>c</sup> Research Group for Electrochemical Methods and Corrosion, TU Wien, Vienna, Austria

Preparation of metal components by a modified powder technology was checked. Iron powder is used for manufacturing of an object of arbitrary form. Its final treatment occurs in nitrogen at 1120 °C.

### Introduction

Biodegradable material is a promising candidate for the improvement of bone injury treatments. Its main advantage is the compatibility with a human body as well as its spontaneous degradation (reoperation is not needed for its removal). Generally, biodegradable materials exhibit many suitable properties, but on the other hand, they must meet a lot of strong requirements. In the research and development of biodegradable materials, the emphasis has been put on sufficient strength, but sufficient flexibility, fast degradation and good compatibility with human tissue.

Currently, there are several research groups which examine these materials. For example, Wegener *et al* (1) described the manufacturing of implants by powder metallurgy enabling the production of specially tailored objects for medical applications. Our group also have introduced the modification of powder metallurgy for this purpose (2), (3), (4).

The aim of this work was to create samples of biodegradable materials and monitor their properties. For this work, we decided to use polyurethane sponge. A foam from polyurethane is used as a carrier matrix. Prepared samples were annealed in an inert atmosphere. The polymer is supposed to evaporate or vanish from the material, leaving a porous structure of the metal untouched. As the temperature increases, the metal is sintered to a solid form.

### Preparation of Samples

The starting material iron was prepared by the hydrogen reduction of commercially available iron oxides and commercially available polyurethane foam was used as a carrier matrix. The samples were prepared by immersing the pieces of the polyurethane foam into the suspension of iron in distilled water. After sufficiently long soaking, the samples were taken out from the suspension and placed in an oven at 37 °C for 24 hours.

All the samples went through the following annealing process that provided the necessary strength and removal of the polymer. Our previously verified temperature profile was used, firstly – 2 hours at temperature 450 °C followed by 1 hour at temperature 1120 °C in a nitrogen atmosphere.

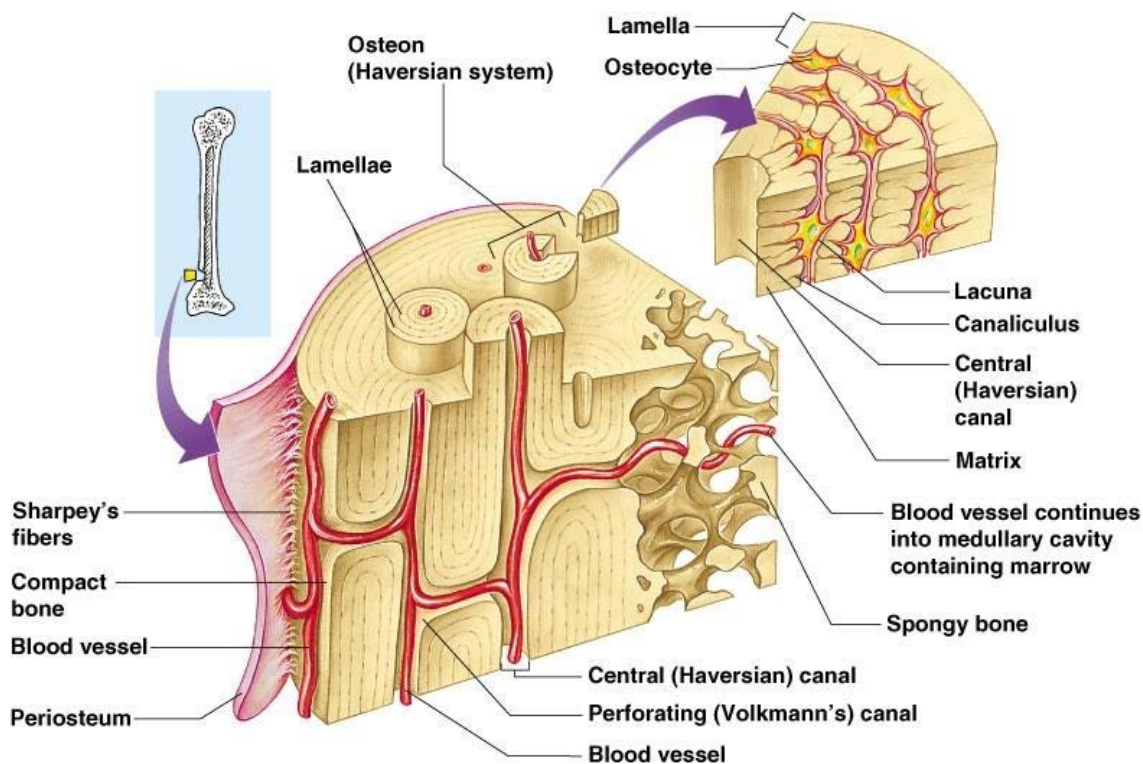


Figure 1. Structure of bone tissue.

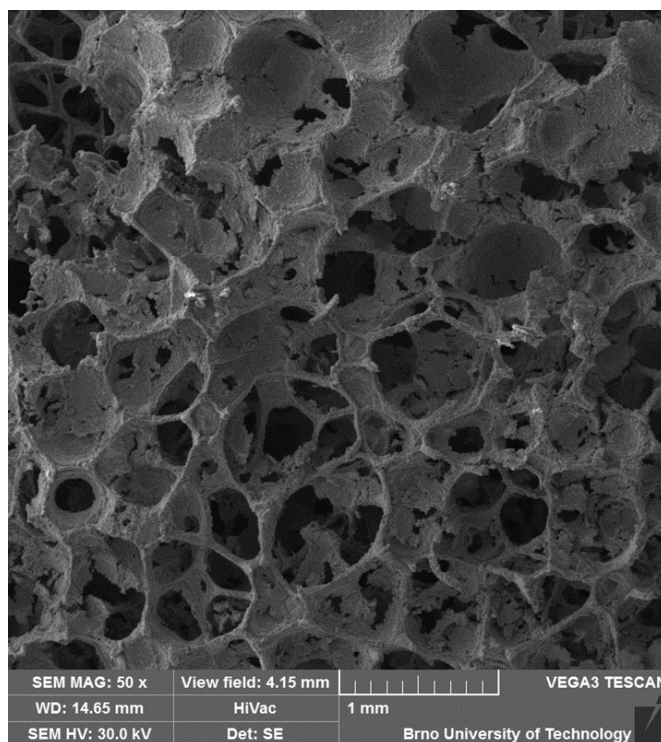


Figure 2. Spongy structure of PUR matrix sample containing iron.

### Characterization of PUR samples containing iron

The structure of the annealed samples was investigated by an electron microscope. Moreover, EDX analysis was also performed because it was important to determine the distribution of elements in the samples. The analysis was performed on the samples before immersing them into the simulated body liquid (SBL) or NaCl and also after 147 days of soaking the samples in these solutions. From the table 1, it is obvious that after the soaking the concentration of individual elements changed. Potassium and chlorine were observed in the structure of the sample after the treatment. Potassium was present in small concentrations and the presence of chlorine was caused by the content of chlorine ions in the solutions.

**Table 1.** Amount of individual elements in the sample (PUR+iron)

| Element    | wt. %        | wt. %                  | wt. %                 |
|------------|--------------|------------------------|-----------------------|
| Oxygen     | 30.04        | 30.65                  | 30.1                  |
| Magnesium  | 6.41         | -                      | -                     |
| Iron       | 57.85        | 62.14                  | 60.27                 |
| Sulfur     | 1.22         | -                      | -                     |
| Sodium     | 4.49         | 2.19                   | 3.81                  |
| Chlorine   | -            | 3.9                    | 5.82                  |
| Potassium  | -            | 1.12                   | -                     |
| Conditions | no treatment | after 147 days in NaCl | after 147 days in SBL |

Samples placed in the solutions were kept at 37 °C and their corrosion potentials, weight loss and solution conductivity were measured monthly. Standard solution such as NaCl contains only several ions which are present in body fluids, but SBL contains most of these ions and can sufficiently simulate the environment inside a human body. Chloride and phosphate ions have a great influence on the corrosion because the chloride ions can disrupt passive layers but the phosphate ions can cause the opposite effect. The changes of the corrosion potential changes of the samples in Table 2 were measured using the working PIGE electrode with the sample attached, support Pt electrode and Ag/AgCl reference electrode. The effect of the chloride ions on the sample in simulated body fluid was almost negligible and the final corrosion potential was more positive than initial. On the other hand, the final corrosion potential in the sample in NaCl was more negative than the initial value.

**Table 2.** Changes of corrosion potential of the samples

| Sample         | Solution | E <sub>corr</sub> [V] |         |         |         |         |
|----------------|----------|-----------------------|---------|---------|---------|---------|
| Fe             | NaCl     | -0.5496               | -0.3574 | -0.3467 | -0.3958 | -0.5774 |
| Fe             | SBL      | -0.5496               | -0.5037 | -0.3360 | -0.4108 | -0.4492 |
| Number of days |          | 0                     | 35      | 63      | 84      | 147     |

### Summary

For the PUR samples containing iron and immersed in NaCl, we observed significant changes after 35 days of soaking. The weight of the sample increased that was probably caused by the formation of a passive layer because the corrosion potential was shifted to more positive values. Later, the values gradually stabilized closer to the initial values and the final corrosion potential was more negative than the initial ones due to disrupting the passive layer. After 147 days, the weight

decreased due to accelerated corrosion, the corrosion current increased and the pH and conductivity continued to increase.

For the samples immersed in SBL, the measured values did not change so significantly as for the samples in NaCl. The weight gradually decreased, the corrosion potential was shifted to more positive values, which indicated the precipitation effect of phosphate ions. There is a gradual attenuation of corrosion, probably due to the accumulation of corrosion products on the surface of the material. The pH value was shifted to higher values probably due to the release of alkaline ions.

### Acknowledgments

This work was supported by the specific graduate research of the Brno University of Technology No. FEKT-S-20-6206.

### References

1. B. Wegener, B. Sievers, S. Utschneider, P. Müller, V. Jansson, S. Rößler, B. Nies, G. Stephani, B. Kieback, P. Quadbeck, *Microstructure, cytotoxicity and corrosion of powder-metallurgical iron alloys for biodegradable bone replacement materials*, p. 1789-1796, *Materials Science and Engineering: B*, (2011)
2. J. Vondrák, M. Sedlaříková, A. Košíček, M. Hávová and J. Kadlec, *ECS Trans.*, **87**(1): 415-421 (2018)
3. J. Vondrák, M. Sedlaříková, Z. Galánová, P. Čudek and T. Binar, *ECS Trans.*, **87**(1), 423-429 (2018)
4. M. Sedlaříková, J. Hrabovský, M. Růžička, P. Čudek, *ECS Trans.*, **95**(1), 437-448 (2019)

## Iron-Magnesium Materials for Biodegradable Implants Prepared by Powder Metallurgy

M. Sedlaříková<sup>a</sup>, M. Míka<sup>b</sup>, J. Hrabovský<sup>a</sup>, T. Tkáčová<sup>a</sup>, G. Fafílek<sup>c</sup> and P. Čudek<sup>a</sup>

<sup>a</sup> Faculty of Electrical Engineering and Communications, Brno University of Technology, Brno, Czech Republic

<sup>b</sup> Department of Glass and Ceramics, University of Chemistry and Technology, Prague, Czech Republic

<sup>c</sup> Research Group for Electrochemical Methods and Corrosion, TU Wien, Vienna, Austria

The preparation of metal components by a modified powder technology was tested. Iron and magnesium powders are used for the manufacturing of objects of arbitrary form. Its final treatment was in nitrogen atmosphere at 1120 °C.

### Introduction

Biodegradable materials can help to improve the treatment of bone injuries. Their main advantage is a controlled compatibility with a human tissues and spontaneous degradation, thus, reoperations to remove the implant are not required. Biodegradable materials exhibit advanced properties to satisfy many requirements. In the research and development of biodegradable materials, the emphasis is placed on sufficient strength, but also flexibility, fast degradation process and good compatibility with body tissues.

There are currently several research groups that study such materials. For example, Wegener *et al* (1) described the manufacturing of implants by powder metallurgy enabling production of specially shaped objects for medical purpose. Our group also have introduced the modification of powder metallurgy for medical applications (2), (3), (4).

The goal of this work was to create samples of biodegradable materials and monitor their properties. For our work, we decided to use polyurethane sponge and the mixture of powdered iron and magnesium to modify the properties of samples. Prepared samples were annealed in an inert atmosphere. The polymer was supposed to evaporate or vanish from the material, leaving a porous structure of the metal untouched. As the temperature increases, the metal is sintered to a solid form.

### Preparing of Samples

As the starting materials, commercially available powdered iron and magnesium were used. As a carrier matrix was used a commercially available polyurethane foam. The samples were prepared by immersing pieces from the polyurethane foam in a suspension of iron and magnesium with distilled water. After sufficient soaking, the samples were removed from the suspension and placed in an oven for 24 hours at 37 °C.

All samples were then annealed. Annealing provided the necessary strength and removal of the polymer (PUR). An already known temperature profile was used – 2 hours at temperature 450 °C and then 1 hour at temperature 1120 °C in a nitrogen atmosphere.



**Figure 1.** Annealed samples with PUR matrix

#### Observation of the samples with iron and magnesium

The structure of the annealed samples was investigated by an electron microscope. As the samples must not be dangerous to a body, it is important to know their composition and therefore an EDAX analysis was performed. EDAX analysis was performed on the samples before placing them into simulated body liquid (SBL) or NaCl and also after 147 days of treatment of the samples with these solutions.

EDAX analysis actually showed presence of magnesium in all samples containing magnesium. All samples containing magnesium in the elemental analysis actually showed its presence. Unfortunately, some elements of the impurities turned out to be more prevalent. It could be due to samples handling or the purity of the powdered metals. It is also important from which part of the sample the analysis was made, because powdered magnesium did not have to be homogeneously distributed.

The amount of oxygen and magnesium increased more significantly in the sample immersed in the NaCl solution, and the amount of iron decreased. These changes may be due to the surface effect of corrosion, which in the case of this sample was the fastest after the first month of soaking in NaCl.

In the iron sample with the addition of magnesium immersed in the SBL, magnesium was probably released from the structure due to the interaction with the ions contained in the SBL.

**Table 1.** Amount of individual elements in the sample (PUR+Fe+ 5 % Mg)

| Element           | wt. %               | wt. %                         | wt. %                        |
|-------------------|---------------------|-------------------------------|------------------------------|
| Oxygen            | 22.64               | 41.54                         | 25.40                        |
| Magnesium         | 2.64                | 21.93                         | -                            |
| Iron              | 67.88               | 33.75                         | 74.15                        |
| Nickel            | 6.85                | -                             | -                            |
| Sodium            | 4.49                | 1.95                          | -                            |
| Chlorine          | -                   | 0.83                          | 0.45                         |
| <b>Conditions</b> | <b>no treatment</b> | <b>after 147 days in NaCl</b> | <b>after 147 days in SBL</b> |

Samples placed in these solutions were maintained at 37 °C and their monthly corrosion potentials, weight loss and solution conductivity were measured. Standard solution such as NaCl contain only some ions contained in body fluids, but SBL contains most of these ions and perfectly simulates the body's environment. Chloride and phosphate ions have a great influence on the corrosion because chloride ions should disrupted passive laves meanwhile phosphate has the opposite effect. Using PIGE working electrode with attached samples, Pt support electrode and Ag/AgCl reference electrode, the changes of corrosion potentials of the samples were measured (Table 2.).

**Table 2.** Changes of corrosion potential of the samples

| Sample                | Solution | E <sub>corr</sub> [V] |           |           |           |            |
|-----------------------|----------|-----------------------|-----------|-----------|-----------|------------|
| Fe + 0.5 % Mg         | NaCl     | -0.5090               | -0.5304   | -0.5518   | -0.4738   | -0.5090    |
| Fe + 0.5 % Mg         | SBL      | -0.5090               | -0.5678   | -0.3552   | -0.4172   | -0.4150    |
| <b>Number of days</b> |          | <b>0</b>              | <b>35</b> | <b>63</b> | <b>84</b> | <b>147</b> |

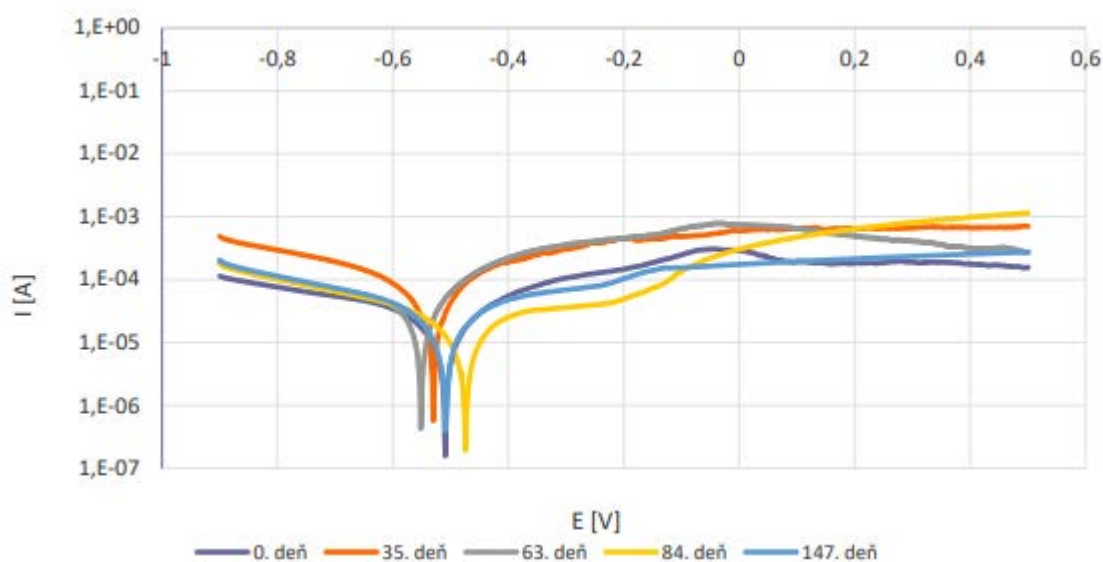


**Figure 2.** Corrosion potentials of the sample Fe + 0.5 % Mg in NaCl

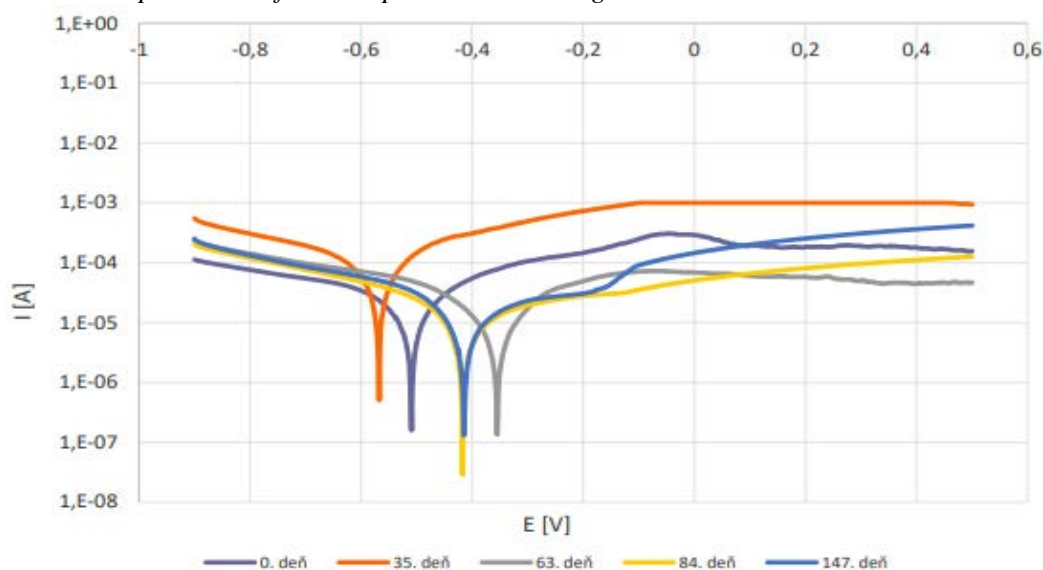


**Figure 3.** Corrosion potentials of the sample Fe + 0.5 % Mg in SBL

### Summary

For the sample (Fe + 0.5% Mg) in NaCl (figure 2), the corrosion potential values are constantly fluctuating around the initial value. This is because chloride ions disrupt the passive layer, which prevents corrosion and thus, retains the ability to corrode.

In the case of the sample (Fe + 0.5% Mg) immersed in SBL (figure 3), it is evident that during the reaction of the solution, there is a more significant shift of values. After 35 days, the effect of chloride ions was probably predominant and the values were shifted to be more negative; corrosion was accelerated. Subsequently, more positive values were measured, so it can be assumed that phosphate ions were taking over, which caused the slowing down of the corrosion. In the last two measurements, the corrosion potential has already been stabilized around -0.41 V.

### Acknowledgments

This work was supported by the specific graduate research of the Brno University of Technology No. FEKT-S-20-6206.

### References

1. B. Wegener, B. Sievers, S. Utzschneider, P. Müller, V. Jansson, S. Rößler, B. Nies, G. Stephani, B. Kieback, P. Quadbeck, *Microstructure, cytotoxicity and corrosion of powder-metallurgical iron alloys for biodegradable bone replacement materials*, p. 1789-1796, *Materials Science and Engineering: B*, (2011)
2. J. Vondrák, M. Sedlářiková, A. Košíček, M. Hávová and J. Kadlec, *ECS Trans.*, **87**(1): 415-421 (2018)
3. J. Vondrák, M. Sedlářiková, Z. Galánová, P. Čudek and T. Binar, *ECS Trans.*, **87**(1), 423-429 (2018)
4. M. Sedlářiková, J. Hrabovský, M. Růžička, P. Čudek, *ECS Trans.*, **95**(1), 437-448 (2019)

## **Innovative Non-Destructive Electromagnetic Testing of Interface Resistance - the Basis of New Technologies for Production Electrodes of High-Energy Batteries**

V. Redko<sup>a</sup>, V. Khandetsky<sup>a</sup>, E. Shembel<sup>a,b</sup>, A. Straková Fedorková<sup>c</sup>, T. Pastushkin<sup>a</sup>, P. Novak

<sup>a</sup> Enerize Corporation, Coral Springs, FL, 33067, USA

<sup>b</sup> Scientific Research Laboratory of Chemical Power Sources of Ukrainian State University of Chemical Technology, Dnipro, 49005, Ukraine.

<sup>c</sup> Pavol Jozef Safarik University, Košice, SK-04154, Slovak Republic

The efficiency of an electrochemical power source, to a great degree, depends on the internal resistance of the system. This internal resistance includes interface resistance between current collector and active electrode mass. The developed method and device enable non-destructive non-contact evaluation of the interface resistance. Results enable the prediction and optimization of electrochemical power sources properties, especially their power.

*More detailed information will be presented in the followed version of this abstract*

## Approximation of Alkaline Battery Transfer Function Using Neural Network

R. Cipin, M. Toman, P. Prochazka, I. Pazdera and J. Miklas

Department of Power Electrical and Electronic Engineering, Brno University of Technology, Brno,  
Technicka 12 6161 00, Czech Republic

This paper deals with a mathematical description of an alkaline battery impedance dependence on frequency. This mathematical description is done in two different ways. In the first case, a general fractional transfer function is used and in the second case an artificial neural network is used. Both approaches are discussed and compared with real measurements.

### Introduction

Mathematical modeling of the electrical behavior of batteries is usually done with an equivalent circuit consists of some linear elements, e.g. resistance and capacitance, and nonlinear elements, e.g. Warburg impedance, see (1) and (2) for detail battery modeling.

Generally, any battery is a highly nonlinear system and a description of its electrical properties with the only equivalent circuit, although nonlinear, can be very inaccurate and even sometimes misleading. Another problem can be an identification of this linear and nonlinear elements. It can be very difficult and, in many cases, even ambiguous, i.e. for battery description can be used the same structure of mathematical model but with different values of individual components and with different nonlinear dependencies.

Based on these reasons, it is used for description of battery dependency on frequency, i.e. dependence of battery admittance on frequency, a general fractional transfer function and an artificial neural network.

Battery admittance  $Y$  can be very simply calculated from voltage  $V$  applied to battery with given angular frequency  $\omega$ , measured battery current  $I$ , and measured phase shift between voltage and current  $\varphi$  as follows

$$Y(\omega) = \frac{I}{V} e^{-j\varphi}, \quad [1]$$

where  $j$  is imaginary unit.

In the previous paper, see (3), the authors presented the general shape of admittance transfer function [2] usable for approximation arbitrary dependency of admittance on frequency for alkaline batteries and Li-ion batteries in form

$$F(s) = G s^{q_1} \prod_{i=2,3,\dots} \frac{(s + \omega_i)^{q_i}}{\omega_i^{q_i}}, \quad [2]$$

where  $s$  is dummy variable of Laplace transform,  $q$  is an arbitrary real number ( $q \in \mathbf{R}$ ),  $\omega_i$  is cutoff frequency, and  $G$  is gain. This transfer function is advantageous to use in case that we do not know value of the battery internal resistance. Because for very low frequencies the value of TF gets in a limit case to zero and battery resistance approaches infinity. For many cases this type of battery

modelling is inadequate and the DC battery internal resistance must be considered so the TF [2] can be easily transformed to

$$F(s) = G_0 \prod_{i=0,1,2,\dots} \frac{(s + \omega_i)^{q_i}}{\omega_i^{q_i}}, \quad [3]$$

where  $G_0$  is the reciprocal value of the DC battery internal resistance.

The main drawback of representation of battery transfer functions by [2] or [3] is the coefficients  $q_i$  which can be generally any real numbers. This causes many problems because working with such a system, i.e. with the fractional system, is very complicated and there is not much available software for numerical simulation of such a system at the present time. The usual way to working with the system described by [2] or [3] is to approximate these TF by rational transfer functions with only integer coefficients  $q_i$ , see (4) and (5).

Base on previous reasons, we use for modeling such a nonlinear transfer function an artificial neural network (NN) in this paper. We deal with choosing the right network structure for minimizing the difference between measured values and values estimated by used NN.

### Neural Network for Battery Transfer Function Approximation

The neural networks can precisely model highly nonlinear processes and found application in many scientific fields, see (6). We use their capability to precisely approximate any function to approximate the battery transfer function. An example of a measured Bode plot for an alkaline battery is shown in Figure 1. This TF can be relatively precisely approximated using [3] but we on the other hand use artificial NN. Because the obtained results by this method may be relatively easily generalized and it can be constructed general NN for an approximation of TF which can take into account the actual state of the battery, i.e. temperature, state of charge, and so on. This generalization is in a case using only TF is almost impossible.

For a simple approximation of TF can be used NN schematically shown in Figure 2. The main aim of this article is to show the influence of the number of neurons in the hidden layer and influence of the shape of activation function on the ability to NN approximated the battery transfer function with sufficient accuracy.

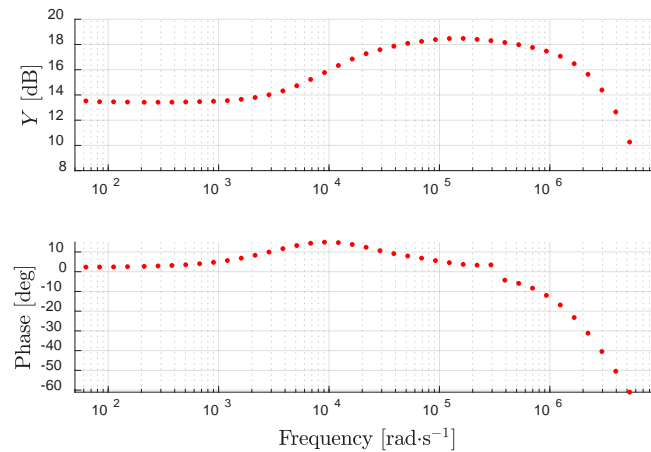


**Figure 1.** Measured Bode plot for alkaline battery.

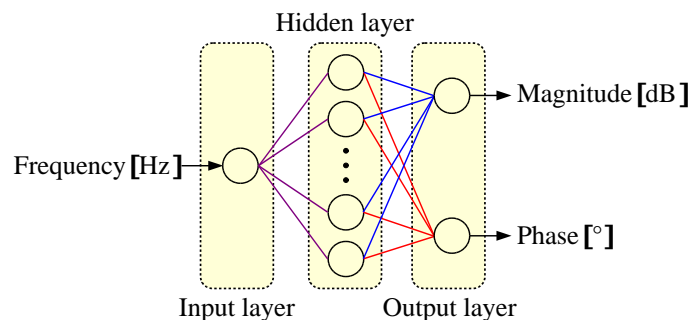


**Figure 2.** Neural network for approximation of battery transfer function.

## Conclusions

The paper deals with a description of the dependence of alkaline battery admittance on frequency. This dependence can be classically described by the general fractional transfer function. In the paper, it is used for mathematical modeling such a dependency on the artificial neural network. There is a discussed choice of an optimal number of neurons in the hidden layer and the optimal choice of activation function for an individual layer of the neural network. Obtained results from fractional transfer function and neural network are compared with measured frequency characteristics.

## Acknowledgments

This research work has been carried out in the Centre for Research and Utilization of Renewable Energy (CVVOZE). Authors gratefully acknowledge financial support from the Ministry of Education, Youth and Sports under institutional support and BUT specific research programme (project No. FEKT-S-20-6379).

## References

1. G. Saldaña, J. I. San Martín, I. Zamora, F. J. Asensio, O. Oñederra, *Energies*, **12** (14), 2750 (2019), 12, 2750. DOI: 10.3390/en12142750.
2. S. Li, K. Li, E. Xiao and C. Wong, *IEEE Transactions on Industrial Electronics*, **67** (10), 8484 (2020). DOI: 10.1109/TIE.2019.2949534.
3. R. Cipin, M. Toman, P. Prochazka, I. Pazdera, *ECS Transactions*, **87** (1), 269 (2018). DOI: 10.1149/08701.0269ecst.
4. S. Mahata, S. K. Saha, R. Kar and D. Mandal, *IET Signal Processing*, **13** (1), 112 (2019). DOI: 10.1049/iet-spr.2018.5128.
5. A. Yüce, F. N. Deniz, N. Tan, *IFAC-PapersOnLine*, **50** (1), 9736 (2017). DOI: 10.1016/j.ifacol.2017.08.2177.
6. O. I. Abiodun, A. Jantan, A. E. Omolara *et al.*, *IEEE Access*, **7**, 158820 (2019). DOI: 10.1109/ACCESS.2019.2945545.

## Obtaining Quantum Dots of Graphene from Partially Unzipped Multi-Walled Carbon Nanotubes

M. O. Danilov<sup>a,\*</sup>, S. S. Fomanyuk<sup>a</sup>, G. I. Dovbeshko<sup>b</sup>, I. A. Rusetskyi<sup>a</sup>,  
G.Ya. Kolbasov<sup>a</sup>, G. G. Yaremchuk<sup>a</sup>

<sup>a</sup>Institute of General and Inorganic Chemistry of the NAS of Ukraine,  
32/34 Academic Palladin Avenue, Kyiv, 03142, Ukraine.

<sup>b</sup>Institute of Physics of the NAS of Ukraine, 46 Nauky avenue, Kyiv, 03039, Ukraine.

\*Corresponding Author E-mail Address: danilovmickle@rambler.ru

### Introduction

Emitted nanostructures are very attractive because of their widely used in optoelectronic devices, and in biomedicine as biological markers. Consider nanostructured forms of carbon such as fullerene, single-walled carbon nanotubes (SWCNTs) and multi-walled carbon nanotubes (MWCNTs), graphene, which have many properties that differ from their bulk counterpart. Recently it has been reported that carbon nanotubes [1] and graphene nanoparticles in special condition [2] effectively emit in the visible range. Using some kind of oxidizing effect applied to nanotubes, it is possible to longitudinally unzipped MWCNTs and obtains graphene sheets with the corresponding number of layers [3]. By controlling the process of unzipping nanotubes, it is also possible to obtain MWCNTs with a defective structure or, as they are also called, partially unzipped multi-walled carbon nanotubes (PUMWCNTs). Unusual electronic properties of PUMWCNTs with a structure called a chair were discovered, depending on the degree of unzipping of such nanotubes. The literature describes various methods for unzipping nanotubes, which differ only in the method of exposure to multi-walled carbon nanotubes leading to the unzipping of nanotubes or the possible creation of quantum dots. In [1] the authors reported about a method for producing carbon nanocrystals emitting a strong blue glow after electrochemical treatment of MWCNTs. In our previous works, the possibility of the controlled opening of MWCNTs was shown [3]. Therefore, we investigated the most promising, in our opinion, electrochemical method for the synthesis of PUMWCNTs [4]. We have proposed a method of ultrasonic crushing of PUMWCNTs.

The aim of our work was to apply the electrochemical synthesis for the PUMWCNTs production and after it application of ultrasonic crushing technology for luminescent graphene quantum dots obtaining.

### Experimental part

TEM micrograph of PUMWCNTs sample 1 is presented on Figure 1 as well those for fully unzipped MWCNTs (sample 2) - on Figure 2. Figure 3 shows the results of photoluminescent (PL) studies of the PUMWCNTs samples after ultrasonic treatment. Namely, blue emission appeared at the 400–430 nm region (Figure 3 a, b) from the colloidal carbon nanotube solution excited with UV light at wavelengths 220, 255 and 320 nm. During luminescence studies, it was determined that the degree of unzipping of carbon nanotubes after ultrasonic treatment influences the increase in the luminescence intensity (Figure 3 b, sample 2) compared to (Figure 3 a, sample 1), but the shape and position of the PL spectra does not practically change. The authors of [5] suppose that carbon materials luminesce is due to edge and internal structural defects in carbon nanoparticles. We observed the maximum of the PL spectrum in Figure 3 (a, b) at 400 nm and photoluminescent

excitation (PLE) at 220–240 nm with a shoulder of 257 nm and a peak at 320 nm, respectively. A wide peak in the 220–240 nm with a shoulder of 257 is attributed to the interband  $\pi - \pi^*$  transition being a signature  $sp^2$  hybridized electronic orbitals [6]. For bilayer and single-walled carbon nanotubes with a decrease in diameter from 3 to 1 nm, the peak at 240 nm shifts to the UV region to 206 nm [7]. Based on these data, the size the carbon nanoparticles in our experiment are equaled to 1.5–3 nm. The peak of PL excitation at 320 nm is caused by the terminal groups C=O / COOH, OH, and C-O-C of carbon nanoparticles [8]. Typically, this peak for carbon nanoparticles is observed at 350–360 nm [9], but in the case of one or two-layer carbon nanoparticles with a lateral layer of 0.5–1.3 nm, it shifts to the UV region at 320 nm. Accordingly, it can be concluded that during ultrasonic treatment in a colloidal solution, one or two-layer carbon nanoparticles of small size 1.5–3 nm dominate.

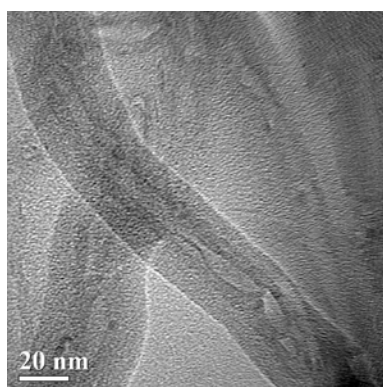


**Figure 1.** TEM micrograph of PUMWCNTs the sample 1.

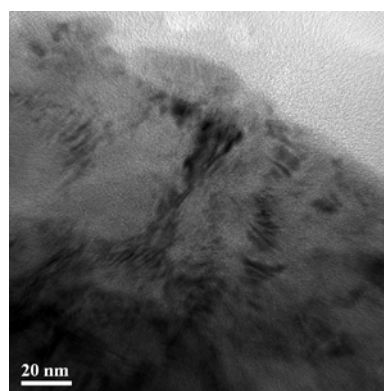


**Figure 2.** TEM micrograph of fully unzipped MWCNTs the sample 2.

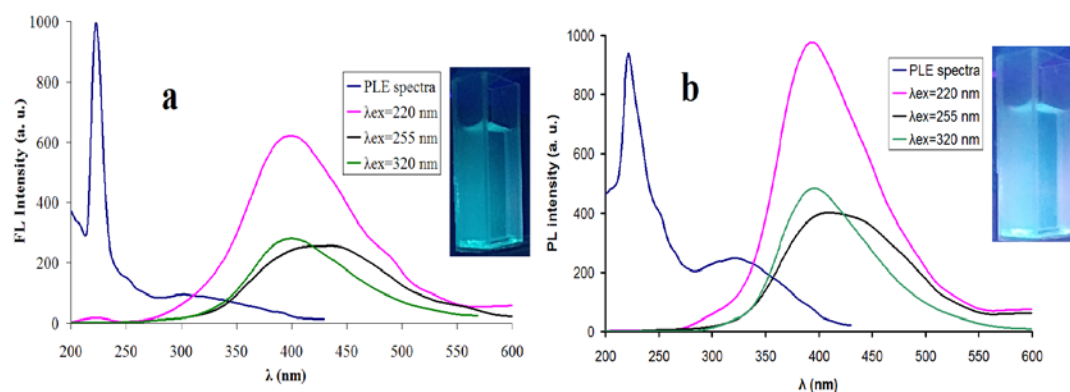


**Figure 3.** Photoluminescence excitation spectrum and photoluminescence spectra at different excitation for: sample 1 (a); sample 2 (b).

After nanotubes unzipping, the studied samples contain both small graphene particles with a unit size of up to ten nm, the so-called nanodots, and large fragments - microns or more, as well as oxidized forms of graphene particles - graphene oxide particles. It is known that nanotubes possess luminescent properties in the NIR-IR region (more than 1  $\mu\text{m}$ ). Under normal conditions, graphene does not emit in visible region, but small grains (nm and tens of nm - usually no more than 20 nm) can produce blue photoluminescence, which usually does not depend on the wavelength [10] and decreases in intensity with increasing excitation wavelength. Our experiment showed the same for all samples under study. Regardless of the excitation wavelength (220 nm and 300 nm), we

observed PL at a wavelength of about 400 nm, and the PL intensity decreased with an increase in the excitation wavelength (or a decrease in the energy of the exciting quantum). The value of the PL maximum is higher in energy than in the case of [11], but we suppose that the latter is due to the fact that our graphene nanoparticles are curved and have twisted edges, since they are the result of exfoliation from the walls of nanotubes 2–40 nm in diameter and possibly strained. Study the electrocatalytic characteristics of quantum dots as material for oxygen electrodes showed that they can be used as a catalyst support.

### Conclusions

Here we proposed a method for producing graphene quantum dots by ultrasonic grinding of PUMWCNTs. Exfoliation from the walls of nanotubes as result of ultrasonic grinding produced quantum dots of graphene and possibly curved strained single or double layer graphene nanoparticles of cup-shaped shape with a size of 1.5–3 nm. Received photoluminescent quantum dots of graphene have the blue glow.

### Acknowledgement

We are thankful to NATO 985291 Project, Ukrainian-Polish research project 2018-2020” development of enhanced substrates based on 2D nanomaterials for fluorescent microscopy and spectroscopy: physical aspects and application.

### References

1. J. Zhou, C. Booker, R. Li, X. Zhou, T.-K. Sham, X. Sun, Z. Ding, *J. Am. Chem. Soc.*, **129**(4), 744 (2007).
2. V. Boiko, R. Tomala, O. Posudievsky, V. Moiseienko, G. Dovbeshko, W. Strek, *Optical Materials*, **101**, 109744 (2020).
3. M. O. Danilov, I. A. Slobodyanyuk, I. A. Rusetskii, G. Ya. Kolbasov, in *Graphene Science Handbook: Fabrication Methods*, M. Aliofkhazraei, N. Ali, W. I. Milne, C.S. Ozkan, S. Mitura, J.L. Gervasoni, Editors, p. 205, CRC Press/Taylor & Francis, London/New York (2016).
4. M. O. Danilov, I. A. Rusetskii, G. I. Dovbeshko, S. S. Fomanyuk, G. Ya. Kolbasov, *ECS Trans.*, **95**(1), 273 (2019).
5. L. Lu, Y. Zhu, C. Shi, Y. T. Pei, *Carbon*, **109**, 373 (2016).
6. G. I. Dovbeshko, V. R. Romanyuk, D. V. Pidgirnyi, V. V. Cherepanov, E. O. Andreev, V. M. Levin, P. P. Kuzhir, T. Kaplas, Yu. P. Svirko, *Nanoscale Res. Lett.*, **10**, 234 (2015).
7. G. A. Rance, D. H. Marsh, R. J. Nicholas, A. N. Khlobystov, *Chemical Physics Letters*, **493**(1-3), 19 (2010).
8. D. Pan, J. Zhang, Z. Li, M. Wuet, *Adv Mater.*, **22**(6), 734 (2009).
9. W. Bin, R. Zhu, M. Wang, P. Liang, Y. Qian, S. Wang, *J. Mater. Chem. B*, **5**, 7796 (2017).
10. S. H. Jin, D. H. Kim, G. H. Jun, S. H. Hong, S. Jeon, *ACS Nano*, **7**(2), 1239 (2013).
11. Y. Dong, J. Shao, C. Chen, H. Li, R. Wang, Y. Chi, X. Lin, G. Chen, *Carbon*, **50**(12), 4738 (2012).

## Change of Geometric Accuracy of Structural Steels after Carburizing in Gas

D. Dobrocky<sup>a</sup>, Z. Pokorný<sup>a</sup>, Z. Joska<sup>a</sup>, Z. Studeny<sup>a</sup>, J. Prochazka<sup>a</sup>, E. Svoboda<sup>a</sup> and P. Dostal<sup>b</sup>

<sup>a</sup> Department of Mechanical Engineering, University of Defence in Brno, Kounicova 65 602 00 Brno, Czech Republic

<sup>b</sup> Department of Technology and Automobile Transport, Mendel University in Brno, Zemědělská 1, 613 00 Brno, Czech Republic

Chemical-thermal treatment of steels differs from other methods of heat treatment in that, in addition to structural changes, it also changes the chemical composition of the surface layer due to the diffusion of certain suitable elements into the steel. Carburizing can be defined as the saturation of the steel surface with carbon at a temperature above  $A_3$ . The resulting surface layer is characterized by high hardness and abrasion resistance after quenching. Carburizing also increases fatigue strength. Nowadays, carburizing at low pressure or vacuum carburizing is often used, which is a modification of carburizing in gas, while carburization is performed at pressures well below the level of atmospheric pressure (101 kPa). The advantage of this process is that no internal oxidation occurs; carburizing has a higher rate and uniformity of carburization, good reproducibility of the process and lower deformation. Carburizing is mainly used for parts subjected to abrasion (eg gears). However, even with this process, the geometric accuracy and surface texture of the parts change. The changes of geometric accuracy of ground samples from carbon steel C45, low-alloy Mn-Cr carburizing steel 16MnCr5 and medium-alloyed Ni-Cr carburizing steel 14NiCr14, which were vacuum-carburized in a CO/CH<sub>4</sub> atmosphere, were evaluated in this work. Geometric accuracy was evaluated by measurement using a 3D coordinate measuring machine, surface texture using a coherent correlation interferometer. After the carburizing process, changes in the dimensions of the samples were found in all steels. For C45 steel, the sample dimensions were reduced by  $0.028 \text{ mm} \pm 0.004 \text{ mm}$ , the surface roughness expressed by the parameter Ra decreased by  $0.28 \text{ } \mu\text{m}$ , which is 20%. In case of carburizing steels there was an increase in the dimensions of the samples, especially in the case of 14NiCr14 steel and a smaller difference in surface roughness. The same parameters of the carburizing process lead to different behaviour of carburized parts in different steels, in terms of changes in dimensions and surface texture.

## Battery Powered Multipurpose DC-DC Converter

M. Folprecht <sup>a</sup>, P. Prochazka <sup>a</sup> and D. Cervinka <sup>a</sup>

<sup>a</sup>Department of Power Electrical and Electronic Engineering, Brno University of Technology, Brno, 616 00, Czech Republic

This contribution refers about a design and development of a multipurpose DC-DC converter with pulse transformer, which is powered from a battery or an on-board car network. The converter with adjustable output voltage and current can supply many appliances. The design of pulse transformer, secondary rectifier, output filter, switching transistors and control circuits is included.

### Introduction

Power supplies with one adjusted output voltage value are a common application of DC-DC converters. Typical example is a notebook charger. This contribution deals with a less common sample of DC-DC converter, which is powered from the on-board car network or the battery. The output voltage and current values can be continuously set by user. Maximal output voltage value is 24 V and maximal output current is 5 A. Nominal input voltage is 12 V, maximal value is 15 V. This converter can work as a battery charger for many devices (mobile phones, notebooks) or a power supply for audio sets, cooling boxes, fans and similar appliances used in cars. It can be also used as a common service supply at places, where the electricity is not available. A built-in battery allows to work out of the car. The power part of the converter contains pulse transformer, although the galvanic isolation is not needed at this application. The converter is built in compact portable case, the output values are measured by V-meter and A-meter.

### Power Part and Pulse Transformer Design

For converters with low input voltage, a push-pull topology is suitable. The main advantage of this topology are source electrodes of both switching MOSFET transistors connected to ground. For that reason, gate drivers can switch these transistors directly without galvanic isolation. Circuit diagram of the power part is in Figure 1. Primary winding of the transformer consists of two identical sections  $N_1$  and  $N_2$  with the same number of turns. A common terminal of these sections is connected to a positive pole of the battery, the second terminals of windings are connected to ground (a negative pole of the battery) by switching transistors  $T_1$  and  $T_2$ . When the one transistor is switched on, a primary voltage appears at the appropriate section and it is transformed to the secondary winding  $N_3$ . At the same time, the second transistor is switched off and it is stressed by double of the battery voltage, because both sections of the primary winding work as an autotransformer. The voltage on the switched-off transistor is also raised up by voltage peaks caused by leakage inductance between both sections of the primary winding. These voltage peaks rise with load current. Double primary winding is the main disadvantage of this topology, which does not allow to use it for higher input voltage, for example rectified AC mains (1).

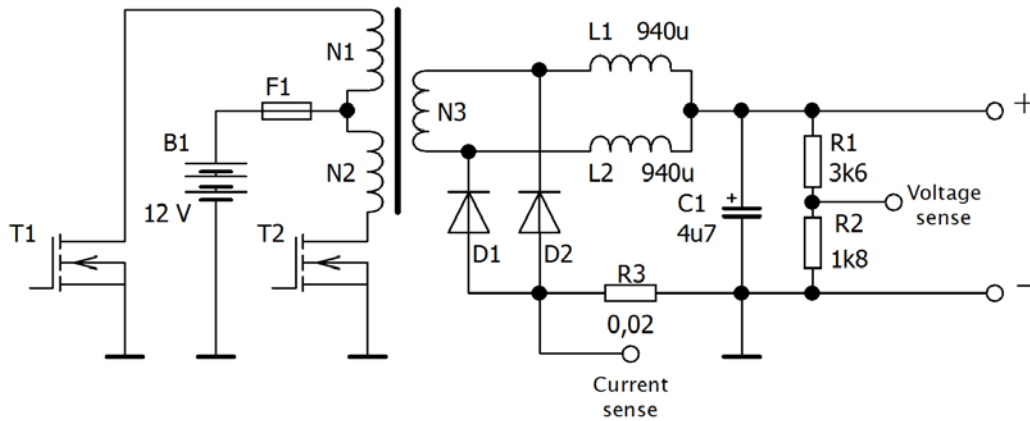


**Figure 1.** Circuit diagram of the power part

Flux linkage  $\Psi$  in a transformer core and a magnetizing current  $i_{\mu}$  are an integral of primary voltage, which has rectangular shape, so the magnetizing current and flux linkage has triangular shape. Primary current  $i_1$  is a sum of the magnetizing current and the load current transformed to primary side. Secondary voltage is also rectangular, and a height of the pulses is different with transfer ratio  $N_3/N_1$ . Secondary rectifier and output filter consist of two diodes  $D_1$  and  $D_2$ , inductors  $L_1$  and  $L_2$  and capacitor  $C_1$ . Two inductors are needed to eliminate the DC magnetization of pulse transformer. This problem is caused by synchronous interference, when PWM modulator is affected by noise from the power part. The interference leads to a deviation of duty cycles of power transistors. Load current is divided into two halves, which flow through inductors  $L_1$  and  $L_2$ . The use of two inductors allows a slight difference between maximal values of these two currents. For this reason, positive pulses can be wider and negative pulses can be narrower, when the deviation of duty cycles occurs. And as a result, transferred charges are the same, so the secondary current does not contain a DC component (2). A count of primary turns is given by equation [1]:

$$N_1 = \frac{U_1}{4 f B S_{Fe}} \quad [1]$$

Where  $U_1 = 12 \text{ V}$  is a battery voltage,  $f = 80 \text{ kHz}$  is a switching frequency,  $B = 0.35 \text{ T}$  is a chosen flux density and  $S_{Fe} = 75 \text{ mm}^2$  is a cross section area of the ETD-29 core. For mentioned values,  $N_1 = 2$  is obtained. A low number of primary turns leads to a low primary inductance. In that case, magnetizing current should have unacceptably high value and leakage inductance should be also significant. These are other disadvantages of the topology supplied from the low voltage. For this reason, the count of primary turns  $N_1 = 3$  was chosen and larger core ETD-39 with cross section area  $S_{Fe} = 128 \text{ mm}^2$  was used. To eliminate leakage inductance, each section of primary winding consists of two parallel legs. For the secondary winding, the count of turns  $N_3 = 9$  is obtained. But the secondary rectifier works as a current doubler. RMS value of the secondary current is only a half in comparison with a bridge rectifier, so it must be compensated by double value of secondary voltage because of energetic balance. Consequently, the count of secondary turns obtained from transfer ratio  $N_3/N_1$  must be doubled. Maximal value of magnetizing current is given by equation [2], where  $l_{Fe}$  is an effective magnetic length of the core and  $\mu_r$  its relative permeability (2).

$$I_{\mu\max} = \frac{4 f B^2 l_{Fe} S_{Fe}}{U_1 \mu_0 \mu_r} \quad [2]$$

Flux density  $B = 0.098$  T is obtained from [1], values  $l_{Fe} = 92.2$  mm,  $S_{Fe} = 126$  mm<sup>2</sup> and  $\mu_r = 1660$  are taken from data sheet (3). Maximal value of magnetizing current is 1.42 A. Cross section area of primary and secondary conductor is dimensioned to RMS value of current. In the case of primary current RMS calculation, magnetizing current cannot be neglected, because its value is comparable to working current with peak value 15 A. Because of skin effect, primary and secondary conductor must be divided into many thin insulated conductors. Primary winding is created from high frequency litz wire 70x0.15 mm with total cross section area  $S_{Cu1} = 1.9$  mm<sup>2</sup> and for secondary winding, wire 480x0.071 mm with total cross section area  $S_{Cu2} = 1,23$  mm<sup>2</sup> is used. Inductors  $L_1$  and  $L_2$  in output filter are constructed on ETD 34 core. Each inductor with inductance  $L = 940$   $\mu$ H is dimensioned to the half (2.5 A) of nominal load current value (5 A). A length of an air gap is 0.7 mm. For both inductors, conductor with cross section area  $S = 0.86$  mm<sup>2</sup> is used and winding has  $N = 79$  turns (1), (2). As the switching transistors  $T_1$  and  $T_2$ , MOSFET IRLI2910 are used. The main features of these transistors: drain-to-source voltage  $U_{DS} = 100$  V, nominal drain current  $I_D = 31$  A and drain-to-source resistance  $R_{DSon} = 0.026$   $\Omega$  (4). Low drain-to-source resistance is very important at this application. Transistors are driven directly from PWM modulator circuit SG3525. A regulation scheme is based on operational amplifiers and consists of two loops: master voltage loop and slave current loop. Output current is sensed by shunt resistor  $R_3$  and output voltage by divider  $R_1$  and  $R_2$  (Figure 1).

### Conclusion

This abstract deals with problematics of DC-DC converter powered from the battery. For this converter, the push-pull topology with pulse transformer was chosen. The body of the abstract is focused on the design of the transformer. Design problems and their solutions are explained. At following extended version of the contribution, design of other parts will be described, and results of the measurement will be summarized.

### Acknowledgment

This research work has been carried out in the Centre for Research and Utilization of Renewable Energy (CVVOZE). Authors gratefully acknowledge financial support from the Ministry of Education, Youth and Sports of the Czech Republic under institutional support and BUT specific research program (project No. FEKT-S-20-6379).

### References

1. A. I. Pressman, *Switching Power Supply Design-2<sup>nd</sup> ed.*, **669**, New York (1998).
2. M. Patočka, *Magnetické jevy a obvody ve výkonové elektronice, měřicí technice a silnoproudé elektrotechnice.*, p. 459-509, Brno (2011).
3. Ferroxcube, *ETD39 ferrite core data sheet.* (2008).
4. International Rectifier, *IRLI2910 power MOSFET data sheet.* (1998).

## Adhesion of PVD coatings on surface of small arm

Z. Joska<sup>1\*</sup>, L. Rak<sup>2</sup>, Z. Pokorný<sup>1</sup>, J. Horníček<sup>1</sup>

<sup>1)</sup> Department of Mechanical Engineering, Faculty of Military Technologies, University of Defence in Brno

<sup>2)</sup> Department of tactics, Faculty of Military Leadership, University of Defence in Brno

Corresponding author. [zdenek.joska@unob.cz](mailto:zdenek.joska@unob.cz)

### Abstract:

This work deals with the possibility of increasing the utility properties of the functional part of the weapon by deposition of PVD coating. These coatings are widely known for their high hardness and abrasion resistance without affecting the anti-corrosion properties. The experimental part evaluates the created duplex coating on the piston of the assault rifle Sa vz. 58. The evaluated coating was verified and durability tests were performed by the instruments from the Department of Mechanical Engineering. Evaluation of the duplex coating has been done on the Rockwell HRC 8150 L hardness tester, PVD coating adhesion was evaluated by indentation and scratch test which was performed on Bruker UMT 3 tribometer. Duplex coating adhesion, surface morphology and coating thickness was evaluated on optodigit microscope Olympus DSX 500. In addition, the impact resistance of the coating was evaluated by dynamic impact test. The durability tests of the coating were carried out during the training of students in the military training area in Vyškov. During the test, approximately 2000 rounds were fired. The results showed the application of PVD coating significantly reduced piston head wear and increased user comfort in the form of shortening time of the cleaning and maintenance process after firing.

## Ex-situ cell with positioner for XRD measurements in an inert atmosphere

O. Klvač<sup>a</sup>, O. Čech<sup>a</sup>

<sup>a</sup> Department of Electrical and Electronic Technology, Faculty of Electrical Engineering and Communication, BUT, Technická 10, 616 00 Brno, Czech Republic

This paper describes the construction of a hermetically insulated cell for post-mortem research of electrode materials of electrochemical cells. The first part specifies the problems of XRD characterization, followed by a description of the cell solving problems with hermetic insulation and distortion of diffraction patterns. Then, a positioning system for sample displacement error correction is described. Finally, attenuation of the used materials and the suitability of inert gases are discussed.

### Introduction

X-ray diffraction spectroscopy (XRD) is a widely used method of material analysis and can be well applied in the production and study of electrochemical cells. During the research, changes in the crystallographic parameters of electrode materials after intercalation are often investigated. However, these samples are highly sensitive to the atmosphere and must be encased in a suitable cell. It must provide good hermetic insulation, but at the same time, it must not significantly attenuate X-rays and distort the diffractogram. The requirement is also a simple assembly due to the limited manipulation in the glove box and the possibility of the sample displacement error correction [1].

### Experimental

A Rigaku MiniFlex 600 diffractometer in a theta-2theta arrangement is used for analysis, where Cu-K $\alpha$  emission line is detected. The first measurements of intercalated electrodes took place in a standard glass holder, which was covered with Kapton foil in a glove box filled with argon. However, due to the diffusion of air humidity through the film, the samples were discarded before the measurements were completed. From this point of view, coffee bag foil (CBF), where a thin layer of aluminum is applied to the polymer, has better properties. On the other hand, it has a high attenuation for X-rays and significantly distorts the diffractogram around the angle of 27 ° (see Fig. 2). An effective solution is to place it in a circle, as the same and thinnest layer of material is penetrated at all angles. Several types of plastic cells were created, where the foil was glued after inserting the sample and were practically tested and used [2]. For easier assembly and the possibility of displacement error correction, the cell in Figure 1 was finally manufactured.

The cell (1) is made of a duralumin rod. There are threads on the round edges that allow attaching the CBF (7) and the seal (8) by pressing U-profiles (6). In the glove box, the sample from the bottom part is inserted only by screwing on the sealing "plug" (9) serving as a holder. This hermetically closes the sample, it is possible to take it out of the glove box and place it on the positioning system.

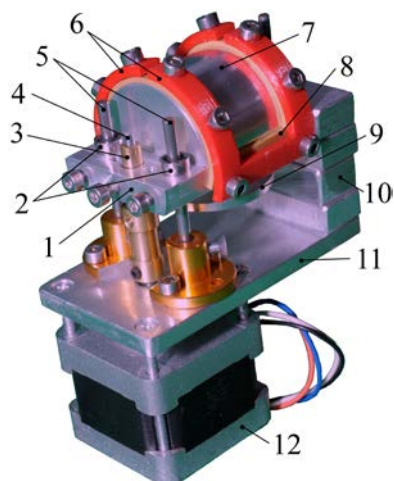


**Figure 1.** XRD cell in positioner system

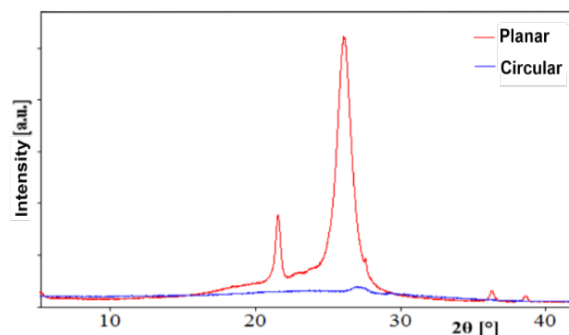


**Figure 2.** Comparison of the CBF contribution

The stepper motor (12) rotates a threaded rod (4) that passes through a brass nut (3) in the cell. Thanks to the smooth chromed rods (5) and linear ball bearings (2), the steps are converted to a change in height with a theoretical accuracy of 0,16  $\mu\text{m}$ . The smooth rods and the motor are screwed to the base (11), which is attached to the goniometer of the diffractometer via spacer blocks (10). A driver Polohu md09b and an ATmega8 processor are connected to the motor, which communicates with the PC via a serial terminal.

After inserting the cell into the diffractometer, the sample height is set manually. A quick scan is then performed to compare the peak position of a material that does not change its properties during intercalation, such as a copper substrate at a graphite electrode. To illustrate, Figure 3 compares the first scan of a clean electrode in a cell with an accurate measurement in a standard holder. Peak Cu (111) is shifted by 0.32  $^\circ$ . Taking into account the dimensions of the instrument, it can be calculated that the sample is 450.6  $\mu\text{m}$  above the center of the goniometer. After moving the cell down by this value, the position is correct (see Figure 4).

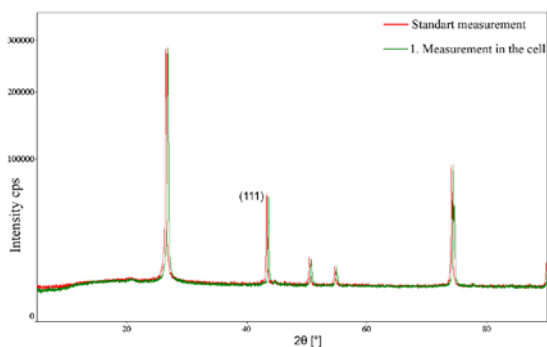


**Figure 3.** Graphite electrode before correction

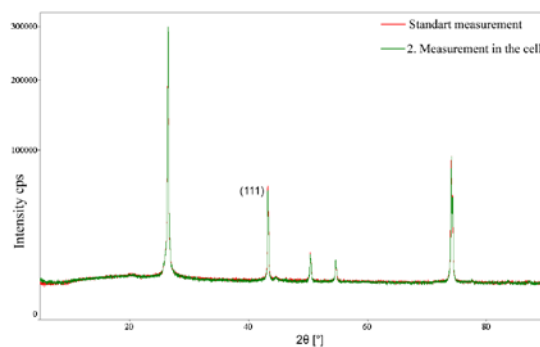


**Figure 4.** Graphite electrode after correction

## Discussion

The electrode materials are applied in a thin layer, and especially in the case of graphite, there is also a preferred orientation. Therefore, some peaks may not be visible. Low attenuation of the materials used is therefore a necessity.

Paradoxically, while the measured attenuation for Cu-K $\alpha$  by the two layers of CBF is only 7.2 %, in the case of argon inside the cell the attenuation is about 40 %. Using Beer-Lambert's law, general gas equation and values of mass attenuation coefficients from NIST, this value can also be calculated theoretically.

Figure 5 shows the ratio of the intensity of radiation that passes through argon to the intensity in air (standard measurement) as a function of the cell radius. The dependence is shown for different argon pressures. Figure 6 shows the same dependencies for helium.

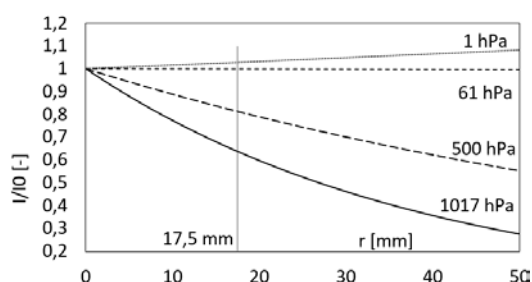


**Figure 5.** Attenuation of argon

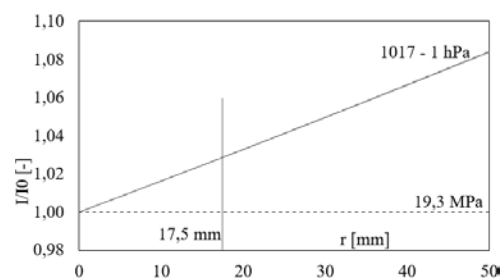


**Figure 6.** Attenuation of helium

At atmospheric pressure (1017 hPa), argon has about 17 times higher attenuation coefficient than air. The longer path through this environment, the more radiation will be attenuated and vice versa. While maintaining the cell radius (17.5 mm), it can only be decreased by decreasing the pressure. At half pressure, the attenuation is about 20 % and at about 61 hPa argon has the same attenuation coefficient as air. However, it is too low pressure and there is a risk of air being sucked in. Helium, on the other hand, has very small attenuation, it acts almost like a vacuum at atmospheric pressures and up to 19,3 MPa, it is lower than air. It, therefore, seems like more appropriate gas to improve the insulation properties and the readability of the diffraction patterns.

## Acknowledgments

This work was supported by the project of specific research: Materialy a technologie pro elektrotechniku III, reg. no. FEKT-S-17-4595. CzechNanoLab project LM2018110 funded by MEYS CR is gratefully acknowledged for the financial support of the measurements at CEITEC Nano Research Infrastructure.

## References

1. HARKS, P.P.R.M.L, F.M MULDER, and P.H.L NOTTEN. In situ methods for Li-ion battery research: A review of recent developments. Elsevier B.V, 2015, 288(C), 92-105. DOI: 10.1016/j.jpowsour.2015.04.084.
2. ORTIZ, Mariela G., Ondřej ČECH, and Marie SEDLAŘÍKOVÁ. Improved Electrochemical Performance of NCM Cathode Materials Based on the Modification of the Salt Content in the Electrolyte. ECS Transactions 2019, 95(1), 3-8. DOI: 10.1149/09501.0003ecst.

## Corrosion Resistance of Plasma Nitrided Austenitic Stainless Steel AISI 304 (X5CrNi18 10)

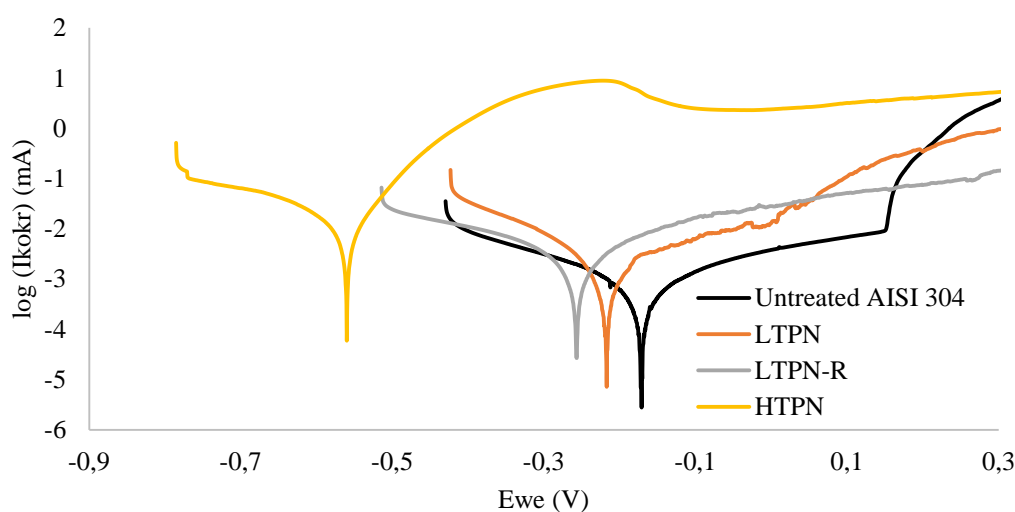
D. Kusmič<sup>1</sup>, O. Čech<sup>2</sup>, L. Klakurková<sup>3</sup>

<sup>1</sup>University of Defence, Department of Mechanical Engineering, Brno, Czech Republic, EU

<sup>2</sup>Brno University of Technology, Department of Electrical and Electronic Technology, Brno, Czech Republic, EU

<sup>3</sup>CEITEC Brno University of Technology, Research Group RG 1-06, Brno, Czech Republic, EU

In this paper, austenitic stainless steel AISI 304 (X5CrNi 18 10) has been subjected to low-temperature plasma nitriding (LTPN) at 400 °C (673 K) in 24H<sub>2</sub>:8N<sub>2</sub> (l/h) and in the reverse working atmosphere of 8H<sub>2</sub>:24N<sub>2</sub> (l/h) marked as LTPN-R, and additionally to high-temperature plasma nitriding (HTPN) at 550 °C (823 K) in 24H<sub>2</sub>:8N<sub>2</sub> (l/h) working atmosphere, for 15h for all PN processes. The microstructure, microhardness, and phase evaluation of the nitrided steel were studied. Nitrogen expanded austenite  $\gamma_N$  and Fe<sub>3</sub>N was identified after the LTPN process. After LTPN-R the  $\gamma_N$ , Fe<sub>2</sub>N, Fe<sub>3</sub>N, Fe<sub>4</sub>N, CrN, and Cr<sub>2</sub>N phases were identified. The HTPN process led to the formation of an increased volume of  $\alpha$ Fe, Fe<sub>3</sub>N Fe<sub>4</sub>N, and CrN phases. The LTPN techniques led to an increase of surface hardness, from initial 186 ± 3 HV1 (untreated steel) to 281 ± 15 HV1 (for LTPN and LTPN-R). The highest surface hardness reached the HTPN process (734 ± 5 HV1), thanks to the formation of CrN, Fe<sub>3</sub>N, and Fe<sub>4</sub>N rich nitride layer on the surface. microhardness profile measurement, scanning electron microscopy (SEM), and light microscopy study showed the formation of thin nitrogen expanded  $\gamma_N$  layer after LTPN and LTPN-R process, and a very thin nitride layer on the surface and thicker nitrogen expanded  $\gamma_N$  layer beneath it after HTPN process. The corrosion properties of the untreated, LTPN, LTPN-R, and HTPN treated steel were evaluated using the anodic potentiodynamic polarization tests (PPT) in neutral 2.5% NaCl deaerated solution. The corrosion rate CR (mm/y) increased only approx. 3-times for LTPN, 4-times for LTPN-R to untreated steel. The most negative E<sub>corr</sub> (V) and highest CR values were found after HTPN (increased 44-times to untreated steel) due to reduced passivation ability by chromium depletion caused by the forming of CrN. Additionally, the pitting was evaluated, and the pitting coefficient was calculated as well.



*PPT curves of untreated and plasma nitrided AISI 304 (X5CrNi 18 10) stainless steel in deaerated 2.5% NaCl solution*

## Numerical Model of a Scanning Electrochemical Microscope

M. Mačák<sup>a</sup>, P. Vyroubal<sup>a</sup>

<sup>a</sup> Department of Electrical and Electronic Technology, Brno University of Technology, Brno 616 00, Czech Republic

The presented article describes a numerical model of a scanning electrochemical microscope used for investigating topography and conductivity of various surfaces. The numerical model is based on Poisson-Nernst-Planck equations coupled with electrochemical reactions. Presented simulations investigate the influence of the distance between the electrode and the substrate, as well as the difference between the insulating and conducting substrate.

### Introduction

Scanning electrochemical microscopy (SECM) is a very precise analytical technique used for detailed studying of topography, conductivity, and reactivity of samples (for example live cells, electrodes, membranes, or thin films) (1). The core of this method is based on the recording of Faradaic currents along with the position of the micro-electrode. The obtained data is then used to create detailed maps of samples. SECM uses added or already present redox species in the system (1, 2). A typical microscope consists of an electrochemical potentiostat, a high-resolution positioning system and a small diameter micro-probe. The resolution and the response depend on various variables such as: size of the electrode, concentration of species, distance between the substrate and the electrode and the conductivity of the substrate. As a result, identifying the influence of these parameters by numerical simulations could lead to enhanced electrochemical microscopes with better characteristics (1).

### Numerical model

The numerical model is based on Poisson-Nernst-Planck equations coupled with the description of electrochemical reactions. Poisson's equation describes the electric field as well as the effects of ions charge density. Nernst-Planck equations describe the transport of ionic species due to convection, diffusion, and migration. In many cases, not every source of motion of species must be considered. In this case, the migration source term can be neglected due to the high amount of the electrolyte, which suppresses the voltage gradient in the electrolyte. The convection term can be ignored as well, as no flow is expected. This means, that species can be transported only by the diffusion, which greatly simplifies the model (2, 3, 4). The rate of electrochemical reactions is described through the Butler-Volmer reaction (4).

In this work, a response of a general one-electron redox reaction, with the reduction potential of 0 V, has been investigated. Figure 1 shows the illustration of the computational domain. The diameter of the electrode is 20  $\mu\text{m}$ . The influence of the distance between the electrode and the substrate (1  $\mu\text{m}$ , 5  $\mu\text{m}$ , 10  $\mu\text{m}$ , 200  $\mu\text{m}$ ) has been studied. A sweeping triangle signal from -0.5 V to 0.5 V has been applied to the electrode. In the second case, a part of the insulating substrate has been transformed (shown in Figure 1) to conducting and a potential of -0.25 V has been applied.

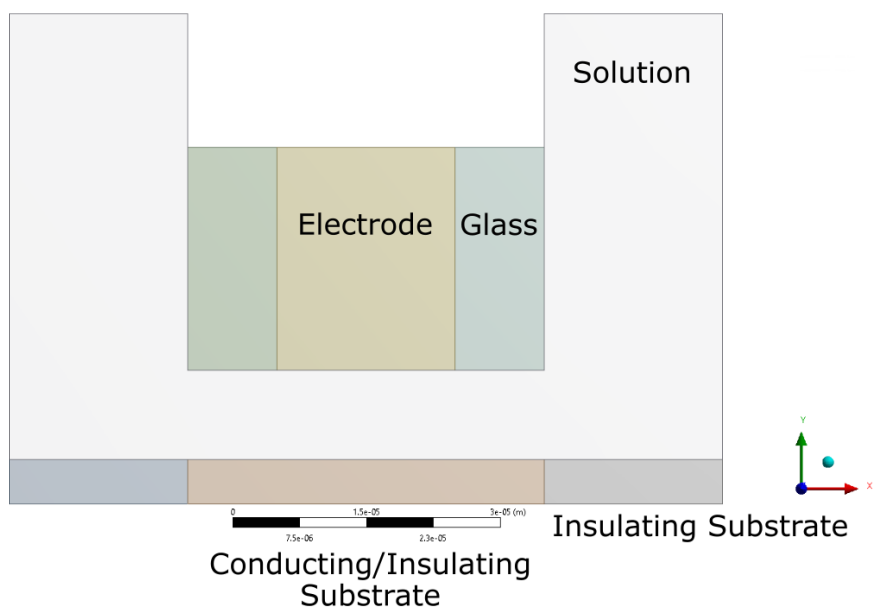


**Figure 1.** Illustration of the computational domain

## Results

In the first case, whole substrate was considered insulating and the voltammetric response was recorded. Figure 2 shows resulting voltammograms for different distances between the electrode and the substrate. The distance of 200  $\mu\text{m}$  mimicked the response of the unhindered micro-electrode. As the distance decreased it was possible to notice a change of shape and a decrease of the current density as the diffusion became limited. Even though a micro-electrode has been used, the effects of the diffusion were still visible.

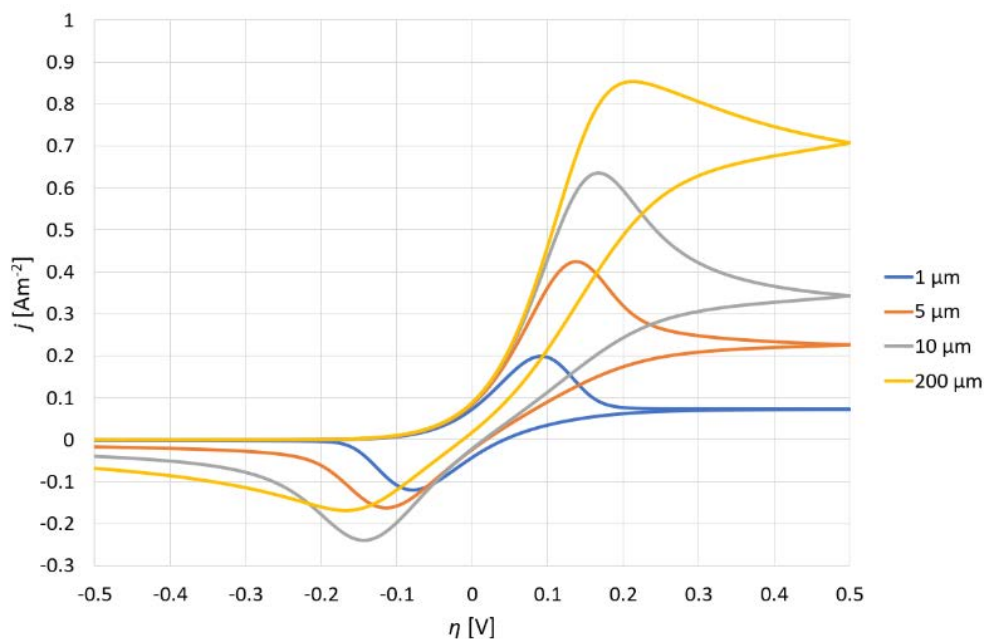


**Figure 2.** Voltammograms for insulating substrate

In the second case, the conductive part of the substrate created a positive loop, which increased the recorded current density. As the oxidation occurred at the electrode, the product was quickly reduced back. The amplification of the current density was inversely proportional to the distance between the electrodes. The response for 200  $\mu\text{m}$  is the same as in the previous case as no species had time to travel to the substrate electrode.

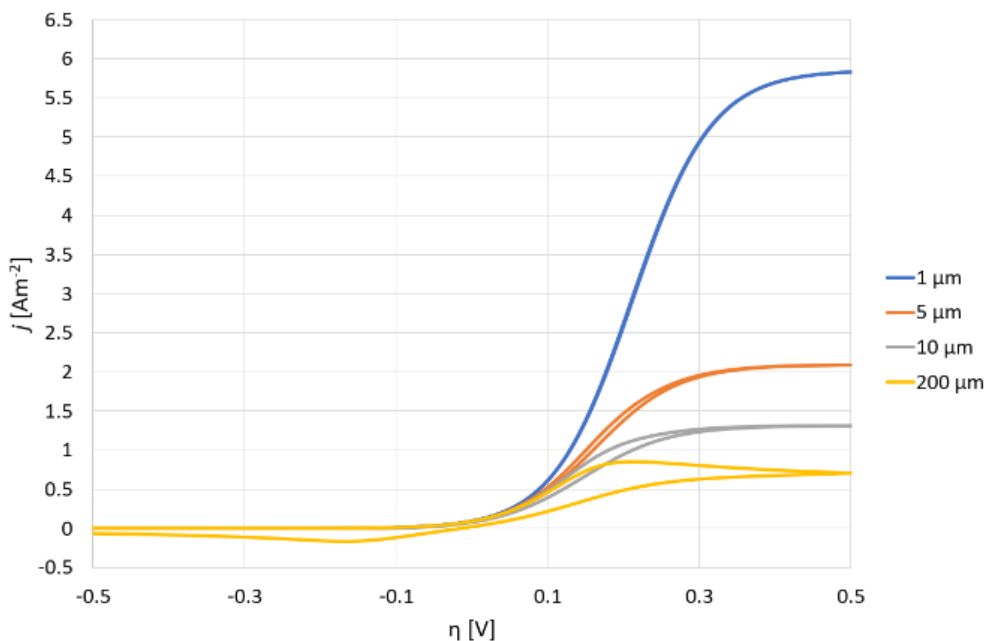


**Figure 3.** Voltammograms for conducting surface with the potential of -0.25 V.

### Conclusions

The results suggest that the presented model can study complex phenomena in the scanning electrochemical microscope. The results show that it is possible to differentiate between the insulating and the conducting surface. The resolution of the microscope greatly increases with decreasing distance between the surfaces. Ideally, their distance should not be larger than the length of the radius of the electrode. The results also indicate that the size and properties of the glass sheath might influence the electrodes response.

### Acknowledgments

This work was supported by the BUT specific research program (project No. FEKT-S-20-6206).

### References

1. F. P. Filice and Z. Ding, "Analysing single live cells by scanning electrochemical microscopy", *The Analyst*, vol. 144, no. 3, pp. 738-752, Jan. 2019.
2. A. L. Whitworth, D. Mandler, and P. R. Unwin, "Theory of scanning electrochemical microscopy (SECM) as a probe of surface conductivity", *Phys. Chem. Chem. Phys.*, vol. 7, no. 2, pp. 356-365, 2005.

3. S. -yin Tan, D. Perry, and P. R. Unwin, “Double layer effects in voltammetric measurements with scanning electrochemical microscopy (SECM)”, *Journal of Electroanalytical Chemistry*, vol. 819, pp. 240-250, 2018.
4. P. Vyroubal, J. Maxa, T. Kazda, and J. Vondrak, “The Finite Element Method in Electrochemistry - Modelling of the Lithium-Ion Battery”, *ECS Transactions*, vol. 48, no. 1, pp. 289-296, Feb. 2014.

## Numerical Model of a Magnetohydrodynamic Pump

M. Mačák<sup>a</sup>, P. Vyroubal<sup>a</sup>

<sup>a</sup> Department of Electrical and Electronic Technology, Brno University of Technology, Brno 616 00, Czech Republic

The presented article describes a numerical model of a magnetohydrodynamic pump used for transporting conductive fluids, in which the electromagnetic field accelerates the fluid. The model has been derived from Navier-Stokes equations and coupled with Maxwell equations. Presented simulations investigate the influence of the electromagnetic field on the acceleration of the electrolyte flow.

### Introduction

Magneto-hydrodynamics (MHD) describes the influence of electromagnetic fields on the flow of electrically conducting fluids such as plasma, liquid metals, or electrolytes. This effect can be used for driving and controlling flows without utilizing any moving mechanical parts, which makes the design of devices simple and effective. Apart from applications in propulsion systems or in power generation, the use of MHD can be found in microfluids. Microfluidic devices can be used as reactors, micropumps, pressure flow sensors, mixers or even microfluidic fuel cells and batteries. Due to their flexibility, they are attracting interest from researchers as well as technology companies. This article presents a custom numerical model implemented into Ansys Fluent describing an MHD micropump. The model and obtained results might be used for design and optimization of new MHD micropumps as well as other devices (1, 2).

### Numerical model

The description of the steady state MHD model consists of Navier-Stokes equations (3) describing the flow of an electrolyte and Maxwell equations describing the electromagnetic domain (4). The effect of the electromagnetic field is described by the Lorentz force, which acts as a source term in the momentum equation of Navier-Stokes equations. As a result, the flow can be created even without any pressure difference. Additionally, the magnetic induction equation shows that the motion of the electrolyte in an external magnetic field induces a magnetic field in the medium. The induced magnetic field can be often neglected due to the low fluid velocity (5). The current density is defined through Ohms law in a conducting fluid as (4):

$$\mathbf{J} = \sigma(\mathbf{E} + \mathbf{v} \times \mathbf{B}) \quad [1]$$

To compare the results, the simulations were based on the work of Ito et al. (6), which studied the fluid behaviour in an MHD micropump. The illustration of the geometry is shown in the Figure 1.

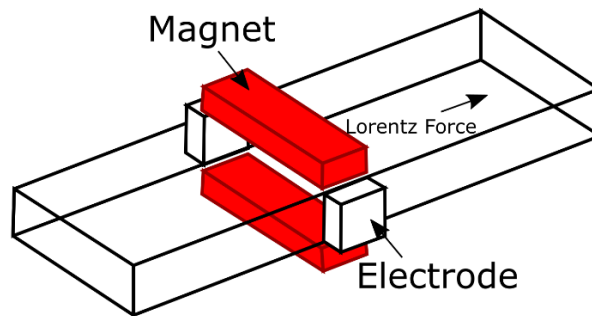


**Figure 1.** Simplified illustration of an MHD micropump

## Results

The results obtained by the presented numerical model are in great agreement with the findings of Ito et al. (6) and Hasan et al. (1). For the driving current of 8.4 mA, the maximum velocity in the centre of the channel was  $2.52 \text{ mm}\cdot\text{s}^{-1}$ . For the driving current of 14.6 mA, the maximum velocity in the centre of the channel was  $4.52 \text{ mm}\cdot\text{s}^{-1}$ . Figure 2 shows the comparison of obtained velocity profiles with characteristics of a Poiseuille flow, with the profile of a Hartmann's flow, which is characterised by strong coupling between electromagnetism and hydrodynamics. Figure 3 shows the velocity distribution in the cross section of the channel.

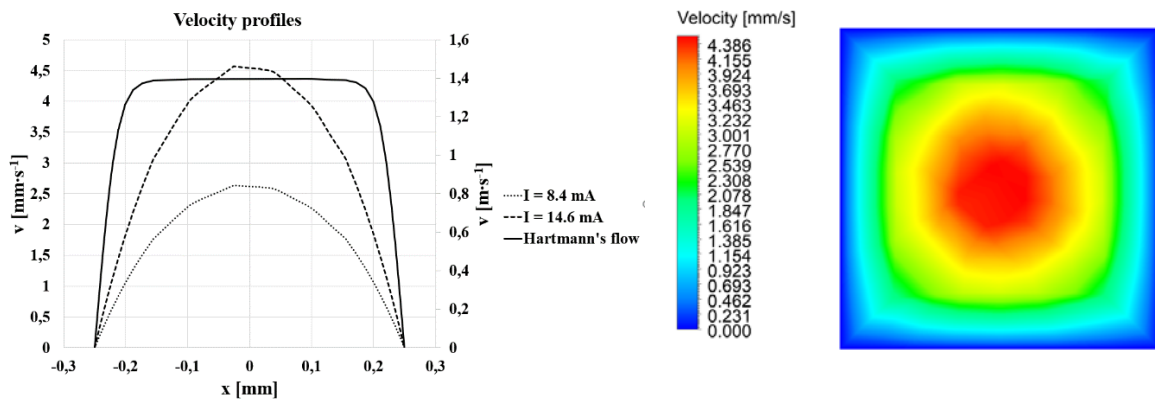


**Figure 2.** Velocity profiles of the electrolyte flow. Comparison to a general Hartmann's flow

**Figure .3** Velocity distribution in the cross-section of the channel for  $I = 14.6 \text{ mA}$

## Conclusions

The presented numerical model can be used for the modelling of MHD effects in microfluidic devices. The study also investigated the effect of induced field by the flowing electrolyte. The results suggest that the effect of the induced current density is insignificant due to the low velocity of the fluid and the term can be neglected. As a result, the solution can be greatly simplified without decreasing its accuracy. For higher velocities or macroscopic applications such simplification might not be valid, and the effects should be considered. To observe the effects of the induced field (a Hartmann's flow), it would be necessary to replace the used electrolyte for a liquid metal with high electrical conductivity or change the dimensions of the micropump.

### Acknowledgments

This work was supported by the BUT specific research program (project No. FEKT-S-20-6206).

### References

1. M. I. Hasan, A. J. F. Ali, and R. S. Tufah, “Numerical study of the effect of channel geometry on the performance of Magnetohydrodynamic micro pump”, *Engineering Science and Technology, an International Journal*, vol. 20, no. 3, pp. 982-989, 2017.
2. O. M. Al-Habahbeh, M. Al-Saqqa, M. Safi, and T. Abo Khater, “Review of magnetohydrodynamic pump applications”, *Alexandria Engineering Journal*, vol. 55, no. 2, pp. 1347-1358, 2016.
3. J. Maxa, P. Hlavata, and P. Vyroubal, “Analysis of Impact of Conic Aperture in Differentially Pumped Chamber”, *Advances in Military Technology*, vol. 14, no. 1, Jul. 2019.
4. P. Fiala, R. Kadlec, and J. Zukal, “Measuring Fluid Flow Velocities in the Context of Industry 4.0”, in *2019 12th International Conference on Measurement*, 2019, pp. 295-298.
5. L. P. Aoki, M. G. Maunsell, and H. E. Schulz, “A Magnetohydrodynamic Study of Behavior in an Electrolyte Fluid Using Numerical and Experimental Solutions”, *Revista de Engenharia Térmica*, vol. 11, no. 1-2, pp. 53-60, Dec. 2012.
6. K. Ito, T. Takahashi, T. Fujino, and M. Ishikawa, “Influences of Channel Size and Operating Conditions on Fluid Behavior in a MHD Micro Pump for Micro Total Analysis System”, *Journal of International Council on Electrical Engineering*, vol. 4, no. 3, pp. 220-226, Sep. 2014.

## Thermal management of lithium ion batteries

S. S. Madani

Aalborg University, Department of Energy Technology, Aalborg, DK-9220, Denmark

Email: ssm@et.aau.dk,

The problem of air pollution and increasing emission of carbon dioxide in the world in recent years has been in the news and concerns of citizens of megacities. From the society perspective air pollution which produces NO<sub>x</sub> and Carbon Dioxide is a problem that has existed in various cities of the world. Anywhere that has managed to reduce air pollution and its control. In other words, they have worked on process and targeted programs which contribute to renewable energy development. Limited fossil fuels resources and the problems caused by greenhouse gas emissions is obvious to everyone and it is necessary to pay more attention to renewable energy. With the development of clean energies, emissions of carbon dioxide will be controlled. Special capacity for economic development, Particularly in the areas of business and employment Supply and energy security , Protect the environment and reduce air pollution are three important advantages of Renewable energy sources. The unique status of renewable energy in reducing air pollution and tackle climate change causes to develop renewable energies to reduce the risks of climate change.

### Introduction

The more we use combustion engines the more we have vehicle emissions which contribute to air pollution. for reduction of dangerous gasses in cars , using green vehicles, such as electric vehicles is inevitable .To reduce NO<sub>x</sub> and Carbon Dioxide which are greenhouse gasses and global warming factor, renewable transportation is needed and in consequence the need for electrification of the transportation sector. Easy Charging, Low maintenance costs, are some of the advantages of these vehicles and also they decrease dependence on oil and so their advantages greatly outweigh their disadvantages.

Development of electronic devices such as mobile phones and laptops has increased the demand for rechargeable batteries, especially lithium-ion batteries. In the meantime, among other types of batteries, lithium-ion batteries have shown better performance and efficiency and has the highest production rate among other types of batteries. These batteries like other types of batteries consist of electrochemical cells and two electrodes and an electrolyte material. In the process of lithium batteries charging, in the positive electrode lithium is converted to positive lithium - ion , and in negative electrode lithium ion is turned into LiC<sub>6</sub>[1]. In Lithium-ion batteries, usually the positive electrode or cathode is made up of a lithium compound, such as lithium cobalt oxide and the negative electrode, or anode made up of carbon and there is a separating layer between them. The electrolyte in lithium-ion batteries is composed of the lithium salt in an organic solvent. A view of a lithium ion battery is shown in Figure1.

### State-of-the-art description

For the first time in 1786 Galvani discovered a new way to generate electricity by chemical materials. Later these cells became known as galvanic cells. From 1800 onwards great progress in the field of batteries was seen. But first, lead-acid rechargeable batteries that are used in vehicles today, were built in 1859 and the next evolution in rechargeable batteries occurred with the construction of nickelcadmium batteries in 1960 (Ni-Cd). But in 1990, these batteries have been replaced

with Nickel-Metal Hydride batteries. The development cycle of rechargeable batteries was completed with the invention of lithium-ion batteries in 1991 and the first lithium-ion-polymer batteries were made in 1999. In recent years, with the use of nanoparticles in these batteries, their efficiency increased dramatically [2]. In 1991, Sony and Asahi Kasei released the first commercial lithium-ion battery [3]. Lithium-ion batteries are appropriate for hybrid electric vehicles attributable to their high energy density correspondent to other rechargeable cell chemistries. Nevertheless, these batteries have not been redeployed to a wide extent and in a commercial manner in these vehicles yet attributable to safety, cost, and poor low temperature performance, which are all confrontation correlated to battery thermal management. Although lithium-ion batteries present many advantages, but there is a room for improvements of battery packs thermal management. Thermal issues associated with electric vehicle (EV) and hybrid electric vehicle (HEV) battery packs can significantly affect performance and life cycle. It is so important to improve thermal design of the battery packs in EVs because in future batteries will need to have even higher energy densities in order to achieve driving ranges of the conventional combustion vehicles 400-800 km. This means that there will be a higher energy density cells (higher heat dissipation due to losses) encapsulated in even smaller footprints, what will result in self-heating up of battery cells in the battery pack. Thus, efficient and cheap cooling strategies are required in order to: - maximize lifetime; - improve battery pack performance;

Better distribute heat in the battery pack (equal temperature of cells will result in more uniform battery aging); - avoid abusive temperature conditions (safety). Another important aspect is to cool battery cells during the fast charging (high heat dissipation). In this research, by considering the other researchers' works which have been done related to lithium-ion batteries for electric vehicles. A new method will be presented by considering different flow distribution in coolant channel with different coolant fluids and Optimization with CFD and Thermal management of lithium-ion batteries for electric vehicles and compare them with the experimental result to find the best and efficient way for Thermal management of lithium-ion batteries. This model and method can be applied to many other batteries. Although lithium-ion batteries present many advantages, but there is a room for improvements of battery packs thermal management. In recent years, several studies have been done in order to achieve a proper heat management systems for these batteries. But the impact of the cooling fluid flow distribution has not been sufficiently studied. Rao and Newman have estimated the amount of heat generated inside the cells with the energy balance laws and enthalpy changes to the system [5]. Sato offered a thermodynamic model and compared the results with laboratory studies to scrutiny the amount of heat generated in a battery [6]. Kizilel and his colleagues have compared two different thermal management system using CFD modeling [7]. Booth and his colleagues have examined the effects of design on the thermal performance of batteries [8]. Karimi and li used a mathematical model to evaluate the performance of different systems in the thermal management of these batteries [9]. so far the focus was put mostly on thermal management of battery cells, but I want to focus on battery packs and their optimal thermal management and multi-objective optimization.

### Methodology to be used in this study

Thermal problems related to lithium-ion batteries have restricted their usage for high energy applications. Since a single cell from the battery pack, does not provide a lot of power and energy, thus, for high-power applications, such as electric vehicles, a large number of the cells should have come together in series and parallel to provide sufficient power to move the car.

Battery temperature rise is caused by electrochemical reactions. If the battery temperature is not properly controlled, then it will cause shortening of its lifespan, faster capacity reduction or even in severe cases, might cause battery explosion. For commercial high-energy applications, a proper battery thermal management allows to overcome problems related to heat production and improves significantly the performance of the battery. The uneven temperature distribution in a battery pack causes cells to experience different temperatures. And thus, the output voltage of each cell will differ depending on battery cell temperature. This causes uneven battery cell degradation and in consequence even higher temperature discrepancies between each battery cell. According to the above-mentioned problems, the use of a heat management system to control the operating temperature in a set of batteries will be required. This system should also reduce the temperature of the entire set, and causes a homogeneous temperature distribution within the different cells. In recent years many efforts have been done to avoid battery thermal runaway situations that can appear when a cell would attain a high enough temperature to commence exothermic reactions that often are at first sluggish to progress. Such conditions could be the consequence of a prompt cell discharge, of cell flaw, or of a variation in ambient situations. Well-designed thermal management systems should be able to control the pack temperature and protect the battery pack from these exothermic reactions. Then again, a badly devised system would allow the temperature climb to a spot where a thermal runaway becomes unavoidable. Good battery pack management system should be able to manage not only fresh but also aged cells. In this research, in order to demonstrate the effect of different flow distribution in coolant channel and with a different coolant fluid, a CFD modeling will be used and the results will be compared to experimental results by considering different battery shapes and models for flow distribution in coolant channel and also different conventional coolant fluids. Moreover, for each item, the fluid pressure drop in the collection and flow distribution will be calculated and required a fan or pump power to drive the fluid will be calculated and compared to experimental results. Although the fluids heat capacity is very important coefficient, the costs related to pressure drop and power or fan or pump power to drive the fluid and also less complexity in design and low cost and weight should be considered, and also simpler control mechanism should be considered. Then the multi objective optimization problem can be designed and solved. The results can be used to optimize system performance according to required power for the battery thermal management system in different situations. In this research, it will be considered a substructure for evaluating the effect of thermal management systems. To survey heating scenarios of the cell due to innate inner resistance, cells will be discharged at dissimilar rates and their inner impedance will be calculated. Moreover, it will be studied the self-heating process of cells due to the sluggish exothermic reactions that are usually the forerunner to a thermal runaway occurrence. Using the experimental results information, which will be incorporated in a Computational Fluid Dynamics (CFD) model of a lithium-ion battery pack. The CFD model will be used to quantify the experiment. Common thermal managements systems exert the compelled movement of a fluid such as air or water or other common liquid to take away heat from regions that produce heat. The rate of heat obviation in such systems is contingent to the rate of fluid flow and the heat relocation virtues of the fluid. To faultlessly estimate and optimize a thermal management system, the system can be modeled in Computational Fluid Dynamics (CFD), which is able to model the thermal management system, along with the heat generation effect of battery cells during charging/discharging. A CFD model has the gross benefit of preparing stringent temperature

and heat flux repartition within the battery module. The outcome authorizes for the reconnaissance of the attendance of hot spots, comprehension the time-dependent dissemination of thermal waves within the pack as well as studying the effect of non-inductive heating in territorialized contribution of the module. A finite volume model of the battery module will be developed. The numerical model will be generated till arithmetic for the multi-layer construction of the pouch cells concluding in a non-isotropic medium. Resolving of the temperature dispensation inside the cell will be obtained by solving a three-dimensional conductive heat transfer equation in the cell domain:

### References

1. Wakihara, M., Recent developments in lithium ion batteries. *Materials Science and Engineering: R: Reports*,. 33(4): p. 109-134. 2001
2. [https://en.wikipedia.org/wiki/History\\_of\\_the\\_battery](https://en.wikipedia.org/wiki/History_of_the_battery)
3. "Keywords to understanding Sony Energy Devices".
4. Huang, S., et al., Improvement of the high-rate discharge properties of LiCoO<sub>2</sub> with the Ag additives. *Journal of Power Sources*, 148: p. 72-77, 2005.
5. L. Rao, J. Newman, Heat generation rate and general energy balance for insertion battery systems, *J. Electrochem. Soc.*, 144 (1997) 2697–2704.
6. N. Sato, Thermal behavior analysis of lithium-ion batteries for electric and hybrid vehicles, *J. Power Sources*, 99 (2001) 70-77.
7. R. Kizilel, R. Sabbah, J.R. Selman, S. Al-Hallaj, An alternative cooling system to enhance the safety of Li-ion battery packs, *J. Power Sources*, 194 (2009) 1105–1112.
8. G.G. Botte, B.A. Johnson, R.E. White, Influence of some design variables on the thermal behavior of a lithium-ion cell, *J. Electrochem. Soc.*, 146 (1999) 914–923.
9. G. Karimi, X. Li, Thermal management of lithium-ion batteries for electric Vehicles, *Int. J. Energy Res.*, 37 (2013) 13–24.

## Battery thermal management using air-cooling

S. S. Madani

Aalborg University, Department of Energy Technology, Aalborg, DK-9220, Denmark

Email: ssm@et.aau.dk,

Environmental problems such as air pollution, lack of energy sources, carbon dioxide emissions are increasing and destructive effects of fossil fuels on climate change is noticeable. Electric Vehicles (EVs) and Hybrid Electric Vehicles (HEVs) could be a beneficial solution to these problems. EVs, which employ batteries as their principal power source, produce no pollutions and are independent on oil and gas. Because of these advantages, EVs are considered as powerful candidates for the future of transportation systems.

### Introduction

Lithium-ion batteries are the main source of energy for the EVs. During discharge and charge processes, heat is generated inside Li-ion batteries that leads to rise their temperatures.

Temperature is one of the most important parameters of a lithium ion battery that needs to be attentively controlled, owing to the optimal working condition is generally limited between 20 and 65 °C [1]. Additionally, the battery's functioning temperature remarkably influences the battery's lifetime, cell degradation and efficiency. To achieve this goal many researchers are investigating to find new procedures for maintaining the temperature of Li-ion batteries in an appropriate functioning temperature range.

These batteries have so many advantages compared to other battery chemistries such as competitive cost and high-energy storage density. Notwithstanding, these batteries produce considerable heat during high power discharge and charge. Therefore, cooling of the Li-ion batteries has been the center of attention of automotive manufacturers and researchers in the past few years as a main issue for the expansion of EVs.

An extreme local temperature increase in Li-ion batteries is a principal issue in the thermal management correlated to Lithium-ion batteries, which causes a decrease of cycle life and may result in thermal runaway of an individual cell or entire battery pack.

Between different approaches for thermal management of the Li-ion batteries such as air-cooling, liquid cooling, pipes cooling and using phase change materials air-cooling has attracted more considerations among researchers owing to its simplicity, design flexibility, low cost and compactness.

Mohsen Mousavi and his colleagues [2] analyzed and optimized the influencing parameters on Lithium-Ion (Li-Ion) battery air-cooling which were used in Electric Vehicles (EVs) by considering their practical constraints. In addition, a genetic algorithm procedure was used to optimize the decision variables. Interpreting the outcomes showed that by enlarging the tubes diameter on the battery and keeping the air velocity in a specified range, Number of Transfer Unit (NTU) could be maximized.

Heesung Park [3] introduced a design of airflow arrangement for cooling the battery system by employing numerical calculations. The cooling efficiency was analyzed by implementing the thermal resistance model. The needed cooling performance was accomplished by using the suggested tapered pressure relief ventilation and manifold. In addition, the power consumption for functioning fan was improved owing to air pressure relief.

G. Y. CHO research team [4] developed a transient numerical model of a lithium ion battery (LiB) pack thermal management system by employing air-cooling for electric vehicle applications. The effects of module configuration in a battery pack were investigated with various ambient temperature situations. They concluded that the arrangement that more LiB cells were located near the airflow inlet is more efficient to decrease the temperature deviation between modules.

A Mariani [5] did an experimental investigation to evaluate the cooling of the batteries for electric car application. The position with maximum temperature were found by employing infrared camera together with two thermocouples. The location was found 27 mm under the negative pole. Air and water were selected as cooling fluids. They concluded that the water provides a lower temperature, but the employment of air is suggested because of its greater simplicity and safety.

S. K. Mohammadian proposed a specific type of pin fin heat sink for thermal management of Li-ion battery pack. Three-dimensional transient thermal analysis of an air-cooled module were investigated. The effects of various pin fin configurations, inlet airflow temperatures, inlet airflow velocities and discharge rates on the efficiency of the battery were studied. It was concluded that by employing this kind of pin fin heat sink compare to the heat sink deprived of pin fins not only reduces the bulk temperature inside the battery, but also reduces the alteration of the temperature field.

### Reference

1. M. Mousavi, S. Hoque, S. Rahnamayan, I. Dincer, and G. F. Naterer, "Optimal Design of an Air-Cooling System for a Li-Ion Battery Pack in Electric Vehicles with a Genetic Algorithm," pp. 1848–1855, 2011.
2. H. Park, "A design of air flow con figuration for cooling lithium ion battery in hybrid electric vehicles," *J. Power Sources*, vol. 239, pp. 30–36, 2013.
3. G. Y. Cho, J. W. Choi, J. H. Park, and S. W. Cha, "TRANSIENT MODELING AND VALIDATION OF LITHIUM ION BATTERY PACK WITH AIR COOLED THERMAL MANAGEMENT SYSTEM FOR ELECTRIC VEHICLES," vol. 15, no. 5, pp. 795–803, 2014.
4. O. Access, "Qualitative thermal characterization and cooling of lithium batteries for electric vehicles Qualitative thermal characterization and cooling of lithium batteries for electric vehicles," 2014.
5. S. K. Mohammadian and Y. Zhang, "Thermal management optimization of an air-cooled Li-ion battery module using pin- fi n heat sinks for hybrid electric vehicles," *J. Power Sources*, vol. 273, pp. 431–439, 2015.

## **Possibilities of the Utilization of Nitriding on Case-Hardening Steels**

J. Prochazka, Z. Pokorny, H. Ch. Nguyen

Department of Mechanical Engineering, Faculty of Military Technology, University of Defence in Brno, Brno 612 00, Czech Republic.

This paper studies the possibility of using plasma nitriding for treating case-hardening steels. For the experiment, the case-hardening steels equivalent 1.7131 (i. e. CSN 41 4220) and equivalent 1.5752 (i. e. CSN 41 6426), used in manufacturing of exposed parts of military and special vehicles as well as in parts of weapons, were selected. The verification of chemical composition was performed by the optical emission spectrometer Tasman Q4 Bruker. For observations of the microstructure and assessment of compound layers, the instrument Olympus DSX500i was used. In accordance with ISO 18203:2016(E), the depth of diffusion layers was evaluated from profiles of microhardness measured by the automated microhardness tester LM247 AT LECO. The results of the experiments show some benefits of applying plasma nitriding upon the selected case-hardening steels.

## The Usage of the Power Load as a Physical Diagram for Electric Vehicle Charging Modelling

V. Sít'ář<sup>a</sup>, L. Raková<sup>b</sup>, T. Hruška<sup>c</sup>, T. Vysloužil<sup>a</sup>

<sup>a</sup> Institute of Machines and Power Engineering, Faculty of Mechanical Engineering, UJEP, Na Okraji 1001/7, 400 01 Ústí nad Labem, Czech Republic

<sup>b</sup> Department of Electric Power and Environmental Engineering, Faculty of Electrical Engineering, UWB, Univerzitní 26, 301 00 Plzeň, Czech Republic

<sup>c</sup> ČEZ Distribuce, Teplická 1086/10, Podmokly, 405 02 Děčín, Czech Republic

The development of electric vehicles (EVs) brings a lot of new problems from the point of view of the electrical grid. Electric vehicles (EV) charging causes an impact load on the distribution grid, which is often non-symmetrical, and can reach high levels in relevant parts of the grid. This leads to the deterioration of electrical energy parameters, mainly voltage level and its symmetry. The inverters operation in electric vehicle charging stations (EVCSs) generates harmonics, which also leads to the deterioration of voltage quality. In the case of simultaneous charging of a large number of EVs from a poorly designed distribution grid, significant losses inside conductors occur and the service life of the distribution grid is shortened. In order to find out feedback influences of the EVCSs on the electrical grid when EV charging, it is desirable to simulate these states on a suitable software before installing EVCSs to the grid. This may eliminate problems with the voltage quality during the actual charging.

In the paper, the authors deal with the modelling of EVCSs by using an alternative simulation tool when charging them as a power load, which consumes predefined active power with desired level and duration at supply voltage changes in the grid. Such defined load differs from a general load in its behaviour. The authors' created load model is based on the real measured data. The behaviour of the created power load model is verified in the paper on a small distribution grid, where individual power consumers correspond to the standardized daily load diagrams of households and services. The goal of the paper is to verify proposed power load model. The load model is used for solving of active power losses in conductors of the electrical distribution lines, and mainly the level of supplied voltage and its symmetry.

## Tribological Properties of DLC Coating for Parts of Weapons

Z. Studeny<sup>a</sup>, Z. Pokorny<sup>a</sup>, D. Dobrocky<sup>a</sup>, Z. Joska<sup>a</sup> and J. Prochazka<sup>a</sup>

<sup>a</sup> Department of Mechanical Engineering , University of Defence in Brno, Brno, Czech Republic

The article deals with surface of material, which is suitable to produce parts of weapons. These parts of weapons are exposed to external influences during their service life, which reduce their service life. There are both external and internal surfaces of the functional parts of weapons. These surfaces particularly exposed to increased pressure and temperature. The environments, in which they work, are very often aggressive and extreme. There is an increased risk of wear and corrosion on the external and internal surfaces of such components. Suitable surface treatment can increase the surface hardness, abrasion resistance, corrosion resistance, etc. of surface weapons parts.

This article comprehensively evaluates the tribological properties of the DLC coating on a steel substrate and on an aluminum alloy substrate. It is important to know the properties of the coating on these substrates when designing weapon components. The use of lighter materials reduces the overall complexity of each soldier's combat mission.

### Introduction

Weapon components are currently made not only of steel, but also of aluminum alloys or non-metallic materials. In the case of steels and aluminum alloys, it is possible to modify these surfaces by depositing e.g. the PVD technology (1, 2, 3). For the purpose of this study, the DLC coating was deposited on steel CSN EN 10083-1 (42CrMo3) and on aluminum alloy EN AW 6082 (DIN 3.2315). Subsequently, the tribological characteristics of the coating on the base material were measured. A scratch test (4) was performed on the Tribolab UMT-3 devices. The results were used to determine the forces, which lead to damage or breaking of the coating (5). At constant loading, the coefficient of friction can be determined. The scratch hardness number of the DLC coating deposited on the aluminum alloy was also evaluated. The results thus obtained show the dependences of the surface characteristics after the application of the DLC coating by the PVD technology. The use of the analyzed coatings on these substrates is in the application and use of parts of the weapon (6).

The need to test coatings on weapon components is necessary to acquire knowledge of their resistance in extreme conditions. During testing and military exercises, these components are exposed to extreme conditions that are close to the conditions on the battlefield in a real combat situation. In such a situation, it is then necessary to rely on every part of the armament. If the shooting is stopped due to the low resistance of the surface of important parts of the weapon, the soldiers' lives are endangered. The proper functioning of weapons is very important to fulfill their combat mission. The study of surface properties and dependencies between materials brings valuable knowledge to the process of acquisition and introduction of military equipment into the army (7, 8).

## Materials and Methods

### Materials under Investigation

To support the experiment, two substrate materials were selected, on which a DLC coating was deposited. The first base material was 42CrMo4 steel (9), marked A for the purpose of the experiment. The DLC-coated backing material was marked A-DLC. The chemical composition of the steel was analyzed on a TASMEN Q4 optical spectrometer, the excitation source of which is the excitation of a spark discharge. The result of the analysis of the chemical composition of the sample is shown in Tab. 1. The resulting values are compared with the standardized values and it can be stated that the chemical composition corresponds to the guaranteed composition of 42CrMo3 (4) steels according to ČSN EN 10083-1.

**TABLE I.** Analysis of the chemical composition of a sample marked A made of 42CrMo3 steel.

| Content of elements (wt%)                                    |      |       |       |       |       |       |       |       |       |
|--|------|-------|-------|-------|-------|-------|-------|-------|-------|
| C  | Mn   | Si    | Cr    | Mo    | Ni    | P     | S     | Cu    | Al    |
| 0.54   | 0.65 | 0.249 | 1.045 | 0.149 | 0.128 | 0.005 | 0.15  | 0.176 | 0.016 |
| Recommended values of ČSN EN 10083-1 steel 42CrMo3 (42CrMo4) |      |       |       |       |       |       |       |       |       |
| 0.38   | 0.60 | <     | 0.90  | 0.15  | ----- | <     | <     | ----- | ----- |
| 0.45   | 0.90 | 0.40  | 1.20  | 0.30  |       | 0.035 | 0.035 |       |       |

The second base material analyzed was a sample made of aluminum alloy EN AW 6082. The sample of the base material made of EN AW 6082 alloy was marked B. The DLC-coated sample was analogously marked B-DLC. The chemical composition was analyzed again on the TASMEN Q4 optical spectrometer. The analysis result of the the sample chemical composition is shown in Tab. 2. Upon comparing the resulting values with the normalized values, it can be stated that the chemical composition of the samples corresponds to the guaranteed composition of the aluminum alloy EN AW 6082.

**TABLE II.** Analysis of the chemical composition of a sample marked A made of 42CrMo3 steel.

| Content of elements (wt%)        |       |       |      |       |       |       |      |        |       |
|----------------------------------|-------|-------|------|-------|-------|-------|------|--------|-------|
| Mn                               | Fe    | Mg    | Si   | Cu    | Zn    | Ti    | Cr   | Ni     | V     |
| 0.632                            | 0.327 | 0.726 | 1.22 | 0.056 | 0.109 | 0.051 | 0.01 | 0.0065 | 0.003 |
| Recommended values of EN AW 6082 |       |       |      |       |       |       |      |        |       |
| 0.40                             | <     | 0.60  | 0.70 | <     | <     | <     | <    | ----   | ----  |
| 0.10                             | 0.50  | 1.20  | 1.30 | 0.10  | 0.20  | 0.10  | 0.25 |        |       |

A carbon-based sliding coating – DLC – was applied to both substrates. The parameters of the DLC coating deposition will not be discussed in the article. The coating was formed on a Platit device to a thickness of up to 3  $\mu\text{m}$  for the A-DLC sample and up to 5  $\mu\text{m}$  for the B-DLC sample.

## Samples Characterization

### Microstructural Analysis

Experimental samples of materials A and B were divided by a grinding wheel from the Struers Company on a metallographic circular saw LECO VIPER-300M2. The parts formed by separation from the individual supplied samples were pressed, sample A at high temperature into

the Struers Isofast molding compound on a LECO RR-4X metallographic press at a press pressure of 2600 kPa. Pressing was performed for 4 minutes at 180°C. Samples B were pressed at low temperatures. After pressing, the individual samples were described and their surface was mechanically ground on a semi-automatic universal grinder/polisher KOMPAKT 1031 MTH. Prior to the surface treatment, the flat faces of the samples were ground with silicon carbide grinding paper from Hermes Company in a sequence with increasing mesh (#80, #120, #240, #400, #600, #1000 and #1000) according to the European FEPA marking. Then the samples were polished on LECO Brown Technotron sanding cloth with diamond paste LECO PREMIUM GRADE with an abrasive size of (1 and 3) μm, in order to obtain low roughness, almost no plastic deformation and consequently low initial residual stresses on the surface (10).

### Surface Hardness

The micro-hardness of the base material and the coating was evaluated on the cross-section of the samples. An automated LM 247 AT LECO micro-hardness tester, equipped with AMH 55 LECO software, was used for the experiment.

### Tribological tests

The scratch test was performed on samples A-DLC and B-DLC. This test was performed on a UMT-3 device. The scratch test is one of the basic methods for monitoring the adhesion of the coating - substrate system, or coating - layer - substrate (5, 11). The principle of the method is the loading of the indenter, which moves horizontally. The indenter is loaded with a constant or continuously increasing force. Penetration of the indenter into the sample creates a scratch. This generates stress at the interface that, when a critical value is reached, causes the coating to tear off the substrate.

The tribometer records the course of the normal force  $F_z$  and the tangential force  $F_t$  acting on the indenter, the values of the coefficient of friction and the acoustic emission signal. If the scratch test is performed at a constant loading force, the scratch hardness number  $HS_p$  can be calculated.

The scratch hardness number, expressed in units of force per unit area, that characterizes the resistance of a solid surface to penetration by a moving stylus of a given tip radius under a constant normal force and speed (4):

$$HS_p = \frac{k \cdot P}{w^2} \quad (1.1)$$

where:

$HS_p$  = scratch hardness number,

$k$  = a geometrical constant,

$P$  = applied normal force,

$w$  = scratch width.

The scratch hardness number can also be calculated if the load force increases continuously. However, it is necessary to measure the width of the track and the adequate load in several places.

## Results and Discussion

### Microstructure of basic material

After polishing, the samples were ultrasonically cleaned in a POLSONIC-2 instrument. The microstructure of the prepared samples was evaluated and the chemical composition was measured by the OES method. Upon preparing the samples, the microstructure in the cross-section was assessed. After the etching operation (12) with 5% NITAL solution (sample A-DLC) and 0.5% hydrofluoric acid (sample B-DLC), the microstructure of the samples is documented in a 3D inverted optodigital microscope image of OLYMPUS DSX 500 from the middle part of the samples. It is clear from the documented microstructure of the base material of Sample A in Fig. 1 that it is a martensitic structure with residual austenite with very fine manganese carbides and sulfides. This microstructure corresponds to a hardened and tempered state. The microstructure of the core of the aluminum alloy sample B is shown in Fig. 2.

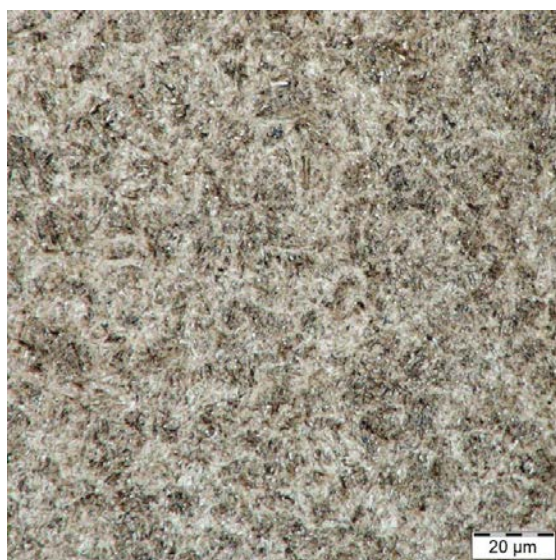


**Figure 1.** Microstructure of sample core A, etched NITAL 5%



**Figure 2.** Microstructure of sample core B, etched hydrofluoric acid 0,5%

### Evaluation of micro-hardness of samples with DLC coating

The Vickers method was chosen for the measurement. The load size of the A-DLC sample was 0.1 kgf, a load delay of 10 s. The micro-hardness of the base material was evaluated for sample B. The magnitude of the load was 0.5 kgf, the delay under load was also 10 s. The final value of the micro-hardness was given by the arithmetic mean of all the three measured values of the micro-hardness at a given distance from the edge of the measured sample.

From the measurement of the micro-hardness of the transverse cut of the sample, it was found that the mean value of the micro-hardness of the base material in sample A reached the value of  $340 \pm 5.2$  HV 0.1. The micro-hardness value of the A-DLC coated sample reached  $750 \pm 10.1$  HV 0.1. The mean value of the micro-hardness of the core of the material in sample B reached  $115 \pm 7.5$  HV 0.05.

### Evaluation of tribological testing

The parameters of the scratch test are given in Table 3. For samples with the DLC coating (A-DLC and B-DLC), the scratch test was performed with a linearly increasing force. The load was chosen with respect to the substrate.

**TABLE III.** Scratch test parameters

| Samples | Normal force<br>$F_z$ [N] | Feed speed<br>$v$ [ $\text{mm}\cdot\text{s}^{-1}$ ] | Scratch length<br>$s$ [mm] |
|---------|---------------------------|---|----------------------------|
| A-DLC   | 0 - 190                   | 1   | 10                         |
| B-DLC   | 0 - 10                    | 1   | 10                         |
| B       | 5; 10; 30                 | 1   | 10                         |
| B-DLC   | 5; 10; 30                 | 1   | 10                         |

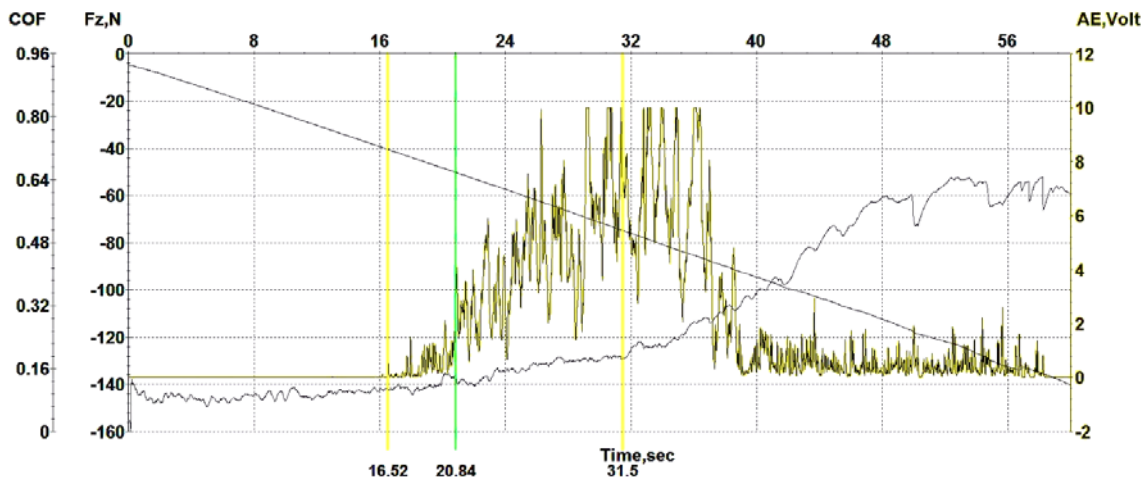


**Figure 3.** Record of the scratch test for the A-DLC sample

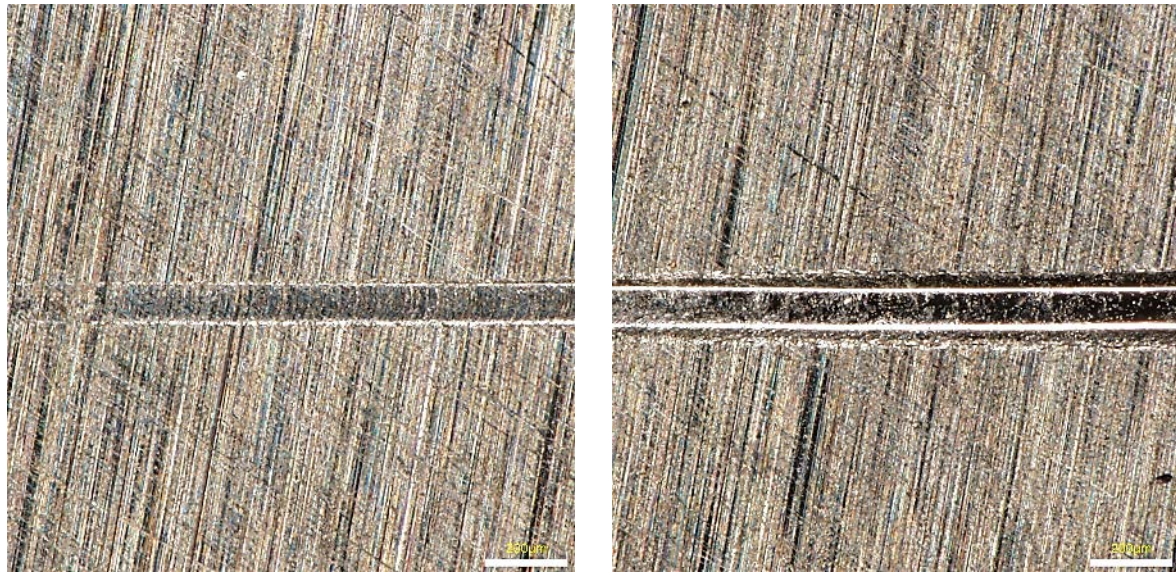
Fig. 3 shows a scratch test record for an A-DLC sample with a linearly increasing loading force  $F_z$  [N]. The record shows the evolution of the friction coefficient (COF) and the evolution of the acoustic emission signal (AE). The record in Fig. 3 is supplemented by images of the indenter trace after the scratch test in Fig. 4. The values of coating cracking correspond to the critical force of 54 N and the values of coating breakage correspond to the critical force of 94 N.

Fig. 5 shows a scratch test record for the B-DLC sample with a linearly increasing loading force  $F_z$  [N]. Due to the substrate, a lower range of loading forces (0 - 10) N was chosen. The transient behavior of COF is obvious in the record. The record in Fig. 5 is supplemented by images of the indenter trace after the scratch test in Fig. 6. The values of coating cracking correspond to the critical force of 5.07 N and the values of coating breakage to the critical force of 6.17 N.

As an additional measurement for the DLC coating deposited on the aluminum alloy (sample B-DLC), a comparison of the scratch resistance with the base material (sample B) was performed. The comparison was made at the levels of the three normal forces (see Table 3). The feed rate of the indenter and the path on which the test was performed remained the same.



**Figure 4a.** The record of the scratch test sample A-DLC



**Figure 4b.** A-DLC sample, critical point No.1

**Figure 4c.** A-DLC sample, critical point No.2

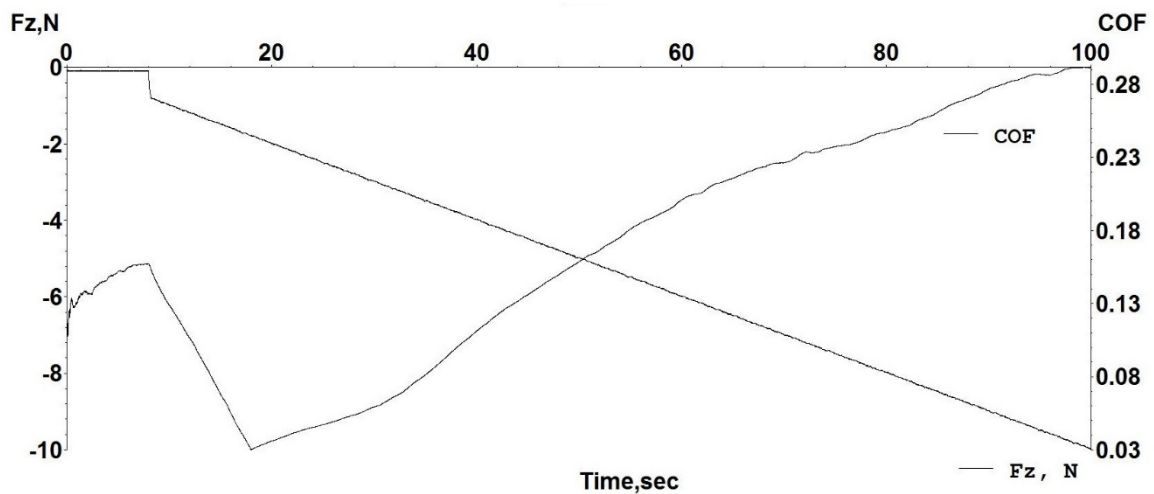


**Figure 5.** Record of the scratch test for the B-DLC sample

The scratch hardness number expresses the wear value of the part surface. Wear can be expressed as an undesirable permanent change in the surface quality, or dimensions of rigid bodies. This change can occur either directly – by contact of two bodies – or indirectly – by means of an inserted medium, gas or liquid. In addition, other physical and/or chemical processes can affect the change in surface quality.

Execution of the scratch removes or displaces the particles of the solid body mass from its functional surface. This changes the geometry, structure and properties of the functional surfaces, which leads to deviations from the optimal behavior in operation. The speed of these changes also depends on the relative hardness of functional areas, their preparation and processing, and other conditions that are set in the tests on tribometer. The UMT-3 tribometer allows evaluating the position of the indenter along the vertical axis, i.e. along the z-axis. After the scratch, it is possible to evaluate the change in the position of the indenter, which indicates the degree of wear of the test specimen and indenter.



**Figure 6a.** The record of the scratch test sample B-DLC

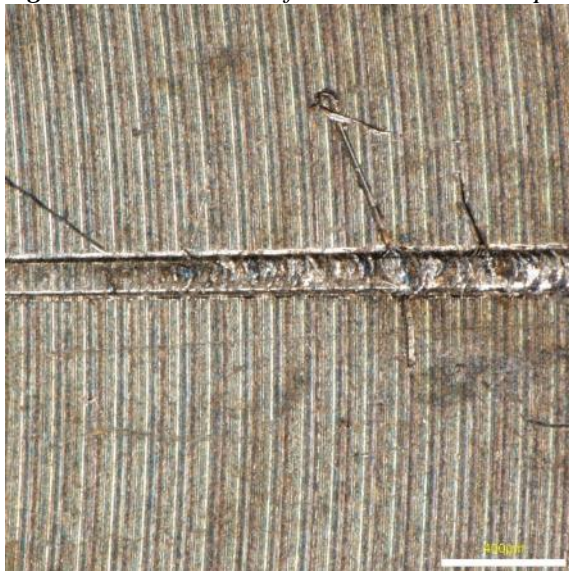


**Figure 6b.** B-DLC sample, critical point No.1



**Figure 6c.** B-DLC sample, critical point No.2

If, during the test, wear occurs predominantly on the test surface of the material, the value of the change in the position along the „z“ axis corresponds to the degree of wear of the test specimen. However, if the indenter is also worn, this value is unreliable and another method, e.g., profilometric, must be used to evaluate the trace in terms of wear. The profilometric analysis evaluates track data, such as the width, profile depth and cross-sectional area of the track. For statistical analysis and comparison, measurements are always performed at the same locations. The track width was measured 2 mm from the track end, then 5 mm from the track end and 8 mm from the track end. The end of the track is always clearly identifiable. The track width is important for evaluating the scratch hardness number.

The scratch hardness number was calculated in accordance with the standard ASTM G171-03 (4) by dividing the applied normal force on the stylus by the projected area of scratching contact, assuming that the hemispherically-tipped stylus produces a groove, whose leading surface has a radius of curvature  $r$ , the tip radius of the stylus. The projected area of the contact surface was therefore a semi-circle, whose diameter was the final scratch width. Therefore, it is possible to complete equation (1.1) to the computational relation:

$$HS_p = \frac{8 \cdot F_z}{\pi \cdot w^2} \quad (1.2)$$

where:

$HS_p$  = scratch hardness number [Pa],

$F_z$  = normal force [N] and

$w$  = scratch width [m].

The scratch hardness number ( $HS_p$ ) validation is suitable for a wide range of base or coated materials. The test is not suitable for assessing the adhesion of a layer to a substrate. The scratch hardness number expresses the ratio of the loading force to the area of the created scratch. The  $HS_p$  value can be affected by the strain rate. A low indenter feed rate was used in the test (see Table 3). The advantage of a low indenter feed rate is the minimal effect of heat generated by the friction of the tip across the sample. The resulting  $HS_p$  values are given in Table 4.

**TABLE IV.** Resulting values of  $HS_p$  (scratch hardness number)

| $F_z$ [N] | $HS_p$ [GPa] - samples |       |
|-----------|------------------------|-------|
|           | B                      | B-DLC |
| 5         | 2.025                  | 0.802 |
| 10        | 2.079                  | 0.466 |
| 30        | 1.842                  | 0.368 |

By interpolating the obtained  $HS_p$  values at the selected load levels, the curves of the scratch hardness number of the base material (sample B) and the coated material (sample B-DLC) were obtained (see Fig. 7).

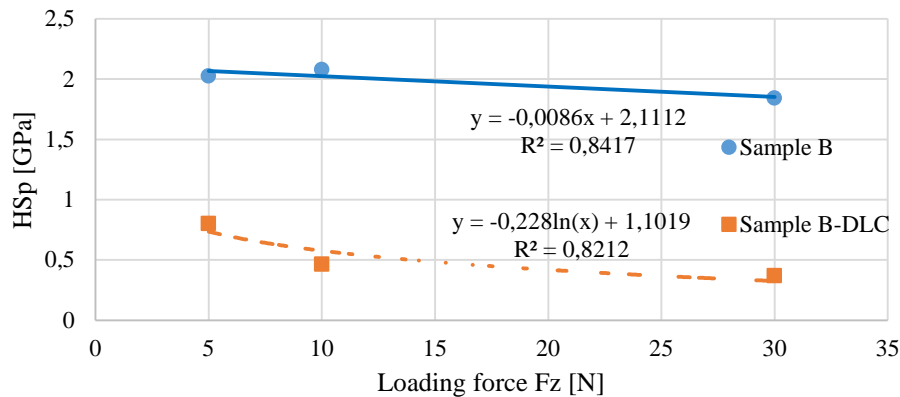


**Figure 7.** Record of  $HS_p$  values

To evaluate the friction coefficient, it is necessary to state that it is a dimensionless quantity defined as the ratio of normal and friction forces. This value is influenced by the condition of the sample surface, the path traversed by the indenter, or measurement time, environmental influences and other influences. The friction coefficient also depends on the surface roughness, due to the influence of surface irregularities, the contact area of the indenter-test specimen pair changes as the load changes.

When evaluating the friction coefficient, its value is usually considered to be the average value measured in the "stable" part of the friction coefficient record depending on the measurement time of the samples. The average values from the measurement of the friction coefficient with the standard deviations of all samples are summarized in Table 5. Fig. 8 shows the curves of the friction

coefficient of the evaluated samples (samples B and B-DLC) under normal load (5, 10 and 30) N. The stable part of the record can be discussed only from the time of the test 10 s.

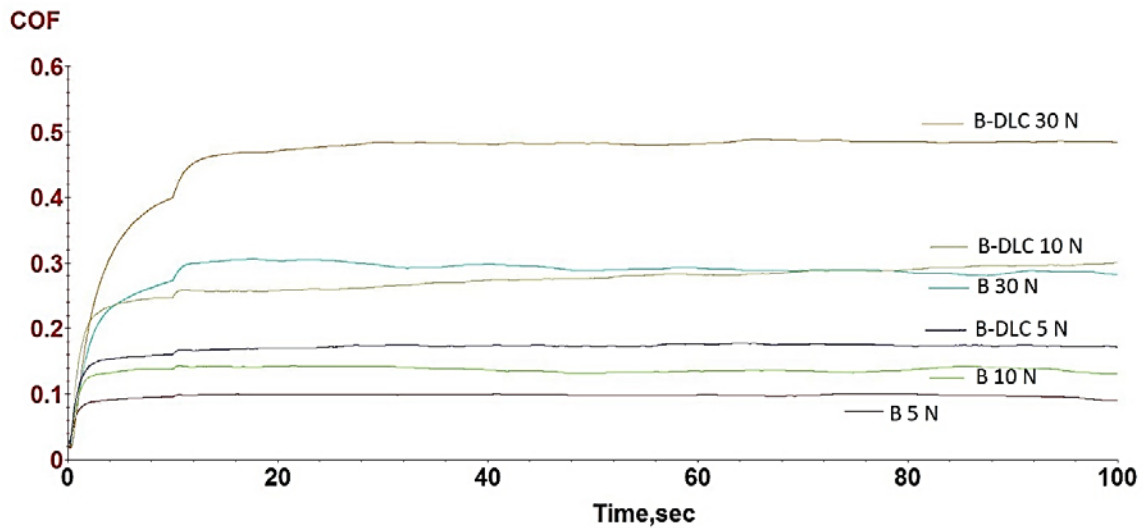


Figure 8. Record of COF values

TABLE V. Resulting values of COF (coefficient of friction)

| $F_z$ [N] | COF [-] - samples     |                      |
|-----------|-----------------------|----------------------|
|           | B                     | B-DLC                |
| 5         | $0.09691 \pm 0.00633$ | $0.1701 \pm 0.01337$ |
| 10        | $0.1362 \pm 0.00976$  | $0.272 \pm 0.02824$  |
| 30        | $0.2842 \pm 0.03308$  | $0.4614 \pm 0.06733$ |

## Conclusions

The subject of this study was the analysis of selected tribological properties of the DLC coating deposited on steel substrate 42CrMo4 (sample A-DLC) and on aluminum alloy substrate EN AW 6082 (sample B-DLC). For the mentioned aluminum alloy, a comparison of the basic tribological characteristics with the base material without coating (sample B) was performed.

After metallographic preparation of the samples, tribological tests were performed as a scratch test with linearly increasing force. The maximum value of the loading force was chosen with respect to the base material (substrate). For the DLC-coated samples, the values of the coating cracking and the values of the coating breakage were determined. These places have been documented (see Figures 4 and 6).

Furthermore, attention was focused on the samples of the aluminum alloy (samples B and B-DLC). The scratch hardness number ( $HS_p$ ) and the friction coefficient (COF) were evaluated for these samples. From the obtained values (Tables 4 and 5) and the compiled  $HS_p$  and COF waveforms (Fig. 7 and 8), the effect of the increasing loading force can be observed. With the increasing loading force, the COF increases, but the  $HS_p$  value decreases. The values of this indirect dependence of the analyzed tribological characteristics correlate.

The obtained tribological characteristics of the DLC coating on the base materials are important to assess the use of specific materials in the construction of weapon components and they

testing (13, 14). Using the obtained values, it is possible to take into account their properties in terms of the surface resistance with the applied DLC coating when designing parts of weapons.

### Acknowledgments

The paper has been prepared thanks to the support of the project The Development of Technologies, Design of Firearms, Ammunition, Instrumentation, Engineering of Materials and Military Infrastructure "VÝZBROJ (DZRO K201)" and Surface technology in applications special techniques SV20-216.

### References

1. I. Barényi, J. Majerík, Z. Pokorný, J. Sedlák, J. Bezecný, D. Dobrocký, A. Jaroš, M. Eckert, J. Jambor and R. Kusenda. Material and technological investigation of machined surfaces of the OCHN3MFA steel. *Metallic Materials*, 2019, 57(2), 131-142. ISSN 0023-432X.
2. Z. Pokorný, J. Kadlec, V. Hrubý, Z. Joska, Q. D. Tran and D. Beran. Plasma nitriding of bored Barrels. *Advances in Military Technology*, 2011, 6(1), 69-76. ISSN 1802-2308.
3. Z. Pokorný, D. Dobrocký, J. Kadlec and Z. Studený. Influence of alloying elements on gas nitriding process of high-stressed machine parts of weapons. *Kovove Materialy-Metallic Materials*, 2018, 56(2), 97-103. ISSN 0023-432X.
4. ASTM G 171 - 03 Standard Test Method for Scratch Hardness of Materials Using a Diamond Stylus1
5. M. Krbaťa, J. Majerík, I. Barényi, I. Mikušová and D. Kusmič. Mechanical and tribological features of the 90MnCrV8 steel after plasma nitriding. *Manufacturing Technology*, 2019, 19(2), 238-242. ISSN 1213-2489.
6. M. Krbaťa, J. Majerík, I. Barényi and M. Eckert. Experimental determination of continuous cooling transformation diagram for high strength steel OCHN3MFA. *IOP Conference Series: Materials Science and Engineering*. Vol. 776, No. 012095, Issue 1, 2020, Slovakia, ISSN: 17578981, DOI: 10.1088/1757-899X/776/1/012095.
7. O. Klanica, D. Dobrocký and F. Onderka. The changes of surface texture parameters of the duplex systems: nitrided layer - coating at CoCrMo alloy. In: *ECS Transaction 15th ABAF BRNO 2014 Advanced Batteries, Accumulators and Fuel Cells*. Brno: Electrochemical Society Inc., 2014, p. 255-259. ISSN 1938-5862.
8. L. Sniezek, I. Szachogluchowicz, M. Wachowski, J. Torzewski, and J. Mierzynski. High cycle fatigue properties of explosively welded laminate AA2519/AA1050/Ti6Al4V. *Procedia Structural Integrity*, Vol. 5, 2017, Pages 422-429. ISSN: 24523216, DOI: 10.1016/j.prostr.2017.07.191.
9. D. Dobrocký, Z. Pokorný, Z. Joska, E. Svoboda and P. Dostál. Surface Structure Evaluation of Functional Surfaces after Plasma Nitriding of Barrel Steel 42CrMo4. In: *ECS Transactions*. New Jersey, USA: ECS The Electrochemical Society, 2019, No. 95, p. 407-418. ISSN 1938-5862.
10. D. Dobrocký, Z. Studený, Z. Pokorný, Z. Joska and P. Faltejsek. Assessment of Surface Structure of Machined Surfaces. *Manufacturing Technology: Journal for Science, Research and Production*, 2019, 19(4), 563-572. ISSN 1213-2489.
11. M. Krbata, M. Eckert, L. Bartosova, I. Barenyi, J. Majerik, P. Mikus and P. Rendkova. Dry Sliding Friction of Tool Steels and Their Comparison of Wear in Contact with ZrO<sub>2</sub> and X46Cr13. *Materials*, Vol. 13, Issue: 10, No. 2359, DOI: 10.3390/ma13102359, 2020.

12. D. Dobrocký, Z. Pokorný, Z. Studený and M. Surlakova. Influence of the carbonitriding to change the surface topography of 16MnCr5 steel. In: METAL 2017 - 26th International Conference on Metallurgy and Materials, Conference Proceedings. Brno: TANGER Ltd., 2017, p. 1085-1091. ISBN 978-808729479-6.
13. J. Balla, Z. Krist, F. Racek, P. Melša, V. Neumann, and C. I. Le. Analysis and Parameter Identification of Automatic Cannon Carriages. Defence Science Journal, 2018, 68(6), 525-532. ISSN 0011-748X.
14. V. Hutsaylyuk, M. Chausov, V. Berezin, A. Pylypenko and K. Volyanska. Influence of Dissipative Structures Formed by Impulsed Loads on the Processes of Deformation and Fracture. Advances In Fracture And Damage Mechanics XII, Key Engineering Materials, vol. 577-578, p. 273, 2014, DOI: 10.4028/www.scientific.net/KEM.577-578.273. ISSN: 1013-9826.

## Thermal Model of Li-ion Battery Pack in PCM Case

M. Toman<sup>a</sup>, R. Cipin<sup>a</sup>, and P. Vorel<sup>a</sup>

<sup>a</sup> Department of Power Electrical and Electronic Engineering, Brno University of Technology, Technicka 12, Brno 616 00, Czech Republic

The paper deals with the thermal model of a battery pack made of a phase-change material. The model is based on the finite element method and is created in the ANSYS software. The performed simulations indicate that the maximum temperatures are lower compared to a battery pack made of an ordinary material without the possibility of phase change.

### Introduction

At present, we can observe a very rapid development of battery-powered devices. These devices can be realized from relatively low power to very powerful devices such as electric cars or even electric-powered airplanes, see (1). Battery packs for such performance applications need to be designed so that their safety as well as durability is as high as possible. Both of these parameters can be strongly influenced by temperature and therefore thermal analysis plays an important role in the design of battery packs. For this reason, the design of the battery packs and also their thermal models are needed to be constantly improved.

To achieve sufficiently low temperatures, there are usually used fans that blow cooling air through battery packs or liquid cooling systems in heavy-duty. However, another possible way to keep temperatures low is to use special materials that use latent heat to keep the temperature low. These are the so-called phase change materials (PCMs) or sometimes called latent heat systems (LHS), see (2). These materials serve as thermal protection especially in nonstandard conditions, for example, during short circuits or accidents, when they absorb increased heat into themselves. Temperature simulation of a battery pack which uses PCM is the subject of this article. The authors have already dealt with this issue, see (3). But in this article, the issue will be studied more thoroughly and it will be performed a comparison with a battery of the same parameters, which however does not use the PCM.

### Finite Element Model of Battery Pack

The subject of the analysis is a simple battery pack, which can be seen in Figure 2. The thermal model is based on the finite element method and is created in a well-known ANSYS software. The battery pack consists of nine 18650 battery cells. The individual battery cells are modeled as cylindrical bodies with different thermal conductivities in radial and axial directions. This method of battery cell modeling has already been used by the authors, see (4), and gives expected results with sufficient accuracy. The individual battery cells are placed in a case made of PCM. The method of PCM modeling is described below.

### Modeling of Phase Change

For modeling of the phase change, an effective heat capacity method can be used. The principle of this method should be clear from Figure 1. It is obvious from this figure that the specific heat  $c$  of the PCM is temperature-dependent thus  $c = c(T)$ . The material properties describing the phase-change material are the nominal specific heat  $c_n$ , the specific latent heat  $I$ , and the temperature range of the phase transition  $\Delta T$ . The goal is to obtain a value of  $\Delta c$ , see Figure 1. A general dependence between the mentioned parameters can be written as follows:

$$I = \int_{T_1}^{T_2} [c(T) - c_n] dT, \quad [1]$$

where  $T_1$  is the temperature at the beginning of the phase change and  $T_2$  is the temperature at the end of the phase change. Due to the rectangular shape in Figure 1, equation 1 can be simplified into following form:

$$\Delta c = \frac{I}{\Delta T}. \quad [2]$$

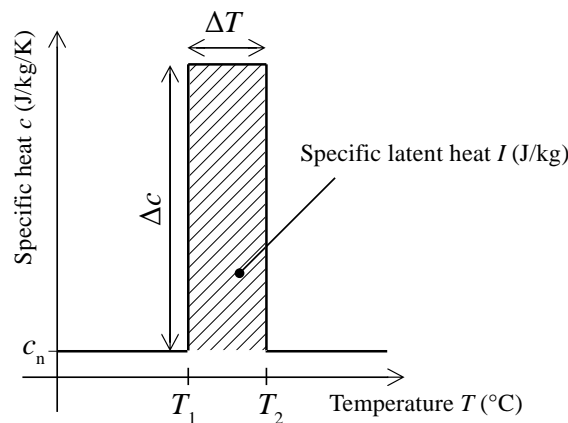
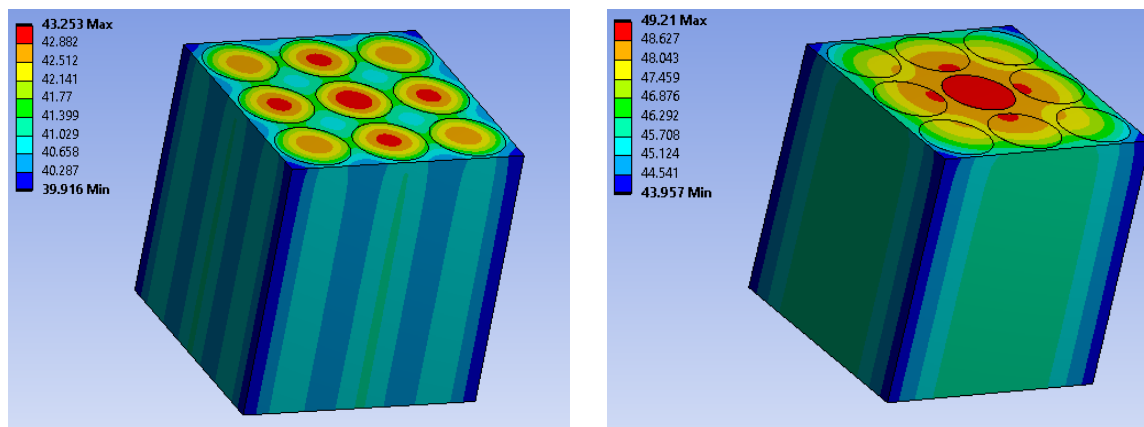


**Figure 1.** Dependence of the specific heat of the PCM on the temperature.

### **Simulations**

The battery pack model was created in the ANSYS software. There was performed a transient analysis with a simulation time of 1 hour. Battery cells LG INR18650 MH1 with nominal capacity 3200 mAh were considered in the simulations. Additional manufacturer data of battery cells can be found in (5). Some special thermal properties of the battery cells such as thermal conductivity in the axial and radial direction were used from (6). Properties of the PCM were used from (2). Power losses of 0.3 W were considered in each cell, which is the value obtained with respect to the rated current and the rated internal resistance of one cell. The battery is cooled by natural convection with the heat transfer coefficient of  $5 \text{ W}\cdot\text{m}^{-2}\cdot\text{K}^{-1}$  on side surfaces and  $2 \text{ W}\cdot\text{m}^{-2}\cdot\text{K}^{-1}$  on top of the pack (side of cell outlets), ambient temperature is considered  $35 \text{ }^\circ\text{C}$ . Simulation results can be seen in Figure 2 (a). For comparison, the simulation was also performed without considering the phase-change material. The results of this simulation are shown in Figure 2 (b).



(a) with phase-change material

(b) without phase-change material

**Figure 2.** Simulation results.

## Conclusion

The paper deals with thermal modeling of the battery pack made of the phase-change material. A model based on the finite element method was created in ANSYS software. Using this model, the transient simulation was performed at rated battery load. In the end time, the maximum temperature reaches about 43.3 °C. For the comparison, there was also created the model without considering the phase-change material. In this model, the maximum temperature was almost 50 °C and the temperature throughout the battery pack was less evenly distributed. In the full version of the article, the simulations will be more expanded, and the results will be discussed in detail.

## Acknowledgments

This research work has been carried out in the Centre for Research and Utilization of Renewable Energy (CVVOZE). Authors gratefully acknowledge financial support from the Ministry of Education, Youth and Sports under institutional support and BUT specific research programme (project No. FEKT-S-20-6379).

## References

1. J. Kadlec, R. Cipin, B. Klima, D. Cervinka, and P. Vorel, *Li-ion accumulators for propulsion system of electric Airplane VUT 051 RAY*, *Journal of Solid State Electrochemistry*, **18**, p. 2307-2313, (2014). DOI: 10.1007/s10008-013-2312-z.
2. Outlast Latent Heat Systems, <https://lhsmaterials.com/> (2020).
3. M. Toman, R. Cipin, and P. Vorel, *Thermal Calculation of Li-Ion Battery Pack*, *ECS Transactions*, **81**, p. 105-110, (2017).
4. M. Toman, R. Cipin, P. Vorel, and D. Cervinka, *Dynamic Thermal Model for Cylindrical Battery Cell Temperature Modeling*, *ECS Transactions*, **95**, p. 371-377, (2019).
5. LG Chem, <https://www.lgchem.com/> (2020).
6. S.J. Drake, D.A. Wetz, J.K. Ostanek, S.P. Miller, J.M. Heinzl, and A.Jain, *Measurement of anisotropic thermophysical properties of cylindrical Li-ion cells*, *Journal of Power Sources*, **258**, p. 298-304, (2014).

## Design of Power Coupled Resonant Circuit for Wireless Power Transfer

R. Tomanek<sup>a</sup>, J. Martis<sup>a</sup>, and P. Vorel<sup>a</sup>

<sup>a</sup> Department of Power Electrical and Electronic Engineering, Brno University of Technology, Technicka 12, Brno 616 00, Czech Republic

This paper describes the design of a power coupled resonant circuit for wireless power transfer with coils distance of 600 mm and a nominal power of 20 kW. The transfer is provided by the inductive coupling of the resonant circuit with 800 mm diameter coils. The resonant circuit is powered by an inverter with IGBT modules working on frequency 130 kHz. The functionality of the realized device is verified by measurements, the evaluation of which is at the end of the article.

### Introduction

Due to the rapid development of electromobility, the demands on the recharging of vehicle batteries are also increasing. In addition to reducing the charging time, and thus increasing the charging power, the aim is also to enable easy charging even during short stops (eg in front of an intersection or for electric buses at a stop). Last but not least, the comfort of the operator is also addressed.



**Figure 1.** *Designed device during the measurement.*

These factors lead to the development of chargers with wireless power transmission, which will enable high-power charging with high efficiency. In this work we deal with the design and implementation of wireless transmission of 20 kW at a distance of 600 mm, which with its parameters could be the basis for a wireless charging station.

### Wireless Power Transfer Concept

Wireless power transfer is designed as a power coupled series resonant circuit with inductive coupling. The design of coupled resonant circuits involves both the design of optimal dimensions and the number of turns of the coils, as well as the determination of the parameters of capacitors.

The resonant circuit is powered by a power inverter with zero-switching at a resonant frequency. The control of the primary coil current is ensured by the pulse-density modulation (PDM). (1)

### Series Resonant Inductive Coupling Circuit

#### Inductors

Inductors were designed as cylindrical single-layer air coils with a diameter of  $D = 800$  mm. The total inductance factor of the coils is  $A_L = 1.284$   $\mu\text{H}$  and the coefficient of coupling is  $k = 0.063$ .

The number of turns of the coils to transfer the required power with optimization for maximum transmission efficiency can be determined as follows (2):

$$N = \frac{V_{\text{in,ef}}}{\sqrt{\omega \cdot k \cdot A_L \cdot P_L}} = \frac{486}{\sqrt{880 \cdot 10^3 \cdot 0.063 \cdot 1.28 \cdot 10^{-6} \cdot 24 \cdot 10^3}} \doteq 11. \quad [2]$$

The windings are made of a copper high-frequency lacquered cable to reduce the skin effect. The assumed value of the current through the coupled resonant circuit is  $47 A_{\text{RMS}}$ , for which the cross-section of the conductor is also dimensioned.

#### Capacitors

To achieve a resonant frequency of 140 kHz, a capacitor with a nominal capacitance according to [3] is required.

$$C = \frac{1}{\omega^2 \cdot N^2 \cdot A_L} = \frac{1}{(880 \cdot 10^3)^2 \cdot 11^2 \cdot 1.284 \cdot 10^{-6}} \doteq 7.5 \mu\text{F} \quad [3]$$

The capacitors must be rated for a current of  $47 A_{\text{RMS}}$  and a maximum voltage of 15 kV. For technological reasons, the capacitor is realized by a series combination of eight capacitors with a partial capacitance of 60 nF. Each capacitor is dimensioned for a current of  $60 A_{\text{RMS}}$ , and a maximum voltage of 6 kV.

### Results of Measuring

The device is not yet completely finished, but they have already performed the initial measurement with reduced power. During testing with power supply from a three-phase network with a nominal voltage of  $3 \times 400$  V, a power almost 13 kW was transmitted over a distance of 600 mm into a resistive load with a resistance of 10  $\Omega$ . Under these conditions, the wireless transfer reached a total efficiency of 80 %. The important values from a measurement are given in Tab. 1.

**TABLE I.** Measured Parameters.

|                     |                      |
|---------------------|----------------------|
| Input phase voltage | 237 V                |
| Input power         | 15.93 kW             |
| Coil distance       | 600 mm               |
| Output voltage      | 355 $V_{\text{RMS}}$ |
| Output power        | 12.78 kW             |
| Total efficiency    | 80.2 %               |

In Fig. 2 they can be seen waveforms of one IGBT in the power inverter on the primary side. The blue curve is the output voltage from half-bridge  $V_{\text{CE}}(t)$ , the green curve is resonant circuit

current  $i_1(t)$  and the red curve is the gate voltage  $V_{GE}(t)$ . The principle of pulse-density modulation is obvious from the gate voltage waveform.

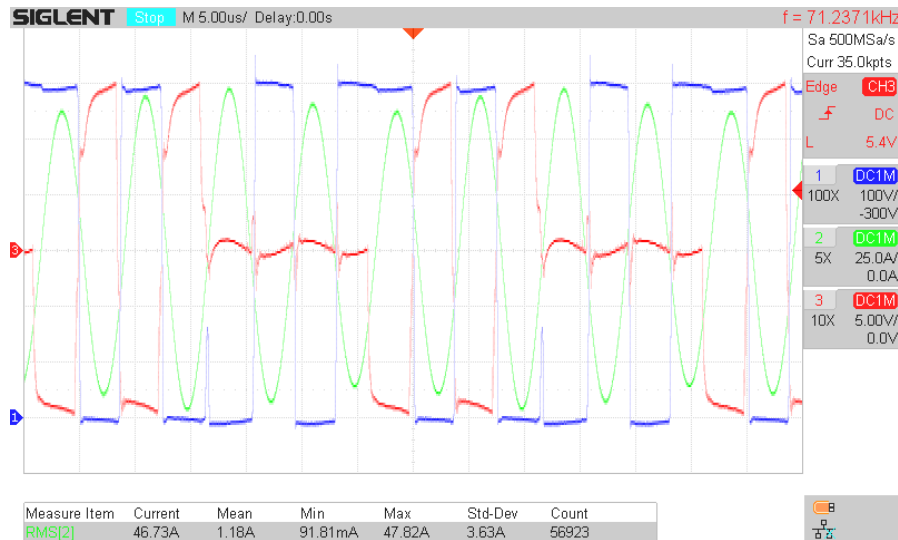


**Figure 2.** Measured waveforms of IGBT in the power inverter: CH1:  $V_{CE}(t)$ , CH2:  $i_1(t)$ , CH3:  $V_{GE}(t)$ .

## Conclusion

Concept of wireless power transfer including basic parameters is described in the article. Furthermore, the measurement on the realized device is documented here. Although the device is not yet completely finished and tuned, it has already been possible to perform the measurement at a reduce power transfer of 13 kW. For this power, the efficiency of 80% was reached. The realized device during the measurement is shown in Fig. 1.

In the next steps, it is planned to finish the adjustment of all parameters to achieve optimal power transmission. It is also planned to perform loss analysis in individual parts and the sensitivity analysis of transmitted power and overall efficiency on some parameters like the mutual position of transmitting and receiving coils, the influence of nearby objects, etc.

## Acknowledgments

This research work has been carried out in the Centre for Research and Utilization of Renewable Energy (CVVOZE). Authors gratefully acknowledge financial support from the Ministry of Education, Youth and Sports under institutional support and BUT specific research programme (project No. FEKT-S-20-6379).

## References

1. J. Martis and P. Vorel, Wireless Power Transfer 2.5 kW with Simple Control and High Efficiency. In Proceedings of the 2018 18th International Conference on Mechatronics – Mechatronika (ME). 1. (2018). p. 93-98. ISBN: 978-80-214-5543-6.
2. T. Pitner, *Wireless Energy Transfer Using Tied Resonance Circuits*. Brno: (2017). Final thesis. Brno Grammar School, Captain Jaros's class 14.

## Compact Battery Power Source for Oscilloscope

J. Martis<sup>a</sup>, P. Vorel<sup>a</sup>, T. Lažek<sup>a</sup>

<sup>a</sup> Department of Power Electrical and Electronic Engineering, Brno University of Technology, Brno 61600, Czech Republic

### Introduction

Oscilloscope measurements in power electronics (transistor converters) very often require a galvanic separation of the oscilloscope ground from the mains supply. However the simple isolating supplying transformer (50 Hz or 60 Hz) is not sufficient because of its high parasitic capacitance between the primary and secondary side (often several  $nF$ ). In many cases (when measuring waveforms with high  $dv/dt$  slope) this capacitance causes unacceptably high parasitic current pulses and ringing, influencing not only the measurement results but also the measured inverter with a risk of its damage.

This is why a supply source with a low parasitic capacitance (less than 50 pF) is required. It can be constructed as a DC source powered from the mains (modern oscilloscopes don't include an input supply transformer but a DC/DC converter powered from the mains through a rectifier). So not only AC but also DC supplying voltage can be used. However a battery supplied source is advantageous. The parasitic capacitance to the mains (or to the surround ground) is suppressed, although it can never be zero because of non-zero dimensions of batteries, wiring etc. Battery supplied oscilloscopes can be bought but they are very expensive.

The constructed battery powered source provides the DC output voltage of ca. 300 V and power of 60 W. This is enough for many common smaller oscilloscopes. There are 14 pieces of 18650 Li-ion cells used in the device. All the batteries are connected in parallel so the input voltage of the converter is very low – it can drop to ca. 3 V at the discharged cells. This is why a high input DC current is necessary. This solution with no series cells is advantageous because of no need of any balancing circuits. However the extremely low input voltage presents a small complication to the construction of the converter.

### Battery selection

There are 14 cells type NCR18650A from Panasonic used in the device. As they are connected in parallel, the battery voltage varies in the range from ca. 3 V to ca. 4.2 V. The used type of cells include a protecting over-current (ca. 6 A) circuit and also over-voltage and under-voltage protection. These cells were optimized by the manufacturer to high energy but not high power. Therefore the cell capacity is higher (3100 mAh) and the internal resistance is slightly higher (110 m $\Omega$ ). The total pack energy capacity is ca. 150 Wh (11.2 Wh per cell). This is enough for our application.

### Main DC/DC converter

The DC/DC converter in Figure 1 represents the core of the device. A push-pull resonant forward converter with a pulse transformer is used. As the input voltage is extremely low, there is no problem with a higher turn-off drain-source voltage (higher in comparison with a full-bridge

connection). Furthermore, there are half conduction losses in comparison with the full bridge, which is advantageous as the drain current is high.

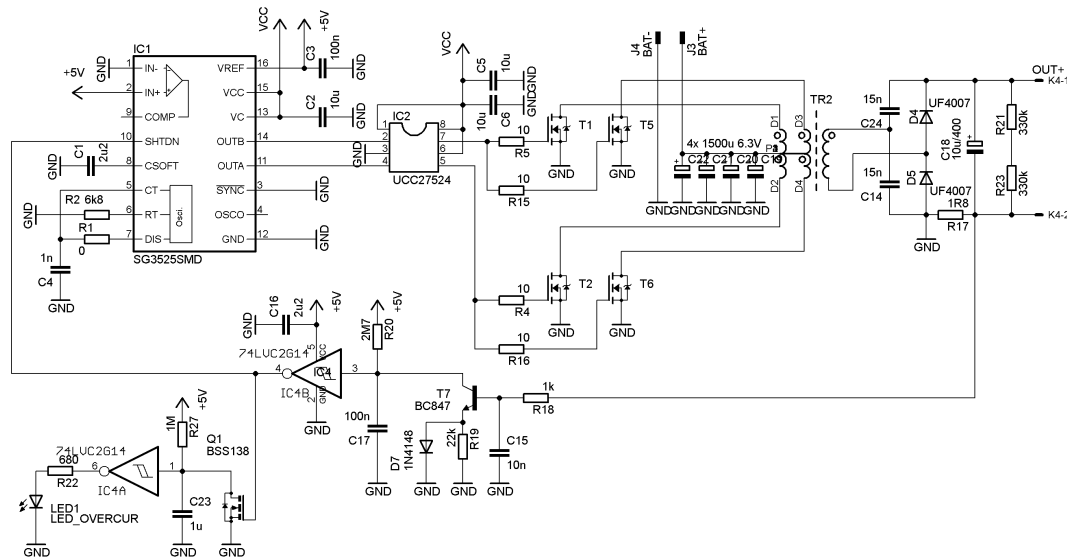


**Figure 1.** Schematics of the converter power and control part.

There is no choke on the output (behind the output rectifier). This is why no control of the output voltage via PWM is possible. In both half-periods the short circuit created with the switched-on transistors T1 and T5 (or T2 and T6) is transformed to the secondary side but a leakage inductance remains there (on the secondary side). This is tuned to the resonance with resonant capacitors C24 and C14 (effectively in parallel for AC signal). The switching frequency corresponds to the resonant frequency. This is why the secondary and primary current waveforms are sine and there are almost zero turn-on and turn-off losses of the power transistors on the primary side (zero current switching ZCS). Further this principle enables to compensate for the drop of the output voltage caused by the transformer leakage (1).

The secondary rectifier is connected as a voltage doubler. This brings a small disadvantage of higher RMS current of the secondary winding and of the diodes but at the same time it enables to decrease the secondary voltage in half in comparison with a bridge rectifier. This enables us to reduce the number of secondary turns in half (production simplification).

As the output voltage is not controlled it varies in range of ca 200 V (battery discharged, full power) to 340 V (battery fully charged, no load). This is fully acceptable by the oscilloscope. There is an over-current protection in the converter based on the transistor T7. The secondary current is measured with the resistor R17. In the case of an over-current the transistor T17 switches-on and the SHTDN pin of the control IC SG3525 receives a log. 1 signal which blocks the PWM. This state is prolonged with the capacitor C17 which is discharged by the transistor but it is charged only slowly through a high resistance of R20 to avoid fast oscillations of the protection.

### Auxiliary power supply

As the control circuits of the main converter need a DC supply voltage of around 10 V there must be an auxiliary low-power DC/DC converter generating the supply voltage (VCC) from the cell voltage. Its schematics is in Figure 2. This converter also provides the required under-voltage protection (constructed around IC3).

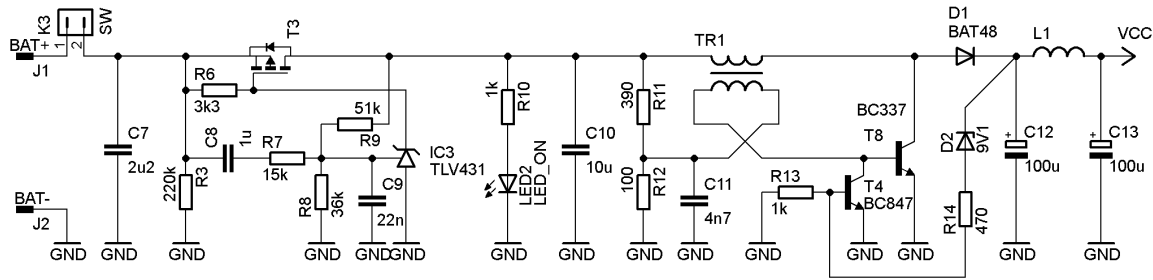


**Figure 2.** Schematics of the auxiliary power supply.

## Prototype

The DC/DC converter is realized on a single PCB. Both sides of this PCB can be seen in Figure 3. Also the whole device including the battery built into a housing is presented here. There are also the connectors for battery charging and an output power socket for the oscilloscope. Also a battery fuse is included.



**Figure 3.** Voltage converter board (left and middle) and a finished prototype (right).

## Conclusion

The battery supply for an oscilloscope is a very useful device when working in the field of power electronics. There are battery supplied oscilloscopes in the market but their price is high. The presented source construction can significantly improve the user parameters of the oscilloscope. The construction is not difficult and it is not expensive. The device was fully tested with the load (oscilloscope) and also the thermal tests were successfully performed.

## Acknowledgment

This research work has been carried out in the Centre for Research and Utilization of Renewable Energy (CVVOZE). Authors gratefully acknowledge financial support from the Ministry of Education, Youth and Sports under institutional support and BUT specific research programme (project No. FEKT-S-20-6379).

## References

1. M. Salem, A. Jusoh, N. R. N. Idris and I. Alhamrouni, "Performance study of series resonant converter using zero voltage switching," 2014 IEEE Conference on Energy Conversion (CENCON), Johor Bahru, 2014, pp. 96-100, doi: 10.1109/CENCON.2014.6967483.

## Simulation of Thermal Runaway Effect in Lithium-Ion Batteries

P. Vyroubal<sup>a</sup>, T. Kazda<sup>a</sup>, M. Mačák<sup>a</sup>

<sup>a</sup> Department of Electrical and Electronic Technology, Brno University of Technology, Technická 10, 616 00 Brno, Czech Republic

This article deals with the simulation of thermal abuse model in ANSYS Fluent software in lithium ion battery e-bike pack. The e-bike battery pack is made by 40 pieces of standard 18650 li-ion cells. The model of each battery cell was created as homogenous, using MSMD modelling approach.

### Introduction

Safety is a major obstacle to the wider use of lithium-ion batteries in electric vehicles. With the constant improvement of lithium-ion batteries in energy density, increasing their safety for the development of electric vehicles is an increasingly relevant topic. Thermal runaway is a key scientific issue in battery safety research. This article provides an insight into the possibility of numerical simulation of the thermal runaway effect.

The mechanisms that lead to the thermal runaway effect can be of the mechanical, electrical or thermal type.

The consequence of these factors is an internal short circuit in the battery and the formation of subsequent chain exothermic reactions, which lead to decomposition reactions of the materials of which the battery is composed.

#### Mechanical initiation

Destructive deformation or displacement of a structure under the action of force are two common features of a mechanical type of damage [1]. Collisions and subsequent crushing or penetration of a foreign body into the battery are typical factors. If the battery is deformed, the separator may rupture and thus an internal short circuit may occur, or the electrolyte may leak, causing a subsequent fire. During penetration, a foreign body penetrates into the battery structure (e.g. in the event of an accident) and in the case of a conductive body, the internal structure of the battery is short-circuited.

#### Electrical initiation

In the case of electrical initiation, it is mainly a short conductive connection of the battery electrodes, so we speak of an external short circuit. Furthermore, overcharging the battery, for example by a failure of the BMS, which has the task of monitoring and stopping the charging process [2]. This is then accompanied by gassing and heat generation (Joule heat and heat generated by electrochemical reactions). Another factor can be excessive battery discharge (BMS failure).

#### Thermal initiation

Local overheating of the battery can be caused by either mechanical and electrical initiation or poor thermal management of the entire system, when the battery is excessively burned by its

surroundings [3]. Overheating is then associated with an internal short circuit in the battery and the breakdown of the separator and the ingress of spontaneous exothermic reactions.

### Results and discussions

The numerical model was compiled on the basis of findings from previous measurements. It was necessary to measure the charging and discharging curves of one cell and implement them together with the geometry and boundary conditions into ANSYS Fluent [4]. The following Figure 1 illustrates the geometric model of a 1/4 e-bike battery pack (left) and a comparison of the measured and simulated discharge curve (at current 1C) of one cell (right). Here was the MSMD simulation approach used [5].

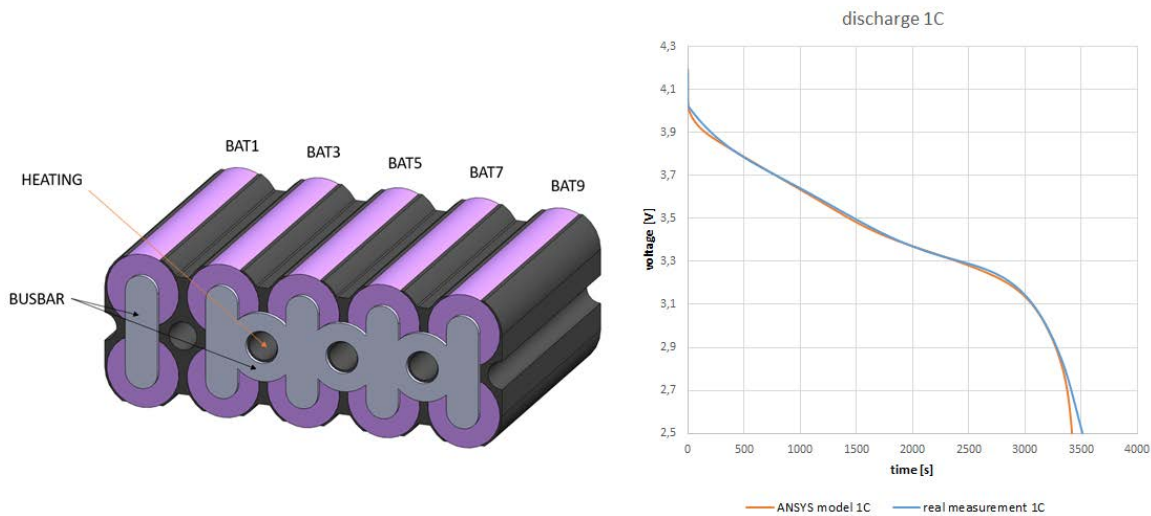


**Figure 1.** Temperature map on the battery pack.

The next Figure 2 shows a color temperature map of the whole battery pack, with constant heating. Simulation is steady-state, without considering startup thermal mechanisms.

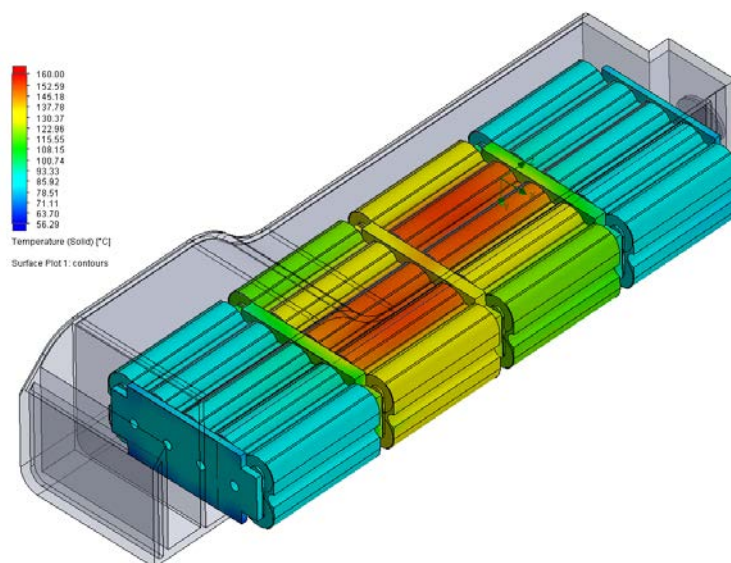


**Figure 2.** Temperature map on the battery pack.

The following graph shows the temperature profile on the individual cells (as they are named in Figure 1 on the left site). This simulation is already transient (time-dependent) and considers the thermal processes, that occur when the battery overheats. It is clear from the figure, how the temperature rises uncontrollably on cells near the heating system and the subsequent triggering of exothermic reactions in other cells.

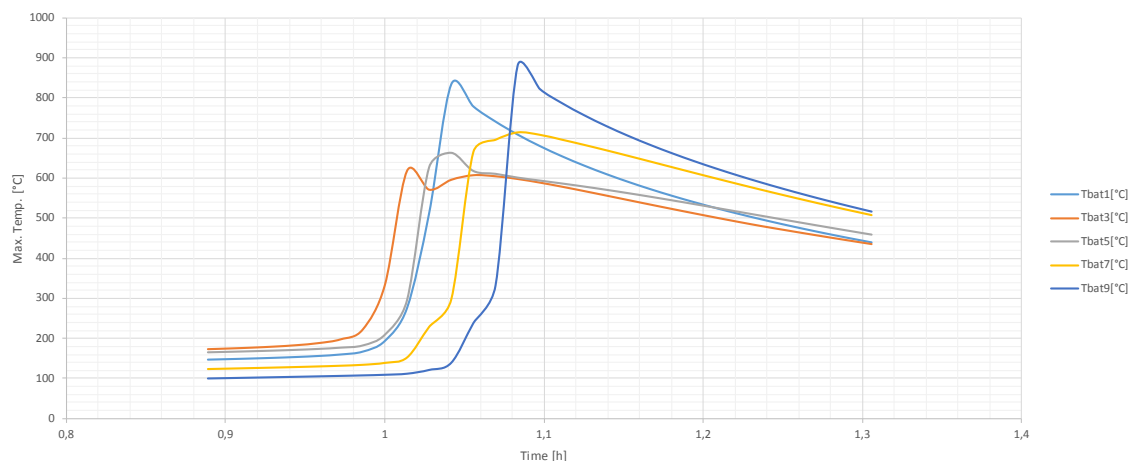


**Figure 3.** Temperature profiles on individual cells of the battery pack.

### Acknowledgments

This work was supported by the specific graduate research of the Brno University of Technology No. FEKT-S-20-6206 and National Centre for Energy TN01000007.

### References

1. X. Feng and X. Minggao, *Energy Storage Materials*, **10**, (2018).
2. ANSYS Fluent Theory Guide, (2019).
3. ANSYS Fluent Customization Manual, (2019).
4. P. Vyroubal and T. Kazda, *Journal of Energy Storage*, **11** (2018).
5. P. Vyroubal, T. Kazda and M. Mačák, *ECS Transactions*, **87**(1) (2018).

## Testing of a Prototype Device using Electrochemical Impedance Spectroscopy (EIS) Method

A. Zsigmond<sup>a</sup> and J. Libich<sup>a</sup>

<sup>a</sup>Department of Electrical and Electronic Technology, Faculty of Electrical Engineering and Communication, Brno University of Technology, 616 00 Brno, Czech Republic

This paper deals with the electrochemical processes in lithium-ion batteries. To characterize the different electrochemical processes a method called electrochemical impedance spectroscopy (EIS) is used. The devices which perform EIS analysis are spread in all electrochemical laboratories but are expensive and their operation need certain level of knowledge and experience. This work is aiming to provide low-cost, user friendly device for EIS analysis. The prototype of experimental device which utilize EIS method to characterize electrochemical parameters of cell is described. The prototype EIS device is tested and obtained results are compared with reference unit.

### Introduction

Work with the lithium battery (LIB) began in 1912 but it was not until the early 1970s when the first non-rechargeable lithium batteries became commercially available. The use of lithium metal was not possible due to the instability of the material, especially during charging. Research shifted to a non-metallic lithium battery using lithium ions. In comparison lithium-ion is more stable than pure lithium, however it is lower in energy density. These can be divided into four groups. Small cylindrical, which has a solid body without terminals and can be used in laptop batteries. Large cylindrical with solid body and large threaded terminals. Batteries with soft, flat body called pouch. These are mainly used in cell phones. The fourth type is a semi-hard plastic case with large threaded terminals, called prismatic and they are used as vehicle traction packs. The primary components of a lithium-ion battery are the positive and negative electrodes, the separator and the electrolyte. The negative electrode is generally made from carbon, while the positive electrode is metal oxide. Lithium salt in an organic solvent is used as the electrolyte. Depending on the direction of current flow the electrochemical roles of the electrodes reverse between anode and cathode. The most popular material used as the negative electrode is graphite. The positive electrode is either, layered oxide (lithium cobalt oxide), a polyanion (lithium-iron phosphate) or spinel (lithium - manganese oxide) [1 – 12].

### Experiments and Results

The experimental device was used for EIS measurements see Figure 1 below. For measuring, this unit is connected to a computer via USB and is controlled by software. Through this software the unit is run by typing in commands into command line.

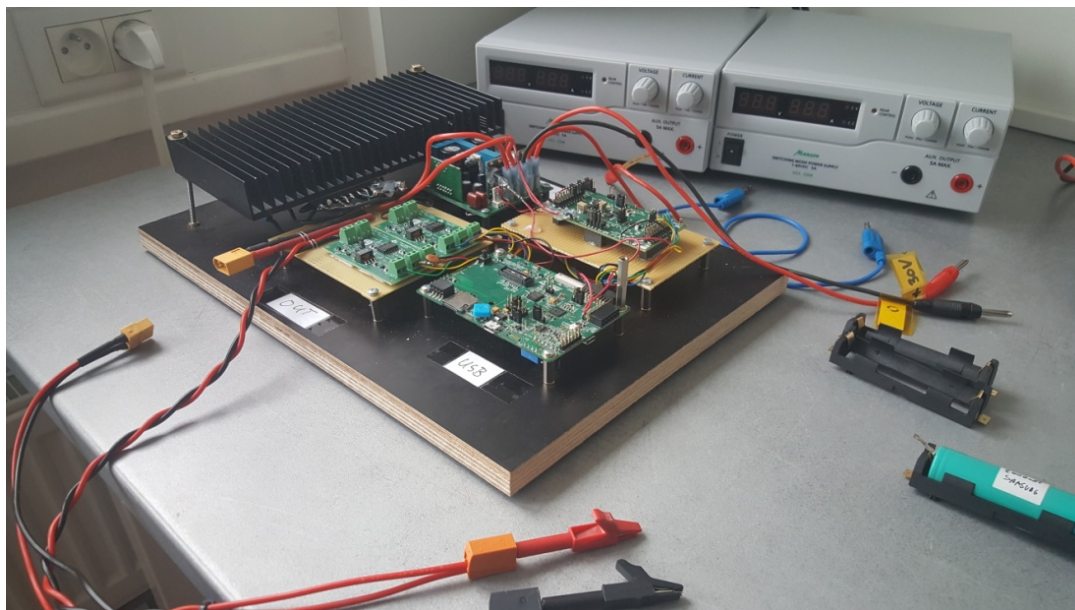


**Figure 1.** Experimental device with power supply and other accessories.

### Acknowledgments

This work was supported by specific graduate research project of the Brno University of Technology: Materialy a technologie pro elektrotechniku IV., reg. no. FEKT-S-20-6206.

### References

1. R. Xiong, Y. Pan, W. Shen, H. Li, and F. Sun, *Renewable and Sustainable Energy Reviews*, **131** (2020).
2. L. J. Aaldering and C. H. Song, *Journal of Cleaner Production*, **241** (2019).
3. G. Pistoia. *Elsevier*, (2014).
4. M. Winter, B. Barnett, and K. Xu, *Chemical Reviews*, **118** (23), 11433-11456 (2018).
5. G. Zubi, R. Dufo-López, M. Carvalho, and G. Pasaoglu, *Renewable and Sustainable Energy Reviews*, **89**, 292-308 (2018).
6. V. H. Nguyen, D. -H. Lee, S. -Y. Baek, and Y. H. Kim, *Materials Letters*, **228**, 504-508 (2018).
7. M. A. Varnosfaderani and D. Strickland, *Vacuum*, **139**, 185-195 (2017).
8. N. Wolff, N. Harting, M. Heinrich, F. Röder, and U. Krewer, *Electrochimica Acta*, **260**, 614-622 (2018).
9. K. W. Knehr, T. Hodson, C. Bommier, G. Davies, A. Kim, and D. A. Steingart, *Joule*, **2**(6), 1146-1159 (2018).
10. P. Korth Pereira Ferraz, R. Schmidt, D. Kober, and J. Kowal, *Journal of Energy Storage*, **18**, 40-49 (2018).
11. D. Sauerteig, N. Hanselmann, A. Arzberger, H. Reinshagen, S. Ivanov, and A. Bund, *Journal of Power Sources*, **378**, 235-247 (2018).
12. J. Wiley, *Hoboken*, 97-105 (2008).

## Pragolab and Bio-Logic SAS: General Company Presentation

Pavel Janderka

**Bio-Logic Science Instruments SAS** is a French designer and manufacturer of high performance laboratory research instruments and software. The headquarters are based in Seysinnet-Pariset, France (close to Grenoble in the French Alps).

Founded in 1983 by a CNRS researcher Yves Dupont and an industrial partner, Bio-Logic SAS is currently headed by François GOY.

- Bio-Logic SAS has designed instruments for a variety of domains and applications:
- Electrochemistry
- Rapid-Kinetics, Spectroscopy & Photosynthesis, including Circular dichroism
- Battery & energy devices testing
- Materials testing
- Electrochemical Scanning systems
- Electrophysiology

And wide range of tools and accessories, including Quartz crystal microbalances, rotating electrodes, spectroelectrochemistry, etc. Software EC-Lab® is a common platform for controlling all Bio-Logic potentiostats/galvanostats, be it single channel or

- multichannel systems and across all our hardware technologies. It is Windows based,
- compatible with either 64-bit or 32-bit operating systems.

Bio-Logic is a rapidly growing global company with affiliate offices in USA (**Bio-Logic USA**) and India (**Bio-Logic India**), and has a large and growing network of worldwide distributors (with representatives in most large and developing countries).

In 2012 **Bio-Logic acquired Uniscan Ltd.**, a British specialist manufacturer of electrochemistry scanning instruments, expanding its product range in order to satisfy the expanding market of scanning electrochemical applications.

### Our GOALS:

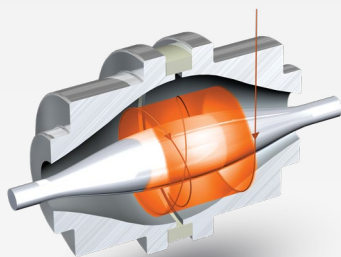
Developing high performance products with unmatched value and providing a high level support to our customers. Together with exclusive Czech and Slovak distributor Pragolab s.r.o., Biologic SAS guarantees the best quality of electrochemical instruments and their support on Czech and Slovak market.



**Figure 1.** VMP-300, new research grade multi-channel potentiostat/galvanostat/FRA, engineered by Bio-Logic, offering up to 16 fully independent channel, optionally with EIS up to 7 MHz and current resolution 80 atto A. The VMP-300 belongs to the SP-300 family (SP-200, SP-240, SP-300, VSP-300) which provides high accuracy in current, potential and EIS measurements.

# Pragolab

Špičkové služby a přístroje z oboru analytické chemie,  
mikroskopie, materiálografie a fyzikálního  
měření pro český a slovenský trh.  
Již více než 30 let.



**ORGANICKÁ ANALÝZA  
A SEPARAČNÍ  
TECHNIKY**



**MIKROSKOPIE  
A PŘÍPRAVA VZORKŮ  
PRO METALOGRAFII**



**FYZIKÁLNÍ  
A MATERIÁLOVÉ  
ANALÝZY**

plynová chromatografie ICP-OES příprava vzorku elementární analýza elektrochemie testery akumulátorů EIS SEA analýza povrchů separační techniky DVS reologie  
atomová spektroskopie GC temperace kapalinová chromatografie UV-VIS spektrometrie GC-MS lyofilizátory konfokální B.E.T. lims mikroskopie materiálografie metalografie  
technická čistota optická mikroskopie elektronová mikroskopie koncentrátory CHNSO analýza AAS analýza částic HPLC hmotnostní spektrometrie centrifugy extruze ICP-  
MS servis AIR monitoring XPS widefield textura spotřební materiál NMR DLS automatické dávkování iGC TOC analýza RVC stopped-flow cirkulární dichroismus XRF XRD

# Lithium batteries that move you further... and higher



## Stability. Reliability. Power. Longevity. For Your Profitability.

Our batteries are different. Why?

Because we don't rely on spec sheets or brand of the cell producer. We do measurements. We test. And analyse. With more than 300 traction batteries in daily operation and 10 years of experience in cell integration, we know how to build a battery up on your requirements.

Based on lab testing and real-life conditions, we know how to create a solution that will bring you maximum stability, reliability, power and longevity. And thus, your profitability.

Industry level lithium battery production represents one of the top-notch sectors of this day. There can be an uncountable list of options with different parameters and use - and the selection of the most appropriate is the key to success. That's why our know-how in this field may secure your investments in any project.

Applications:

- Battery Trolleybus
- Pure Battery Buses
- Hybrid Locomotives
- Construction Machine Electrification
- Batteries for Material Handling and Construction Machines
- And Any Other Of Your Projects



Nadrazní 804  
768 24 Hulín  
Czech Republic

phone: (+420) 720 935 565  
e-mail: [info@evcgroup.cz](mailto:info@evcgroup.cz)  
[www.evcgroup.cz](http://www.evcgroup.cz)

**Title:** Advanced Batteries Accumulators and Fuel Cells – 21<sup>st</sup> ABAF  
**Edited:** Marie Sedlaříková  
Vítězslav Novák  
Tomáš Kazda  
Petr Bača  
**Publishing Office:** Marie Sedlaříková  
Vítězslav Novák  
Tomáš Kazda  
Petr Bača  
**Deadline:** August 14<sup>th</sup> 2020  
**Publisher:** Brno University of Technology  
Faculty of Electrical Engineering and Communication  
Department of Electrical and Electronic Technology  
**Year:** 2020

The authors are fully responsible for the content and language of their contribution

**ISBN 978-80-214-5889-5**